Multiscale investigation of room-temperature viscoplasticity and sustained load cracking of Titanium. Influence of hydrogen and oxygen content.

Arina Marchenko

ParisTech
INSTITUT DES SCIENCES ET TECHNOLOGIES
PARIS INSTITUTE OF TECHNOLOGY

MINES ParisTech

École doctorale 432: Sciences des métiers de l'ingénieur

Doctorat ParisTech

THÈSE

pour obtenir le grade de docteur délivré par

L'École Nationale Supérieure des Mines de Paris

Spécialité: "Sciences et Génie des matériaux"

Présentée et soutenue publiquement par:

Arina MARCHENKO

le 23 novembre 2015

Analyse multi-échelles de la viscoplasticité à froid et de la rupture différée du titane en relation avec ses teneurs en hydrogène et oxygène

---

Multiscale investigation of room-temperature viscoplasticity and sustained load cracking of Titanium. Influence of hydrogen and oxygen content

Directeurs de thèse: **Samuel FOREST**

Matthieu MAZIÈRE

Jury:

M. Xavier FEAUGAS, Professeur, Université de la Rochelle, La Rochelle	Président
M. Bernard VIGUIER, Professeur, Université de Toulouse, Toulouse	Rapporteur
M. Fionn DUNNE, Professeur, Imperial College, Londres	Rapporteur
M. Mikhail LEBEDKIN, Directeur de Recherche CNRS, LEM3, Metz	Examinateur
M. Jérôme CRÉPIN, Professeur, CdM, Mines ParisTech, Paris	Examinateur
Mme Véronique DOQUET, Directrice de Recherche CNRS, LMS, École Polytechnique	Examinateur
M. Samuel FOREST, Directeur de Recherche CNRS, CdM, Mines ParisTech, Paris	Examinateur
M. Matthieu MAZIÈRE, Chargé de Recherche, CdM, Mines ParisTech, Paris	Examinateur
M. Jean-Loup STRUDEL, Professeur, CdM, Mines ParisTech, Paris	Invité

THÈSE

Mines ParisTech
Centre des Matériaux
10 rue Henri-Auguste Desbruères, 91000, Evry, France

Remerciements

Dans la vie, rien n'est à craindre, tout est à comprendre.

Marie Curie

D'après ma courte expérience, cette citation représente "a rule of thumb" dans la vie. Je dirais également : plus le chemin est incertain au début, moins on craint de ne pas réussir, et plus les grandes découvertes nous attendent. C'est grâce à ce futur inconnu qu'on parvient à sortir de sa "zone de confort" plus facilement, ce qui nous permet de se lancer dans des projets d'aventure, de rencontrer des gens qui peuvent complètement changer nos vecteurs de vie. Dans mon cas j'ai eu beaucoup de chance de pouvoir participer au projet FLUTI, de poursuivre mes études doctorales à l'Ecole des Mines, ainsi que d'être encadrée par des gens extrêmement compétents qui m'ont tant appris pendant ces trois années et demi d'études. Naturellement, mes premiers remerciements sont dédiés à mes deux encadrants de thèse : Samuel FOREST et Matthieu MAZIÈRE. Leur professionnalisme, leurs connaissances, leur exigence et leur rigueur alliés à leur patience, leur tolérance, leur écoute, et leur enthousiasme constituent un joli cocktail qui m'a permis d'aller au bout de ma thèse.

Au cours de ma thèse j'ai eu la chance de travailler avec Jean-Loup STRUDEL qui a contribué à donner un sens physique à notre modèle et qui a perfectionné notre fameux article qui qui sera bientôt soumis ! Merci également Jean-Loup pour toutes nos riches discussions, pour votre bonne humeur et votre aide permanente.

Je souhaite remercier chaleureusement la coordinatrice de notre projet FLUTI Véronique DOQUET grâce à qui j'ai pu évoluer dans un environnement de travail rythmé et efficace. Je remercie Bassem BARKIA du Laboratoire de Mécanique des Solides (LMS) qui était toujours prêt à m'aider et à qui je souhaite une belle carrière académique. Merci beaucoup à Ivan GULLOT de l'Institut de Chimie et des Matériaux Paris-Est (ICMPE), Olivier HARDOUIN DUPARC du Laboratoire des Solides Irradiés (LSI), Liang LIANG (LSI), Jean-Phillipe COUZINIÉ (ICMPE), Eva HÉRIPRÉ (LMS), Fabrice COURTAS (ICMPE), Alexandre TANGUY (LMS) pour notre constante collaboration. Un grand merci à Jérôme CRÉPIN pour son attitude toujours amicale, sa capacité d'écoute et son désir d'aider.

Je tiens à remercier les membres du jury qui malgré leurs emplois du temps chargés ont accepté d'être rapporteurs, président et examinateurs. En particulier merci à Fionn DUNNE et Bernard VIGUER qui ont accepté la responsabilité de rapporteur sur ce travail dans un délai si court.

Je suis reconnaissante à l'ensemble des membres du Centre des Matériaux de l'École des Mines, et en particulier à Regis CLEMENT, Abdennour MEDDOUR et René CLUZET pour leur appui lors des nombreuses manipulations ; Olivier DELHOMME et Gregory SAINTE-LUCE pour le support informatique, indispensable; Odile ADAM pour le support bibliographique et pour les références bibliographiques de mon manuscrit ; Veronique MATOS pour la logistique à l'occasion des conférences, séminaires, et ma pré-soutenance; Catherine ROUIL pour son sympathique accueil quotidien. Merci beaucoup à Anne PIANT, Konaly SAR et Liliane LOCICERO qui m'ont beaucoup aidé au cours de ma première année de thèse.
Mes remerciements vont également aux directeurs de l'École des Mines, Benoît LEGAIT et Romain SOUBEYRAN, aux directeurs du centre Jacques BESSON et Jean-Yves HERRY pour avoir su créer et conserver un cadre de travail efficace et agréable pour les doctorants.
Enfin, merci à l'équipe VAL pour m'avoir introduite et guidée dans le monde de *ZeBuLoN*.
Un grand merci à Monsieur PINEAU pour nos nombreux échanges sur le monde de la recherche, mais aussi sur la France et plus accessoirement sur les œuvres de Tolstoi. Merci beaucoup Monsieur PINEAU d'avoir participé à ma répétition de soutenance et à la soutenance elle-même. Je reste toujours impressionnée par vos connaissances pointues sur la mécanique de la rupture et par votre curiosité envers ce monde.
Je souhaite remercier mes super collègues français avec qui on a traversé côte à côte les épreuves et qui m'ont appris beaucoup de choses sur la France, au niveau culturel, culinaire et linguistique. Je pense à Raphael MAESTRACCI, Geoffray BEGUE, Harry POMMIER, Samuel JULES, Aurelien VILLANI, Victor DE RANCOURT, David MASSON, Guillaume MARION, Nicolas GUENINCHAULT, Adrien LEBRUN, Erembert NIZERY. Merci aux thèsards d'hier et d'aujourd'hui: Pierre SALLOT, Prajwal SABNIS, Justin DIRRENBERGER, Guillaume MARTIN, Jia LI, Basava-raju AKULA, Isabelle TURQUE, Franck TANKOUA, Victor FABRE.
Merci à la team russe Vlad YASTREBOV, Nikolay OSIPOV, Vladimir ESSIN pour leur joyeuse compagnie, leur partage d'expérience, et leur aide dans les situations difficiles.
Enfin, je suis heureuse de terminer ces remerciements en pensant à mes proches et ceux qui comptent le plus pour moi : mon mari Jean-Baptiste, mes parents, ma sœur, mon grand-père et ma belle-famille. Sans vous la réalisation de ce projet aurait été impossible. Vous êtes mon back-up et ma source d'inspiration. Merci à vous.

Abstract

Widely used for aircraft or rocket engine manufacturing titanium and its alloys are prone to the room-temperature creep that leads to the phenomenon of sustained load subcritical crack growth. One of the major cause of such unusual viscoplastic behavior of titanium is the phenomena of static and dynamic strain aging which represents an interaction between dislocations and interstitial atoms of oxygen and hydrogen. The aim of the present experimental and numerical multiscale study is to investigate the influence of the interstitial hydrogen and oxygen on the viscoplastic behavior and the resistance to sustained load cracking in commercially pure titanium of phase alpha.

In a first step, a scenario of static and dynamic strain aging was proposed. The presence of the stress peak was attributed to the segregation of interstitial atoms of oxygen on the edge $< c + a >$ dislocations. In case of dynamic strain aging, the observed instabilities, typical for the Portevin-Le Chatelier effect, were associated with the non-planar core of screw $< a >$-type dislocations. The crystal plasticity was introduced into the phenomenological model in order to capture the strain aging phenomena and the anisotropy of the mechanical properties. The modeling approach for strain aging suggested by Kubin-Estrin-McCormick is based on the internal variable called the aging time which corresponds to the waiting time of a dislocation in a pinned state. Finite element simulations were then performed on the polycrystalline aggregates for different number of grains.

At next step, fracture toughness and sustained load cracking tests were performed on the material with different level of hydrogen. Finally, numerical simulations of toughness and sustained load cracking tests using the identified viscoplastic model were carried out for all experimental conditions. A cohesive zone model was then introduced ahead of the crack tip to simulate crack propagation.

Keywords: titanium, toughness, sustained load cracking, hydrogen and oxygen influence, dynamic and static strain aging, numerical crack propagation

Contents

Introduction

Résumé

Grâce au rapport résistance/masse volumique élevé, et à ses performances à haute température, le titane et ses alliages sont largement répandus dans l'industrie aéronautique. Les alliages de titane sont également employés dans d'autres secteurs tels que la chimie, l'énergie, la construction navale et la désalinisation de l'eau de mer pour leur bonne résistance à la corrosion. La biocompatibilité du titane le rend intéressant pour les applications biomédicales comme les prothèses articulaires, les implants dentaires ou les montures de lunettes.
Par ailleurs, le titane flue à température ambiante ce qui conduit à une réduction de la résistance du matériau et provoque un phénomène de rupture différée. La rupture différée se produit dans la structure lors de l'application d'un chargement de niveau inférieur à la ténacité pendant un certain temps d'incubation allant de quelques heures à quelques jours. Une partie des études montrent que ce comportement viscoplastique inhabituel à température ambiante est lié aux phénomènes d'interactions entre les dislocations et les atomes interstitiels comme l'hydrogène et l'oxygène, aussi appelés vieillissement statique et dynamique. L'hydrogène diffuse sans difficulté dans les structures cristallines du titane à cette température, il peut interagir rapidement avec les dislocations sans en diminuer leur mobilité, contrairement aux autres atomes interstitiels comme l'oxygène dont la diffusion est beaucoup plus lente. De nombreuses études ont suggéré que l'oxygène stabilise la phase α et durcit le matériau.
Pour comprendre les effets souvent antagonistes et en parti couplés de l'oxygène et de l'hydrogène en solution sur le comportement viscoplastique du titane, une étude expérimentale et numérique multi-échelle, a été lancée sur du titane non-allié de phase α. La thèse se décompose en 4 parties: la première introduit les alliages de titane et les mécanismes de déformation. On s'intéresse également aux effets de l'oxygène et de l'hydrogène sur les phénomènes de vieillissement ainsi que sur le phénomène de rupture différée. La deuxième partie présente le modèle de vieillissement statique et dynamique couplé avec l'approche de la plasticité cristalline. La troisième partie présente l'ensemble des résultats des essais de rupture différée. Enfin le quatrième chapitre est consacré à l'identification d'un modèle macroscopique viscoplastique qui permettra de décrire la fissuration brutale et lente. Les essais seront simulés par éléments finis prenant en compte la surconcentration en hydrogène en pointe de fissure.

Context

Combination of high strength to density ratio and good corrosion resistance makes titanium (Ti) and its alloys attractive materials for aerospace, chemical and petrochemical industries. At the same time it was noticed that Ti is sensitive to room-temperature creep which can lead to the associated phenomena such as dwell-fatigue effect and subcritical crack growth under sustained load. The phenomenon of delayed cracking or sustained load cracking (SLC) representing the slow extension of the crack occurs at stress intensity factors below the fracture toughness of the material [218]. The safety design of Ti structures for a long time was based on the notion of fracture toughness and fatigue crack growth that can be assessed by following some guidelines and prescriptions. The SLC phenomenon is of a great concern and it can lead to some dangerous problems since the service stresses may well exceed those permitted by a general engineering design prescriptions [102]. The SLC of titanium alloys is a complex phenomenon influenced by many metallurgical variables and by external environment. One major cause of SLC is the presence of interstitial atoms like hydrogen that can be concentrated at the crack tip leading to the creep-induced cracking at low hydrogen content, or to hydride precipitation and embrittlement at high hydrogen content [227]. In the range between 60 and 200 ppm hydrogen has a large but yet unexplained influence on room-temperature creep. For some alloys solute hydrogen can enhance the cold creep and thus trigger the SLC, while for others it slows down the creep and increases the threshold for slow crack extension [88, 218]. Furthermore, the interstitial oxygen also plays a crucial role in the viscoplastic behavior of titanium by increasing the yield stress through a reduction in the mobility of screw dislocations [141]. A clear insight in the physical mechanisms governing the influence of hydrogen on SLC is necessary in order to predict the optimum range of hydrogen content to improve the resistance of Ti structures to delayed fracture.

Another phenomenon associated with a drastic effect of interstitial atoms of oxygen and hydrogen on the viscoplastic behavior was observed in Ti alloys. The phenomena of dynamic and static strain aging have been the object of multiple researches over the past few decades. Strain aging can cause inhomogeneous yielding such as Lüders bands and Portevin-Le Chaterlier (PLC) instabilities. Static strain aging (SSA) is usually related to the emergence and subsequent propagation of plastic deformation bands. Dynamic strain aging (DSA) is associated with the decrease in the strain rate sensitivity (SRS) parameter which tends to negative value [106].

Several constitutive models attempting to reproduce the SSA and DSA phenomena have been suggested in the literature. The first class of models is based on the physical origin of the strain aging, i.e. the pinning of dislocations by solute atmospheres that diffuse during straining or waiting time. This elastic-viscoplastic constitutive models proposed by Kubin and Estrin [158, 106] accounts for an explicit mathematical description of strain rate sensitivity, which tends to zero or negative values in some range of strain rate and temperature when the PLC serrations are observed. The second class of models is based on an internal variable t_a, called aging time, that controls the increase in the local solute concentration at temporarily arrested dislocations [129, 132]. This model was implemented in finite element codes and allowed the simulation of both Lüders and Portevin-Le Chaterlier (PLC) instabilities, by choosing the appropriate set of parameters [85]. Some attempts to introduce crystal plasticity formulation into a multiscale modeling of the jerky flow in polycrystals were done by Kok [101] and later by Fressengeas [75]. However, for the sake of simplicity, those models were not taking into account the strain and strain rate localization phenomena inside the grains.

In spite of the large number of studies devoted to the SSA and DSA in commercially pure (CP) α-Ti, up to date no experimental evidence of macroscopic band nucleation and propagation at room temperature in CP α-Ti has been reported in the literature. One of the possible explanation of the absence of macroscopic bands in Ti can be related to the difference in manifestation

of deformations at macro and micro length scales [66]. Héripré and Crepin [90], studying local variations of plastic deformation in polycrystalline Zr by strain field mapping, reported strongly heterogeneous distributions of strain in relation with the underlying crystal grain orientations on a tensile specimen yet deforming homogeneously on the macro-scale. They concluded that for an accurate description of the mechanical properties of the material, it is necessary to account for the local microstructure and crystalline nature of the specimen at the grain scale. Many recent experimental and numerical investigations [66, 90, 50, 165, 14, 15] confirm that heterogeneous straining patterns and strain localization modes observed in materials with low symmetry crystal structure such as HCP α Ti, are correlated with their locally activated slip systems, the local texture and possibly the nature of the grain boundaries. Therefore, a numerical model at finer scale (micrometer) taking into account the local arrangement of grains and a detailed description of their slip systems is necessary to understand the deformation heterogeneities of α Ti.

Project ANR-FLUTI

The work presented in this thesis was carried out as part of the ANR-FLUTI (*Fluage-titane*) project which is a collaborative research project between *Centre des Matériaux* of Ecole des Mines de Paris, *Le Laboratoire de Mécanique des Solides* of Ecole Polytéchnique and *Institut de Chimie et des Matériaux Paris-Est* of University Paris XII. The project was coordinated by Véronique Doquet from LMS. The main goal of the project is to study the combined influence of residual oxygen and hydrogen on the deformation mechanisms and the resistance to slow fracture of CP α Ti alloys. One of the important objective of the project is to give some guidelines for the optimization of chemical composition of Ti alloys in order to increase their resistance to room-temperature creep, SLC and related phenomena. Emphasis is made on the experimental investigation as well as multi-scale modeling (ab initio, polycrystalline plasticity and continuum description of the behavior). The work presented and developed in this thesis is categorized under mesoscopic and macroscopic levels.

Objectives

Accounting for the points mentioned above, the objectives of the present study are as follows:

- Develop a better understanding of the physical mechanisms which govern the viscoplastic behavior of α Ti alloys.
- Formulate and identify a constitutive crystal plasticity model able to simulate static and dynamic strain aging.
- Experimentally investigate the phenomenon of SLC in the range of low hydrogen content where creep at the crack tip predominates over Ti-hydrides fracture. Characterize the influence of hydrogen and oxygen on toughness and SLC of titanium alloys.
- Develop a constitutive model able to simulate the SLC which takes into account the anisotropy and the impurity content at the crack tip of the material.

Methodology

In the present work a phenomenological strain aging model is combined with a comprehensive description of slip systems active in HCP crystals in order to take into account the role of crystal plasticity in static as well as dynamic strain aging phenomena. Finite element (FE) simulations are performed on polycrystalline aggregates with various numbers of grains taking

into account the elastic and plastic anisotropy of α Ti. It will be shown that the slip activities can lead to cooperative deformation modes inside the grains of a polycrystal causing the development of plastic heterogeneities inside the material. The model captures the macroscopic viscoplastic anisotropic response and the corresponding slip processes in the grains.

In order to characterize the influence of hydrogen and oxygen on the toughness and SLC phenomenon in CP α Ti, experimental studies are conducted on Compact Tension (CT) specimens followed by fractographic observations. The aim of this study is to determine the evolution of the toughness and the threshold to SLC in Ti alloys and detect possible modifications in fracture mechanisms with increased impurity content. On the basis of the experimental study, it will be shown that the concept of Linear Elastic Fracture Mechanics (LEFM) is not a suitable approach for understanding the fracture behavior in such a viscoplastic material. The alternative local approach to fracture is proposed based on cohesive zone modeling (CZM) combined with a specific elastic-viscoplastic behavior. This approach allows to take into account the micromechanisms of failure such as stress and strain distribution at a crack tip.

Outline

The thesis is divided into four parts, each corresponding to one of the above mentioned objectives. The first part gives a brief review of the fundamentals on crystallography, main deformation mechanisms and the phenomenon of sustained load cracking in titanium alloys. The strain aging phenomenon observed in the material is also revisited. In the second part, experimental evidence of strain aging phenomena is shown. A physical interpretation of the origin of the observed instabilities is proposed. A suitable crystal plasticity model able to capture the strain aging phenomena and the anisotropy of the mechanical properties of CP α Ti at the grain scale is presented. The third part is dedicated to the experimental investigation of fracture toughness and SLC phenomenon on the pre-cracked CT specimens. Finally, the fourth part introduces the motivations behind the constitutive modeling of sustained load cracking. The fracture model based on the local approach to fracture which accounts to hydrogen concentration at the crack tip is presented. Different aspects and limitations of the modeling are explored. Finally, conclusions and avenues for possible future development are discussed [66].

General notation

a	Scalar
$\underline{\boldsymbol{a}}$	Vector
$\underset{\sim}{\boldsymbol{A}}$	Second-order tensor
$\underset{\approx}{\boldsymbol{C}}$	Fourth-order tensor
$\dot{a}$	rate of change of quantity a w.r.t. time

$[uvw]$	Crystallographic direction
$< uvw >$	Family of crystallographic directions
(hkl)	Crystallographic (slip) plane
$\{hkl\}$	Family of crystallographic planes

Chapter 1

Literature review

Résumé

Ce premier chapitre présente brièvement les alliages de titane. La discussion se concentre sur les différents mécanismes de déformation dans le titane ainsi que sur les connaissances actuelles des cissions critiques des systèmes de glissement. On s'intéresse également aux effets des atomes interstitiels et particulièrement de l'oxygène et de l'hydrogène sur la viscoplasticité du titane et aux phénomènes de vieillissement statique et dynamique. Les phénomènes de rupture différée et de fluage (qui sont très importants dans ce genre de matériaux) et leurs effets sur la propagation des fissures sont également discutés. Ce chapitre contient également des éléments fondamentaux qui sont nécessaires pour comprendre les méthodes utilisées dans le développement du modèle de vieillissement présenté en Chapitre 2.

1.1 Some generalities about titanium alloys

1.1.1 Crystallography of α titanium

Pure titanium is an allotropic element. At room temperature, it exists in hexagonal close-packed (HCP) crystal structure, designated alpha (α) phase, and at 882°C it transforms to a body-centred cubic (BCC) beta (β) phase (Figure 1.1 (a) and (b)). The hexagonal unit cell with three possible index systems is shown in Figure 1.2. Lattice parameters a (0.295 nm) and c (0.468 nm) result in a c/a ratio for pure α-Ti of 1.587, which is smaller than the ideal ratio of HCP crystal structures of 1.633. Miller-Bravais system with 4 index notation (see Figure 1.2 (a)) will be used in this manuscript. Detailed information about transformation between different index systems is given in the Appendix A.

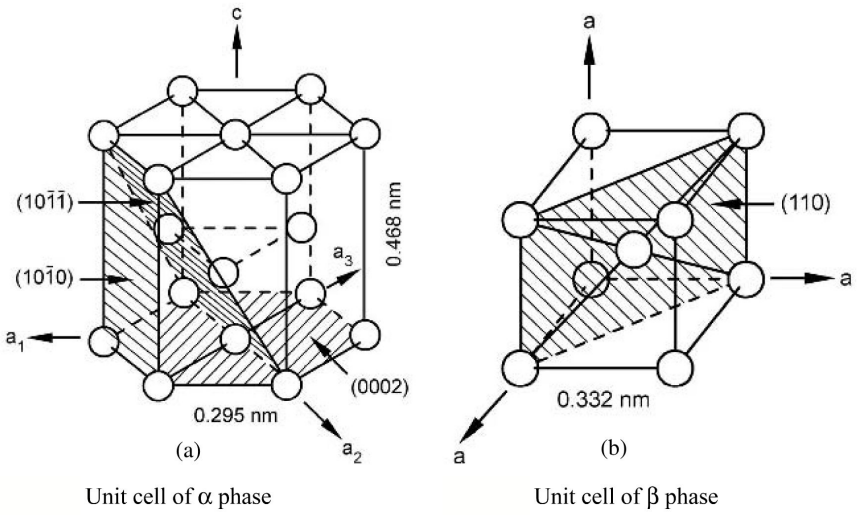

Figure 1.1: Unit cells of Ti [124].

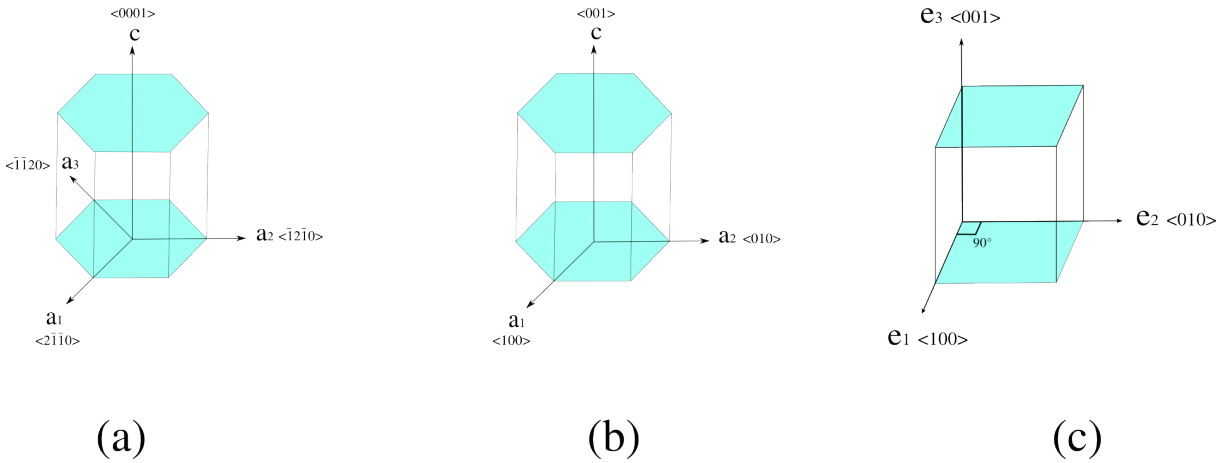

Figure 1.2: Unit cell (a) hexagonal (4 index) Miller-Bravais notation for: (a) non-orthonormal, (b) primitive hexagonal (3 index) non-orthonormal and (c) orthonormal hexagonal (3 index) index systems where $\vec{e}_1 \parallel \vec{a}_1$ and $\vec{e}_2 \nparallel \vec{a}_2$.

Solid solution and precipitation hardening are the most commonly observed hardening mechanisms in CP α Ti. Figure 1.3 shows two kinds of interstitial sites existing in HCP lattice: two octahedral and four tetrahedral interstices per unit cell. Large octahedral voids are surrounded by six atoms arranged on a regular octahedron. The smaller tetrahedral voids are enclosed by four atoms which are tetrahedrally disposed. In α phase there are thus one octahedral and two tetrahedral sites per titanium atom with a size of 0.62 Å and 0.33 Å, respectively [13].

Interstitial atoms of oxygen (with neutral atom radius of 0.6 Å) can significantly harden the α phase by occupying the octahedral sites and causing a tetragonal distortion of the lattice due to an increase in the c/a ratio [56]. Hydrogen atoms with an atomic radius of 0.46 Å enters the smaller tetrahedral sites with a radius of 0.44 Å of the β-phase and produces non lattice distortion. Consequently, atomic oxygen has a very high solubility in α titanium, while hydrogen is a β stabilizer with a high solubility in the β phase.

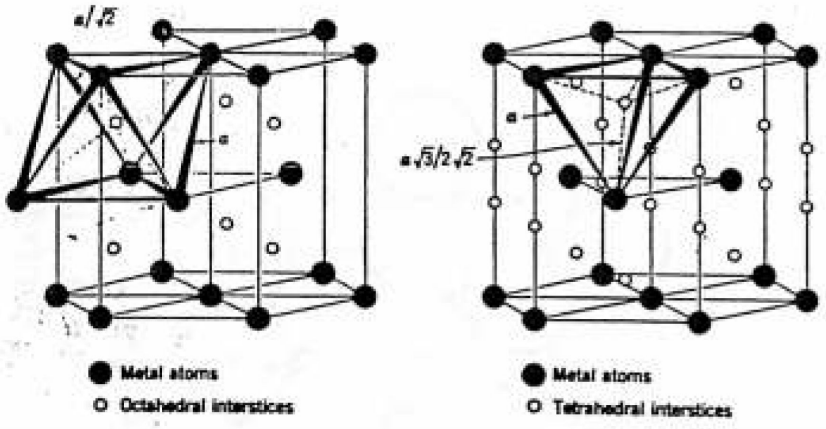

(a) (b)

Figure 1.3: Interstitial voids in HCP structure: (a) octahedral, (b) tetrahedral sites [155].

1.1.2 Deformation modes

Single crystal slip

The conventional slip by dislocations and twinning are two main deformation modes of CP α Ti. Three slip system families with Burgers vector of $\langle a \rangle$-type $\langle \bar{2}110 \rangle$ gliding in basal (0001), prismatic $\{10\bar{1}0\}$ or first-order pyramidal $\{10\bar{1}1\}$ planes constitute 4 independent slip systems (see Figure 1.4). Some additional *non* $\langle a \rangle$-type deformation mechanisms such as pyramidal $\langle c+a \rangle$ dislocation slip and four twinning systems accommodate the plastic deformation of polycrystal along the c-axis [124]. The list of the most commonly observed slip systems in α Ti is given in Table 1.1.

For a single crystal α Ti, the prismatic slip is identified as the preferential mode of deformation due to its low value of critical resolved shear stress (CRSS). The prismatic stacking fault associated with the dislocation core has the lowest energy for the $< a >$ dislocation, and the flow on the prismatic plane is controlled by low mobility of screw dislocations arising from non-planar core structures [12, 115]. Due to its ease, prismatic slip has been extensively studied [4, 142, 141, 170]. The CRSS for this slip mode was established over a wide range of temper-

atures and compositions in a work of Conrad [56]. As the temperature increases, the CRSS of the prismatic slip decreases, that might suggest a change in the underlying mechanism of the slip. The similar trend is observed for a basal slip (Figure 1.5). The pyramidal $< a >$ slip has been reported as a secondary slip in the works of [170, 52]. The difference in CRSS between the three slip families with a Burgers vector $< a >$ becomes smaller with increasing temperature.

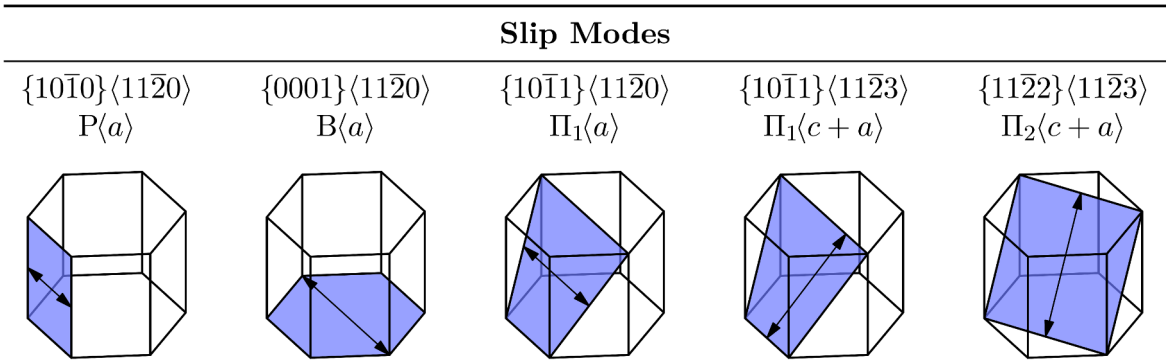

Figure 1.4: Slip systems in Ti of α phase [21].

Slip family	Plane and direction	Total number of slip systems
1. Basal $< a >$	$\{0001\}< 1\bar{2}10 >$	3
2. Prismatic $< a >$	$\{10\bar{1}0\} < 1\bar{2}10 >$	3
3. Pyramidal $\pi_1 < a >$	$\{10\bar{1}1\} < 1\bar{2}10 >$	6
4. Pyramidal $\pi_1 < c+a >$	$\{10\bar{1}1\} < 11\bar{2}3 >$	12
5. Pyramidal $\pi_2 < c+a >$	$\{11\bar{2}2\} < 11\bar{2}3 >$	6

Table 1.1: Slip systems in CP Ti of α phase

Pyramidal $\pi_1 < c+a >$ glide associated with the planes $\{10\bar{1}1\}$ and $\{11\bar{2}2\}$ has been evidenced in a single crystal α Ti [156, 217, 46]. It has been concluded that $< c+a >$ slip is important for deformation accommodation at elevated temperatures. This slip has a CRSS of 3-4 times larger than the CRSS for $< a >$ type slip. The large magnitude of the $< c+a >$ Burgers vectors and atomically rough planes explain the higher resistance to motion of $< c+a >$ dislocations. Pyramidal $\pi_2 < c+a >$ slip was rarely found to be activated in some c-axis tension tests [221].

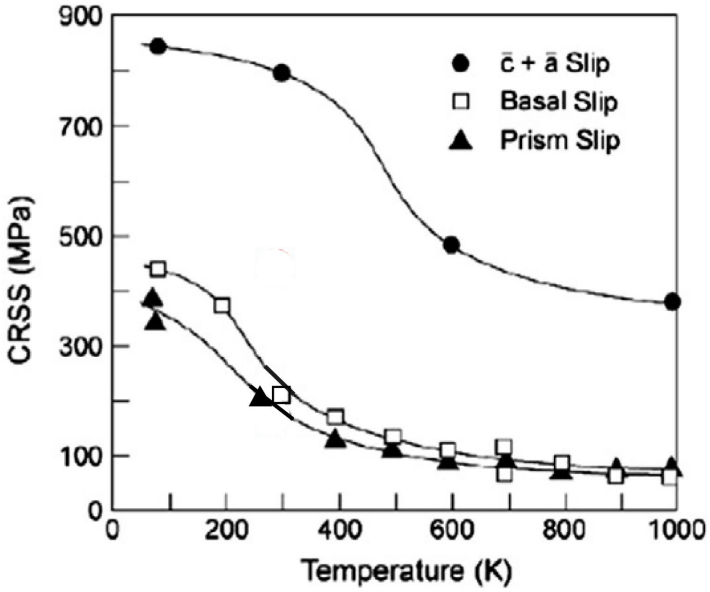

Figure 1.5: The variation of CRSS with temperature [12].

Twinning

Twinning in α Ti occurs on $\{10\bar{1}2\}$ and $\{11\bar{2}2\}$ planes (Figure 1.6) depending upon whether the loading stresses are tensile or compressive [12]. It represents the fifth degree of freedom required for an arbitrary shape change. Twinning significantly contributes to the deformation of the lattice through crystal shear, often involving atomic shuffling in the plane of shear, with associated lattice reorientation [36].

Twinning plays two important roles: it contributes to texture evolution by reorienting the twinned areas [51] and it influences the strain-hardening behavior [11]. The domination of twinning over dislocation slip is affected by grain size, composition, and deformation rate of the material. Twinning is suppressed as the grain size is refined, oxygen content is increased, and deformation rate is slowed [33, 56].

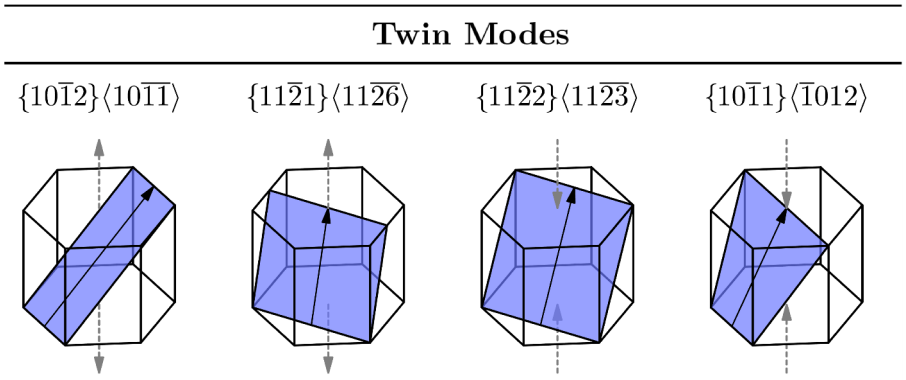

Figure 1.6: Twin systems in Ti of α phase [21].

Polycrystalline slip

An analysis of operating slip modes in polycrystalline Ti alloys has confirmed the dominance of prismatic $< a >$ type slip [56, 48, 180, 160]. Significant pyramidal $\pi_1 < c + a >$ slip was observed at room temperatures [148, 162] when the oxygen content was high enough to suppress the twinning. Pyramidal $\pi_1 < c+a >$ slip was also observed in textured CP Ti rolled at various temperatures [81]. Using X-ray line-broadening techniques it was found that over the entire temperature range 20°-720°C the deformation is dominated by prismatic $< a >$ slip. Rare observations of pyramidal $\pi_2 < c + a >$ slip in polycrystalline Ti were reported by [230, 171].

A possible source mechanism for non-basal $< c + a >$ pyramidal slip was studied by Yoo [228]. According to [228], there are two main ways by which non-basal slip dislocations can be generated: (a) at/near surfaces and interfaces such as grain boundaries, and (b) at heterogeneous sites in the grain interior such as the junction associated with $< a >$ and $< c >$ dislocations. Figure 1.7 (a) illustrates schematically the cross-slip of an $< a >$ dislocation from the basal plane to a prismatic $(1\bar{1}00)$ plane. Next, an active prismatic slip dislocation interacts with a sessile $< c >$ dislocations and a $< c + a >$ dislocation junction along its near-screw orientation is formed (Figure 1.7 (b)). It should be noted that $< c >$ dislocations are assumed to exist in the grain matrix as a part of the initial microstructure. Finally the $< c + a >$ screw dislocation cross slips from the prismatic $(1\bar{1}00)$ plane to the $(11\bar{2}2)$ pyramidal plane (Figure 1.7 (c)). The generation of $< c + a >$ dislocations on the $\{1\bar{1}01\}$ plane is also possible as a result of interaction between $< c >$ dislocations and pyramidal $< a >$ dislocations. The direct evidence of the cross-slip of $< a >$ dislocations from $\{1\bar{1}00\}$ to $\{1\bar{1}01\}$ planes when the specimen was favorably oriented, is provided during an in situ straining TEM experiment on Ti at low temperatures [70]. These results suggest that $< c + a >$ slip is important in plastic deformation of α Ti.

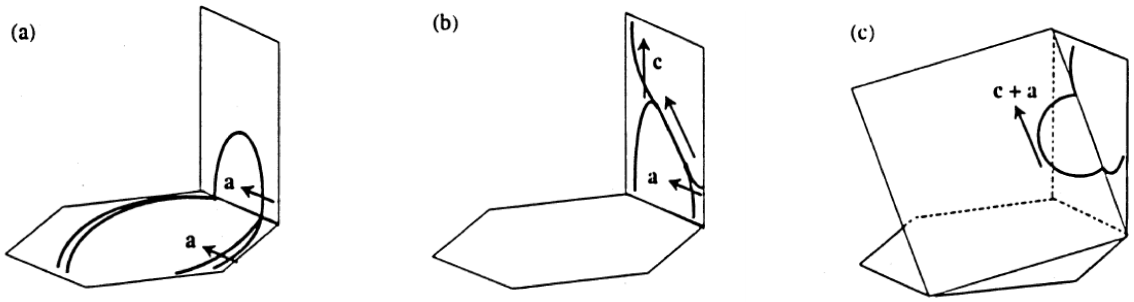

Figure 1.7: Evolution of the dislocation source for a $< c + a >$ pyramidal slip system [228].

Texture of Ti sheet

The deformation behavior of α Ti is strongly affected by its crystallographic texture. The conventional typical crystal orientation of a cold-rolled α Ti polycrystal in Euler angle notation is $g = (0, \Phi, 30)$, where Φ is in a range of 30°- 40°. This typical texture is shown in Figure 1.8. Here the c-axis is inclined about $\pm 30°$ from normal direction (ND) to transverse direction (TD). The typical rolling texture appears to form irrespectively of the initial texture [21]. The rolling

texture in polycrystalline Ti sheets ensures that primary slip is confined to the prismatic slip systems, while secondary slip is either prismatic or pyramidal $< a >$ type [180].

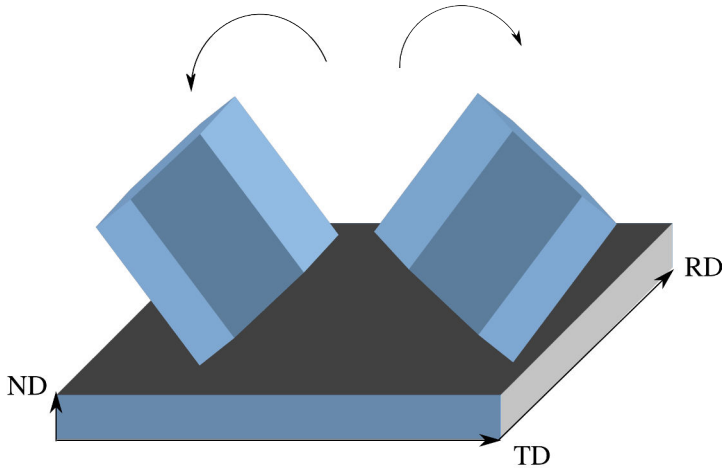

Figure 1.8: Preferential orientation of the α-Ti subjected to cold rolling.

The pronounced texture in Ti after rolling results in highly anisotropic behavior of the material. As a result, mechanical properties of textured material such as elastic modulus, strength, ductility, toughness, creep and fracture behavior might be strongly affected. For a better understanding of the mechanical properties of Ti that depend on the deformation mechanisms, it is necessary to know its texture evolution during plastic deformation. Phillipe [159, 160] studied Ti α and near α alloys, and developed a model of texture evolution during cold rolling that is able to predict the mechanical properties of the material. After the material was tested in tension at different angles to the rolling direction (RD), it was found that the high value of the yield stress in the TD is connected with the crystal orientation which favors the activation of pyramidal $< c + a >$ glide with high CRSS for the deformation accommodation along c-axis (Figure 1.9).

Anisotropic hardening due to evolving texture was also studied by [89, 12]. It was noticed that significant texture strengthening can occur when the loading direction imposes stress parallel to the c-axis. The strain anisotropy in polycrystalline CP Ti was found to be temperature dependent. It is the highest at $973°C$ and decreases rapidly with decreasing in temperature [121].

As can be seen, many mechanical properties depend on the crystalline orientations. Significant improvement in mechanical performance can be achieved through the texture control and optimization.

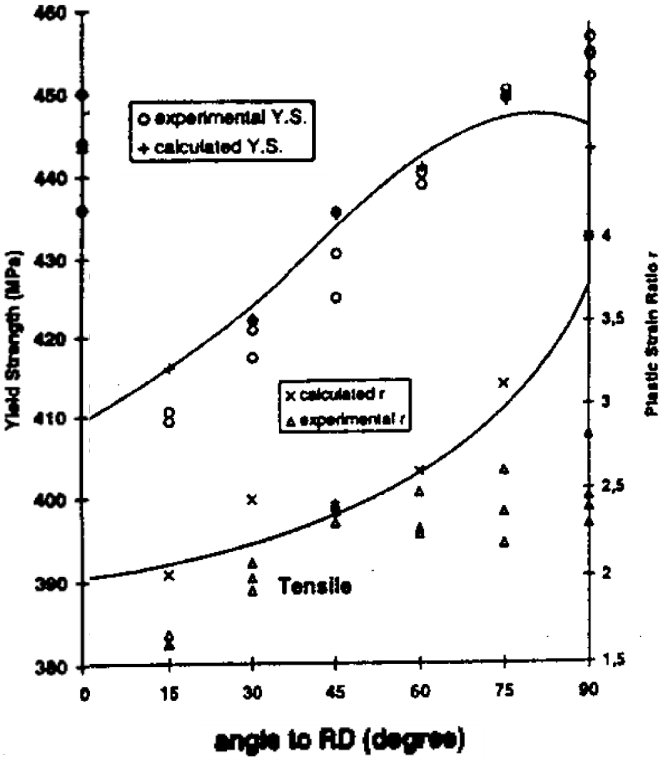

Figure 1.9: Yield stress and plastic ratio vs cutting angle with respect to RD for T60 alloy [159].

1.2 Anomalous macroscopic behavior in strain aging alloys

1.2.1 General information about strain aging

Many structural materials are subjected to the phenomenon of strain aging, that is associated with the solute-dislocation interactions. Two primary mechanisms of solute-dislocation interactions are arising from elastic interactions mediated by a long-ranged strain fields produced by a dislocation, and short-ranged interactions with the dislocation core [229]. The long-range elastic interactions of mobile dislocations with the solute atoms is relatively weak, while the short-range or 'chemical' interaction can significantly change the dislocation core and influence dislocation mobility. This effect can be described indirectly in terms of the generalized stacking fault energy.

The strain aging can induce inhomogeneous yielding and notably reduce the fracture toughness of a material. Two types of instabilities are attributed to strain aging: Piobert-Lüders bands and the Portevin-Le Chatelier (PLC) effect. The typical experimental stress-strain curve affected by Lüders phenomenon takes the form shown in the Figure 1.10 (a). When the specimen is loaded, the Lüders peak, also called upper yield stress, appears. The appearance of the peak can be interpreted as the overstress necessary to move dislocations, which are initially pinned by solute atoms. Upon unpinning, the dislocations suddenly break away from their solute atmospheres provoking an avalanche of dislocations that leads to the strain localization [110]. The propagation of the Lüders band is associated with a plateau at nearly the constant stress, also called 'lower yield stress' [23]. Macroscopically the Lüders front is a delineation between plastically deformed and undeformed material that appears at one end of specimen and propagates

with constant velocity towards the other end [40, 123]. Lüders bands are usually attributed to the phenomenon of static strain aging (SSA).

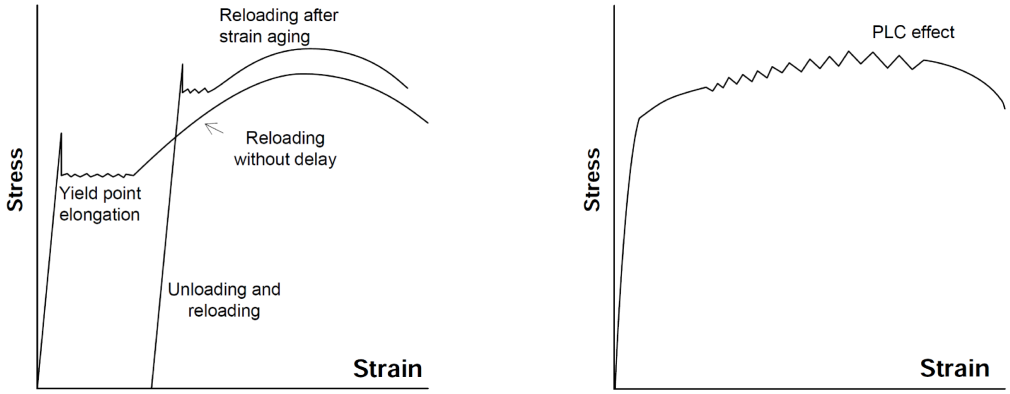

Figure 1.10: Strain aging: (a) static and (b) dynamic.

At sufficiently high temperatures and/or low strain rates, the point defects can diffuse back to dislocations, thus causing repeated locking-unlocking processes called dynamic strain aging (DSA). This leads to the discontinuous yielding phenomenon known as Portevin-Le Chatelier (PLC) effect. At a given temperature and concentration, the average flow stress needed to unpin dislocations, increases with decreasing strain rate or increasing waiting time. As a result, the slope of total glide resistance vs. strain rate is decreasing or may become negative leading to the so-called negative strain rate sensitivity (NSRS) [109]. When the imposed strain rate falls into the range of NSRS, the initiation and propagation of plastic strain rate localization bands in multiple sites of a specimen can be observed during the deformation process [94, 37]. These shear bands can be produced with regular spacing, or as a set of propagating bands with a source at one end of the specimen [49, 132]. The PLC effect manifests itself as an unstable plastic flow that appears as serrations in the stress-strain curve [226]. The serrated flow or jerky flow on the stress-strain curve is illustrated in the Figure 1.10 (b). During a constant-strain-rate tests, each stress drop of a serrated plastic flow corresponds to a macroscopically observable plastic avalanche of one of these localized bands [129, 226]. Figure 1.11 shows various types of deformation bands that are assigned as type A, B, and C [49, 226, 84]. Type A bands are characterized by continuous propagation across the gauge length of the specimen at a nearly constant velocity and band width. It resembles a longitudinal wave [45, 226], with arbitrary located small drops on the regular flow in the tensile stress-strain curve. Type B bands propagate discontinuously along the specimen with roughly equal intervals. The average velocity is significantly lower in comparison with type A bands [84]. Type C bands are randomly nucleated with a limited propagation and a high frequency and chaotic load drops. Usually higher strain rates promote type A bands, lower strain rates promotes type C bands and intermediate level corresponds to the type B bands [2, 226]. Detailed information about strain aging mechanisms is given in the next section 1.2.2.

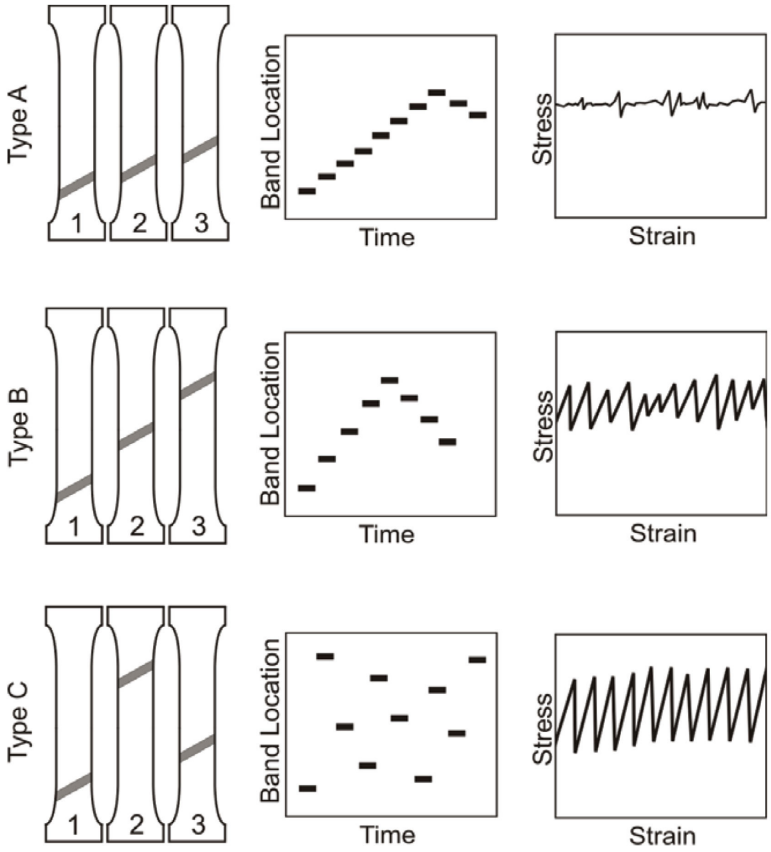

Figure 1.11: Schematics of motion, orientation, spatio-temporal appearance and strain-controlled tensile curve characteristics of the PLC bands [226].

1.2.2 Microscopic mechanisms of strain aging phenomenon

The governing mechanisms of strain aging depend on the relative position of a point defects that will interact with dislocations. The solute distribution is called Cottrell cloud, Snoek ordering or Suzuki atmosphere when the point defects are distributed outside of the dislocation core area. Volume diffusion in the crystal lattice governs the mobility of the point defects. Defects distributed inside the dislocation core area are called a core atmosphere. Their mobility is limited by the pipe diffusion along the dislocation core, or the directional diffusion under the strong interaction force between the dislocation and point defects when the dislocation is in motion [47].

Generally, the Cottrell cloud [58] is produced when impurity atoms bring the distortion in the crystal lattice [94]. This distortion leads to the residual stress field around defects, that can be relaxed by the impurity atom diffusing towards the compressive (in case of substitutional atoms) or tensile (interstitial atoms) part of edge dislocation. Defects tend to congregate in dislocation core regions where the elastic strain energy is large and negative, forming dense atmospheres of solute atoms. As a results, an additional work then will be required to separate the dislocation from these point defects.

Schoeck and Seeger [175, 176] suggested a mechanism that is based on Snoek's ordering [185] of interstitial solute atom pairs in the stress field of dislocations. According to this interpretation,

the application of a stress, parallel to one crystalline axis, decreases the distortion of the lattice filled with randomly distributed interstitial atoms in the octahedral sites. If the dislocation is stationary for a suitable time, the applied stress favors the thermally-assisted jumps into the appropriate preferred sites. Thus the solid solution becomes ordered around the dislocation line and the concentration of solutes around the dislocations is constant. An increment in flow stress is then required to free the dislocation from its ordered atmosphere. This increment may be regarded as a transient increase in the friction stress. Snoek ordering can explain the rapid strain aging phenomena observed by Wilson and Russell in tensile tests on a low carbon steels [69, 219].

As mentioned before, the DSA is a result of the dynamic interaction of mobile dislocations and solute atoms. Aging occurs during the period when the dislocations are temporarily arrested at local obstacles in the glide plane. This time is called the aging or waiting time. On the time scale of tensile test, the aging time of SSA is generally long enough, so unpinning of dislocations is irreversible. Usually this phenomenon is observed at temperatures lower than for DSA. DSA is happening during the on-going plastic deformation. During the waiting time at an obstacle, solute atoms diffuse in the dislocation core and increase activation enthalpy for the unpinning of the glide dislocation segment [37]. Schematically this process is shown in Figure 1.12.

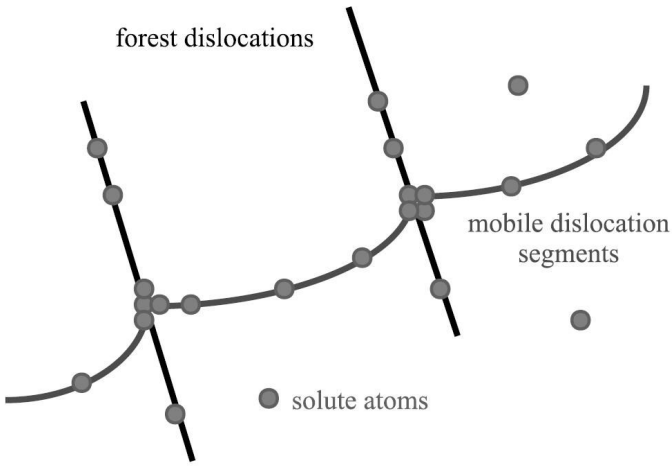

Figure 1.12: Interaction between a mobile dislocation and forest dislocations in the strain aging model [37].

According to the concept of DSA model developed by Cheng [47], the dislocation captures the solutes during its bowing-out process, under applied stress, while being held at forest dislocations. As a result, the concentration of the dislocation core atmosphere increases with the diffusion of the existing core atmosphere along the dislocation, and the new solutes which are encountered and captured by the dislocation. An increase in the core atmosphere density leads to the increase of the total thermal activation energy, mechanical threshold stress and the work hardening rate. Hence the driving stress needed to move the dislocations increases, leading to the DSA. The force exerted on each of the core solutes by the dislocation is inversely proportional to the concentration of the core solute atmosphere, thus DSA can only be observed at low solute concentration. Kubin and Estrin [108, 107] used the similar idea of the mobile dislocation aging during the interaction with forest dislocations (Figure 1.13). According to their model, solute atoms can diffuse towards the mobile dislocations in the presence of extrinsic obstacles,

such as forest dislocations. The densities of mobile and forest dislocations evolve inversely during the straining process. A high concentration of forest dislocations favors the anchoring of mobile dislocations. Hardening due to solute atoms around obstacles depends on this interaction between mobile and forest dislocations. At low strain, the density of mobile dislocations increases rapidly, while the forest dislocation density is almost constant. At high strain, the mobile dislocations density saturates and the forest dislocation density increases and then also saturates [84].

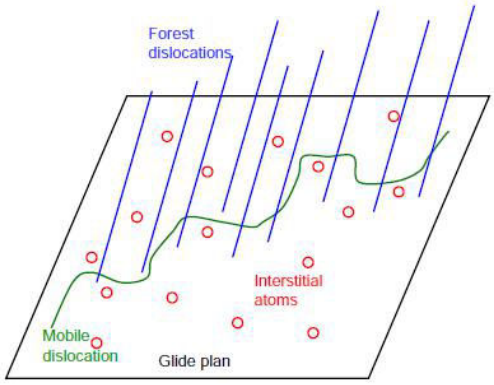

Figure 1.13: Interaction between mobile dislocation and forest dislocations in the strain aging model [108].

1.2.3 Strain aging phenomenon in titanium alloys

A large number of studies devoted to the phenomenon of dynamic and static strain aging and the underlying physical mechanisms has been conducted for Ti over the past decades. Rosi and Perkins [170] were the first to report strain aging phenomena in CP Ti at elevated temperatures and they attributed it to the segregation of nitrogen atoms. According to Doner [62] since pinning is controlled by diffusion, the activation energy of the process is that for the diffusion of the solutes responsible for the pinning. The investigation of SSA in CP Ti at elevated temperatures by Donoso [63] indicates that the activation energy of the process is in good agreement with that for the diffusion of oxygen in Ti. At intermediate and low temperatures, Conrad [56] ascribed the yield peak in CP Ti to dislocation multiplication mechanisms. An alternative explanation of the yield peak in CP Ti observed at room temperature was proposed by Roth [171] who suggested that distinct slip systems have different strain-rate sensitivity. The tendency for the yield peak formation was explained by the initial domination of the pyramidal slip with a high Schmid factor, resulting in a higher yield stress.

The significance of DSA in CP Ti at elevated temperatures was studied by Doner and Garde [62, 79]. They suggested that interstitial oxygen interacting with mobile dislocations through bulk diffusion can be responsible for DSA above 600 K [62, 79], while near 350 K DSA might be due to hydrogen that has a higher diffusivity. According to Senkov and Jonas [178], solute hydrogen reduces the extent of DSA in titanium at high temperatures by weakening the interaction between dislocations and impurity atoms thus causing material softening. Nemat-Nasser [146]

argued that the activation energies for volume diffusion of solute atoms may not be pertinent parameters to determine which solute is responsible for DSA in a given temperature range. He was the first who documented experimentally DSA of CP Ti near room temperature presumably caused by the pipe diffusion of interstitial atoms of oxygen along or inside the dislocation core.

Another mechanism based on the internal lattice friction was proposed to control the movement of screw $\langle a \rangle$ dislocations in Ti. The applied resolved shear stress required to make a dislocation glide in an otherwise perfect crystal is called the Peierls stress and it is a function of the dislocation core structure. The Peierls stress can substantially grow when the local concentration of solute atoms increases. It can also induce stress instabilities contributing to static and dynamic strain aging [42, 94]. Naka [141, 142, 140] and Biget [30] studied the importance of lattice friction in the low-temperature deformation of α Ti single crystals. $Post - mortem$ transmission electronic microscope (TEM) observations [140, 142] have shown a large density of long rectilinear screw $\langle a \rangle$ dislocations in the prismatic planes that govern room-temperature plastic deformation of α Ti. $In - situ$ TEM deformation tests [70, 71] revealed a jerky motion of these dislocations with a series of sudden jumps between locked positions. It was concluded that the plastic flow of α Ti at room temperature is controlled by Peierls type frictional forces in connection with a non-planar core structure of the screw dislocations. According to this model [59], the dislocation takes alternately two configurations: a low energy, stable and sessile configuration with a core spread on several potential glide planes [80], and a high energy, metastable and glissile configuration with a core confined into a single glide plane (prismatic, pyramidal or basal) [54]. In this latter configuration, dislocation segments can jump over variable distances that can range from a single interatomic distance (classical Peierls mechanism) to large distances (locking-unlocking mechanism). Solute atoms of oxygen are expected to harden α Ti through a short range mechanical interaction in which the crystal distortions introduced by the interstitial atoms stabilize the core structure of screw dislocations. This results in a more difficult sessile-glissile transition and thus a larger lattice friction [42]. Transitions from one configuration to another being thermally activated, a decrease of the jump length and an increase in the jump frequency at higher temperature is observed experimentally by means of $in - situ$ experiments. At low temperatures, the deformation is controlled by the locking-unlocking mechanism [59], long rectilinear segments of screw dislocations are observed and the activation parameters are those of the Friedel and Escaig model [76, 68] (transition from a sessile to a glissile configuration before glide in the prismatic planes). At high temperatures, a large density of macrokink pairs is moving along bowed segments of dislocations and the kink pair mechanism (nucleation and mobility) is controlling plasticity [71, 142, 140, 95].

1.2.4 Modeling of strain aging phenomenon

Various constitutive models attempting to reproduce the SSA and DSA phenomena have been suggested in the literature. Two main types of these models are based on the physical origin of the strain aging, i.e. on dislocation-solute interaction. The first type of elastic-viscoplastic constitutive models proposed by Kubin and Estrin [158, 106] accounts for an explicit mathematical description of strain rate sensitivity, which tends to zero or negative values of SRS in some range of strain rate and temperature when the PLC serrations are observed. Using such phenomenological model in finite element (FE) code, the simulation of the propagation of the Lüders bands was implemented by several authors: Tsukhara [198, 199] in 2D plates; Kok [101] in 3D polycrystalline flat specimens; Benallal [24] in smooth and pre-notched axisymmetric tensile specimens. The second type of the model initially proposed by McCormick [129] and later improved by Mesarovic [132], includes an internal variable t_a, called aging time, that controls

the increase in the local solute concentration at temporarily arrested dislocations. This model has been used in many recent PLC FE simulations [231, 85, 84, 128, 55, 125]. Some attempts to introduce crystal plasticity formulation into a multiscale modelling of the jerky flow in polycrystals were done by Kok [101] and later by Fressengeas [75]. However, for the sake of simplicity, those models were not taking into account the strain and strain rate localization phenomena inside the grains [83].

In spite of the large number of studies devoted to the SSA and DSA in CP α-Ti, up to date no experimental evidence of macroscopic band nucleation and propagation at room temperature in CP α-Ti has been reported in the literature. In the recent work, Roth and Lebyodkin [171] reconstructed a strain-rate patterns during the tensile deformation of the sample using a CCD camera. The observation of the evolution of the local strain rate showed no plastic front propagation. At the same time, as it was noticed by Efstathiou [66], the manifestation of deformations at one length scale may be different at larger length scales, especially for the materials with inhomogeneous microstructure [50]. Héripré and Crepin [90] who studied the local variations of plastic deformation in polycrystalline Zr by strain field mapping conclude that an accurate description of the mechanical properties of the material requires the knowledge of the local microstructure and crystalline nature of the specimen at the grain scale. Numerous experimental and numerical investigations [66, 90, 50, 165, 14, 15] confirm that the heterogeneous straining patterns and strain localization modes observed in materials with low symmetry crystal structure such as HCP α Ti, are correlated with their locally activated slip systems, their local texture and possibly the nature of the grain boundaries. Therefore, in order to understand the deformation heterogeneities of α Ti, a numerical model at a finer scale (micrometer) which would take into account the local arrangement of grains and a detailed description of their slip systems is necessary.

1.3 The phenomenon of sustained load cracking (SLC) in titanium alloys

1.3.1 Effect of hydrogen on fracture behavior

For a long time, the safety design of Ti structures was based on the notion of fracture toughness and fatigue crack growth that can be assessed by following some guidelines and prescriptions. In the early 1950th [39], experimental observations of Ti showed that this material is susceptible to time-dependent failures such as cold creep, sustained load cracking, dwell fatigue that can occur at stress intensity factors below fracture toughness K_{Ic} and when static loads are applied [102]. This discrepancy can lead to some dangerous problems since the service stresses may well exceed those permitted by a general engineering design prescriptions. SLC behavior is of concern also when subcritical crack growth occurs internally so as to remain undetected during service inspection [214, 189].

Delayed cracking, or SLC in Ti represents a slow extension of the crack under high sustained loads in the absence of an aggressive environment. This type of cracking resembles stress-corrosion cracking (SCC), where aggressive environments are involved. The main cause of SLC behavior is usually attributed to the presence of interstitial hydrogen either in solid solution [215, 135, 93, 205, 173, 153, 126, 32, 227, 153, 152, 86, 104] or in the local environment [225, 145, 133, 138]. As a result, the hydrogen concentration of alloys for aircraft applications was routinely kept below 125 ppm by weight because of the possible embrittling effect [93, 88]. Embrittlement by hydrogen might happen with or without hydride formation. In non-hydride

systems, hydrogen was proposed to embrittle the material through a decrease in the cohesive strength of the atomic bonds [196] or through the mechanisms of hydrogen enhanced localized plasticity (HELP) around the crack tip [22]. In hydride forming systems, the crack propagation occurs by hydride formation at stress concentrations followed by cleavage of the hydrides [182]. The overview of the main work on sustained load cracking in Ti alloys in the chronological order of its appearance will be discussed below.

Meyn [135] studied the fracture toughness and resistance to inert-environment sustained load cracking propagation of α-β Ti alloys. He stated that the occurrence of SLC is related to hydrogen contents. He observed a decrease of both fracture toughness K_{Ix} and the SLC threshold K_{Ith} with increasing hydrogen content up to 50 ppm. Further increase in the hydrogen level resulted in increased growth rates while the threshold remained constant (see Figure 1.14). The SLC propagation occurred through a mixture of microvoid coalescence (MVC) and transgranular cleavage on the plane oriented 2 to 15 degrees from basal {0001} in the α phase. Meyn discarded the role of hydrides in the cleavage process since the cleavage plane did not coincide with reported hydride habit planes [209]. In pure Ti, the known habit hydride planes are $\{10\bar{1}0\}$, $\{10\bar{1}1\}$ and $\{02\bar{2}5\}$, with $\{10\bar{1}0\}$ being the most common [148, 182]. The fast fracture and SLC behavior were suggested to result from creep-induced cracking at room-temperature that can be facilitated by hydrogen.

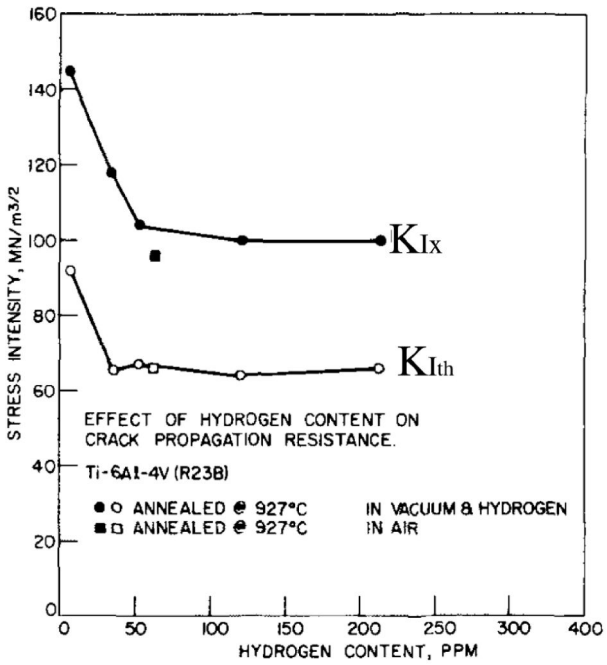

Figure 1.14: Effect of hydrogen on the fracture toughness K_{Ix} and the threshold stress intensity factor for sustained load cracking K_{Ith} for Ti-6Al-4V [135].

Williams [215] observed remarkable increase in fracture toughness in Ti alloys resulting from reduction in hydrogen content. The strain rate had no effect on fracture toughness. All specimens showed ductile rupture regardless hydrogen level. The fracture surface at 60 ppm was slightly rougher and had smaller dimples comparing to the specimen of 7 ppm. The variation of fracture toughness and threshold to SLC with hydrogen content is summarized in Figure 1.15. In both Ti-6Al-4V and Ti-4Al-3Mo-1V alloys, reduced hydrogen content increased fracture tough-

ness K_M, whereas the threshold K_{th} exhibited a minimum value at an intermediate hydrogen content and further increased. Such an unusual beneficial effect of hydrogen on the threshold K_{th} was explained by the reduction of secondary creep rate at low and high hydrogen levels. The minimum K_{th} at an intermediate hydrogen content is due to hydrogen whose insufficient level cannot neither suppress creep nor decrease toughness to a low level, but can promote hydrogen embrittlement in material.

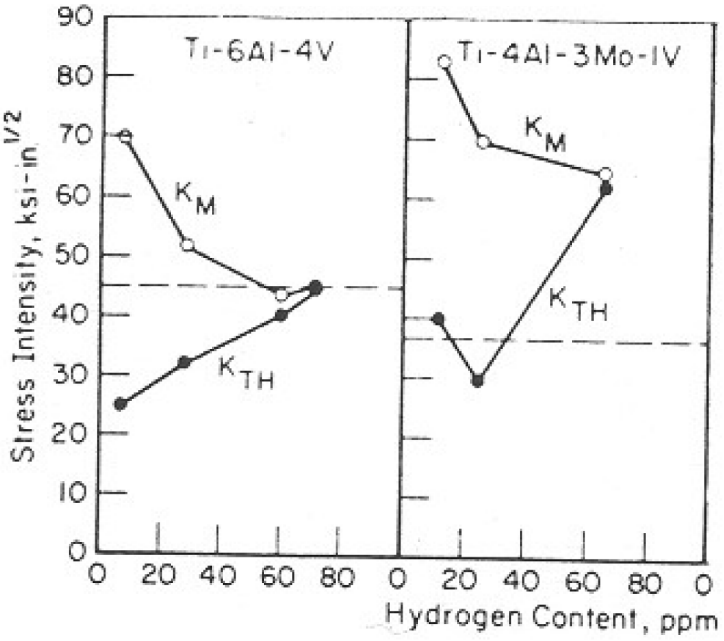

Figure 1.15: Effect of hydrogen on the fracture toughness K_M and threshold stress intensity K_{th} for Ti-6Al-4V and Ti-4Al-3Mo-1V [215].

Similar to Williams [215], the experiments of Vassel [205] at room-temperature single-edge-notched precracked specimens showed that fracture toughness decreases as hydrogen content increases, whereas the sustained load cracking was improved and even absent in the alloys containing 105 ppm of hydrogen (see Figure 1.16). Such an anomalous behavior was suggested to be due to an additional mechanism that must play an important role in crack propagation together with hydrogen embrittlement. Metallographic observations established that SLC is due to the cleavage of the α phase along a plane inclined at about 14° to the basal plane.

Sastry [173] in his exhaustive study on SLC behavior in Ti-6Al-4V came to the same conclusion as Meyn [135] on the influential role of hydrogen in SLC. According to these conclusions, at low hydrogen content, subcritical crack-growth under sustained load was governed by creep deformation, while at high content the role of hydrides becomes increasingly dominant in crack propagation. The effect of hydrogen was more pronounced in β-annealed specimens than in recrystallization-annealed as can be seen in Figure 1.17 due to the higher fraction of β-phase in the structure of the former alloy. It was explained by the higher solubility of hydrogen in the β phase which might either create tensile stresses in the adjacent α-phase and initiate cleavage near the α-β interfaces or result in hydride precipitation along the α-β interfaces and lead to interfacial separation.

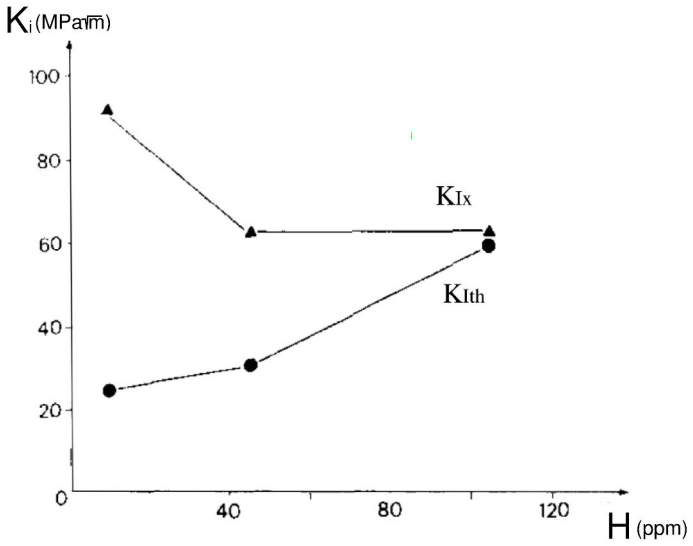

Figure 1.16: Effect of hydrogen on the fracture toughness K_{Ix} and threshold stress intensity K_{Ith} for Ti-6Al-14V [205].

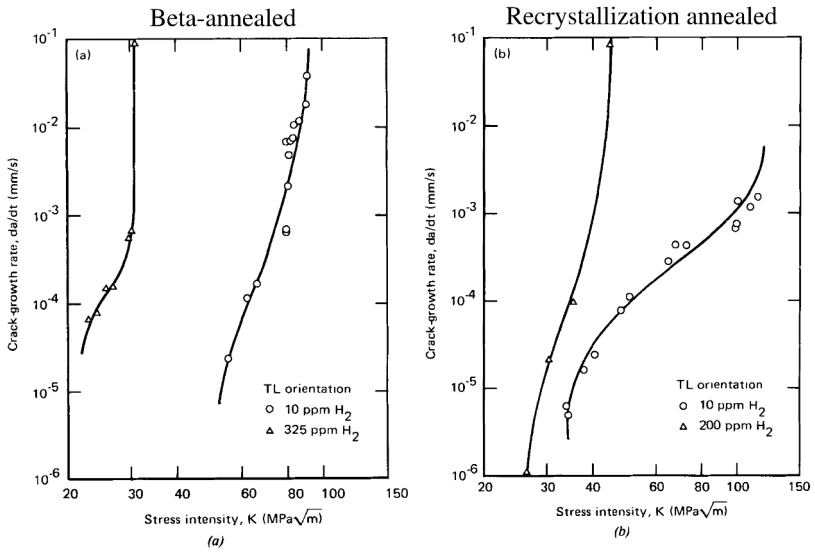

Figure 1.17: Effect of hydrogen concentration on subcritical crack-growth in Ti-6Al-6V-2Sn in humid air atmosphere for (a) β annealed and (b) recrystallization annealed alloys [173].

Gao and Dexter [78] in their investigation of room-temperature creep of Ti-6Al-4V alloy suggested that hydrogen might promote both softening and embrittlement in the same alloy. According to their study, dissolved hydrogen can alter the binding energy of the crystal lattice in such a way that the cohesive energy is reduced and screw dislocation mobility is increased. As a result, the primary creep in Ti can be accelerated leading to hydrogen-induced softening. At the later stage of deformation, hydrogen pile-ups near the subboundaries can cause failure by hydrogen embrittlement.

In the work of Gu and Hardie [86] on Ti-6AI-4V, two regimes of slow crack extension K_s depending on hydrogen content were detected (see Figure 1.18). Up to 90 ppm, K_s is enhanced but the crack propagation resistance is decreased leading to an increasing rate of slow crack growth. Creep was concluded to be a controlling mechanism of slow crack growth at this level of hydrogen. At the content above 125 ppm, hydrogen might induce an expansion of the α lattice and, as a result, the enrichment of hydrogen at the stressed crack tip due to interaction with the triaxial stress and dislocations reduces the threshold stress intensity factor K_s. The crack growth becomes controlled by hydrogen diffusion in the α and β phases. The fractographic observations in the slow cracking region shows a mixture of dimples and cleavage below 90 ppm, while the fraction of cleavage is reduced as the hydrogen content increases.

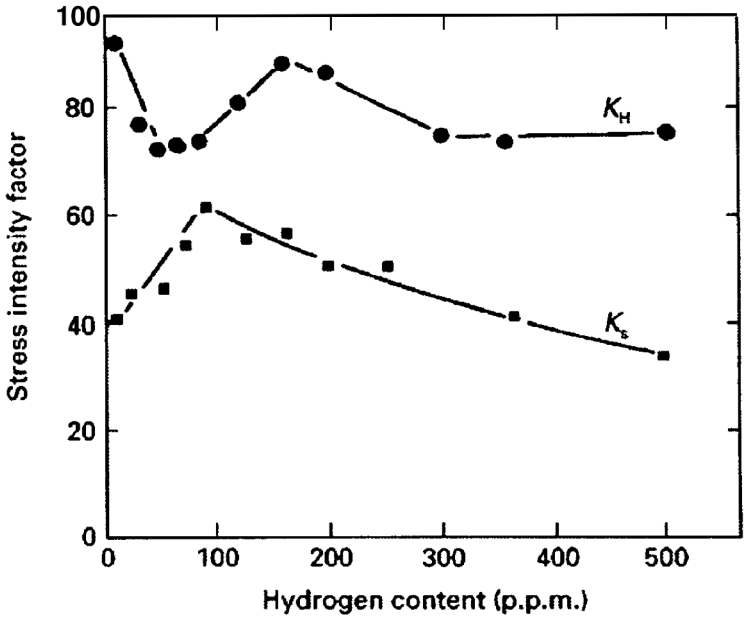

Figure 1.18: Effect of hydrogen on the threshold stress intensity factor for slow crack initiation, K_s, and the critical stress intensity factor for fast cracking, K_H for Ti-6Al-14V [86].

Hardie and Ouyang [88] studied the effect of hydrogen concentration in a large range on slow and fast cracking regimes in Ti-6Al-14V CT specimens. They have found that increasing the hydrogen content up to 60 ppm leads to the higher resistance to slow cracking K_s which is dominated by creep effects (see Figure 1.19). This enhancement is probably due to the restricted plastic zone at the crack tip. In the range between 60 and 200 ppm of hydrogen, the critical stress intensity factors for slow cracking coincides with that for fast fracture K_H. Above the critical hydrogen level of 250 ppm, hydrogen gets accumulated at α/β interfaces, leading to hydride cracking and fast propagation of a brittle crack.

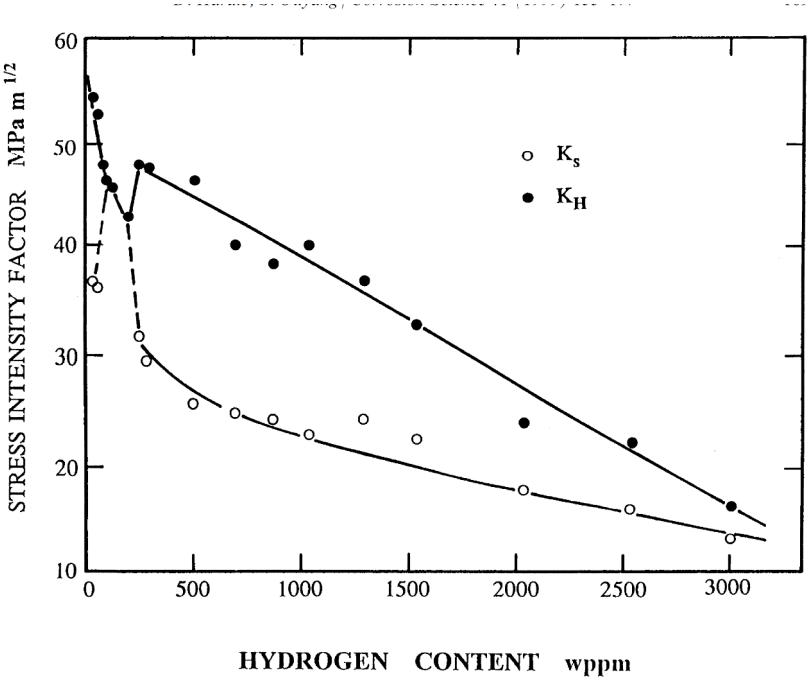

Figure 1.19: Effect of hydrogen content on the stress intensity factors of slow K_s and fast K_H cracking for CT specimens of Ti-6Al-14V [88].

Parameters such as microstructure, temperature, texture are expected to influence SLC characteristics as well. The susceptibility of Ti alloys to hydrogen-induced subcritical crack growth is strongly dependent on the microstructure of the alloy and especially on the amount of β phase which is known to have a higher solubility of internal hydrogen in Ti. The higher solubility and the rapid diffusion of hydrogen in the β phase results from the non compact body center cubic (BCC) structure, which consists of 12 tetrahedral and 6 octahedral interstices in comparison to 4 tetrahedral and 2 octahedral interstitial sites in the HCP lattice of α phase [192].

In a hydride-forming system, Ti alloys of α phase, when exposed to external hydrogen, will degrade primarily through the repeated formation and rupture of the brittle hydrides in the α phase. Three types of hydrides have been observed to form in the α-phase at room temperature: δ, ϵ and γ hydrides. The δ-hydrides which are formed between $TiH_{1.5}$ and $TiH_{1.99}$ have an FCC lattice with the hydrogen atoms occupying the tetrahedral interstitial sites [148, 182, 192, 197]. The δ-hydrides transforms diffusionless into the ϵ hydrides with an face-centered tetragonal (fct) structure ($c/a \leq 1$) below 37 °C. At low hydrogen content (1-3 %) the metastable γ hydrides are formed, with an fct structure of $c/a \geq 1$. Interstitial hydrogen occupies one-half of the tetrahedral interstices in the γ hydride structure.

The high voltage TEM $in-situ$ observations of the HCP α Ti-4%Al alloy [182], exposed to a gaseous hydrogen environment at room temperature, revealed two possible fracture mechanisms which can be operative depending on the level of stress intensity factor. At low stress intensities corresponding to small crack velocities, the fracture proceeded by a stress-induced repeated hydride formation and cleavage mechanism, whereas at high stress intensities corresponding to high crack advance rates, failure occured by hydrogen-enhanced localized plasticity (HELP) at the crack tip. The failure mechanism in case of HELP is similar to the mechanism of crack advance in inert environment, however the stresses needed to move dislocations are significantly reduced by a high hydrogen concentration in solid solution [182]. The role of hydrogen in reduction of the stress for dislocation motion and consequently for dislocation generation has been

extensively studied by Birnbaum [31, 182]. Enhanced dislocation velocities were observed for different kinds of dislocations and materials, indicating the generality of the mechanism [67]. It has been noticed that the stopped cracks continued to propagate under the sustained load when hydrogen was introduced into the environmental cell. The fracture process in the presence of hydrogen was due to localized ductile failure resulting from the increase in the dislocation velocity at the crack tip. Hydrogen locally softens the material in front of the crack, allowing ductile fracture to occur there, prior to general yielding away from the crack tip. The observed deformation occurs along grain boundaries (intergranular fracture) where hydrogen tends to be concentrated. The cause for softening should be sought in hydrogen shielding which greatly reduces the interactions dislocations-point defects and dislocations-internal stress fields. As a result, dislocations velocity increases under stress as the slip barriers can be more easily overcame by thermal activation.

In the α-β alloys, in the presence of significant amount of β phase, environmental hydrogen embrittlement of titanium can be explained in terms of relative hydrogen transport rates within α phase and β-phase. Microstructure with a continuous α-phase matrix with a fine, dispersed β phase in the boundaries were found to be less severely embrittled than microstructures containing a continuous β phase in the boundaries which provided a rapid pathway for hydrogen diffusion into the material (Figure 1.20 (b)) [144]. Brittle fracture in the former microstructure occurred primarily by transgranular separation associated with cleavage and, in the latter by intergranular cracking. From these studies it was suggested that the diffusion rate of hydrogen in the β phase is the rate controlling process of crack growth under sustained load in Ti-6AL-4V.

Ti alloys of β phase are known to be fairly resistant to hydrogen embrittlement due to their higher hydrogen solubility at room-temperature. However, at higher hydrogen pressures, they were found to form brittle δ hydride phases [181] on the $\{10\bar{1}0\}$ slip plane which can have a significant effect on the ductile-to-brittle transition and the change in the fracture mode of the BCC β alloys.

Boyer [32] pointed on the importance of exposure temperature and hydrogen content in SLC of Ti-6Al-4V. He proposed that during the SLC experiments, the stress intensity is high enough to allow crack propagation by any of three mechanisms: (1) creep (2) cleavage and (3) interfacial separation. Increasing the hydrogen content raises the temperature at which SLC will occur and increases the crack growth rate. The crack growth rate was observed to decrease at higher temperatures which was attributed to a decrease in hydride nucleation.

The theoretical model of SLC by hydride growth presented by Pardee and Paton [153] indicated that SLC rate in Ti alloys containing 100 ppm of internal hydrogen increases by several orders of magnitude as temperature decreases from room temperature to approximately -70°C. A rapid increase in the crack growth was attributed to the facilitation for the δ-hydride nucleation in the α phase with the decreased temperature. For a given hydrogen content, at room temperature, the crack growth may be attributed to a creep mechanism, while at lower temperature, hydride precipitation becomes operative, producing more cleavage sites.

Moody [138] investigated the dependence of internal hydrogen-induced subcritical crack growth (SCG) in Ti-6Al-6V-2Sn on the temperature. It was found that, relatively small content of residual internal hydrogen ($\leq$50 ppm) at low temperature (slow strain rate) can increase the crack growth rate due to the increase of hydrogen diffusion at the crack tip under applied stress leading to hydride precipitation. The propagation of the crack in this case occurs by continuous hydride cracking. At high temperatures (high strain rates) hydrogen decreases the crack growth rate which is related to the difficulty of hydride formation.

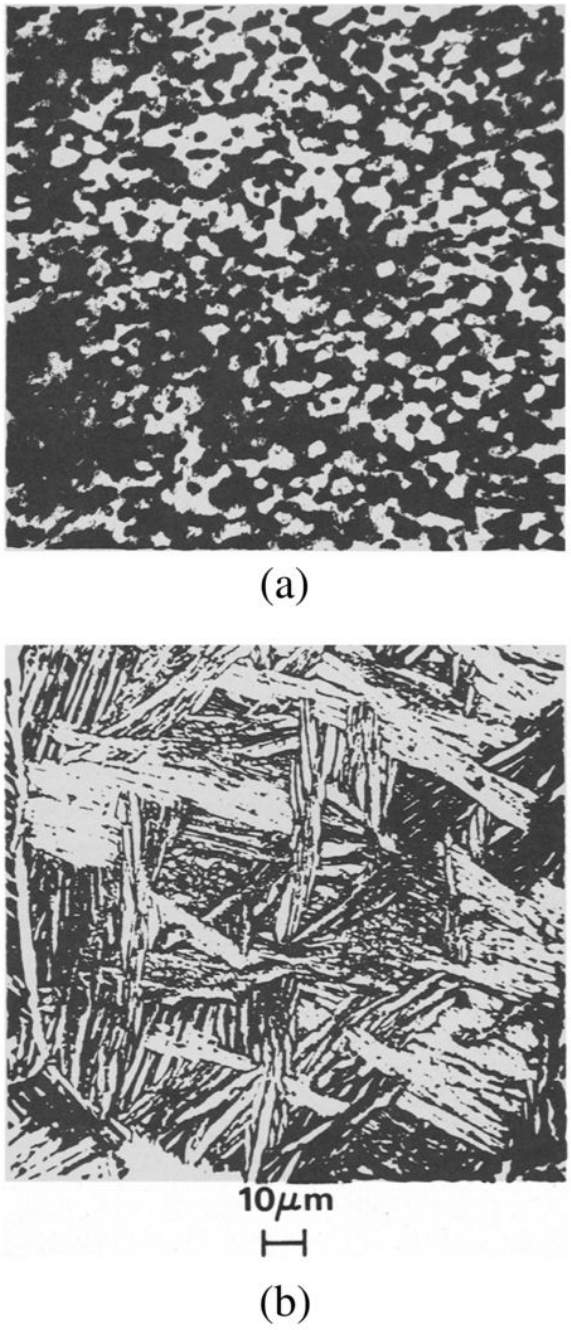

Figure 1.20: Initial microstructure of Ti alloy Ti-6Al-4V: (a) primary α phase, equiaxed grains forming continuous matrix with the retained β phase; (b) Coarse, acicular α phase in a β matrix [145].

The results of the sustained crack growth tests performed by Yeh [224] on Ti-6Al-4V with 47 ppm of hydrogen at temperatures from 20°C to 95°C showed that for all test conditions, the crack growth exhibits the typical three-stage characteristics with a plateau in stage II corresponding to almost constant velocity of crack propagation (Figure 1.21). This plateau was found to increase with temperature. It was concluded that the constant crack growth veloc-

ity may be the result of the competition between the increase of hydrogen diffusion and the decrease of yield strength with increasing temperature. The resistance to hydrogen-induced crack growth is due to crack tip blunting. As the temperature increases, the ability of crack blunting increases resulting in the higher resistance to crack growth. Two possible mechanisms of hydrogen-enhanced localized plasticity (HELP) and dynamic strain aging were proposed to explain hydrogen-induced crack propagation.

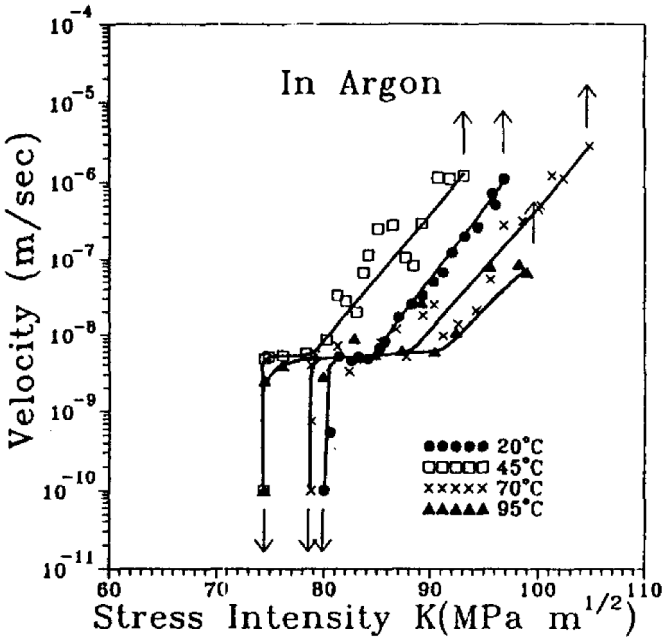

Figure 1.21: Crack growth rate in Ti-6Al-4V from for different temperatures [224].

The kinetics of crack growth and the shape of the crack surface developed under sustained load can be equally affected by specimen dimensions. The threshold stress intensity can increase when the specimen deviates from dimensions required to ensure plane strain conditions across most of the crack front [215, 216]. Higher hydrogen susceptibility during crack growth in the specimens with the plane-strain geometry was explained in terms of the smaller hydrostatic stresses ahead of the crack tip which caused less hydrogen accumulation in the crack tip zone [139]. According to Sastry [173], the greater prestrain and smaller plastic relaxation associated with plane-strain conditions increase the sensitivity to SLC.

The effect of crystallographic texture on SLC crack was studied by Sastry on three different microstructures of Ti-6Al-6V-2Sn shown in Figure 1.22: (a) Beta-annealed texture with a random crystallographic texture; (b) recrystallization annealed and (c) treat-and-aged textures with sharp near-transverse-basal components. The crack growth kinetics was determined in the specimens with TL and LT orientation. The recrystallization-annealed and solution-treat-and-aged specimens exhibited pronounced orientation dependence of crack-growth rate and threshold stress-intensity. In the TL specimens, the cracking plane is parallel to the basal plane, which is known to be the main cleavage plane in Ti [135]. As a result, crack propagation by cleavage is facilitated in the TL orientation, causing a higher crack growth rate and lower K_{th} comparing to the LT direction. Ductile tearing and secondary shear cracking characterized the LT specimens fracture mode. The slow crack-rate growth can be due to the increased resistance to plastic

deformation because of the higher resolved shear stress required for $< c + a >$ slip and lower Schmid factor in $< 11\bar{2}0 >$ slip. In beta-annealed specimens, the randomness of the texture led to the less pronounced orientation dependence of SLC growth.

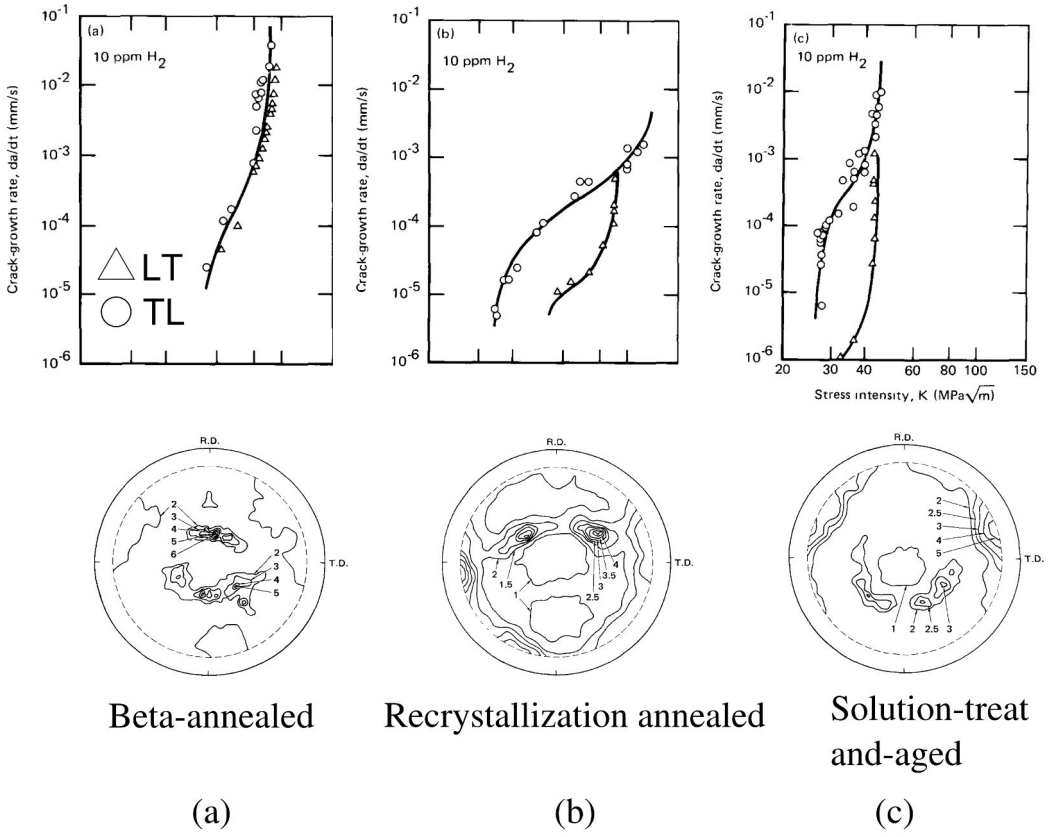

Figure 1.22: Effect of specimen orientation on subcritical crack-growth rate in Ti-6Al-6V-2Sn for (a) beta-annealed, (b) recrystallization annealed, and (c) solution-treat-and-aged microstructures tested in LT and TL orientations [173].

The comprehensive study of the effect of specimen orientation on resistance to hydrogen embrittlement carried by Clarke [53] confirmed that the material is most susceptible to embrittlement when the fracture plane is perpendicular to the direction in the material having the highest concentration of basal poles, i.e. the applied stress is close to the normal to the common habit plane for hydride in the α-phase.

The presented overview of the existing studies indicates that Ti alloys are highly susceptible to inert-environment sustained load cracking propagation. This embrittlement is clearly linked to the internal hydrogen content of the material or external hydrogen from the environment. Depending on the concentration in the material, hydrogen can either precipitate under strain as a hydride and then cracks nucleate, or it can remain in solution leading to hydrogen-induced cracking in regions of high strain where hydrogen concentrates. Hydrogen-induced crack growth is highly affected by temperature, microstructure, crystallographic texture and hydrogen concentration.

1.3.2 Effect of oxygen on fracture behavior

As it is known from the existing phase diagrams, hydrogen stabilizes the β-phase, whereas oxygen, nitrogen and carbon are α-stabilizers. Interstitial oxygen is known to increase the yield stress of Ti alloys while preserving the corrosion resistance of the α-phase provided by a oxide layer spontaneously formed when exposed to air (due to high affinity of titanium to oxygen). Despite beneficial oxygen effect on the resistance to erosive corrosion, the removal of interstitial oxygen is advisable since generally higher oxygen contents may enhance hydrogen embrittlement by reducing the lattice solubility of hydrogen, thereby increasing the amount of precipitated hydride. An extended review on mechanical behavior of oxygen and hydrogen-bearing Ti alloys was given by Wacz [212] and Conrad [56].

At low temperatures, fracture in titanium alloys containing less than 1.5% oxygen occurs by necking and microvoid coalescence followed by ductile shearing. Fracture strains decrease with increasing oxygen content. In the temperature range between 500 and 970 K, CP Ti exhibits a minimum of ductility, and the effect decreases with increasing oxygen content which promote glide over twinning [56]. The fracture surface consists in this case of deeper and larger dimples. Ti alloys with 1.0% oxygen concentration show brittle fracture at 116 K. Microcracks were observed to nucleate at $\{11\bar{2}2\}$ twins and to grow at the boundary between the second order twin and the matrix [7].

Oxygen can significantly lower the secondary creep rates of α Ti alloys especially at high temperatures. This effect was attributed to strain aging, which along with cold working, tended to improve creep resistance [99]. A recent multi-scale investigation of the viscoplatic behavior and SLC under the combined influence of solute oxygen and hydrogen [18, 17] confirmed the effect of dynamic strain aging on the reduction of the creep rate in CP Ti alloys. It was proposed that interstitial oxygen can exert a solute drag force on dislocation which would hinder their motion leading to the incubation period observed in Grade 4 and decrease in the creep rate at the primary stage (see Figure 1.23). The subsequent spontaneous creep acceleration observed in the material was explained to be due to plasticity activated in a large fraction of grains. Hydrogen-enhanced localized plasticity might result in an aging-induced rejuvenation of the creep presented in Figure 1.24. It was concluded, that room-temperature creep is conrtolled by the atomic oxygen to hydrogen ratio, where oxygen hinders the creep through the dynamic strain aging, whereas solute hydrogen atoms shield gliding dislocations from the oxygen drag force, thus enhancing the creep.

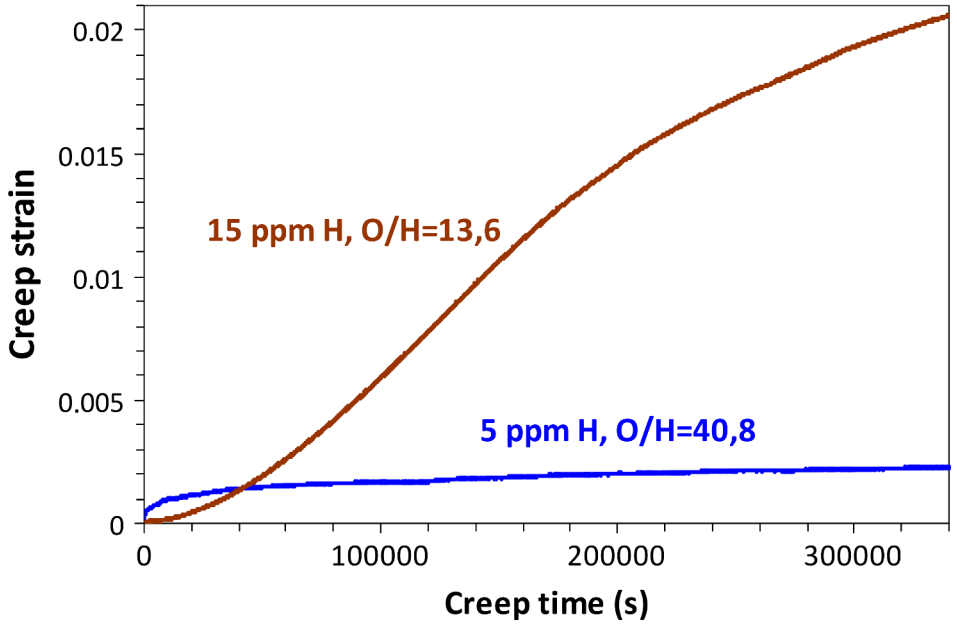

Figure 1.23: Influence of hydrogen depletion on creep in Grade 4 tested in transverse direction at 0,72 $\sigma_{0,2}$ [18].

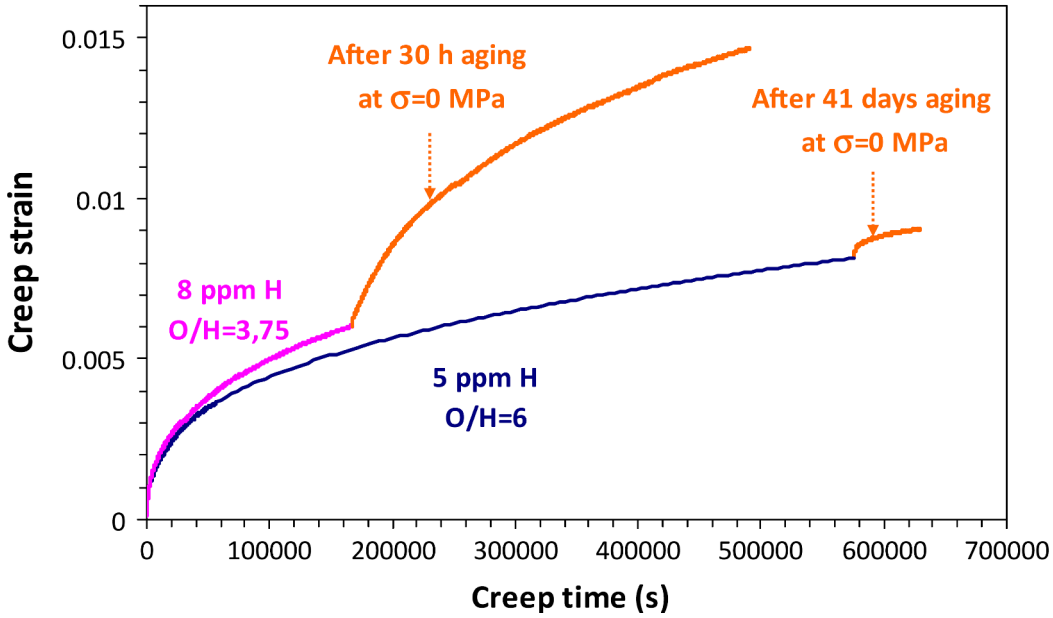

Figure 1.24: Aging-induced rejuvenation of the creep potential [18].

1.4 Conclusions

The presented review shows that crystallography of CP α titanium defines many important features of mechanical behavior of this material. Some of them are:

- Deformation modes: prismatic $\langle a \rangle$ slip is the easiest deformation mode to activate in single and polycrystals. The pyramidal π_1 $\langle c + a \rangle$ slip is generally considered important for accommodating strains along the c-axis. Twinning mode is also important for strain accommodation, however there is less evidence about the overall operation of twinning in CP α Ti at the low level of strain.
- The typical texture component of α Ti after cold rolling is (0, Φ, 30), where Φ ranges from 30 to 40°, which leads to the strong anisotropy of the mechanical properties.
- The phenomena of static and dynamic strain aging observed in CP α Ti is associated with the interaction between interstitial atoms of oxygen and hydrogen with moving dislocations. Existing modeling approaches of strain aging effects are discussed.
- The importance of sustained load cracking in titanium alloys is highlighted. An antagonist role of hydrogen and oxygen in the fast and slow fracture cracking of CP α Ti is discussed.

Chapter 2

Characterization and modeling of strain aging phenomena in Grade 4

Résumé

Le deuxième chapitre vise à modéliser le comportement viscoplastique du titane de la phase α (Grade 4) en tenant compte du vieillissement statique et dynamique mis en évidence lors de la caractérisation expérimentale. L'apparition d'un crochet de traction de quelques MPa suivi d'un palier de type Lüders a été attribué aux interactions entre les atomes interstitiels d'oxygène et les dislocations $< c+a >$ de type coin. Les serrations de type Portevin-Le Chaterlier sont dû au blocage des dislocations $< a >$ vis par dissociation de leur cœur dans la structure cristalline. Un modèle phénoménologique de vieillissement de Kubin-Estrin-McCormick (KEMC) a été couplé avec une approche de plasticité crystalline pour prendre en compte le rôle de la cristallographie dans le vieillissement statique et dynamique. Il a été démontré que la localisation de la plasticité à l'échelle locale et macroscopique se manifeste de manière différente.

Contents

2.1 Introduction

The present chapter is dedicated to the study of viscoplastic behavior of CP α Ti and phenomena of static and dynamic strain aging in the material. A phenomenological strain aging model was combined with a comprehensive description of slip systems active in HCP crystals in order to take into account the role of crystal plasticity in static as well as dynamic strain aging phenomena. Finite element simulations were performed on the polycrystalline aggregates with various numbers of grains taking into account the elastic and plastic anisotropy of α Ti. It will be shown that the slip activities can lead to the cooperative deformation modes inside the grains of a polycrystal causing the development of plastic heterogeneities inside the material. The model captures the macroscopic viscoplastic anisotropic response and the corresponding slip processes in grains.

2.2 Materials and experimental procedures

In the present study CP α-Ti of Grade 2 and Grade 4 were investigated. The nominal chemical composition of the materials is given in Table 2.1. Experimental cylindrical specimens with a 8 mm diameter and a 16 mm gauge length were extracted from cold-rolled plates and cut parallel (longitudinal direction LD) and perpendicular to the rolling direction (transverse direction TD) of the plates. The specimens were then annealed at 500°C during 12 hours under high vacuum.

	H	O	C	Fe	N
Grade 2	6±2	1600±50	40	340	30
Grade 4	15±3	3200±100	70	1700	60

Table 2.1: Chemical composition of the titanium used in this study (wt. ppm).

The electron backscattered diffraction (EBSD) analysis showed that both materials have an equiaxed grained microstructures with average grain size of 30 μm for Grade 2 and 42 μm for Grade 4 (Figure 2.1 (a)). The crystallographic texture of both grades has a $\langle 10\bar{1}0 \rangle$ direction parallel to LD and $\langle c \rangle$ axes tilted from 30 to 90° away from normal direction (ND) towards the TD (Figure 2.1 (b,c)), characters that corresponds to the typical texture of the cold-rolled Ti sheet [97].

Tensile tests were performed at room temperature on both TD and LD cylindrical samples of Grade 2 and Grade 4 at fixed strain rate of 2×10^{-4} s^{-1} and with tenfold upward and downward strain-rate jumps ranging from 2×10^{-6} s^{-1} to 2×10^{-2} s^{-1}.

Additional $in-situ$ tensile tests on the flat TD and LD specimens of 1.2 mm thick and 6 mm width were carried out in a scanning electron microscope (SEM) in order to analyze the main deformation modes. Critical resolved shear stress (CRSS) for each slip system was estimated based on the slip trace analysis coupled with EBDS technique and TEM observations. More information about the employed technique can be found elsewhere [17, 19]. Prismatic slip with the lowest CRSS was found to be the leading deformation mode in LD and TD specimens for both materials. The first-order pyramidal slip of $\langle a \rangle$ dislocations is the second most frequent mode of deformation. The first order pyramidal $\langle c + a \rangle$ slip systems were mostly active in

TD-specimens. No evidence of pyramidal $\langle c+a \rangle$ slip family of the second order was found. Twinning was shown to become operative only at later stages of deformation (at $\varepsilon_p \geq 8\%$) at a lower content of oxygen (for Grade 2). An increase in the oxygen content promotes prismatic and pyramidal $\langle c+a \rangle$ glide and suppresses basal slip and twinning [17].

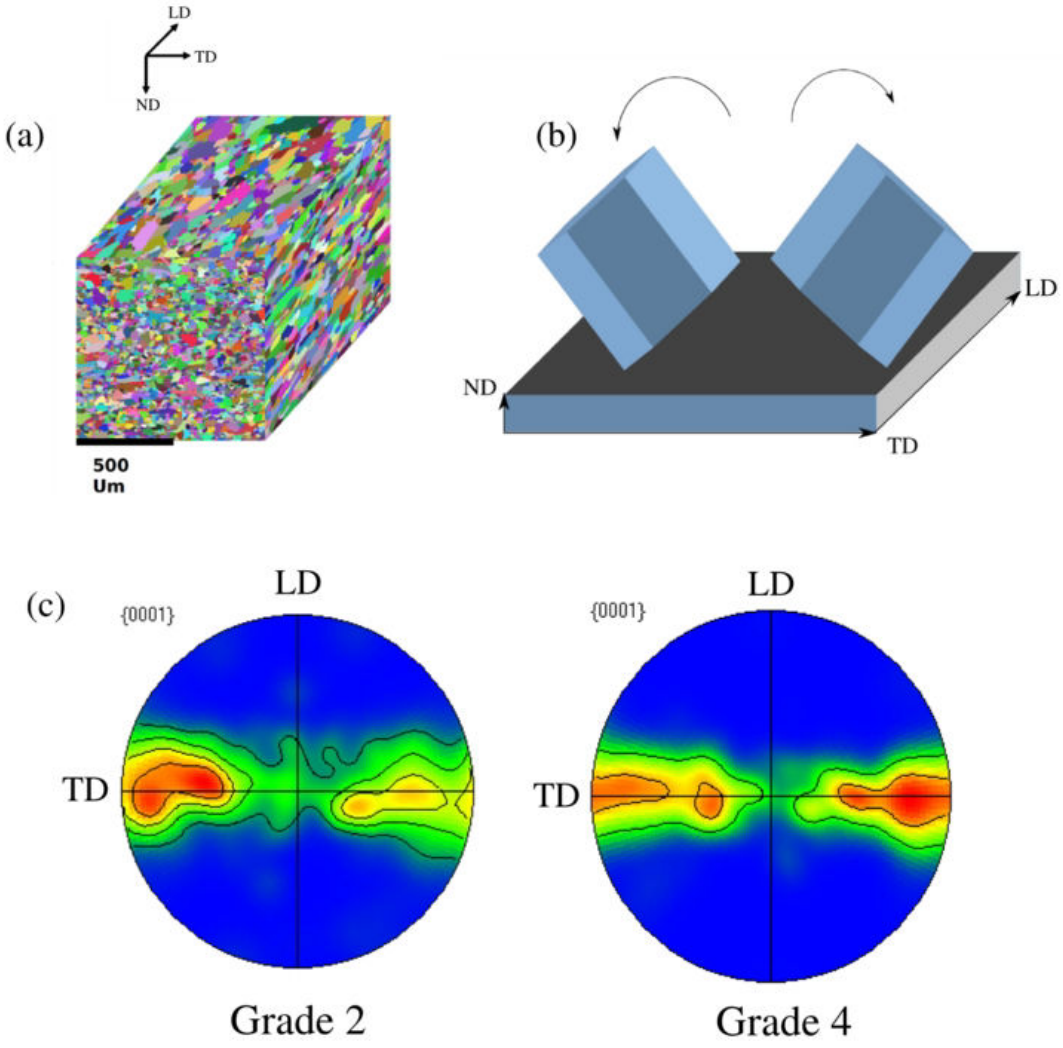

Figure 2.1: (a) Initial 3D microstructure for Grade 2. (b) Schematic illustration of crystal orientation withing the sample. (c) (0001) pole figure of Grade 2 and Grade 4 [17].

2.3 Evidence of strain aging

The engineering stress-strain curves of CP Ti of Grade 2 and Grade 4 strained at 2×10^{-4} s^{-1} are shown in Figure 2.2(a). Both materials show a higher yield stress when specimens are tested along the TD than along the LD. Such anisotropic response can be explained by the lower Schmid factor ($\backsimeq 0.35$ instead of $\backsimeq 0.43$) for the $< a >$ prismatic slip and the higher CRSS for the more favorably oriented $< c+a >$ pyramidal glide. In that orientation the activation of $< c+a >$ pyramidal slip , with the highest CRSS has been repeatedly observed experimentally

[163, 19] just after the yield drop and is expected to contribute to the higher flow stress recorded in the TD. The measured yield stress and elastic modulus are given in Table 2.2. The anisotropic mechanical response of the material in LD and TD directions is mainly due to the pronounced texture, which is a consequence of rolling processing. A stress peak followed by a slight yield drop and a stress plateau have been observed for both Grade 2 and Grade 4 at small strain for the specimen loaded along TD. The stress drop slightly increases with the oxygen level (i.e. for Grade 4). The stress peak and plateau have not been observed in tension along LD for either Grade 2 or Grade 4. The present study will concentrate on the identification of the behavior of Grade 4.

Grade	Orientation	E (GPa)	σ_{ys} (MPa)
Grade 2	LD	114	330
	TD	118	404
Grade 4	LD	112	473
	TD	121	592

Table 2.2: Young's modulus (E) and yield stress (σ_{ys}) for Grade 2 and Grade 4.

Figure 2.2(b) illustrates a tensile test conducted at $\dot{\varepsilon} = 2 \times 10^{-3}$ s^{-1} on the flat tensile specimens of Grade 4 in TD with complete unloading and reloading without hold time. The systematic reappearance of the yield peak after each reloading suggests a phenomenon of SSA, even though the material was not aged before reloading. The absence of the first peak on the stress-strain curve can be attributed to possible slight misalignment of the tensile grips during this particular experiment.

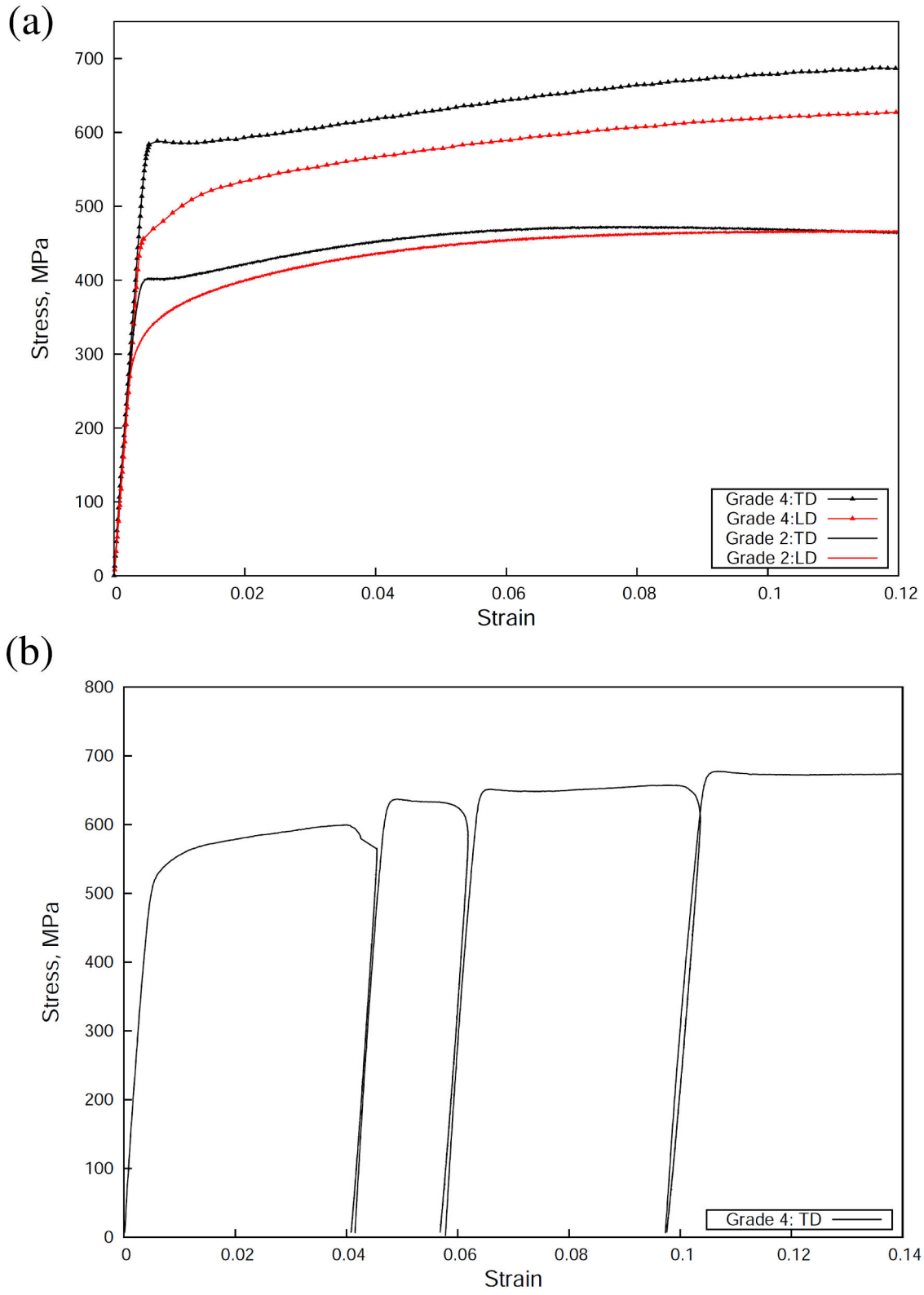

Figure 2.2: Tensile tests on Grade 4: (a) on the cylindrical specimen in TD and LD at $\dot{\varepsilon} = 2 \times 10^{-4}$ s^{-1}. (b) on the flat tensile specimen in TD with unloading and reloading without hold time, $\dot{\varepsilon} = 2 \times 10^{-3}$ s^{-1}.

Similar tensile experiments were performed with partial unloading (see Figure 2.3) in order to check the kinematic hardening components. Slightly opened hysteresis loops revealed the existence of the internal stress component for CP α Ti. Internal stresses can be induced by the formation of appropriate dislocation arrangements such as pile-ups [34].

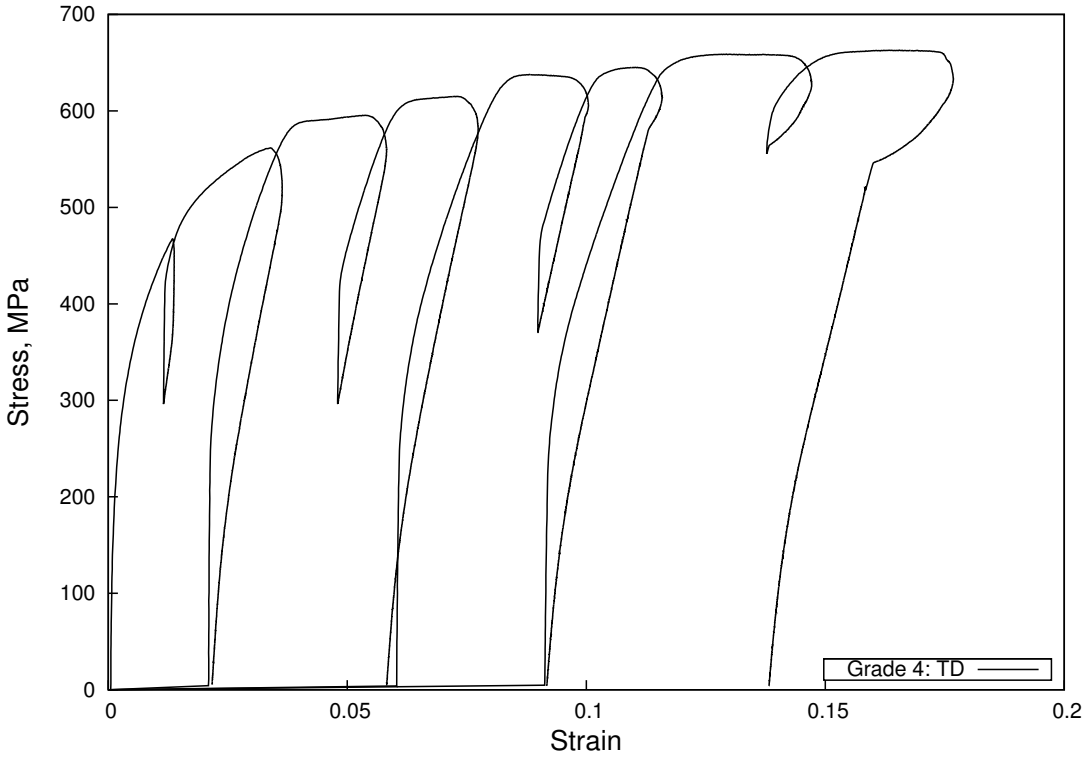

Figure 2.3: Tensile test on Grade 4 on the flat tensile specimen in TD with partial unloading at $\dot{\varepsilon} = 2 \times 10^{-3}$ s^{-1} without hold time.

The strain rate sensitivity (SRS) of the material was determined in the tensile tests with strain rate jumps ranging from 2×10^{-2} to 2×10^{-6} s^{-1}. The SRS parameter is defined as:

$$SRS = (\frac{\partial \sigma}{\partial \log \dot{\varepsilon}_p})_{T,\varepsilon_p} \tag{2.1}$$

where σ is the stress tensor and $\dot{\varepsilon}_p$ is the accumulated plastic strain rate. Small serrations in both TD and LD samples typical for the PLC effect were observed on the stress-strain curves corresponding to strain rates of 2×10^{-5} and 2×10^{-6} s^{-1}. The amplitude of these serrations increased from 1 to 6 MPa as the strain-rate decreased from 2×10^{-4} to 2×10^{-6} s^{-1} (Figure 2.4). The amplitude of the detected serrations largely exceeds the measured noise by the strain gauge of the load cell (0.22 MPa), and cannot be ascribed to the tensile testing machine. The apparent macroscopic SRS during the jump tests between 2×10^{-5} s^{-1} and 2×10^{-6} s^{-1} remains

positive. Note that additional tensile tests at lower strain rates should be carried out to explore further the extent of the negative SRS domain. A physical interpretation of the existence of PLC effect in the presence of positive apparent SRS will be proposed and discussed in the next section.

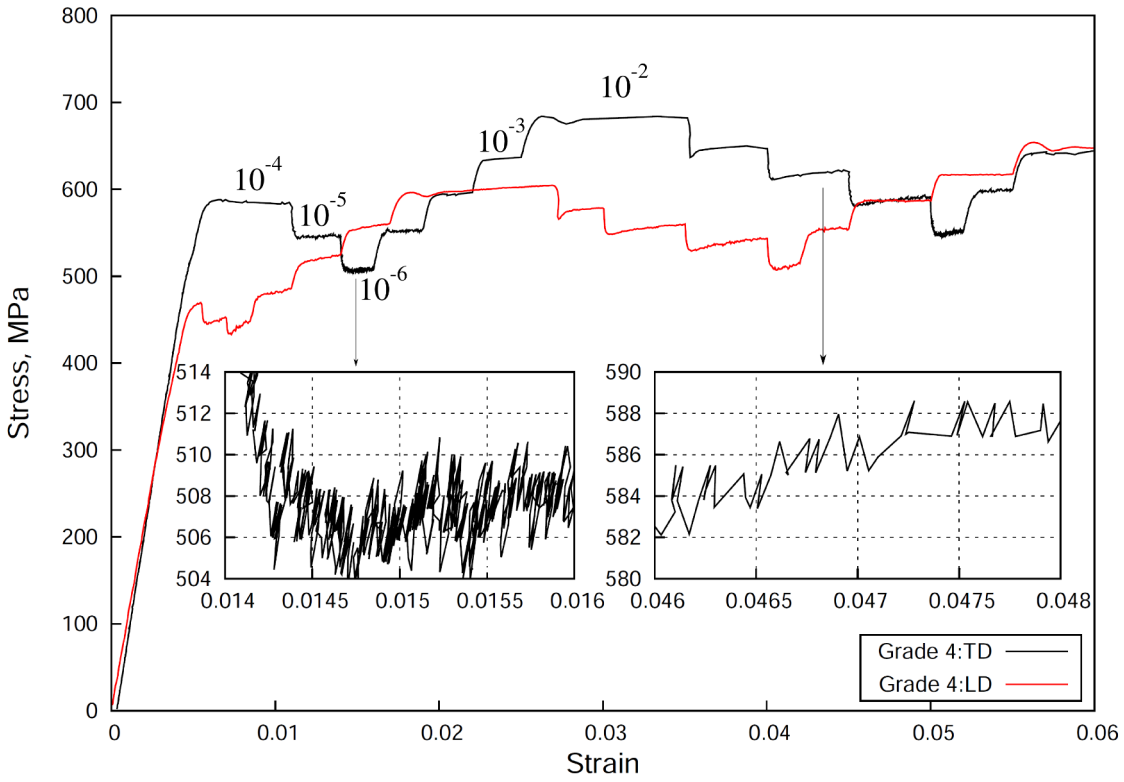

Figure 2.4: Jump tests on the cylindrical specimens on Grade 4 in TD and LD at $\dot{\varepsilon} = 2 \times 10^{-2} - 2 \times 10^{-6}$ s^{-1} [17].

2.4 Proposed scenario

Based on the literature results presented in the Chapter 1, a physical interpretation of the origin of the anomalous yield point and serrations on the stress-strain curves in terms of the main deformation mechanisms in CP α Ti at room temperature is proposed in the present section.

The presence of a yield stress peak followed by a plateau on the tensile curves of TD-samples can be explained by two alternative strengthening mechanisms simultaneously active in the material: dislocation pinning by solute drag force exerted on moving dislocations (static strain aging) and forest type mechanism due to multiplication of dislocations by sources, gliding with a high velocity between long distances obstacles (strain hardening). When age hardening is absent or disappears, strain hardening becomes operative thus sustaining locally a similar stress level [188, 83].

Hardening by solute drag is based on the elastic interaction between dislocations and solute atoms that can take two forms: (1) Snoek ordering of interstitial solute atom pairs in the stress field of dislocations and (2) Cottrell cloud produced by bulk diffusion of solute atoms around edge dislocations. Following the Schoeck and Seeger [176] interpretation of the Snoek-effect [185], an ordering (short-distance rearrangement) of solute interstitials can take place in the immediate vicinity of the dislocation core where the strain distortion of the line is maximal. Snoek pinning of dislocations by paired defects has been invoked as the applicable mechanism in α-Zirconium [157, 98]. In the investigation of the effects of irradiation on Zircaloy-2 [206, 207] oxygen-oxygen pairs were found to be responsible for strain aging. Later in the work of Lacombe [111] it was also concluded that the rapid strain aging in Ti is mainly due to the Snoek ordering of interstitial atoms of oxygen in the stress field of dislocations. During aging, interstitial atoms in the close neighborhood of the dislocation core rearrange by jumps of small amplitude to occupy octahedral sites, thereby minimizing the free energy of interaction with the dislocations. An increment in flow stress is then required to free dislocations from free energy valleys [69]. Donoso and Reed-Hill [63] argued that anelastic effects produced by oxygen ordering and dislocation pinning are not necessarily related. They suggested that the initial rise in flow stress in Ti is controlled by the drift of oxygen atoms to dislocations in agreement with Cottrell mechanism. No matter which detailed mechanism is taking place in the present study, the phenomenon of SSA observed for the material strained along TD can possibly be interpreted by the interaction of oxygen atoms with $\langle c+a \rangle$ dislocations, mobilized in tensile specimens tested along TD.

As was observed in the experiments with partial unloading and reloading, strong internal stress fields develop in the specimen. According to Brandes and Mills [34], this internal stress due to dislocation pile-ups might provide within a short time the driving force for a significant reverse plasticity described by the authors such as 'dislocation recovery'. Thus, the reappearance of the yield peak in the experiments with unloading and reloading might be due to the solute drag stress that can be restored dynamically during straining due to the dislocation recovery.

The appearance of serrations on the tensile curves in both TD and LD samples at 2×10^{-6} s^{-1} can be attributed to the non-planar core of long and rectilinear $< a >$ screw-type dislocations the mobility of which governs the room-temperature deformation of α Ti [142, 70]. Such a non-planar core is the source of a high-lattice friction when screw dislocations are lying in Peierls valleys and their motion can be described as series of jumps between adjacent valleys. Different mechanisms can be suggested to explain the behavior of these dislocations subjected to Peierls friction force: (1) nucleation and propagation of the kink-pairs when dislocation jumps between adjacent Peierls valleys [177]; (2) Friedel-Escaig or Peierls mechanism when dislocations dissociate out of their glide plane via cross-slip [68, 76]; (3) Locking-unlocking model based on the transformation of the dislocation core between non-planar stable and metastable planar glissile configurations [41, 42].

The observation of jerky flow in α Ti at positive macroscopic values of SRS is rather unexpected. However, it should be noted that heterogeneous strain rate inside the grains can be within the negative SRS regime causing the development of the stress-strain heterogeneities during plastic deformation [164], which may explain the appearance of the PLC effect on the stress-strain curve.

Additional confirmation of the proposed scenario can be found in the TEM observations of the dislocation microstructure carried out by H. Jousset [95] on Ti-6242. At room-temperature pyramidal $\langle c+a \rangle$ dislocations tend to have an edge character (Figure 2.5 (a)). The movement of these long edge dislocations is governed by the movement of small screw segments by a macro kink-pair mechanism. As can be seen on scheme 1, under an applied shear stress, edge segments start moving, creating multiple screw segments on the dislocation, called superkinks. It was concluded that SSA is due to the pinning of the pyramidal $\langle c+a \rangle$ edge dislocation by the solute

atoms of oxygen.

Dislocations of $\langle a \rangle$-type slip systems tend to have a screw character (Figure 2.5 (b)) and DSA can be attributed to the non-planar core of these dislocations. The local occurrence of cross-slip (scheme 2) was observed when prismatic screw $\langle a \rangle$-type dislocations glide onto the basal plane generating numerous screw dipoles and dislocation debris (D in Figure 2.5 (b)) leading to wavy slip lines. As described in the literature [59, 42], the sessile core structure of immobile screw dislocations can recombine into planar, glissile and metastable configurations in one of the three possible glide planes. Thus pinned by their core structure, screw dislocations in this waiting position can be mobilized by the arrival of individual or even more efficiently groups of dislocations that will form dislocation avalanches and generate localized strain bursts [95].

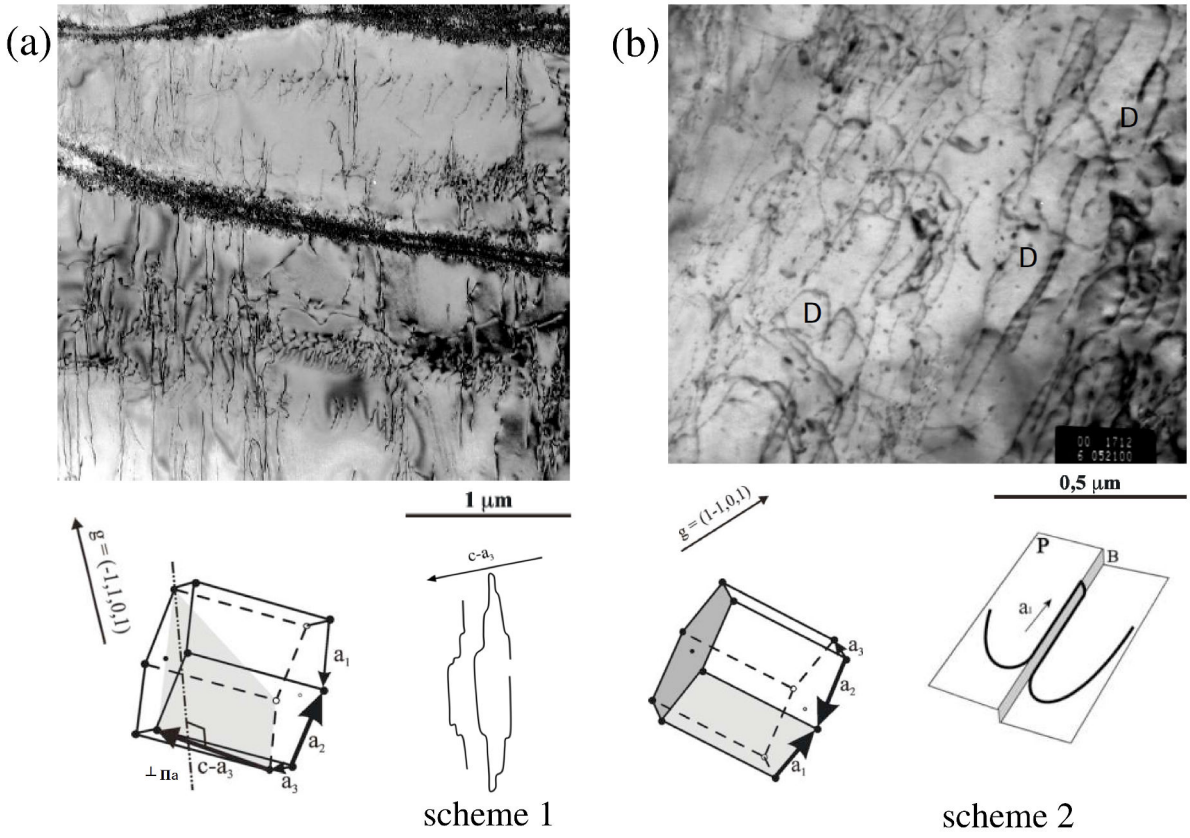

Figure 2.5: TEM observations of Ti-6242 after creep: (a) at 840 MPa at ε_p=3.4% at 20 °C. (b) at 780 MPa at ε_p=8% at 150 °C (taken from the work of H. Jousset [95]).

Localized strain bursts recorded at room temperature in tensile load as well as in relaxation test in Ti alloys [95] and in Ti-O pillars deformed $in-situ$ by TEM [229] imply local values of strain and strain rates in drastic excess of the macroscopic strain and strain rate experimentally imposed to the test piece. Depending on the amplitude of these self-organized critical dynamic events SOCD [75, 29], smaller or larger elastic unloading of the testing machine can occur and are recorded as 'serrations' of various amplitude, testifying of the negative sign of the local SRS. On the other hand, even in the absence of detectable serrations involving unloading, plasticity in crystalline materials has been recognized as intermitten or chaotic in time, a phenomenon enhanced in materials exhibiting PLC effects [213, 114]. In the absence of plastic activity during

these 'waiting periods', aging of the material is taking place even though the macroscopic strain rate is kept constant. Hence, we can conclude that, locally the aging of the material and the pinning of dislocations cannot be directly controlled by the testing equipment and remains as a specific response of the crystal, the grain or an array of grains to the particularly, stress strain, temperature and strain rate values and gradient they are exposed to.

At room temperature, Ti and its alloys when tested at macroscopic 'constant strain rates' in the range 10^{-3} - 10^{-9} s^{-1} will exhibit positive macroscopic SRS values since these testing conditions encompass the low temperature/high strain rate boundary of the PLC domain; yet for the lower values of this strain rate, localized prolonged aging periods will favor the formation of SOCD effects or small strain bursts responsible for the A-type serrations observed on the stress-strain curves (sudden increase in flow stress above the base line of the stress-strain curve due to minor and localized age hardening events).

The above described mechanisms of SSA and DSA were implemented in the present study in the formulation of a phenomenological strain aging model described in the next section.

2.5 Constitutive model

The original formulation of the phenomenological macroscopic viscoplastic model of strain aging proposed by Kubin and McCormick [106, 129] based on an implicit mathematical description of negative SRS, does not allow to simulate such a phenomenon in a range of global strain rate for which the apparent SRS is positive. It is due to the fact that such macroscopic models consider the material at the scale of the sample and they ignore the elementary mechanisms that can cause strain aging effects on a grain scale [83]. Therefore, in order to establish the link between the microstructure and the observed mechanical properties, a model at a crystal scale is needed. In the present study we introduced the aging contribution into the crystal plasticity model [131]. This approach enables an accurate determination of the local mechanical field in polycrystalline α Ti, as well as the strain and strain rate heterogeneities developed in grains during mechanical tests [164]. Depending on the set of the chosen parameters, the model can be used for both static and dynamic strain aging simulation [55].

2.5.1 Aging single crystal model

Continuum crystal plasticity model used in the present study is based on the strain aging constitutive model proposed by Zhang [231]. An additional internal variable t_a called aging time is introduced into the crystal plasticity model for the simulation of strain aging phenomena.

Four slip systems families were considered in the present model: three of them with $\langle a \rangle$-type Burgers vector and the fourth with $\langle c+a \rangle$-type (see Table 2.3).

Slip family $F(s)$	Plane and direction	Slip systems s	ϕ
1. Basal $< a >$	$\{0001\}< 1\bar{2}10 >$	1, 2, 3	I
2. Prismatic $< a >$	$\{10\bar{1}0\} < 1\bar{2}10 >$	4, 5, 6	II
3. Pyramidal $< a >$	$\{10\bar{1}1\} < 1\bar{2}10 >$	7, 8...12	III
4. Pyramidal $< c+a >$	$\{10\bar{1}1\} < 11\bar{2}3 >$	13, 14...24	IV

Table 2.3: Considered slip systems families of α Ti.

The full list of slip systems is given in Table 2.4. In total, we consider 24 slip systems, $N_{total} = \sum_{F=1}^{4} N_F$=24. We introduce the function $F(s)$ which gives the label of the family which slip system s belongs to. Each of the four slip systems families represents a set ϕ of the corresponding slip systems s. The attribution of the slip system to the set $\phi_{F(s)}$ is as follows:
If $1 \leq s \leq 3$, then $F(s)$=I and the corresponding set $\phi_I = \{1, 2, 3\}$.
If $4 \leq s \leq 6$, then $F(s)$=II and the corresponding set $\phi_{II} = \{4, 5, 6\}$.
If $7 \leq s \leq 12$, then $F(s)$=III and the corresponding set $\phi_{III} = \{7, 8..12\}$.
If $13 \leq s \leq 24$, then $F(s)$=IV and the corresponding set $\phi_{IV} = \{13, 14..24\}$.

Resolved shear stress τ^s on each slip system s is defined as:

$$\tau^s = \underset{\sim}{\boldsymbol{\sigma}} : \underset{\sim}{\boldsymbol{m}}^s = \underset{\sim}{\boldsymbol{\sigma}} : \frac{1}{2}(\underline{\boldsymbol{l}}^s \otimes \underline{\boldsymbol{n}}^s + \underline{\boldsymbol{n}}^s \otimes \underline{\boldsymbol{l}}^s) \tag{2.2}$$

where $\underline{\boldsymbol{l}}^s$ and $\underline{\boldsymbol{n}}^s$ are unit vectors directed along the slip direction and along the normal to the slip plane, respectively. $\underset{\sim}{\boldsymbol{\sigma}}$ is the stress tensor.

The plastic strain rate is the sum of the slip rates on all slip systems N_{total}:

$$\underset{\sim}{\dot{\boldsymbol{\varepsilon}}}^p = \sum_{s=1}^{N_{total}} \dot{\gamma}^s \underset{\sim}{\boldsymbol{m}}^s \tag{2.3}$$

The yield function f^s is defined as:

$$f^s(\tau^s, r^s) = |\tau^s| - r^s \tag{2.4}$$

Each slip system family possesses its own material parameters labelled with the exponent $F(s)$.

The plastic strain rate $\dot{\gamma}^s$ on each slip system s is determined by a hyperbolic viscoplastic flow rule:

$$\dot{\gamma}^s = \dot{\upsilon}^s sign(\tau^s), \quad \dot{\upsilon}^s = \dot{\upsilon}_0^{F(s)} \sinh \left\langle \frac{f^s}{\sigma_0^{F(s)}} \right\rangle \tag{2.5}$$

The hardening introduced into material consists of two terms: the initial critical resolved shear stress (CRSS), $\tau_0^{F(s)}$, and subsequent non-linear isotropic hardening including the interaction matrix h_{rs} between the slip systems:

$$r^s = \tau_0^{F(s)} + Q^{F(s)} \sum_{r=1}^{24} h_{rs}[1 - \exp(-b^{F(r)}\upsilon^r)] \tag{2.6}$$

Kinematic hardening should be introduced for a better description of relaxation effects but it is not done here for the sake of simplicity [184].

The interaction matrix includes self (diagonal coefficients of the submatrices: h_1^b, h_1^p, $h_1^{\pi_1}$ ..) and latent (off-diagonal components of the matrix: h_p^b, $h_{\pi_1}^b$, $h_{\pi_1}^p$ $\cdots$) hardening moduli [154]. This also includes interaction hardening between slip systems belonging to distinct families. The interaction matrix $[Q^{F(s)}h_{rs}]$ is given by Eq.2.7. For more realistic description, this anisotropic interaction matrix should be used in the simulations, however very little information is available regarding the hardening moduli h_{rs} of HCP metals including α-Ti. Hence, due to the lack of the relevant data, the isotropic interaction is adopted with $h_{1,2}^{F(s)}$=1 and $h_{F(r)}^{F(s)}$=1, $s \neq r$ for all matrix components.

$$\left[Q^{F(s)}h_{rs}\right] = \begin{array}{c} \\ basal \\ prism \\ \pi_1 \\ \vdots \end{array} \begin{array}{c} \begin{array}{ccc} basal & prism & \pi_1 \end{array} \quad \cdots \\ \begin{pmatrix} Q^b \begin{pmatrix} h_1^b & h_2^b & \cdots \\ h_2^b & h_1^b & \cdots \\ h_2^b & h_2^b & \ddots \end{pmatrix} & Q^b h_p^b & Q^b h_{\pi_1}^b & \cdots \\ Q^p h_b^p & Q^p \begin{pmatrix} h_1^p & h_2^p & \cdots \\ h_2^p & h_1^p & \cdots \\ h_2^p & h_2^p & \ddots \end{pmatrix} & Q^p h_{\pi_1}^p & \cdots \\ Q^{\pi_1} h_b^{\pi_1} & Q^{\pi_1} h_p^{\pi_1} & Q^{\pi_1} \begin{pmatrix} h_1^{\pi_1} & h_2^{\pi_1} & \cdots \\ h_2^{\pi_1} & h_1^{\pi_1} & \cdots \\ h_2^{\pi_1} & h_2^{\pi_1} & \ddots \end{pmatrix} & \cdots \\ \vdots & \vdots & \vdots & \ddots \end{pmatrix} \end{array} \tag{2.7}$$

The aging time $t_a^{F(s)}$ is introduced for each slip system family. The aging time increment is computed from an evolution law depending on the accumulated viscoplastic strain rate $\dot{\vartheta}^{F(s)}$ on the corresponding family:

$$\dot{t}_a^{F(s)} = 1 - \frac{t_a^{F(s)} \dot{\vartheta}^{F(s)}}{\omega^{F(s)}} \tag{2.8}$$

with the initial condition $t_a^{F(s)}(t = 0) = t_{a_0}^{F(s)}$, where $t_{a_0}^{F(s)}$ represents the initial pinning of dislocations leading to the anomalous yield point.

The accumulated strain rate $\dot{\vartheta}^{F(s)}$ is the sum of the cumulative slip rates of the slip system s in the set $\phi_{F(s)}$:

$$\dot{\vartheta}^{F(s)} = \sum_{r \in \phi_{F(s)}} \dot{v}^r \tag{2.9}$$

Strain aging introduces an additional hardening into the material behavior. The corresponding hardening term, $r_a^{F(s)}$, depends on the new internal variable $t_a^{F(s)}$ in the form:

$$r_a^{F(s)} = r_{a0}^{F(s)} \left[1 - \exp\left(-\left(\frac{t_a^{F(s)}}{t_0^{F(s)}}\right)^{\beta^{F(s)}}\right)\right] \tag{2.10}$$

r_a is controlled by aging parameters $r_{a0}, t_0, \beta, \omega$ and by the initial aging time t_{a0} taking different values for each family. The parameter t_{a0} depends on prior aging history of the materials.

The yield function f^s given by Eq.2.4 is enhanced, so as to include the additional hardening term r_a :

$$f^s(\tau^s, r^s) = |\tau^s| - r^s - r_a^{F(s)} \tag{2.11}$$

According to the generalization of Schmid's law, viscoplasticity occurs when f^s becomes positive. In this version of the model, the effect of aging is the same within each system family. The model has been implemented in the finite element code $Z-Set$ [232]. The resolution method is based on an implicit Newton-Raphson algorithm. The numerical integration of constitutive equations is performed at each Gauss point of each element using a second-order Runge-Kutta

method with automatic time stepping [27].

System number	Plane	Direction	Slip system family $F(s)$
Basal $< a >$ (0001) $\langle 1\bar{2}10\rangle$			
1	(0001)	$[1\bar{2}10]$	I
2	(0001)	$[2\bar{1}\bar{1}0]$	I
3	(0001)	$[11\bar{2}0]$	I
Prismatic $< a >$ $\{10\bar{1}0\}$ $\langle 1\bar{2}10\rangle$			
4	$(10\bar{1}0)$	$[1\bar{2}10]$	II
5	$(01\bar{1}0)$	$[2\bar{1}\bar{1}0]$	II
6	$(\bar{1}100)$	$[11\bar{2}0]$	II
Pyramidal π_1 $< a >$ $\{10\bar{1}1\}$ $\langle 11\bar{2}0\rangle$			
7	$(10\bar{1}1)$	$[1\bar{2}10]$	III
8	$(01\bar{1}1)$	$[2\bar{1}\bar{1}0]$	III
9	$(\bar{1}101)$	$[11\bar{2}0]$	III
10	$(\bar{1}011)$	$[1\bar{2}10]$	III
11	$(0\bar{1}11)$	$[2\bar{1}\bar{1}0]$	III
12	$(1\bar{1}01)$	$[11\bar{2}0]$	III
Pyramidal π_1 $< a+c >$ $\{10\bar{1}1\}$ $\langle 11\bar{2}3\rangle$			
13	$(10\bar{1}1)$	$[2\bar{1}\bar{1}3]$	IV
14	$(10\bar{1}1)$	$[11\bar{2}3]$	IV
15	$(01\bar{1}1)$	$[11\bar{2}3]$	IV
16	$(01\bar{1}1)$	$[\bar{1}2\bar{1}3]$	IV
17	$(\bar{1}101)$	$[\bar{1}2\bar{1}3]$	IV
18	$(\bar{1}101)$	$[\bar{2}113]$	IV
19	$(\bar{1}011)$	$[\bar{2}113]$	IV
20	$(\bar{1}011)$	$[\bar{1}\bar{1}23]$	IV
21	$(0\bar{1}11)$	$[\bar{1}\bar{1}23]$	IV
22	$(0\bar{1}11)$	$[1\bar{2}13]$	IV
23	$(1\bar{1}01)$	$[1\bar{2}13]$	IV
24	$(1\bar{1}01)$	$[2\bar{1}\bar{1}3]$	IV

Table 2.4: The full list of considered slip systems of α Ti.

2.5.2 Homogenized polycrystalline model

Identification of material parameters requires a comparison of simulation results with experimental response of polycrystalline specimens. For that purpose, a homogenized polycrystalline model is chosen that makes use of the previous single crystal model at the grain scale.
Homogenized polycrystalline model allowed to estimate the stress and strain based on the mean response of the grains within the material volume element. The formulation of the transition law, common to several simplified homogenization self-consistent schemes [43, 26] is the following:

$$\underset{\sim}{\boldsymbol{\sigma}}_g = \underset{\sim}{\boldsymbol{\sigma}} + 2\mu\alpha(1-\beta)(\underset{\sim}{\boldsymbol{E}}^p - \underset{\sim}{\boldsymbol{\varepsilon}}^p_g) \tag{2.12}$$

where $\underset{\sim}{\boldsymbol{\sigma}}$ is macroscopic stress tensor, $\underset{\sim}{\boldsymbol{\sigma}}_g$ is estimated mean stress tensor within a grain, and μ is the macroscopic shear modulus.

$$\beta = \frac{2(4-5\nu)}{15(1-\nu)}, \quad \frac{1}{\alpha} = 1 + \frac{3}{2}\mu\frac{E^{Mises}}{\Sigma^{Mises}} \tag{2.13}$$

where E^{Mises} and Σ^{Mises} are the macroscopic von Mises strain and stress respectively. This corresponds to an isotropic approximation of the scale transition rule.
The macroscopic plastic strain rate $\dot{\underset{\sim}{\boldsymbol{E}}}^p$ is calculated as the mean plastic strain rate in each grain $\dot{\underset{\sim}{\boldsymbol{\varepsilon}}}^p_g$:

$$\dot{\underset{\sim}{\boldsymbol{E}}}^p = \sum_g f_g \dot{\underset{\sim}{\boldsymbol{\varepsilon}}}^p_g \tag{2.14}$$

where f_g denotes the volume fraction of grains with orientation close to g [127, 43].

This simple model allows for rapid estimation of the material parameters. Validation is performed on the full field simulations of polycrystalline aggregates presented in the next section.

2.5.3 Polycrystalline aggregates

In real polycrystals the averaged response of the grains is strongly dependent on the crystallographic orientation and on the constraints due to neighboring grains [15]. The objective of the present work is to study the deformation modes induced by strain aging in the grains of a polycrystal. This is why several 2D and 3D polycrystalline aggregates were generated via Voronoï tessellation [150, 44]. This model reproduces grains with a given crystallographic orientation and mechanical constitutive equations, allowing to account for the heterogeneity of polycrystalline structures [14]. 2D simulations allow to more easily observe the localization phenomena inside grains and their possible transmission at grain boundaries. Several realizations for statistical representativity were carried out. Validation of the observations is performed on 3D grain samples with periodic constraints . Figure 2.6 (a,b) presents flat polycrystalline mesh with dimensional ratio of $\frac{L}{W} = 2.5$, where L and W are the length and the width of the sample, respectively. The mesh consists of 71 and 432 grains. Note that '2D' means that an extruded meshes was used with columnar grains with a single element in the thickness. As a first step, an idealized texture was used due to the limited number of grains. The crystallographic orientations corresponding to the texture presented on the pole figures were ascribed to the grains. Figure 2.6 (c) shows the obtained geometry of the 3D aggregates of 150 grains made with 100×100×100 μm mesh with 15-node quadratic 3D tetrahedral continuum elements (eighteen Gauss points per element) with periodic boundaries.

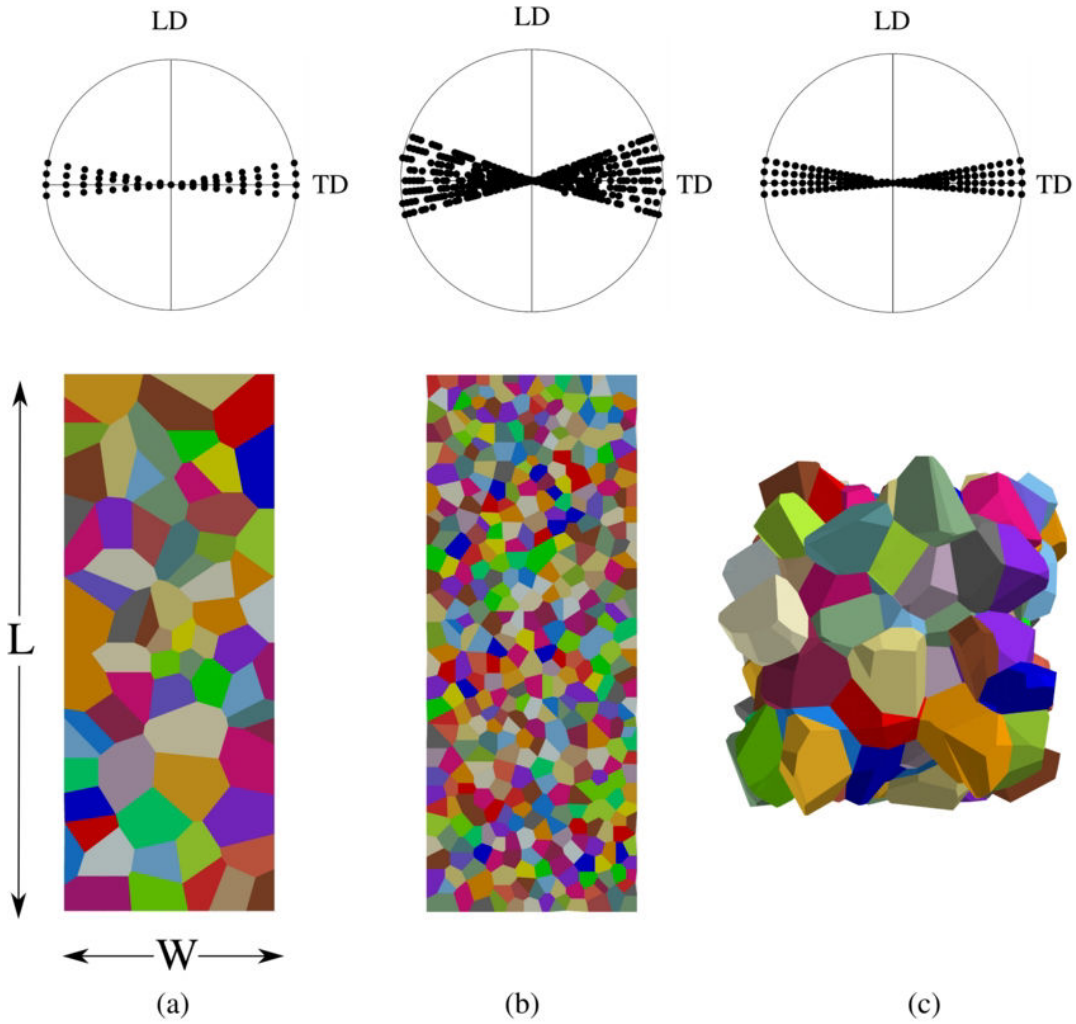

Figure 2.6: Simulated texture of: (a) 71 grains; (b) 432 grains; (c) 150 grains.

2.6 Identification of materials parameters

2.6.1 Identification strategy

A rapid estimate of the elasto-viscoplastic material parameters was first performed with the help of a homogenized polycrystal model in which the mechanical fields are homogeneous, so that the specimen can be considered as a volume element. At this step, the aging contribution of the material parameters was disregarded. Next step was the identification of the aging parameters and validation of the ability of the model to capture the main features of the strain localization phenomena associated with the anomalous yield point and PLC effect. For this purpose, full-field FE simulations are required on '2D' polycrystalline aggregates. (see Figure 2.6 (a,b)). Finally, simulations on the 3D polycrystalline aggregates (Figure 2.6 (c)) were carried out in order to obtain a more qualitative estimate of the material's response. The typical computation time (CPU time) for a precision ratio of 10^{-4} for tensile tests up to $\varepsilon = 2\%$ ranges from 7 to 10 hours for 2D simulations and from 28 to 33 hours for 3D simulations.

2.6.2 Identification procedure of viscoplastic material parameters

The identification of the viscoplastic parameters is performed on flat polycrystalline specimens with either 71 or 432 columnar grains with ascribed crystallographic orientations corresponding to the texture of the pole figures (Figure 2.6 (a,b)). Vertical displacements are applied at the top edge of the mesh (keeping the bottom edge fixed) thus imposing the macroscopic strain and strain rate on the sample at all times, as an infinitely hard machine would do. All lateral faces are free of forces. The identified viscoplastic material parameters are given in Table 2.5. In order to activate the right systems at the right time, appropriate CRSS should be prescribed. Many researchers investigated the CRSS of Ti and its alloys under various conditions of temperature and compositions [82, 230, 56, 117, 21], however, to date, there is no consensus on the precise values of CRSS. For the ease of the comparison, the value of CRSS for various slip systems is usually normalized by the CRSS of the easiest deformation mode. In the present study, the slip trace analysis based on the results of EBSD was employed to estimate the CRSS in CP α-Ti [17, 35, 116]. Table 2.5 gives the list of the CRSS of slip families used in the simulations. The apparent CRSS includes the additive term of hardening due to aging, i.e. $\tau_0^{F(s)} + r_{a_0}^{F(s)}$, $r_{a_0}^{F(s)}$ being identified in a second step.

The elastic stiffness tensor exhibits transversely isotropic symmetry because of the crystallographic structure of α-Ti with the following single crystal elastic constants: C_{11}=153.97 GPa, C_{33}=183.0 GPa, C_{44}=46.27 GPa, C_{12}=85.98 GPa, C_{13}=67.16 GPa [73, 72]. The viscoplastic parameters σ_0 and $\dot{\nu}_0$ were identified from the tensile tests with strain rate jumps. For simplicity the same values of these parameters are adopted for all slip families. The experimental stress-strain curves for CP Ti show a very low hardening rate, thus a quasi-linear isotropic hardening was prescribed for all slip systems (Q=250 MPa, b=1).

Slip systems family	$\tau_0^{F(s)}$, MPa	$\tau_0^{F(s)} + r_{a_0}^{F(s)}$, MPa	Viscosity
Basal $< a >$	232	262	σ_0=10 MPa, $\dot{\nu}_0 = 1.6\times10^{-6}$ s^{-1}
Prismatic $< a >$	161	191	σ_0=10 MPa, $\dot{\nu}_0 = 1.6\times10^{-6}$ s^{-1}
Pyramidal $< a >$	189	219	σ_0=10 MPa, $\dot{\nu}_0 = 1.6\times10^{-6}$ s^{-1}
Pyramidal $< c+a >$	189	299	σ_0=10 MPa, $\dot{\nu}_0 = 1.6\times10^{-6}$ s^{-1}

Table 2.5: Material model parameters.

2.6.3 Identification of static strain aging parameters

Following the scenario discussed in the section 2.4 and adopted in the present study, the origin of the anomalous yield point phenomena observed for the material loaded along TD was interpreted as resulting from the combination of two mechanisms: a higher apparent yield stress due to lower Schmid factors on all potentially active slip systems ($\langle a \rangle$ and $\langle c+a \rangle$), immediately followed by a significant strain softening provided by the unlocking of the $\langle c+a \rangle$ pyramidal slip system and leading to either a stress peak or a plateau. This interpretation is confirmed by the quantitative observations on the contributions of individual slip systems in Grade 4 Ti reported by Barkia [19].

The PLC effect observed during the tensile tests at low strain rate for both TD and LD, was suggested to be due to the non-planar core of the $\langle a \rangle$-type screw dislocations which can switch between sessile and glissile core configurations, causing jerky dislocation motion with a series of

sudden jumps between locking positions.

In order to simulate the described scenario we have introduced two sets of distinct aging parameters into the model: one for all $< a >$ - type slip systems and the second one for $< c + a >$ - type slip systems. The parameters were calibrated so as to locate precisely the domain of negative SRS, associated with plastic strain heterogeneities. For a given temperature, this domain exists where the flow stress decreases when strain rate increases. According to our model, the kinetics of dislocation anchoring is controlled by the parameters t_0, r_{a_0}, β, ω, and by initial aging time t_{a_0}. The identification and the role of the parameters controlling the strain localization phenomena associated with the anomalous yield point are further discussed.

- Time t_0 characterizes the relaxation kinetics between pinned and unpinned states of the dislocations. Aging time t_{a_0} is the initial value of the internal variable t_a and characterizes the initial state of pinning of dislocations leading to the anomalous yield point. In the present model, we take sufficiently large value of t_{a_0} (1000 s) compared with t_0 in order to get a suitable description of the peak stress.
- The plastic strain increment ω is the amount of strain associated with the activated plastic bands when mobile dislocations have to overcome their obstacles. Its value is kept constant here and equal to 10^{-4} as in [125].
- The ratio ω/t_0 determines the position of the center of the NSRS domain. On Figure 2.7, the flow stress (τ, the resolved shear stress) is plotted as a function of the plastic strain rate ($\log \dot{\gamma}$); thus the evolution of the SRS of the phenomenological macroscopic model can be visualized for each slip system family: respectively for Burgers vectors $< a >$ and $< c + a >$. Analytical curves are constructed using the parameters identified in Table 2.6. For $< c + a >$ slip families, the SRS curve goes through negative value at $\omega/t_0 = 10^{-7}$ s^{-1}. The domain of NSRS for the $< a >$-type slip families is located at $\omega/t_0 = 10^{-6}$ s^{-1} leading to the PLC effect. By separating the domains of NSRS for $< c + a >$ and $< a >$ slip families, we insure the PLC effect to be due to the $< a >$ dislocations in the range of strain rates explored.
- The parameter r_{a_0} denotes the interaction force between dislocations and solute atoms, thus it controls the pinning stress. The amplitude of the yield peak is directly related to r_{a_0} value and to the orientation of the texture with respect to the tensile direction.
- The exponent β depends on the type of diffusion and controls the kinetics of the pinning process. In the present model the β=2/3 which corresponds to the pipe diffusion of solute atoms along dislocation lines [76].

Slip systems family	r_{a_0}, MPa	ω	t_0, s	ω/t_0, s^{-1}	β
Basal	30	10^{-5}	10	10^{-6}	0.66
Prismatic	30	10^{-5}	10	10^{-6}	0.66
Pyramidal $< a >$	30	10^{-5}	10	10^{-6}	0.66
Pyramidal $< c + a >$	110	10^{-5}	100	10^{-7}	0.66

Table 2.6: Aging model parameters

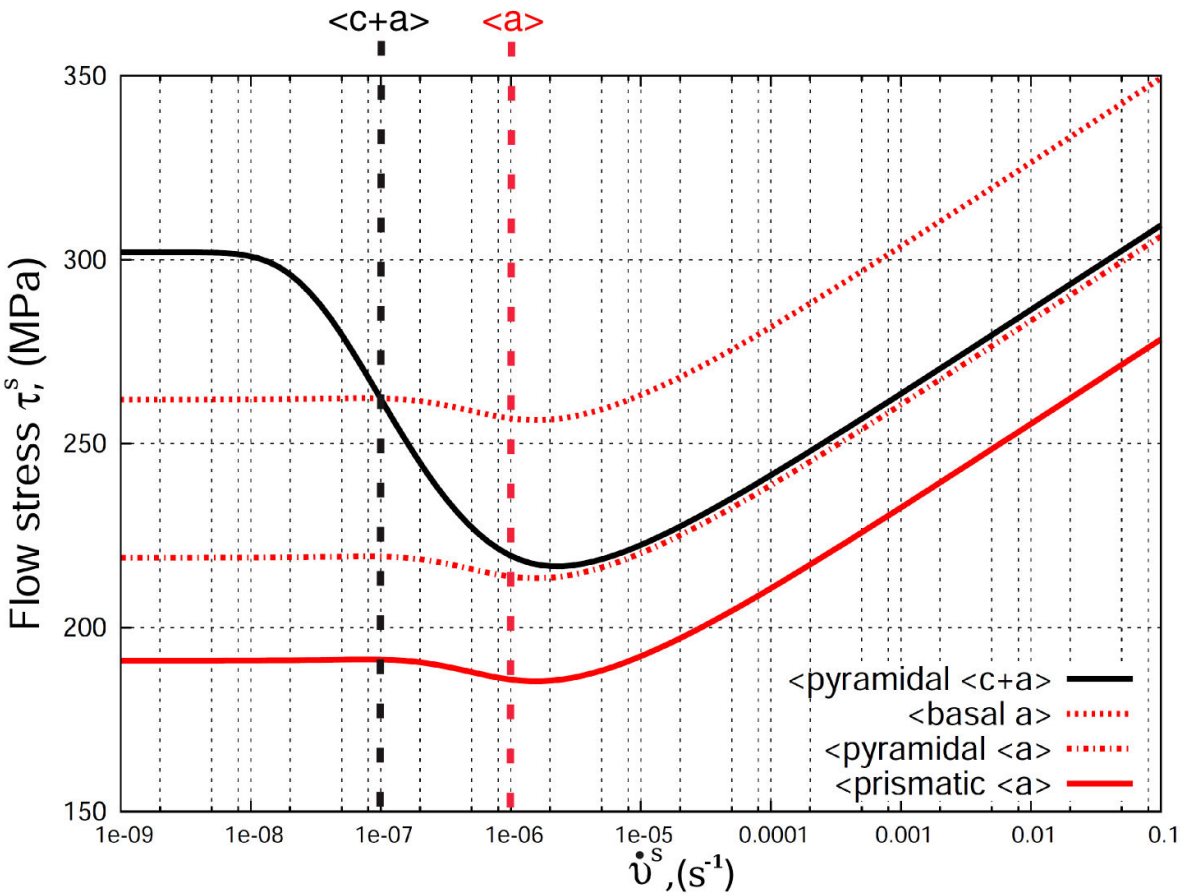

Figure 2.7: The evolution of stress showing the strain rate sensitivity (SRS) parameter as a function of strain rate.

The results of the simulations on the flat polycrystalline specimen of 71 grains of tensile tests under constant strain rate for TD and LD specimens and of the tensile test with loading and unloading are presented in Figure 2.8 and Figure 2.9. The predicted overall stress-strain curves can be compared to the experimental ones. The stress peak is observed in TD specimen and is absent in LD specimen. Moreover, the stress peak appears in TD after each reloading, which is in a good agreement with experimental results. It means that the unloading and reloading were long enough to allow for significant aging to occur. The stress peak and the plateau level are similar to the experimental results.

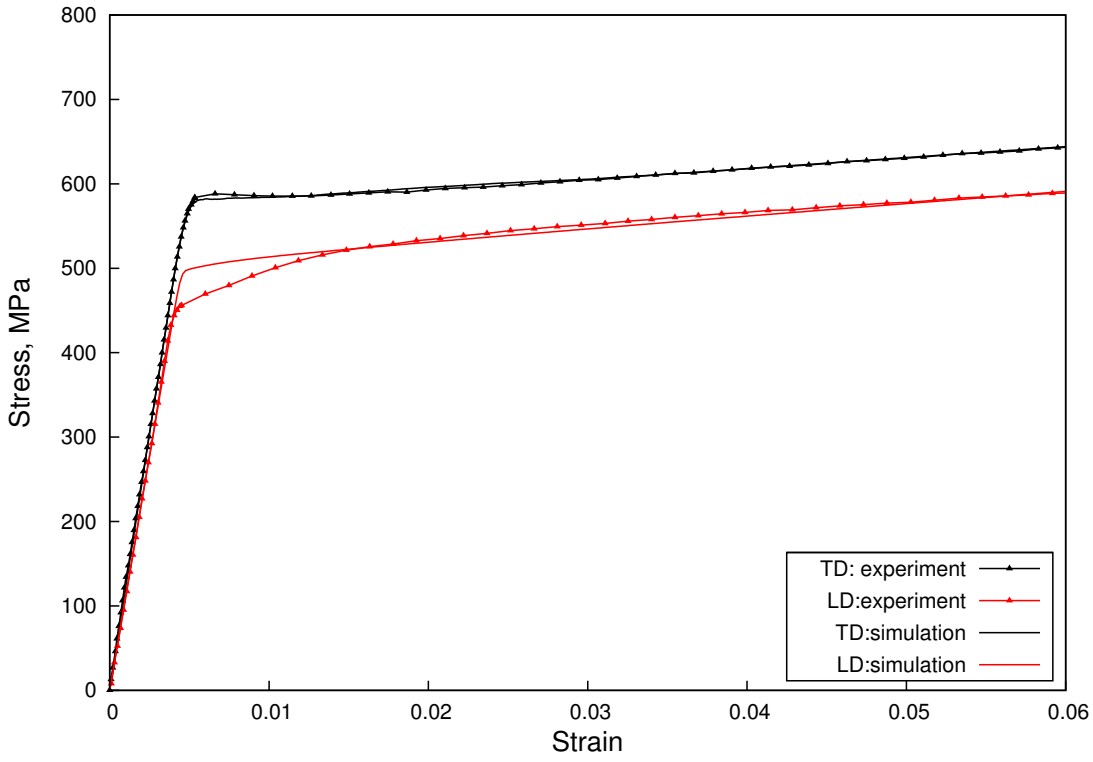

Figure 2.8: Tensile test at $\dot{\varepsilon} = 2 \cdot 10^{-4} s^{-1}$ for Grade 4 on the 71 grain aggregate. Comparison of the model with experiment.

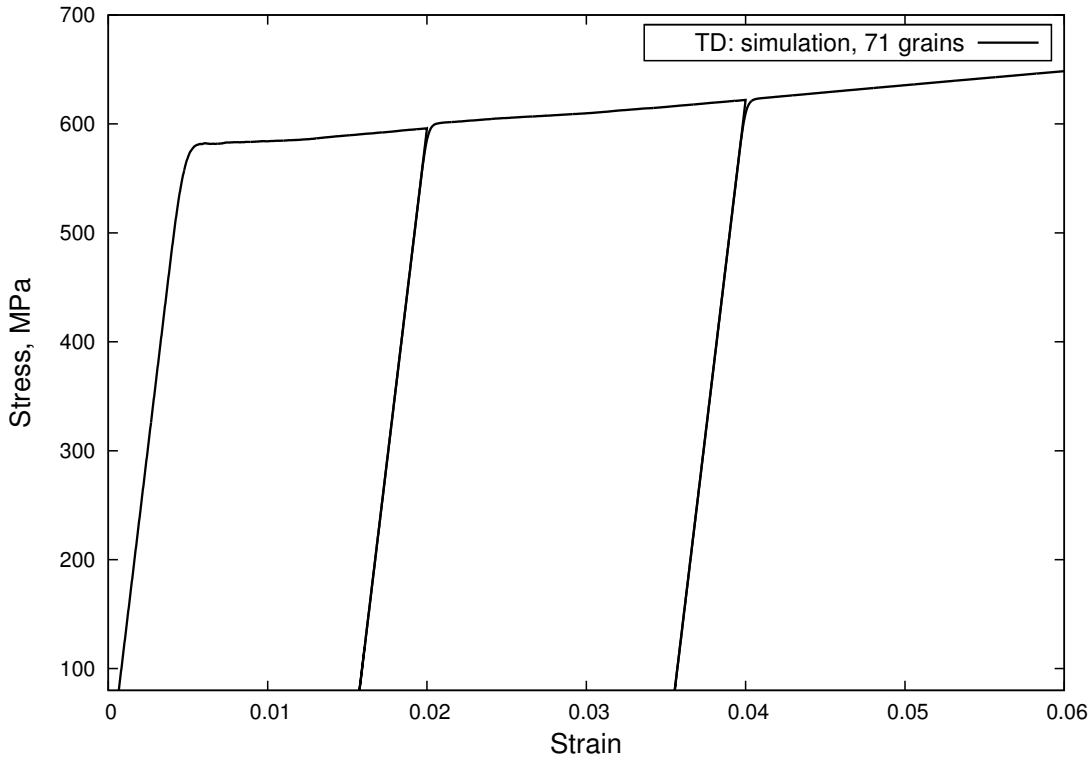

Figure 2.9: Simulated tensile test along TD at $\dot{\varepsilon} = 2 \cdot 10^{-4} s^{-1}$ with loading-unloading on the 71 grain aggregate.

2.6.4 Identification of dynamic strain aging parameters

Simulations of PLC effect were carried out using the above described set of constitutive equations. The main difference in the parameters between SSA and DSA simulations are in the values of t_0, t_{a_0} and r_{a_0}. As stated above, the DSA in α-Ti can be ascribed to the dissociation of the $\langle a \rangle$-type dislocation cores. Consequently, in the model, three slip families of $\langle a \rangle$-type Burgers vector will reproduce the DSA at low strain rates.

A characteristic time t_0 shorter than that of $\langle c + a \rangle$ was ascribed to the $\langle a \rangle$ families. It can be justified by the fact that the dissociation of $\langle a \rangle$ dislocation cores onto various glide planes is shorter than the diffusion of oxygen towards the dislocation in the case of SSA. In addition, the parameter r_{a_0} corresponding to the maximal additional stress needed to switch between pinned and unpinned state (locking-unlocking) is lower for $\langle a \rangle$-systems.

Using the parameters of Table 2.6, the stress-strain curves of the simulation of the tensile test with strain rate jumps are plotted in Figure 2.10. For the better representation, the origins of the simulated curves were slightly shifted. The identification of the material parameters allows to obtain a correct description of the strain rate jumps and of the positive values of the strain rate sensitivity. It should be noted that at $2{\times}10^{-6} s^{-1}$ the PLC serrations observed on the experimental curve are absent on the simulation red curve. The absence of the serrations

can be explained by the short duration of the simulation at the strain rate of $2\times10^{-6}s^{-1}$. When carrying the tensile test simulation at $2\times10^{-6}s^{-1}$ for a longer time, the serrated flow can be observed on the macroscopic stress-strain blue curves for both TD and LD (see Figure 2.10).

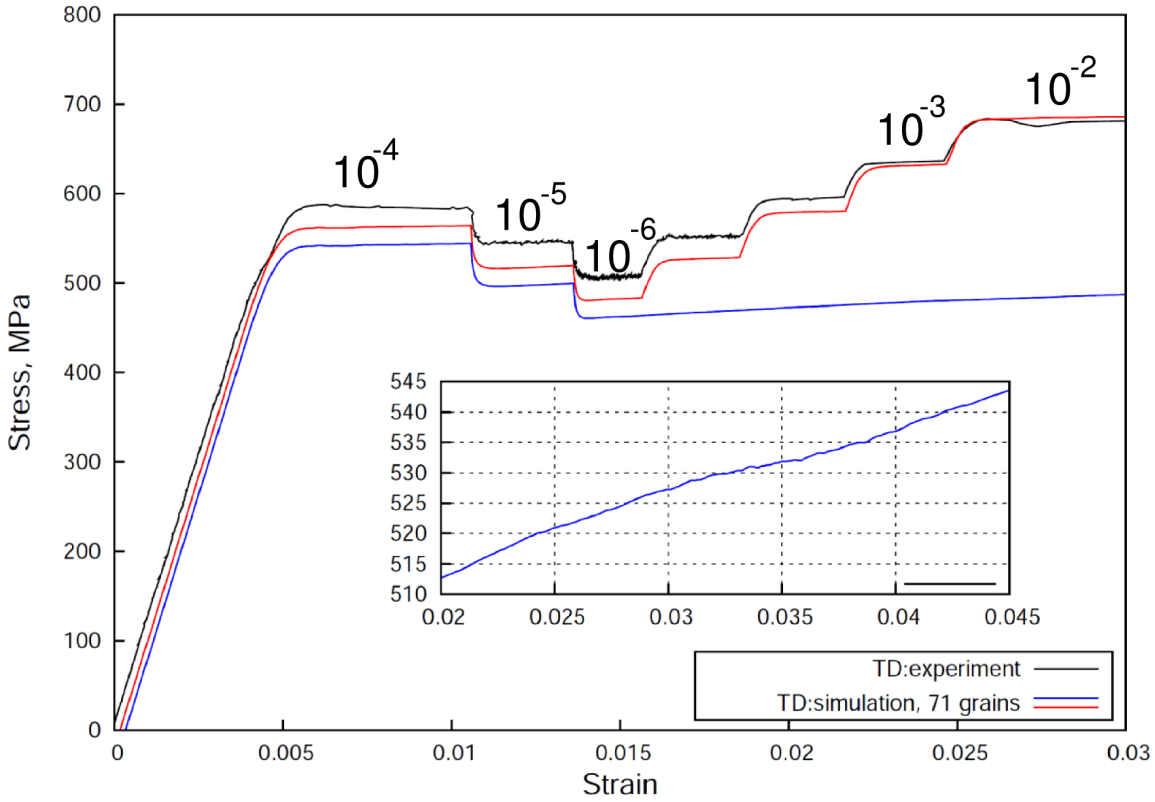

Figure 2.10: Experimental and simulation curves for the 71 grain aggregate for Grade 4 of tensile test in TD with strain rate jumps. The curves are slightly shifted horizontally for the illustration.

2.6.5 Prediction of unconventional behavior

The identified parameters of the strain aging model for Grade 4 (see Table 2.6) were used to predict the domain of NSRS associated with the PLC instabilities observed on the stress-strain curve at $\dot{\varepsilon} = 2 \times 10^{-6}s^{-1}$ (see Figure 2.4). For this purpose simulations were performed on a volume element with 21 grain orientations replicating the texture presented on the pole figures 2.6. The homogenization scheme described in section 2.5.2 was employed. Each simulation was carried out at constant strain rate up to strain of 2%. The range of the explored strain rates varied between $10^{-9}s^{-1}$ to 10 s^{-1}. Figure 2.11 shows the simulated stress σ as a function of accumulated plastic strain rate $\dot{p}$, where $\dot{p} = |\dot{\varepsilon}_p|$. It can be seen that the domain of NSRS is located in the vicinity of $\dot{p} = 10^{-7}s^{-1}$ and not at $10^{-6}s^{-1}$ as it was predicted by the analytical curve in Figure 2.7. It implies that the observed strain heterogeneities on the simulated stress-strain at $\dot{\varepsilon} = 2\times10^{-6}s^{-1}$ (see Figure 2.10) were obtained in the presence of positive SRS. Similar to the simulations, the experimentally observed serrations were also obtained in the presence of positive macroscopic SRS. In order to find the explanation to such discrepancy, the statistical

analysis of the distribution of strain rates within the grains in the simulations at $\dot{\varepsilon} = 2 \times 10^{-6} s^{-1}$ for TD specimen with 71 grains was made. The results are presented in the form a histogram on Figure 2.12. It can be seen that the majority of the prismatic $< a >$ dislocations is moving at $\dot{\varepsilon} = 10^{-6} s^{-1}$. The same is applied to the pyramidal $< c + a >$ dislocations. However, the second most common strain rate for prismatic $< a >$ dislocations is $\dot{\varepsilon} = 10^{-7} s^{-1}$, and it is $\dot{\varepsilon} = 10^{-8} s^{-1}$ for $< c + a >$ dislocations. The present statistics shows that during the simulation at $\dot{\varepsilon} = 2 \times 10^{-6} s^{-1}$, there is quite important amount of the grains that are deforming at lower strain rates than the tested macroscopic strain rate. As a result, these grains will exhibit locally a negative SRS leading to the intermittent age hardening events which are evidenced by the PLC serrations on the stress-strain curves under the form of erratic hardening peaks of short duration on usual tensile tesing machines.

Similarly, if we examine the plastic activity on the local scale of a single grain or even of a single Gauss point of the mesh inside that grain and plot the actual strain rates as a function of strain (Figure 2.13) for an applied control macroscopic strain rate of $2 \times 10^{-6} s^{-1}$ on the sample, large instantaneous and erratic variations are observed. The local strain rates resulting from the activity of all slip systems in that grain can reach twice the macroscopically imposed strain rate or drop down to half of it or else even tend to zero occasionally. As for the plastic strain rate in a single mesh of the grid (red curve on Figure 2.13), it can reach 10 times the controlled strained rate or drop down to zero. This local intermittence of plasticity within a grain is confirmed on Figure 2.14 where the local strain rate is plotted as a function of time for a total of 0.6%, i.e. just after the yield point. Although the plastic activity for the entire grain taken on all slip systems (black curve) drops down below $2 \times 10^{-6} s^{-1}$ (blue line), it never stops; on the other hand, the local plasticity in a given mesh of the FEM grid can stop completely for durations of 10 to 15 minutes, sometimes less, but clearly allowing full aging of the activated slip systems and their necessary unlocking when the plastic activity reappears.

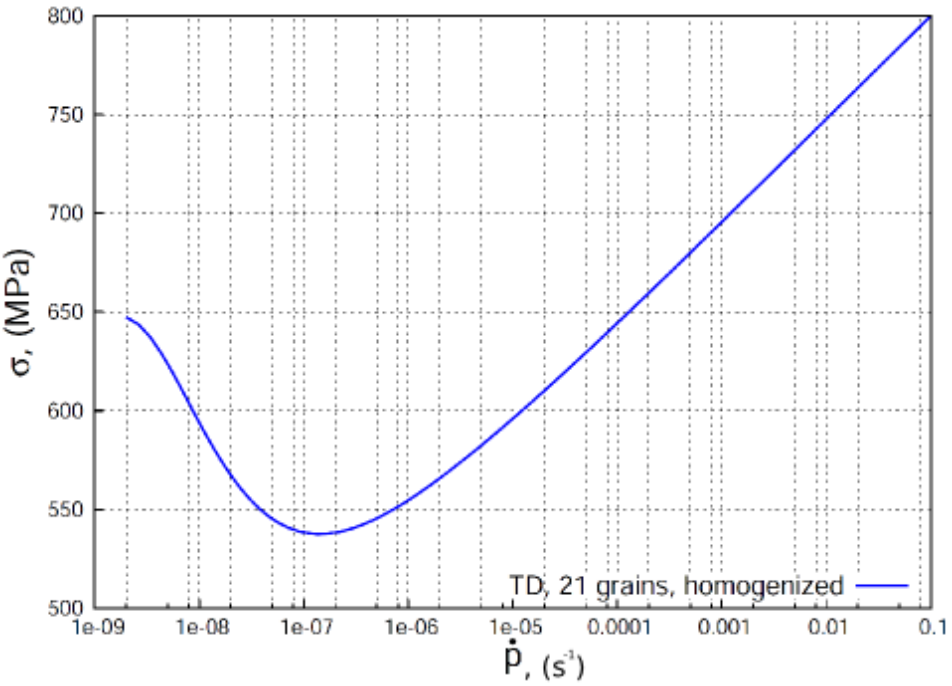

Figure 2.11: Predicted evolution of strain rate sensitivity in simulations performed on a volume element with 21 grain orientations for a TD specimen.

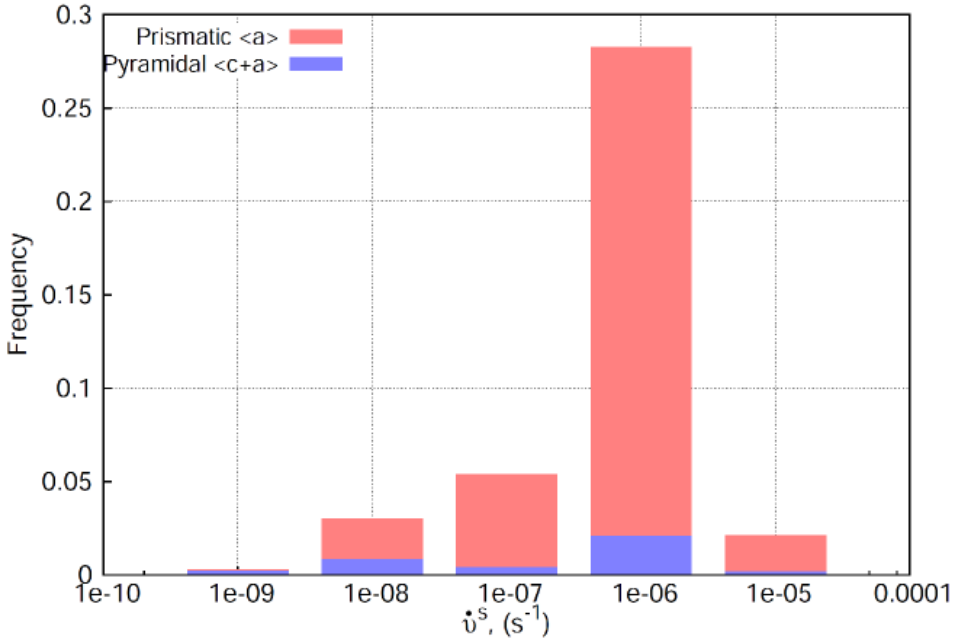

Figure 2.12: Histogram of strain rates distribution in various grains at $\dot{\varepsilon} = 2 \times 10^{-6} s^{-1}$ and ε=10% for a TD specimen with 71 grains.

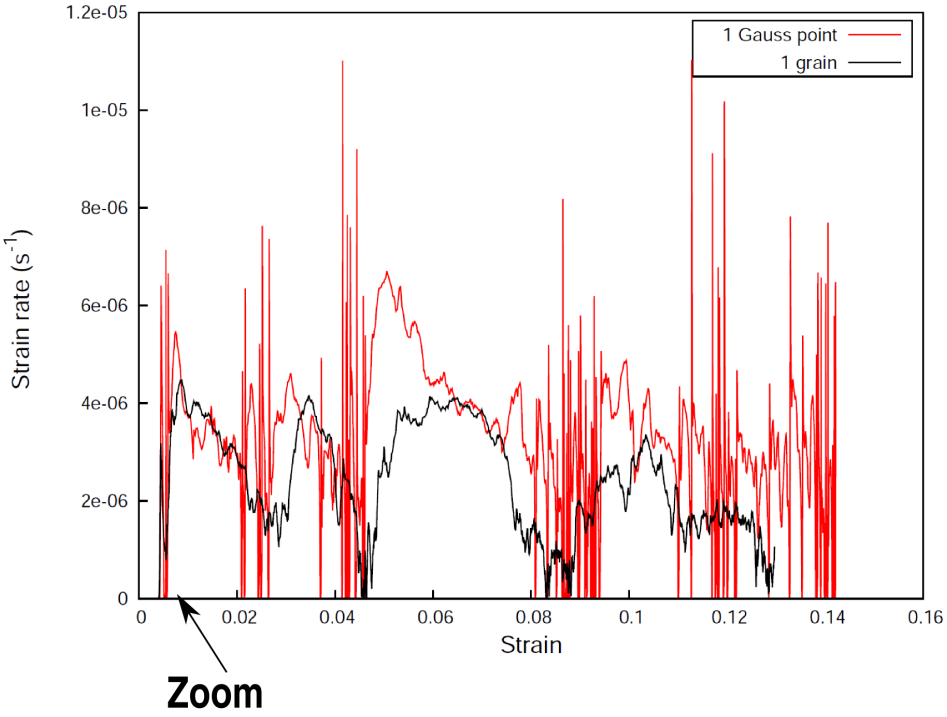

Figure 2.13: Statistical distribution of strain rates in the simulation at $\dot{\varepsilon} = 2 \times 10^{-6} s^{-1}$ for 1 grain and 1 Gauss point for a TD specimen.

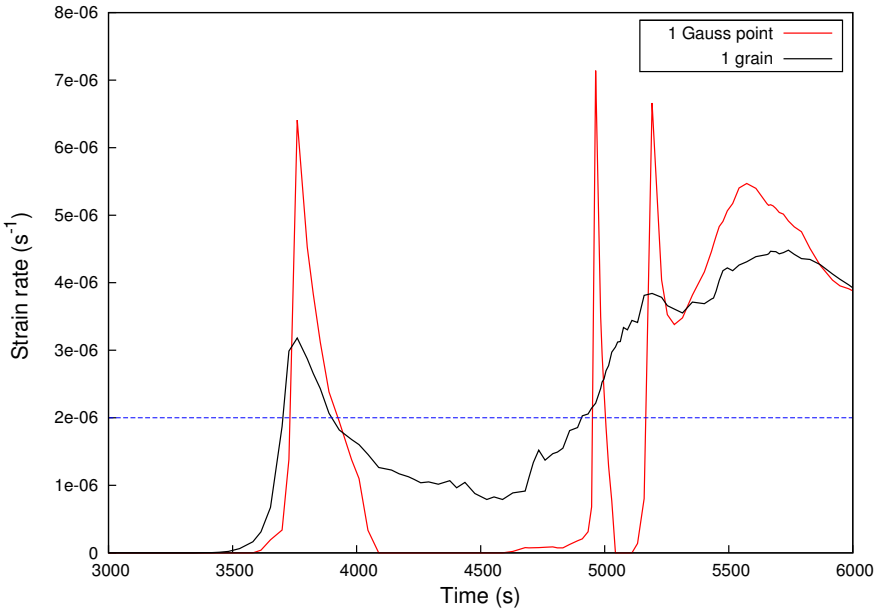

Figure 2.14: The zoom part at ε_p=0.6% of the statistical distribution of strain rates in the simulation for a TD specimen for 1 grain and 1 gauss point.

2.7 Results and discussion

2.7.1 Strain aging induced localization in flat extruded polycrystalline specimen

The identified polycrystalline strain aging model was used to investigate the intragranular strain and plastic strain rate instabilities that developed inside the material. The observed deformation modes differ for SSA and DSA simulations. The results of the SSA simulations are discussed first.

The simulated macroscopic stress-strain curves for the flat polycrystalline mesh with 71 grains plotted in Figure 2.15 are in good agreement with experiments. The anisotropy of the yield stress for TD and LD specimens of α-Ti is well captured. The model reproduces a small yield point and plateau in TD specimen and no peak in LD specimen. The curve for TD specimen simulated without aging is given in blue. As expected, it shows no yield stress anomaly.

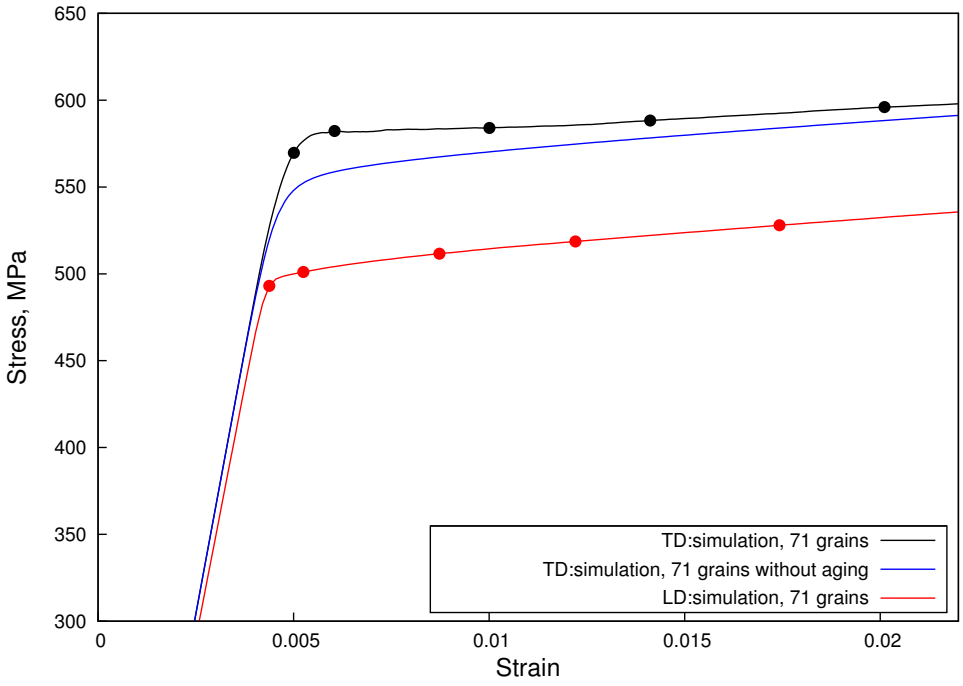

Figure 2.15: Stress-strain curves of tensile simulations at $2 \times 10^{-4} s^{-1}$ for flat extruded polycrystalline samples with 71 grains: TD, LD and TD without aging. Selected maps for Figure 2.17 are indicated on the corresponding curves.

Series of maps of accumulated plastic strain in the TD specimen are shown in Figure 2.17 for 5 macroscopic strain levels defined in Figure 2.15 with points on the stress-strain curve. Note that instead of p defined by Eq. 2.3, we used $\vartheta^{F(s)}$ defined by Eq. 2.9 presented with a logarithmic color scale. With the present numerical model we can separately examine the accu-

mulated plastic strain on four distinct slip system families. For comparison, we show the total plastic strain ϑ^{total} in the specimen with aging contribution (Figure 2.17 (a)), the plastic strain of prismatic $\langle a \rangle$ (Figure 2.17 (b)) $\vartheta^{prismatic}$ and pyramidal $\langle c+a \rangle$ (Figure 2.17 (c)) slip families $\vartheta^{pyramidal}$. The corresponding maps of the total plastic strain without aging contribution are given in Figure 2.17 (d). As can be seen, the 71 TD grain structure with SSA exhibits strong plastic heterogeneities, while deformation appears more homogeneously distributed in space in the absence of aging. No single Lüders-like band propagation through the entire specimen was detected. Instead we observe the nucleation of local strain heterogeneities at multiple sites of the specimen, which later start growing and expanding over several grains cutting across grain boundaries. The observed yield point coincides with the onset of plasticity due to the activation of prismatic $\langle a \rangle$ slip systems, while pyramidal $\langle c+a \rangle$ slip starts later, at the end of the plateau over $\varepsilon \approx 0.7-1\%$ strain. These results are in a good agreement with experimental observations of $in-situ$ tensile tests where prismatic slip was found to be a primary deformation mode for LD and TD specimens due to the lower CRSS [19].

In order to clarify the role of the pyramidal $\langle c+a \rangle$ glide in the stress peak and in general on the stress-strain curve, a simulation on the 71 grain aggregate was carried out at $\dot{\varepsilon}$=$2\times10^{-4}s^{-1}$, in the absence of that slip system for both TD and LD orientations (dotted lines in Figure 2.16) by giving an excessive high value to the CRSS of this system. It appears clearly that the $\langle a \rangle$ systems alone are unable to generate a stress peak, probably due to their low age hardening ability ($r_{a_0}^{<a>}$= 30 MPa in Table 2.6). On the other hand, the strain softening effect provided by the unlocking of the $\langle c+a \rangle$ systems in the favorably oriented grains is responsible for the stress peak and the plateau observed in the TD and for the slight decrement in flow stress and strain hardening in the LD.

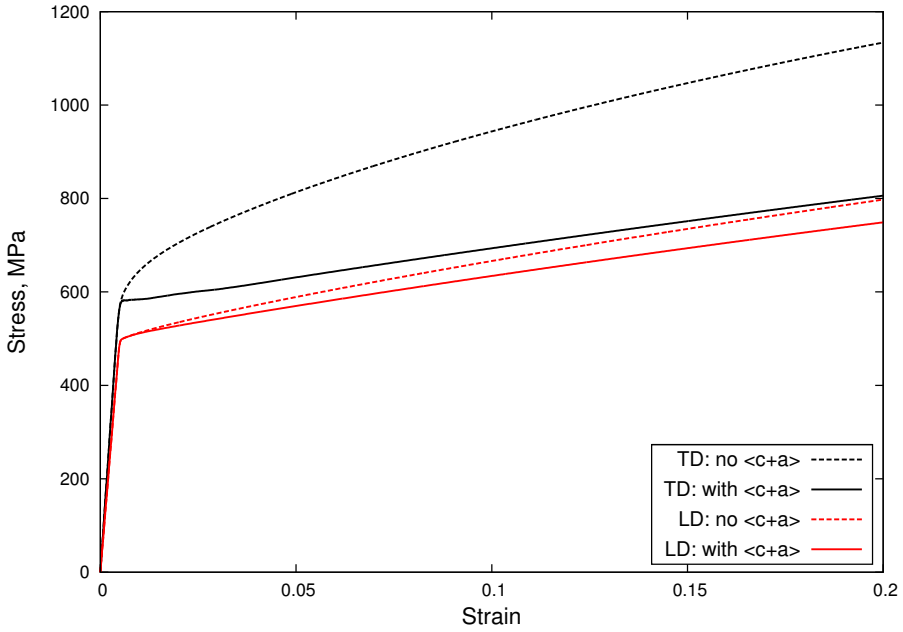

Figure 2.16: Stress-strain curves of tensile simulations at $2 \times 10^{-4} s^{-1}$ for flat extruded polycrystalline samples with 71 grains: LD and TD with and without $\langle c + a \rangle$ slip systems.

Figure 2.17 illustrates the plastic strain fields in the grains with prismatic slip which show larger gradients compared with the strong plastic band front in the grains with activated pyramidal $\langle c + a \rangle$ slip systems. The plastic slip in these grains is mostly localized near the grain boundaries and grain boundaries triple points and later it starts filling the interior of the grain. In case of prismatic slip, the strain field shows less spatial inhomogeneities inside the grains.

A more detailed view of the local total plastic strain localization within couple of grains is given in Figure 2.18. The strain fields formed within the grains show heterogeneities with strains as large as six times the nominal strain. When the strain localization starts extending into neighboring grain interiors, it still stays confined by the grain boundaries forming straining patterns which resembles deformation bands that we called meso-Lüders bands. A consequence of such cooperative grain behavior is the formation of the meso-bands inclined approximately 45° to the LD.

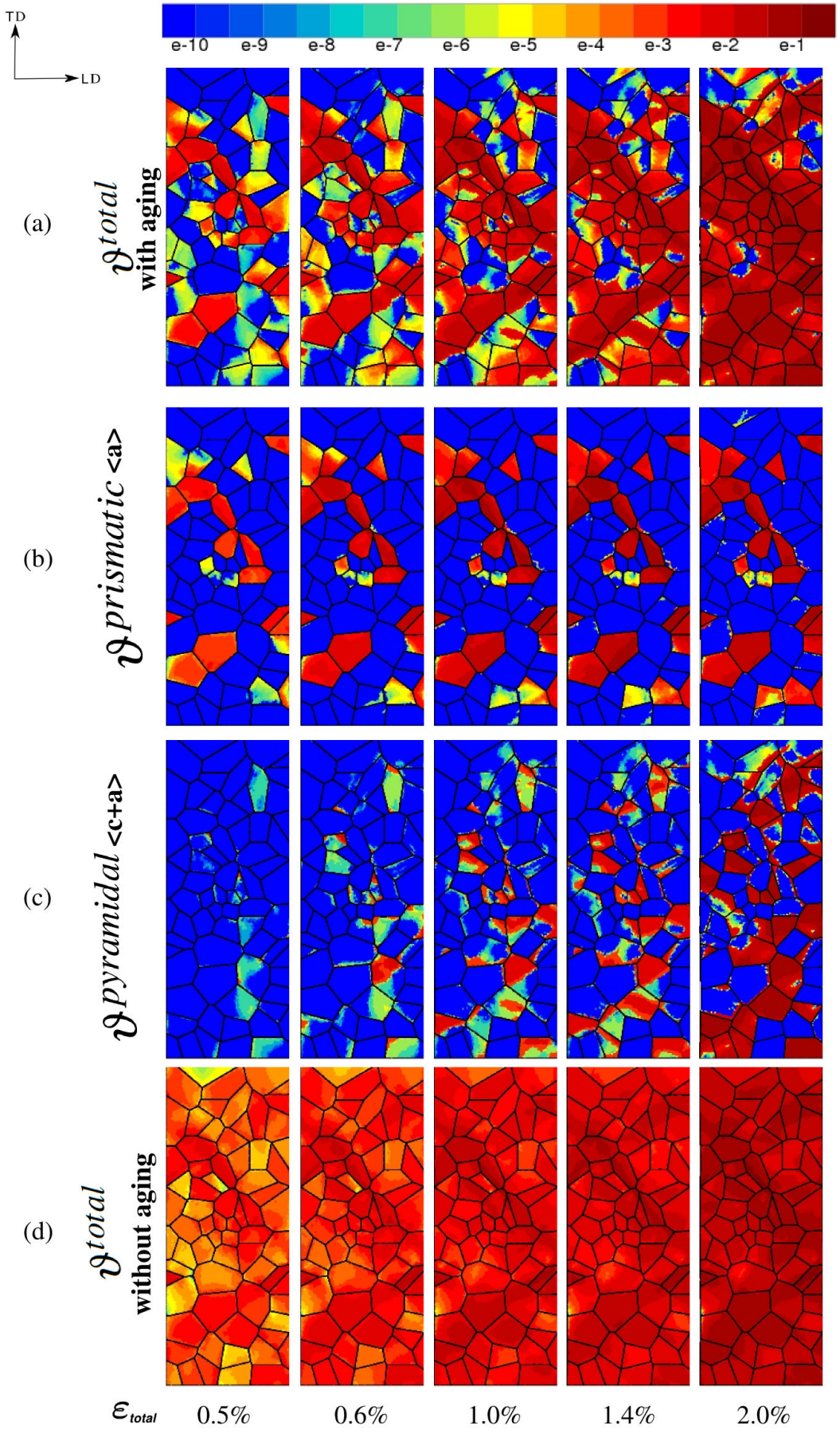

Figure 2.17: Evolution of accumulated plastic strain ϑ for flat extruded polycrystalline sample with 71 grains strained in TD at $2 \times 10^{-4} s^{-1}$: (a) total ϑ^{total}; (b) $\vartheta^{prismatic}$ on $\langle a \rangle$ slip systems; (c) $\vartheta^{pyramidal}$ on $\langle c+a \rangle$ slip systems; (d) total ϑ^{total} for the model without aging contribution.

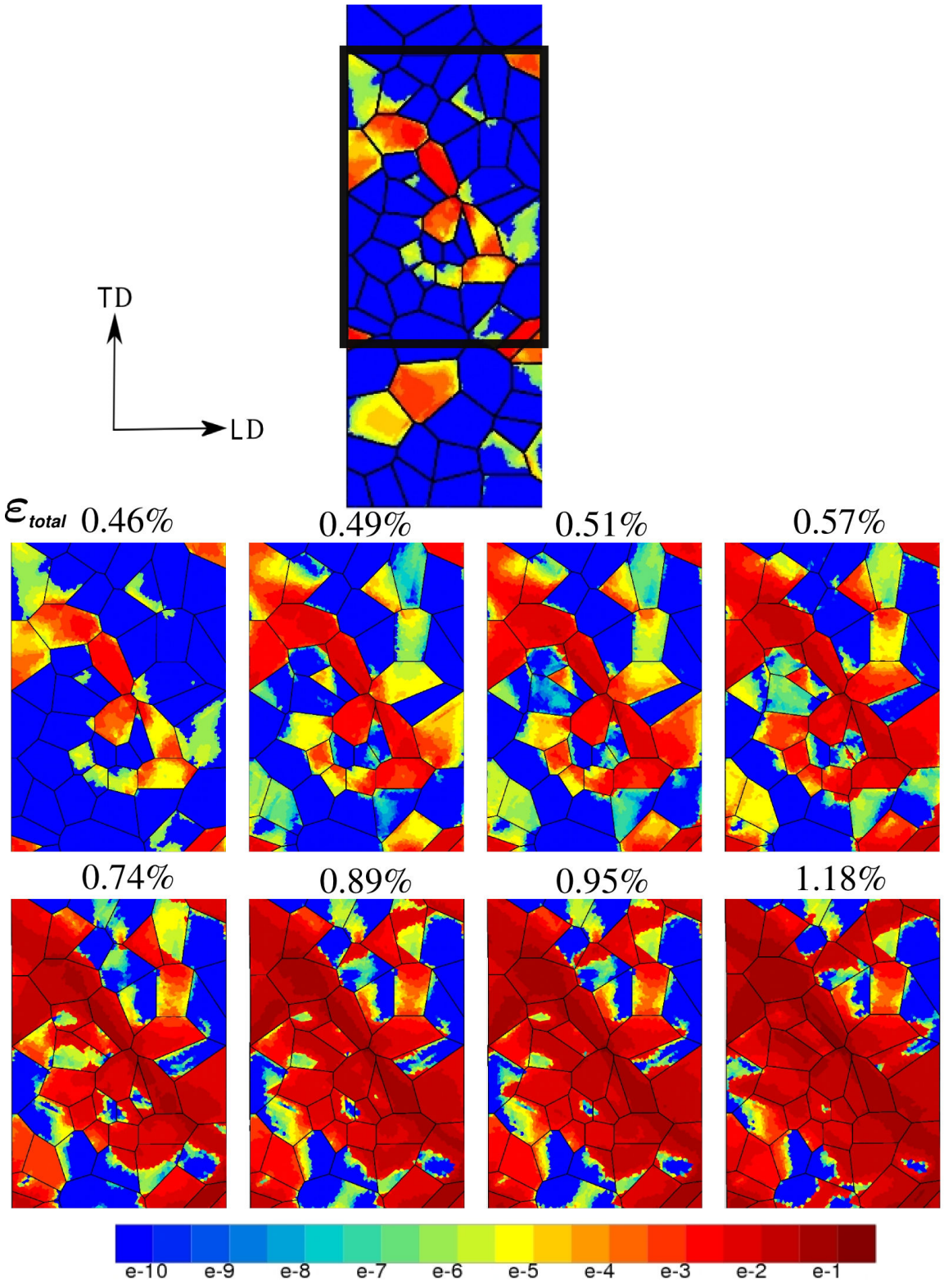

Figure 2.18: Evolution of total plastic strain ϑ^{total} in a small region of the flat extruded polycrystalline TD sample strained at $2 \times 10^{-4} s^{-1}$.

Similarly to the TD specimen, series of maps of accumulated plastic strain in the LD specimen for 5 macroscopic strain levels are shown in Figure 2.19. As in the case of TD specimen, in order to get a better idea of the operating slip modes, we present separately the total plastic strain and the plastic strain in prismatic $\langle a \rangle$ (Figure 2.19 (b)) and pyramidal $\langle c+a \rangle$ (Figure 2.19 (c)) slip families. As expected, prismatic slip is predominant, and almost no pyramidal $\langle c+a \rangle$ was activated. The total strain field remains more or less homogeneous during the tensile test simulation without formation of meso-bands as seen in the case of the TD specimen.

The simulations on the 432 grain TD and LD structures are presented in Figure 2.20. The TD specimen shows strong plastic heterogeneities compared with the homogeneously distributed deformation patterns in the LD specimen. Strain localization patterns are similar for both 71 and 432 grain samples. The stress-strain curves show a similar global mechanical response for 71 and 432 grains. The nucleation of meso-Lüders bands in TD specimen implies the cooperative behavior of neighboring grains.

The numerical observations of the local strain fields at the mesoscale lead to the conclusion, that in the case of SSA the plastic shear bands can penetrate neighboring grains when the latter are favorably oriented, they can also widen within these grains as the tensile test proceeds but will not propagate along the gauge length of the specimen by invading neighboring grains laterally. The texture of the material favors plasticity along predetermined arrangements and associations of grains and inhibits the propagation of strain bands across the polycrystalline microstructure. This conclusion partly explains the absence of the experimental macroscopic observations of Lüders bands in α-Ti [171].

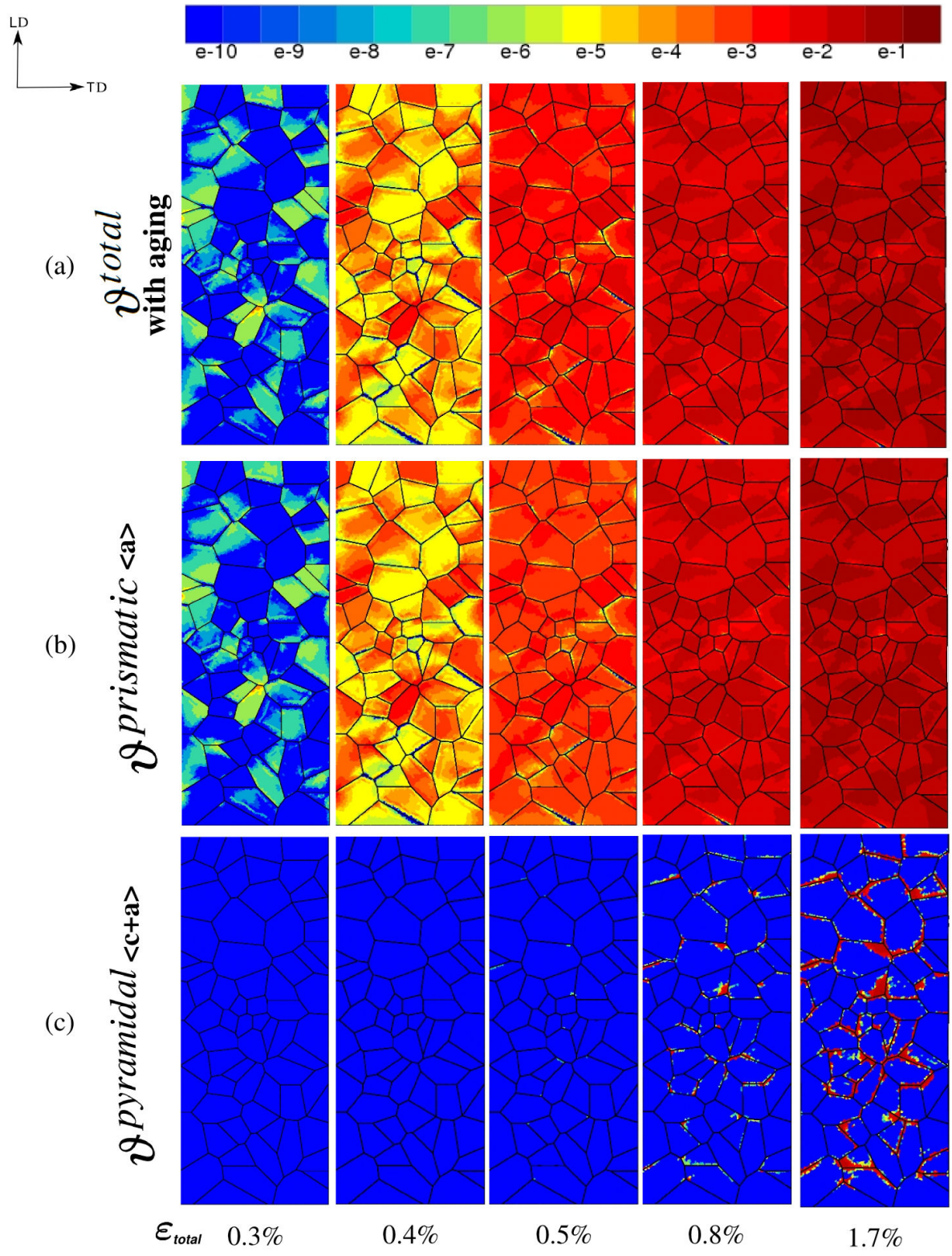

Figure 2.19: Evolution of plastic strain ϑ for flat extruded polycrystalline sample with 71 grains strained in LD at $2 \times 10^{-4} s^{-1}$: (a) total ϑ^{total}; (b) $\vartheta^{prismatic}$ on $\langle a \rangle$ slip systems; (c) $\vartheta^{pyramidal}$ on $\langle c+a \rangle$ slip systems.

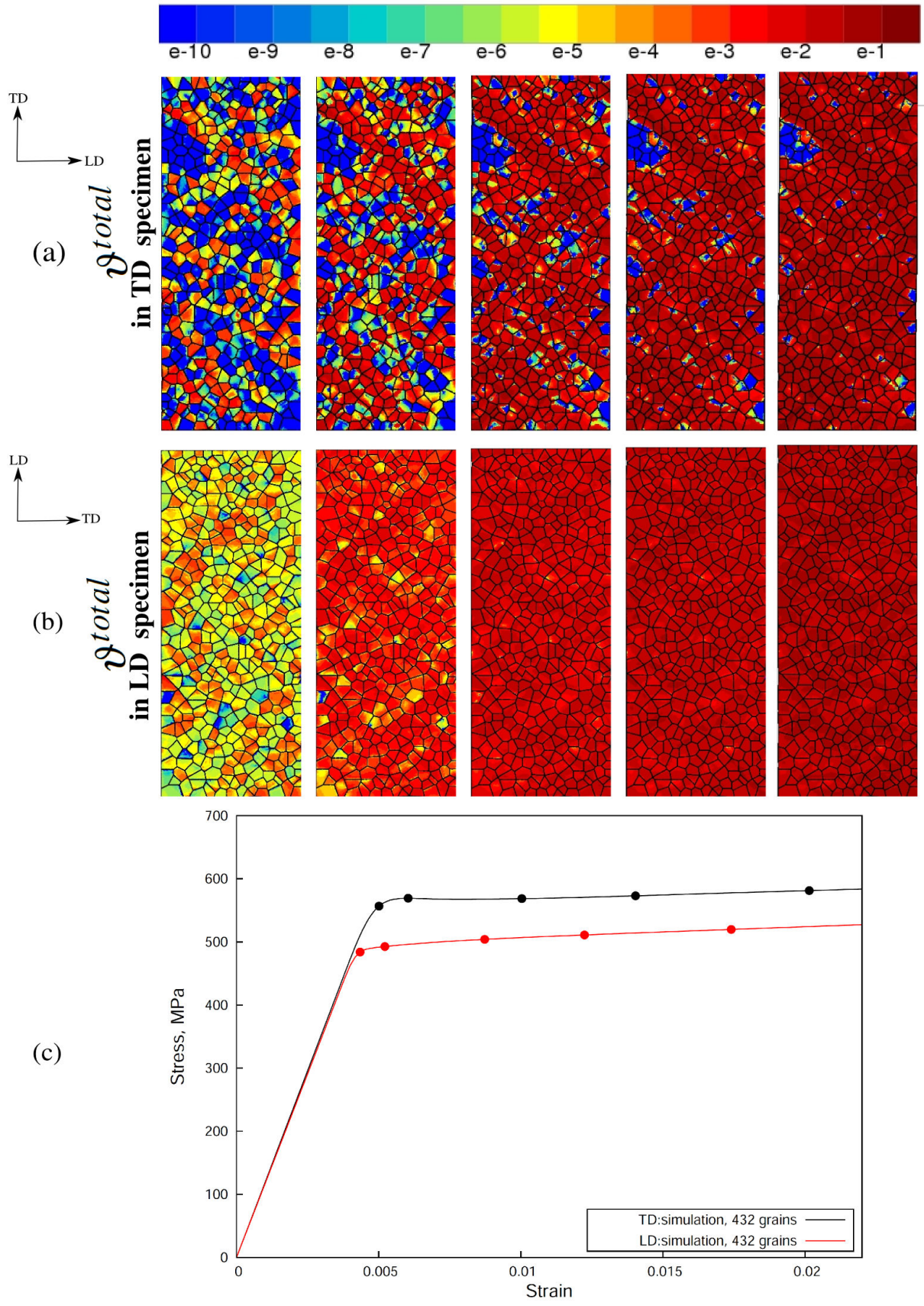

Figure 2.20: Plastic strain ϑ^{total} at $2 \times 10^{-4} s^{-1}$ for flat extruded polycrystalline sample with 432 grains strained in: (a) TD; (b) LD; (c) the overall stress-strained curves.

The proposed strain aging model was equally used to perform the simulations of the PLC effect on the flat LD and TD specimens. Figure 2.21 shows the fields of plastic strain rate $\dot{\vartheta}^{total}$ of the LD specimen and the corresponding simulation curve of the tensile test at $\dot{\varepsilon} = 2\times10^{-6}s^{-1}$. The LD specimen is of particular interest since, due to the crystal texture, we expect only $\langle a\rangle$-type slip families to contribute to the deformation.

The tensile curve revealed slight serrations of 2-3 MPa amplitude corresponding to the PLC effect. A series of macroscopic bands associated with the pointed stress drops on the stress-strain curve can be detected on the specimen. As can be seen in Figure 2.10, the apparent macroscopic SRS remains positive in the range of applied strain rates, however locally at the level of grains, the material can exhibit negative SRS leading to DSA serrations at $\dot{\varepsilon} = 2 \times 10^{-6}s^{-1}$. The PLC bands nucleate at random locations along the specimen and have irregular appearance and orientation. They propagate discontinuously through the grains crossing the grain boundaries and then overlapping in some regions. They eventually cross the entire section of the sample and can be regarded as macro-PLC bands. These bands are most likely of A or possibly B-type [112]. The separated presentation of the strain rate of $\langle a\rangle$ and $\langle c+a\rangle$ slip system families confirms that the observed slip bands are mostly due to the cooperative behavior of the grains with activated prismatic $\langle a\rangle$ slip.

The local total strain rate field observations in Figure 2.22 show the grains with intense permanent slip activity (grain A), while other grains are intermittently activated (grains B,C and D). As a result, macroscopic PLC bands are formed across grains and grain boundaries (bands number 1 and 2). The local increase in plastic strain rate precedes the band formation, and is followed by a local decrease upon disappearance of the band [101].

In the simulations on TD-specimen, the deformation patterns are slightly different due to the higher fraction of grains with activated $\langle c + a\rangle$ type slip (see Figure 2.23 (c)). As a result, we observe the combination of two deformation modes: quick periodic shear activity of the macro-PLC bands due to $\langle a\rangle$ slip systems (Figure 2.23 (b)) and slow permanent meso-Lüders bands thickening due to $\langle c + a\rangle$ slip (Figure 2.23 (c)).

The DSA simulations on the structure with 432 grains show similar localization patterns for LD and TD-specimens (see Figure 2.24 (a,b)) as in the case of 71 grain structure. The strain rate field mapping shows large strain heterogeneities developed within grains, which later collectively form the macroscale deformation bands [90, 165]. These bands nucleate and vanish periodically and erratically, and sweep across the same region of the sample several times [83]. It must be noted, that the amplitude and the frequency of serrations on the tensile curves is smaller than for 71 grains. It might be the consequence of the increased number of grains and possible neighboring effect that can lead to alternating slip activities between grain assemblies of similar plastic potential [193]. The obtained results numerically predict the formation and propagation of macroscopic PLC bands in CP α-Ti. These results are of particular interest since, to date, no experimental evidence of nucleation and propagation of macroscopic PLC bands in Ti alloys at room temperature can be found in the literature.

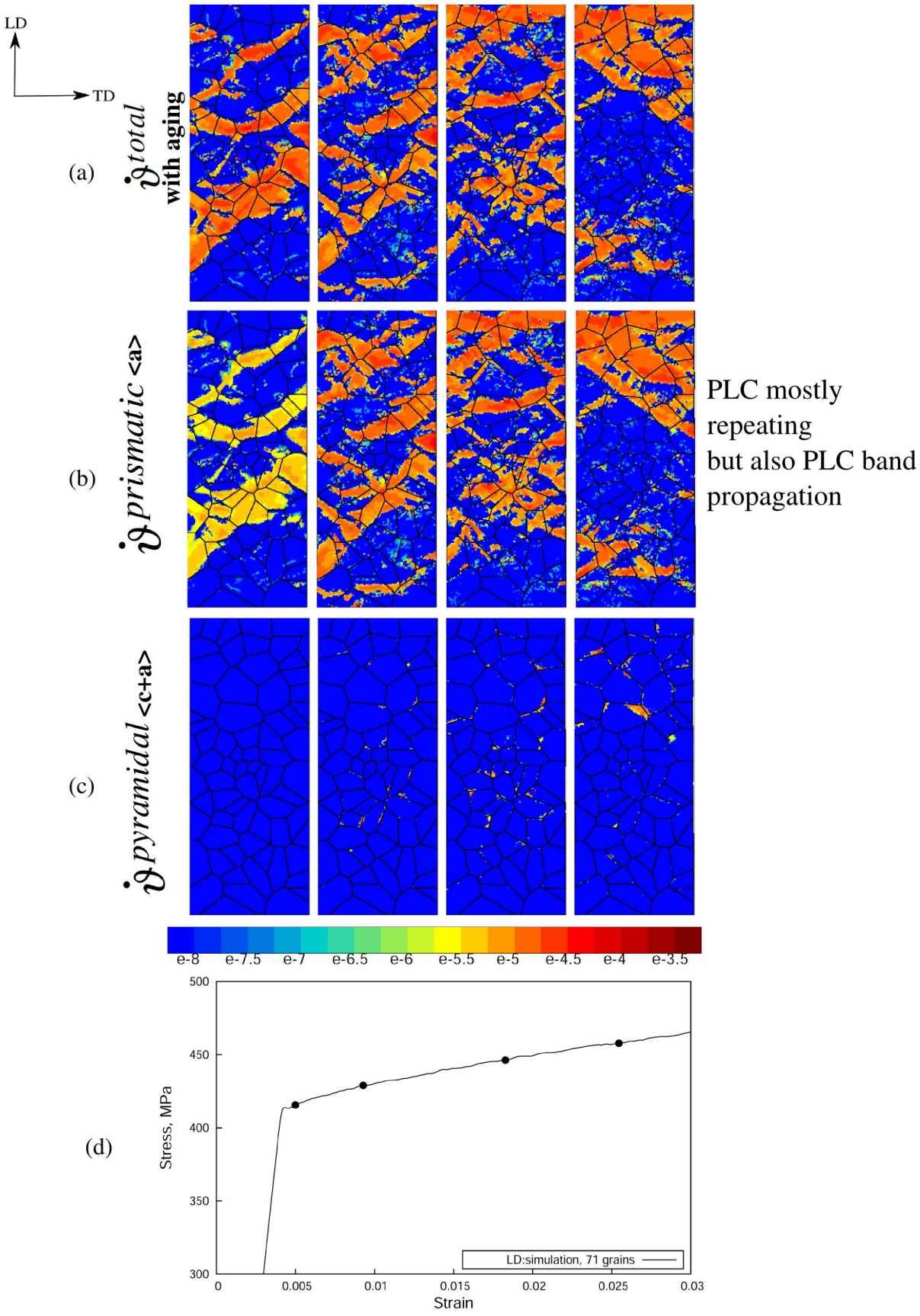

Figure 2.21: Accumulated plastic strain rate $\dot{\vartheta}$ for flat extruded polycrystalline 71 grain sample strained in LD at $2 \times 10^{-6} s^{-1}$: (a) total $\dot{\vartheta}^{total}$; (b) $\dot{\vartheta}^{prismatic}$ on $\langle a \rangle$ slip systems; (c) $\dot{\vartheta}^{pyramidal}$ on $\langle c + a \rangle$ slip systems; (d) the corresponding overall stress-strain curve.

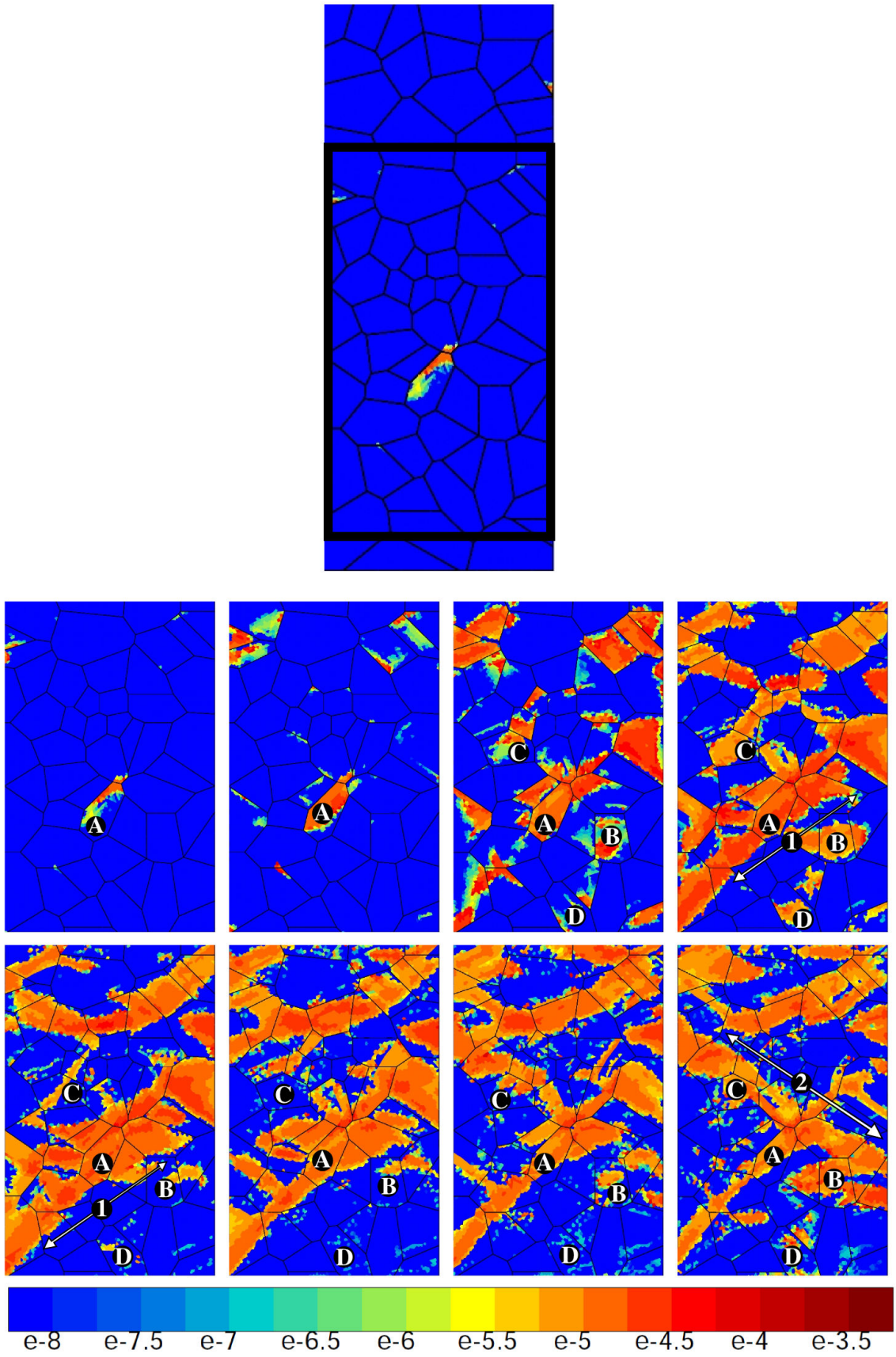

Figure 2.22: Evolution of total plastic strain rate $\dot{\vartheta}^{total}$ for flat extruded polycrystalline sample with 71 grains strained in LD at $2 \times 10^{-6} s^{-1}$. Grain A exhibits quasi permanent plasticity, whereas grains B, C and D experience intermittent activity. Intermittent bands labelled $'1'$ and $'2'$ can evolve in several grains.

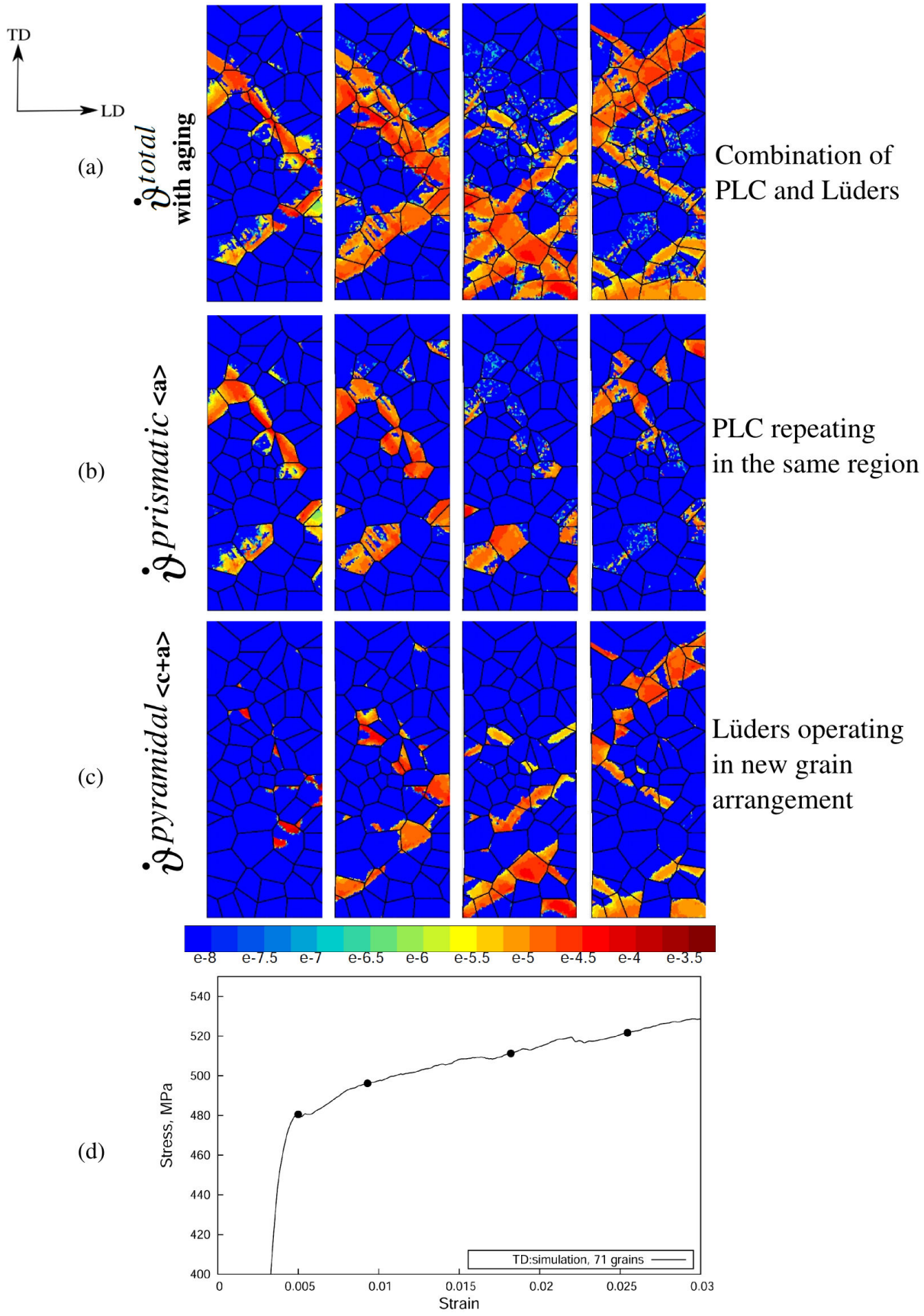

Figure 2.23: Accumulated plastic strain rate $\dot{\vartheta}$ for flat extruded polycrystalline 71 grain sample strained in TD at $2 \times 10^{-6} s^{-1}$: (a) total $\dot{\vartheta}^{total}$; (b) $\dot{\vartheta}^{prismatic}$ on $\langle a \rangle$ slip systems; (c) $\dot{\vartheta}^{pyramidal}$ on $\langle c + a \rangle$ slip systems; (d) the corresponding overall stress-strain curve.

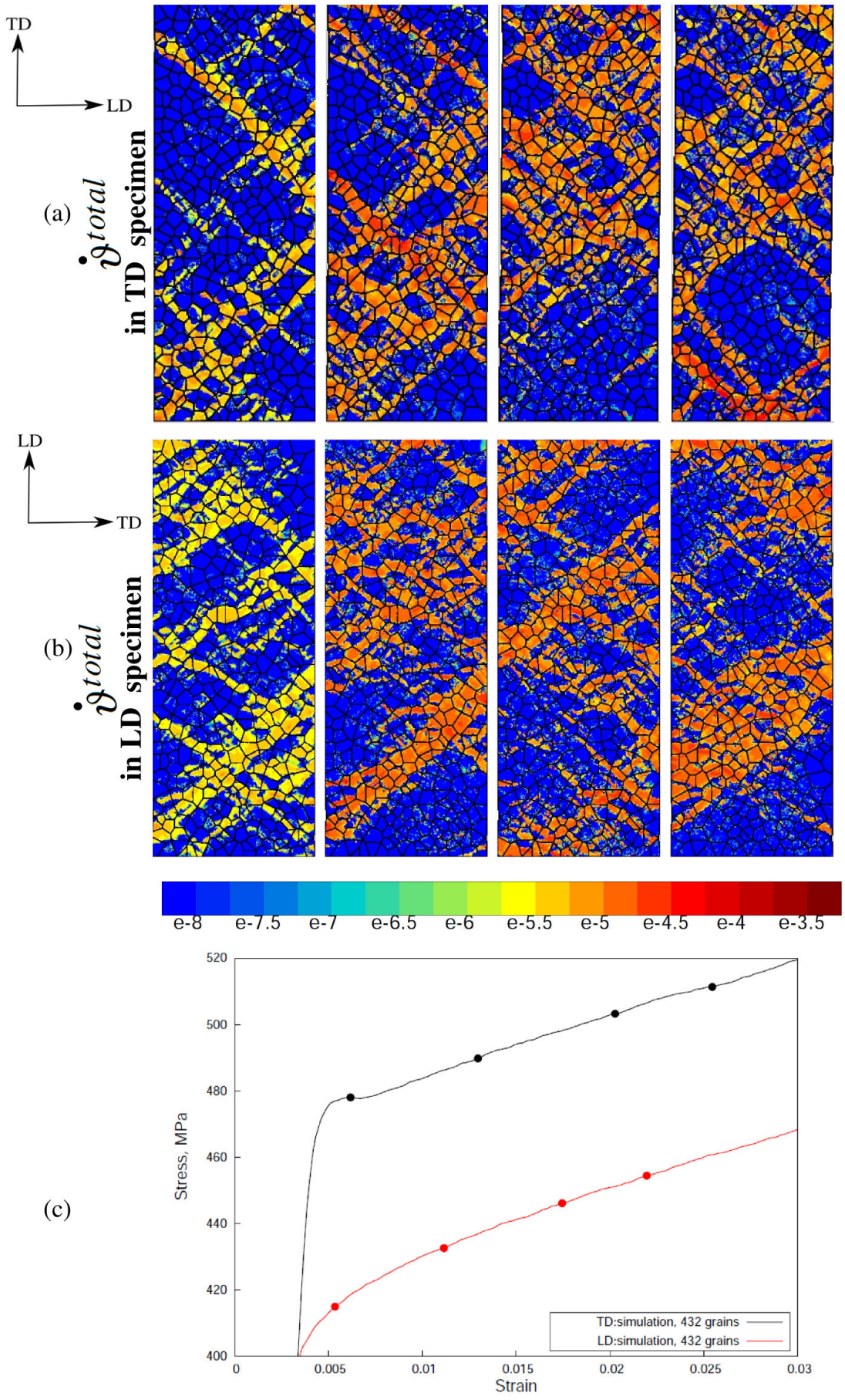

Figure 2.24: Equivalent plastic strain rate $\dot{\vartheta}^{total}$ for flat extruded polycrystalline sample with 432 grains strained at $2 \times 10^{-6} s^{-1}$ in: (a) TD; (b) LD; (c) the overall stress-strain curves.

2.7.2 Strain aging induced localization in fully 3D polycrystalline aggregate

The full 3D simulations were performed on the polycrystalline aggregate of 150 grains in order to check the reference in 3D of the phenomena observed in 2D. Figure 2.25 (a,b) shows the contour maps of the accumulated plastic strain for the tension test carried along LD and TD-specimens at $\dot{\varepsilon} = 2 \times 10^{-4} s^{-1}$ and the corresponding macroscopic stress-strain curves (Figure 2.25 (c)). The deformation pattern of the aggregate strained along LD direction is more uniform than that of the TD-specimen. The strain field of TD-sample reveals the strain localization in the form of the shear bands across couples of grains and at the grain boundaries occurring at the moment of the yield peak at the stress-strain curve.

The results of the DSA simulations on fully 3D aggregates at $\dot{\varepsilon} = 2 \times 10^{-6} s^{-1}$ are shown in Figure 2.26. They display the same type of localization phenomena as in the case of flat extruded specimens, but it is more difficult to observe due to the coarseness of the FEM used.

The comparison of the experimental and simulation results obtained on flat extruded polycrystalline specimens and fully 3D aggregates show the correctly predicted anisotropy of the mechanical behavior of CP α Ti. The set of identified parameters adequately simulates the anomalous yield point for TD-specimen in 2D as well as in 3D. The PLC effect was reproduced on TD and LD-specimens at $2 \times 10^{-6} s^{-1}$, even though the model should be improved to better describe the detailed evolution, especially the frequency and the amplitude of the serrations. One of the possibility to increase the amplitude of serrations is to shift the vertical relaxation for aging t_0^s of each system s to slightly smaller values (5 s and 50 s for $< a >$ and $< c + a >$ respectively instead of 10 s and 100 s, see Table 2.6). The other possibility would be to include in the model the stiffness of the testing machine, which was shown to amplify the DSA effect [208]. Both options should be tried. The numerical results obtained so far support the proposed scenario for the plastic instabilities observed in CP α Ti.

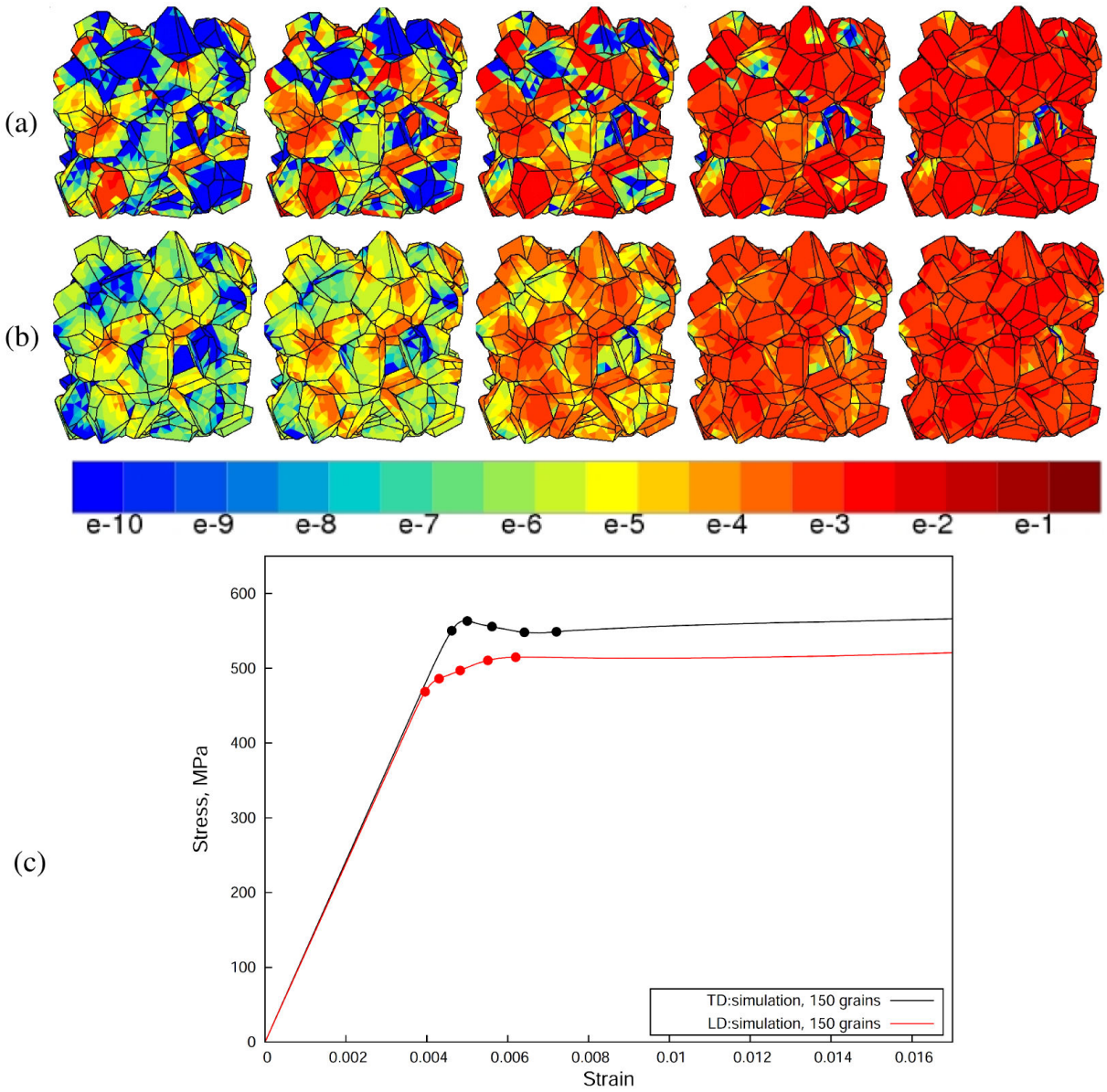

Figure 2.25: Evolution of accumulated total plastic strain ϑ^{total} of a 3D polycrystalline aggregate during a tensile test at $\dot{\varepsilon} = 2 \times 10^{-4} s^{-1}$ for: (a) TD, (b) LD, (c) corresponding stress-strain curves.

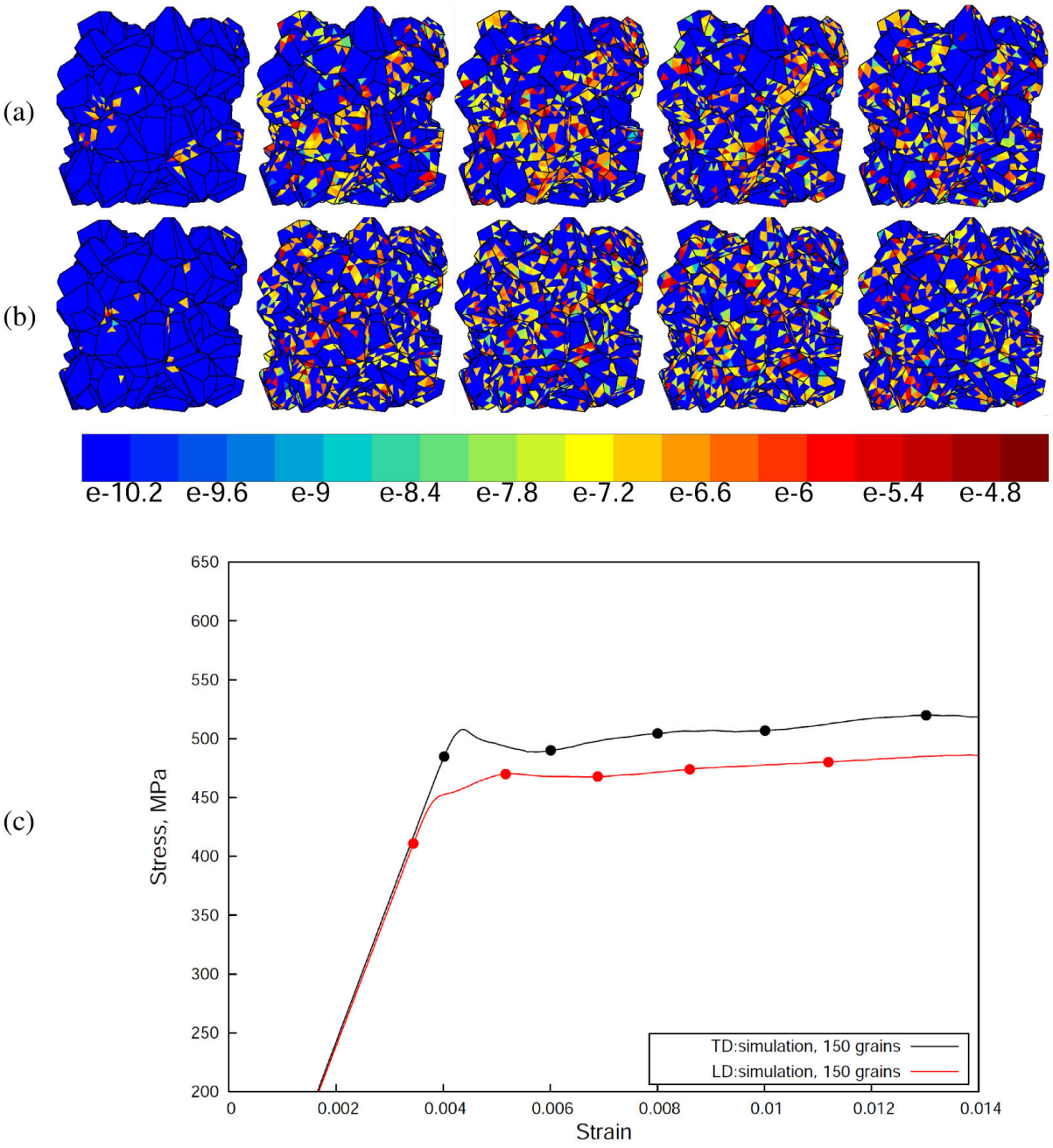

Figure 2.26: Evolution of plastic strain rate $\dot{\vartheta}^{total}$ of a 3D polycrystalline aggregate during a tensile test at $\dot{\varepsilon} = 2 \times 10^{-6} s^{-1}$ for: (a) TD, (b) LD, (c) corresponding stress-strain curves.

2.8 Conclusions

In the present study, we investigated the phenomena of static and dynamic strain aging in cold-rolled CP α-Ti using computational mechanics of polycrystals. The physical mechanisms underlying the existence of strain heterogeneities in CP α-Ti were reviewed. The origin of the anomalous yield point phenomenon in the samples strained along TD was attributed to the interaction of $\langle c+a \rangle$ dislocations with interstitial atoms of oxygen. The PLC effect revealed in TD and LD-specimens was ascribed to the non-planar core structure of screw $\langle a \rangle$-type dislocations that can cross slip on neighboring slip planes and thus change from sessile into glissile core configuration.

Based on the proposed scenario, a new phenomenological elastic-viscoplastic aging model coupled with crystal plasticity was proposed to simulate the SSA and DSA effects. The FEM simulations were carried out for various specimens in tension: on flat extruded polycrystalline specimens and on full 3D samples. The identification method enables calibration of viscosity, hardening and aging parameters.

In the case of SSA, the FEM simulations of the tensile tests give a good description of the stress-strain curves with a correct prediction of the material anisotropy resulting from its crystal texture. As in the experiments, the TD simulation curve shows slight yield peak followed by a stress plateau. When examining strain field simulations, the presence of complex plastic strain localization phenomena was revealed. They take place within specific groups of grains which are sharing crystalline orientations rather favorable for plasticity and therefore tend to retain and concentrate plastic strain. Thus, contrary to the usual Lüders bands (observed on pure Fe, for instance) that easily extend to neighboring grains and propagate across grain boundaries, the strain localization bands generated by the present numerical model appear fairly immobile since anchored by the crystalline texture. We suggest calling them meso-Lüders bands. Such locally persistent straining patterns were recently observed experimentally by Barkia et al. [17] in this material.

The resultant overall stress-strain curves of the DSA simulations show slight serrations on both TD and LD specimens corresponding to the PLC effect. The numerical model predicts initiation and propagation of macroscopic PLC bands in the strain rate domain explored. These macroscopic bands are formed due to the cooperative behavior of the grains, where the strain is localized. PLC serrations were obtained even in the presence of a positive value of the macroscopic SRS.

The model presented here, in making use of a FEM grid, although connecting all points of a structure (test sample, engineering part), enables spacial decoupling of plastic events within the structure at the appropriate scale; in introducing, in addition of the standard strain hardening terms, a time dependent hardening term to the flow stress enables time and space decoupled aging events to take place within the structure. The model recognizes the crystalline nature of the mechanical structure by the use of the identified slip systems and enables to take into account the lower symmetry of the HCP crystals constitutive of CP α Ti, as compared with FCC or BCC crystals of higher symmetry. As a consequence, local strain softening events may occur, associated with strain localization patterns and local strain rates in large excess to the nominal macroscopic strain rate. For rather small spacial extension of these plastic avalanches and when these events concern only a minor volume fraction of the entire sample, the amplitude of the serrations, on the stress-strain curves, remain small and compatible with a positive value of the macroscopic SRS of the sample. This apparent discrepancy between local, micro-scale value of the SRS and its macro-scale value was observed and well simulated here, at room temperature, in the low temperature (or high strain rate) region of the PLC domain of this material. An additional achievement of this model is to provide for SSA as well as for DSA strain localization

bands, by its appropriate crystalline description of the material, a clear interpretation of the lack of mobility or the absence of plastic fronts in this material, in contrast with their counterparts, usually observed in Fe or Al based alloys, which appear highly mobile and able to cross easily all grain boundaries.

Chapter 3

Experimental study of sustained load cracking in commercially pure α Ti

Résumé

Ce chapitre présente une étude expérimentale portant sur les essais de ténacité et de rupture différée réalisés à température ambiante dans le titane non allié de pureté commerciale. Les deux alliages de titane de phase alpha (Grade 2 et Grade 4) sont utilisés. On fait varier la teneur en hydrogène dans la limite des concentrations admises dans les produits industriels. Les techniques permettant de faire varier la teneur en hydrogène dans les matériaux étudiés sont présentés. Les essais de déchirure ont été effectués sur des éprouvettes CT à entaille latérale, préfissurées par fatigue. Des coupes métallographiques de surfaces de rupture ont été examinées. Les principaux résultats issus de ces essais sont:

– La résistance à la déchirure a été dégradée dans le Grade 2 et Grade 4 par une légère augmentation de la concentration en hydrogène. Une grande dispersion des résultats est obervée dans les essais de rupture sous charge constante.
– Un accroissement de la teneur en oxygène de 1600 à 3200 ppm augmente la résistance à la fissuration dans les essais de ténacité et de rupture différée grâce à l'effet durcissant de l'oxygène.
– Des observations fractographiques indiquent que la rupture est du type ductile avec la présence d'une très forte proportion de 'fluting', avec des zones clivées éparses. Dans le Grade 2 les flûtes sont plus courtes et plus larges, contrairement à celles couramment observées sur le Grade 4. D'après l'ensemble des examens, il ne semble pas que la teneur en hydrogène de l'alliage ait une influence sur l'aspect des surfaces de rupture.

Contents

3.1 Introduction

The susceptibility of Ti alloys to hydrogen embrittlement has been investigated for several decades [214, 32, 134, 135, 93, 78]. Different methods have been developed for evaluating the effect of hydrogen content on fracture toughness and subcritical crack growth properties in structural alloys. Generally the methods utilize the concepts of linear elastic fracture mechanics which allows to incorporate the phenomenon of hydrogen cracking into safety design of materials structural integrity [77]. The governing role of K, as the single-parameter descriptor of loading and crack geometry on the rate of subcritical hydrogen crack propagation, was established by pioneering experimental work of Beachem and Brown [38]. Due to the fact that hydrogen can induce subcritical crack propagation under static loads corresponding to the stress intensities less than the critical stress intensity for unstable crack propagation under plane strain loading (below fracture toughness K_{Ic}), it is necessary for a structural integrity model to predict (i) the threshold loading conditions below which hydrogen-assisted cracking is not likely to occur and (ii) the remaining life of a component based on rates of hydrogen-assisted crack propagation. Crack growth threshold and kinetics can be measured in the laboratory with fracture mechanics specimens. At first, smooth or notched specimens were used to evaluate the hydrogen content needed for cracking [39]. Later, pre-cracked specimens which require a lower content of hydrogen to initiate cracking have been used in the experiments [135, 172, 227].

The time-dependent subcritical crack growth is typically described by a functional relationship between crack velocity da/dt and K. Usually the K dependence of da/dt exhibits the specific form with four distinct features (see Figure 3.1) as K increases: (1) a threshold K_{th}, below which stable crack growth is not occurring; (2) stage I just above K_{th} where da/dt rises sharply with increasing K due to presumed mechanical control of crack tip damage; (3) Stage II where crack growth rate da/dt is independent of K due to reaction rate/hydrogen diffusion control; (4) stage III where da/dt increases with rising K approaching K_{Ic}, in which inert-environment fracture mechanisms compete with hydrogen-induced subcritical growth [61]. The precise relationship between da/dt and K depends on a wide variety of test methods, environmental exposure, hydrogen concentration, temperature, alloy strength and metallurgical variables [77]. The whole curve is shifted towards the blue curve with increased local hydrogen concentration, C_h or yield strength, σ_{ys}. It leads to lower thresholds and accelerated growth rates. With increased temperature (red curve), the amount of hydrogen necessary for the threshold regime is decreasing, but the kinetics of the crack velocity (region 2) is increasing [20].

The influence of hydrogen on the unstable crack propagation or plane strain fracture toughness is closely related to the influence of hydrogen on tensile strength and ductility properties of the material. Generally, hydrogen damage is promoted by loading rates that are sufficiently rapid to preclude time-dependent hydrogen-assisted cracking, and does not involve a change in the microscopic fracture mode. Very often fracture toughness of the material is reported both in terms of the 5% secant load (K_Q) and the maximum load (K_M) encountered during the rapidly rising load test. The former is determined by the standard ASTM method from the load-crack opening displacement [10], whereas the latter is calculated by using the maximum load value P_{max} from the same recorded data. The advantage of using K_M is that it is directly translatable to the maximum load-carrying ability of the specimen and thus it can be used to describe the time-dependent degradation in load-carrying capacity. In turn, very often K_Q fails to meet the criteria valid for K_Ic, and therefore it is an invalid, dubious parameter [227].

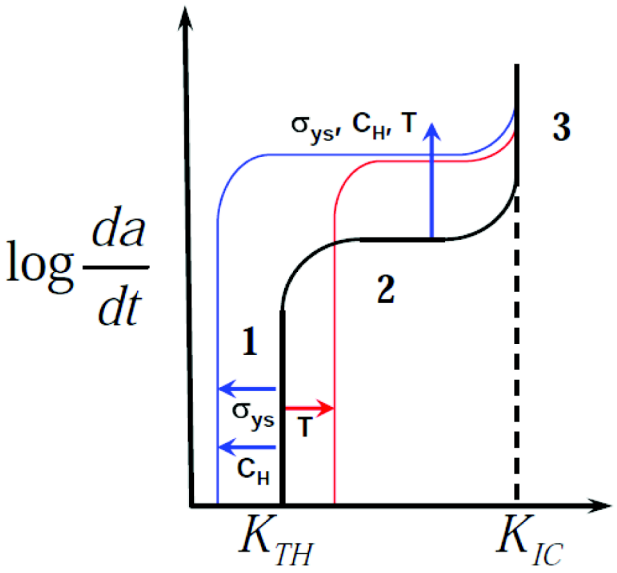

Figure 3.1: Schematic representation of the relationship between crack velocity and stress intensity factor by the hydrogen embrittlement phenomenon [20].

Alternative way to calculate K_{Ic} was used in the study on stress-corrosion cracking (SCC) in high strength steel [38]. A schematic curve presented in Figure 3.2 shows the connected points of the initial stress intensity K_{Ii} with the K_{Ic} points at which condition the remaining ligament of the specimens was separated. The stress intensity parameter K_{Iscc} is a threshold value required to initiate SCC.

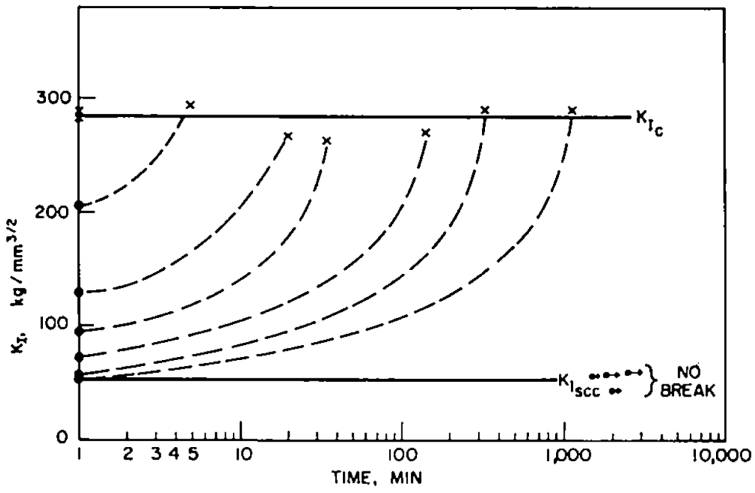

Figure 3.2: Schematic representation of the experiments indicating instantaneous K_I values for beginning of stress-corrosion cracking and for onset of fast fracture K_{Ic}. K_{Iscc} is a threshold value required to initiate SCC [38].

The influence of hydrogen and oxygen on fracture toughness and sustained load cracking (SLC) will be characterized in the present chapter. The tests were performed on compact tension (CT) specimens so as to determine the evolution of the fracture toughness K_{Ic} and the threshold stress intensity factor K_{th} for SLC with the impurity content and detect possible modifications in fracture mechanisms. The fractographic examinations were performed on CT specimens to define important aspects of fracture mechanisms such as ductile voids, interfacial facetted fracture surfaces etc. On the basis of the experimental study, the effect of hydrogen and oxygen on fracture toughness and sustained load cracking is discussed.

3.2 Experimental procedure

3.2.1 Preparation of the specimen

In the present study two grades (Grade 2 and Grade 4) of commercially pure α Ti with different initial content in oxygen and hydrogen were studied. Some samples were heat treated at 500 °C for 12 hours and they will be called Grade 2 *base* and Grade 4 *base*. Other specimens were submitted to hydrogen charging or degassing in order to obtain different hydrogen content in each case. To avoid hydride formation in the material, hydrogen content was kept below the solubility limit in the charged specimens. Prior to hydrogen charging and degassing, the sample surface was grounded sequentially to 4000 grit SiC paper, polished with 3 μm polishing diamond paste, then degreased with alcohol and cleaned in distilled water and dried in cold air. The treatment cycle consisted of ramping up to 550°C for 5 hours, treatment for 12 hours, slow cooling down in the furnace. By holding the same treatment cycle for all specimens, we ensure that the difference in the mechanical properties will be dependent on the chemical composition of each specimen only. The EBSD analysis showed that the texture of the material and the size of grains was not affected by the specimen treatment [18]. The nominal and target chemical composition of the materials is given in Table 3.1.

	H	O	C	Fe	N
Grade 2 *base*	6±2	1600±50	40	340	30
Grade 4 *base*	15±2	3200±100	70	1700	60
Grade 2 *charged*	15±2	1600±50	40	340	30
Grade 4 *charged*	25±2	3200±100	70	1700	60
Grade 4 *degassed*	2±2	3200±100	70	1700	60

Table 3.1: Target chemical composition of the titanium used in this study (wt. ppm).

Among possible hydrogen charging techniques a charging from a gaseous environment was chosen for the present material. This technique ensures uniformity of hydrogen distribution in the material and gives the possibility to control amount of hydrogen in Ti by changing the pressure of H_2 in the bath cell. The hydrogen charging was performed at Institut de Chimie Paris-Est (ICMPE) with the help of the charging facility shown in Figure 3.3. It consists of a hydrogen source, a vacuum pumping system, a capacitance-based manometer and a resistance furnace to heat the specimen. Sample holder with Ti specimen was heated in hydrogen atmo-

sphere in a constant volume [183]. The product of system volume and the difference between the initial and final partial hydrogen pressure of the system allow to estimate the average hydrogen concentration in the sample. The charging was performed at 500°C for 12 hours. As the sample absorbs hydrogen in solution, the hydrogen pressure is decreased. The hydrogen content was measured for verification by Bureau Veritas using inert gas fusion technique.

The aim of the process of degassing is to reduce hydrogen content in Grade 4 *base* from 15 ppm down to zero. Some popular methods of degassing are: helium sparging, warming, and subsequent filtering and vacuum degassing. The last option was chosen since this method can remove more than 95% of the dissolved hydrogen. A vacuum bake out at 550 °C for 12 hours under high vacuum (10^{-7} Torr) was sufficient to reduce hydrogen level in Grade 4 down to 8 ppm. A vacuum system (Figure 3.4) has been designed in ICMPE (Institute of Chemistry and Materials Paris Est) and it includes a quartz tube with the specimen connected to a turbo molecular pump which provides secondary vacuum of 10^{-6} Torr. The high vacuum of 10^{-7} Torr is produced by the ionic pump.

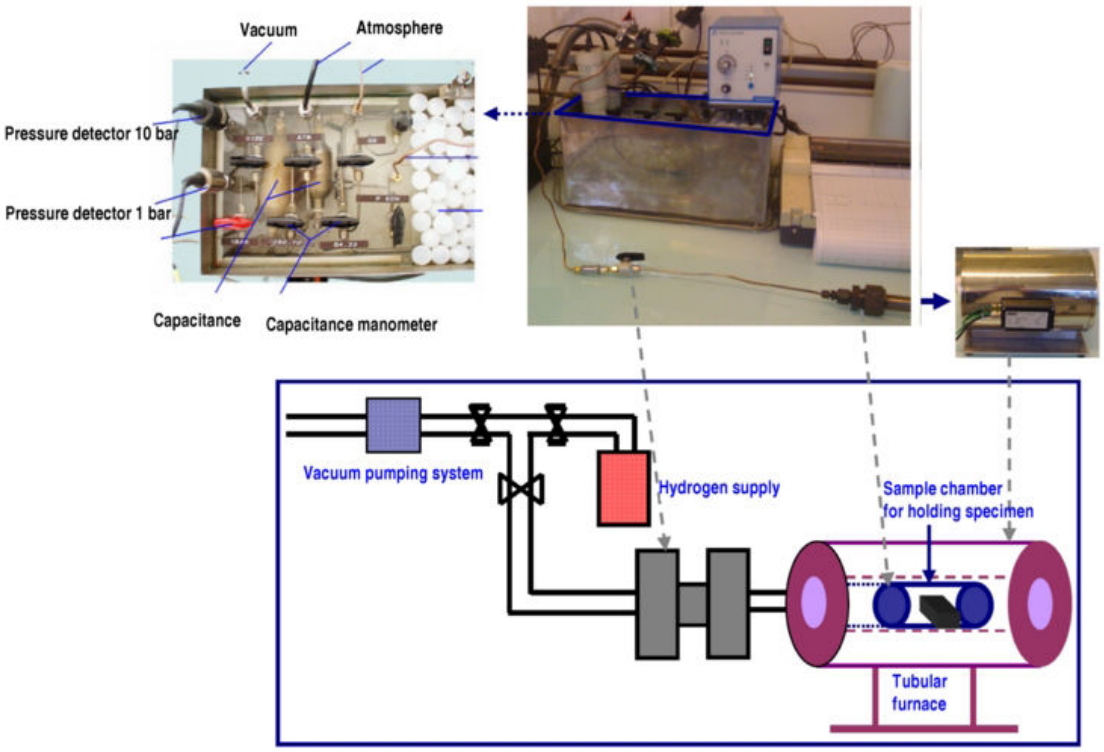

Figure 3.3: The gaseous hydrogen charging facility at ICMPE (Institut de Chimie Paris-Est) [17].

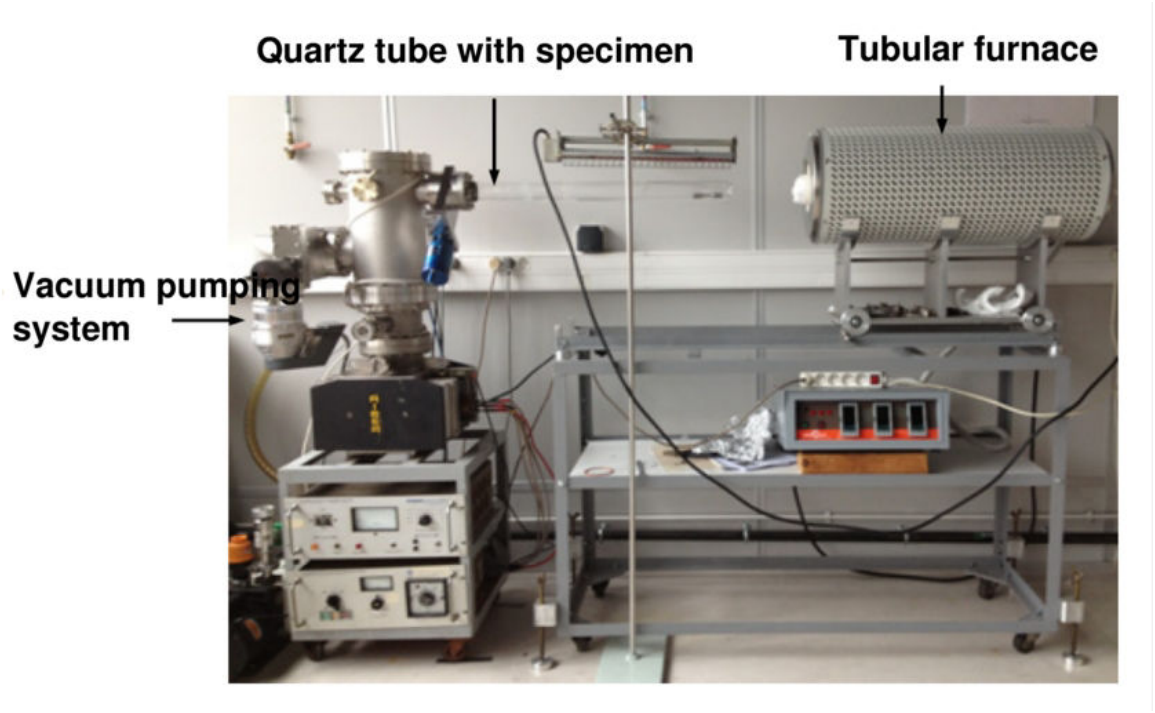

Figure 3.4: The hydrogen degassing device at ICMPE (Institut de Chimie Paris-Est) [17].

Among several existing specimen types used for the evaluation of the fracture toughness of materials, we used compact tension (CT) specimens. The CT specimens were machined from a cold rolled sheet of Ti with a crack plane parallel to the transverse direction (TD). The applied load is parallel to the longitudinal direction (LD). The dimensions of a CT specimen shown in Figure 3.5 are in accordance with ASTM Standard E1820-11 [10], except the thickness B that was reduced in order to enter the specimen in the sample chamber for hydrogen charging.

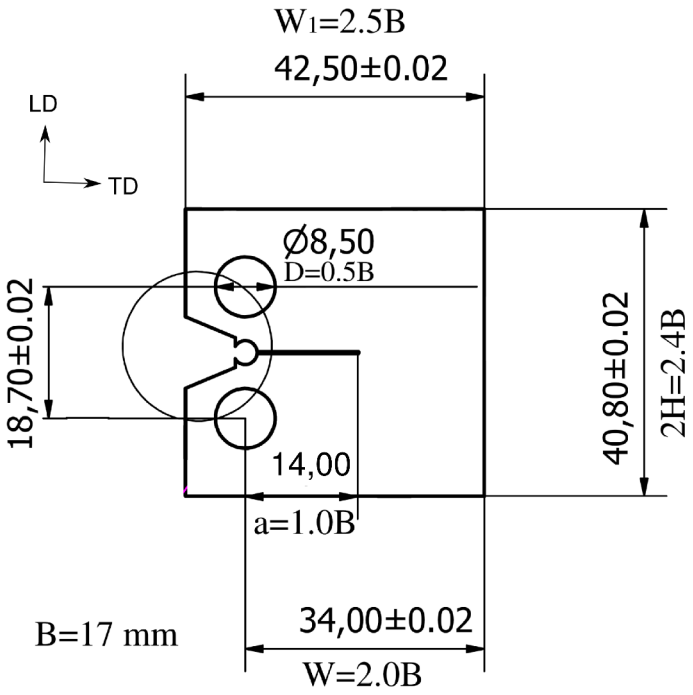

Figure 3.5: Dimensions of the CT specimen, where B is the thickness of the specimen.

All specimens were precracked in fatigue in conditions such that the plastic zone at the crack tip remained sufficiently small. This was achieved by following the crack propagation, which must remain below a specified value of stress intensity factor. A fatigue precrack of 2 mm was produced under force control with the ratio of loads P_{min}/P_{max}=0.1 and at the frequency of 40 Hz. All specimens were precracked on a servo-hydraulic machine MTS in Centre des Matériaux. The initial maximum load in fatigue precracking P_{max} is calculated as follows:

$$P_{max} = \frac{K_i (B^2 W)^{1/2}}{f\left(\frac{a_i}{W}\right)} \tag{3.1}$$

where the crack length/width ratio is defined by ASTM E1820-11 [10] as:

$$f\left(\frac{a_i}{W}\right) = \frac{\left(2+\frac{a_i}{W}\right)\left[0.886+4.64\left(\frac{a_i}{W}\right)-13.32\left(\frac{a_i}{W}\right)^2+14.27\left(\frac{a_i}{W}\right)^3-5.6\left(\frac{a_i}{W}\right)^4\right]}{\left(1-\frac{a_i}{W}\right)^{1/2}} \tag{3.2}$$

The initial maximum load during precracking P_{max} is required to be lower than the limit load P_{lim} which is defined as:

$$P_{max} \leq \eta P_{lim} \tag{3.3}$$

where η is a constant varying from 0.4 to 1. The limit load P_{lim} is a maximal admissible load that a perfectly plastic material can withstand. In case of a CT specimen, it can be defined as:

$$P_{lim} = \frac{0.4B(W-a_0)^2\sigma_{ys}}{2W+a_0} \tag{3.4}$$

where B,W and a_0 are the thickness, width and the initial crack length respectively. At the beginning of the fatigue cycling, the initial P_{max} is applied. The specimen is carefully monitored

until crack initiation is observed on both sides of the specimen. The applied load P_{max} is incrementally decreased as the crack begins to extend. In the present study, the initial load P_{max} corresponding to K_{max}=12 MPa$\sqrt{m}$ was applied at the beginning of the precracking procedure. When the fatigue precrack propagated for 0.1 mm, the applied load P_{max} was decreased to the value of K_{max}=11.75 MPa$\sqrt{m}$ and so on until the precrack length was equal to 2 mm with K_{max}=7 MPa$\sqrt{m}$ etc.

The next step was the to provide the CT specimen with side grooves (Figure 3.6) to maintain a straight crack front during a fracture toughness test [8]. A specimen without side grooves is subject to crack tunneling and shear lip formation because the material near the outer surfaces is in a state of low-stress triaxiality. Side grooves remove the low triaxiality zone and lead to relatively straight crack fronts. A net thickness of a side-grooved specimen is usually 80 % of the gross thickness (i.e. $B_N = 0.8 \times B$).

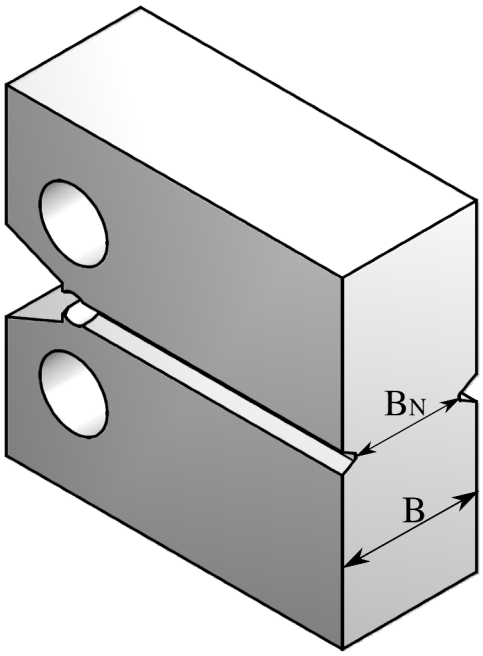

Figure 3.6: Side grooves in a CT specimen.

3.2.2 Fracture toughness test procedure

In the first approximation, a small scale yielding condition was assumed. Small scale yielding corresponds to case where the size of the plastic zone ahead of the crack tip is much smaller than the size of the specimen [25]. The loading curve remains linear up to sudden fracture and Linear Elastic Fracture Mechanics (LEFM) can be used. The fracture toughness K_{Ic} tests were conducted on CT specimens by following ASTM E1820-11 norms [10]. In summary, the determination of the fracture toughness K_{Ic} included the following main steps:

1. Precracked CT specimen was loaded with a displacement rate of 1 mm/min up to fracture. Load vs. load-line displacement was continuously measured and registered. Crack mouth opening displacement (COD) was registered with the help of the clip-gauges.

2. The determination of K_{Ic} was based on the calculation of a conditional result K_Q, which involves a construction of a test record. A line with a slope equal to 95% of the tangent OA to the initial portion of the elastic loading curve as shown in Figure 3.7 was constructed to determine P_5. For fracture mode of Type I, P_Q=P_5.
3. The next step was optical measurement of the initial crack length a_0 after precracking step and calculation of the average value through the relation 3.5:

$$a_0 = \frac{1}{N}\sum_{i=1}^{N} a_i, \qquad N = 9 \tag{3.5}$$

4. Once P_Q and the crack length were determined, a conditional fracture toughness K_Q was computed from the following relationship:

$$K_i = \frac{P_i}{(BB_N W)^{1/2}} f\left(\frac{a_i}{W}\right) \tag{3.6}$$

where $f\left(\frac{a_i}{W}\right)$ is a dimensionless function of a/W defined by Eq.3.2.

5. The validity requirement of ASTM norms [10] was checked for K_Q to be a valid K_{Ic}. It includes:

$$0.45 \leq a_0/W \leq 0.55 \tag{3.7}$$

The thickness of the specimen should be a multiple of the size of the plastic zone, r_p, which is proportional to $\left(\frac{K_I}{\sigma_{YS}}\right)^2$.

$$B, a \geq 2.5\left(\frac{K_Q}{\sigma_{YS}}\right)^2 \tag{3.8}$$

where σ_{YS} is the 0.2% offset yield strength.

$$P_{max} \leq 1.10 P_Q \tag{3.9}$$

6. Once all the conditions were fulfilled, then it was accepted that K_{Ic}=K_Q

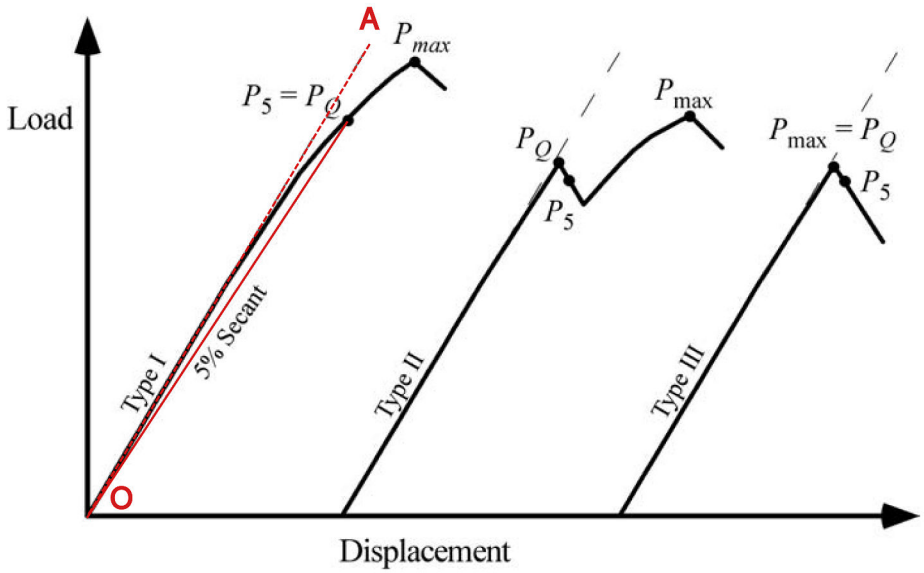

Figure 3.7: Determination of the conventional load F_Q.

3.2.3 Sustained load cracking test procedure

The estimation of stress intensity threshold value (K_{th}) to sustained load cracking might be a complex task which requires an appropriate teasing procedure. In the literature, two different strategies of testing are usually employed, based on either rising or falling K. In a rising K test, a fracture mechanics specimen is held under a constant load. When the crack extends, the K increases resulting in an accelerated crack growth. Decreasing or falling K tests are conducted on fracture mechanics specimens held under a constant displacement [103]. One of the consequence of this type of test is the material relaxation that might result in decreased K over time without necessarily crack propagation. In both procedures, the loading can be applied differently: incrementally rising or a single constant loading. In the former incrementally rising loading procedure or just step-loading, the K_{th} is estimated by first loading a specimen to a certain K somehow lower that the expected fracture toughness K_{Ic}, waiting several hours, and then, if no crack growth is detected, increasing the load to a certain increment. Each load usually allows to remain applied for several hours. The indicator of crack propagation, such as COD clip gage, or potential drop method allow to judge whether the load should be increased at the end of some time interval. The lowest initial value of K resulting in sustained crack propagation and eventual fracture, based on the average crack length measured on the fracture surface, represents the threshold to SLC K_{th} [134].

In the present study, a second type of SLC testing called single-loading was adopted. In this procedure, the value of K_{th} was assessed by applying a single load in both rising and falling K tests. The list of the applied loads for different grades are given in Table 3.2. In some cases, duplicate tests were performed.

Material	Constant load test, kN	Constant displacement test, kN
Grade 2 *base*	16, 15, 14, 13.5, 13, 12, 11	16.6 , 16
Grade 4 *base*	18, 17.5, 17, 16, 15	17
Grade 2 *charged*	15, 14, 13.5, 13, 12.5, 12	10, 14
Grade 4 *charged*	18, 17, 16, 15	15

Table 3.2: Sustained load cracking test matrix.

In both procedures (rising of falling K), the SLC test involved loading the sample in a servo-hydraulic test machine MTS with the displacement rate of 1 mm/min to set loads and then keeping the specimen under constant load or constant displacement. Crack opening displacement was monitored with the help of mounted clip gauge, while crack length was measured with a potential drop method. All tests were performed at room temperature. Testing was continued either until failure, recording the time to failure, or until a stabilization of the electrical signal. On completion of testing, all specimens were broken and the fracture faces examined using scanning electron microscopy. An average depth of fatigue precrack and the depth of SLC were used to calculate the failure stress intensity K using the Eq.3.6. The obtained data were used to estimate a value for the stress intensity factor below which no SLC was observed, K_{th}.

3.2.4 Electrical potential drop method

In order to monitor crack growth during the experiments, potential drop (PD) method was used as one of the most accurate and sensitive of Non-Destructive Testing (NDT) techniques. This method allows the detection and evaluation of crack growth while maintaining the specimen in service. Two types of potential drop methods could be used for crack measurements: Alternating Current Potential Drop (ACPD) and Direct Current Potential Drop (DCPD). As illustrated in Figure 3.8, the PD method consists of injecting electrical currents in the tested specimen and measuring the arising the change in electrical potential difference between two or more electrodes placed on its surface [187] across the crack. As the crack extends, the uncracked cross-sectional area A decreases and the measured electrical resistance R increases leading to the rise of electrical potential V.

$$R = \rho \frac{l}{A} \tag{3.10}$$

R is the electrical resistance, A is the cross-sectional area, l is the length of the uncracked ligament, ρ is the electrical resistivity, and V is the electrical potential.

In the present study the holes for the small metallic screws used as probes were drilled in the specimens. The DC electrical current I is introduced on the top surface of the specimen as shown in Figure 3.9 and the potential difference V is measured from probes located on the front side.

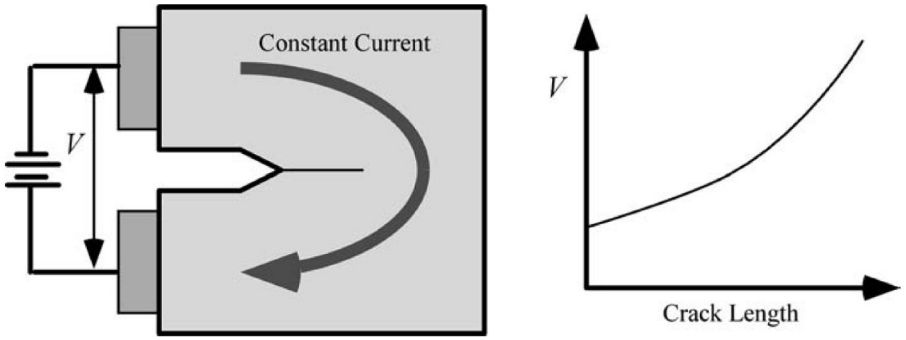

Figure 3.8: Scheme of potential drop method for crack growth measurement [8].

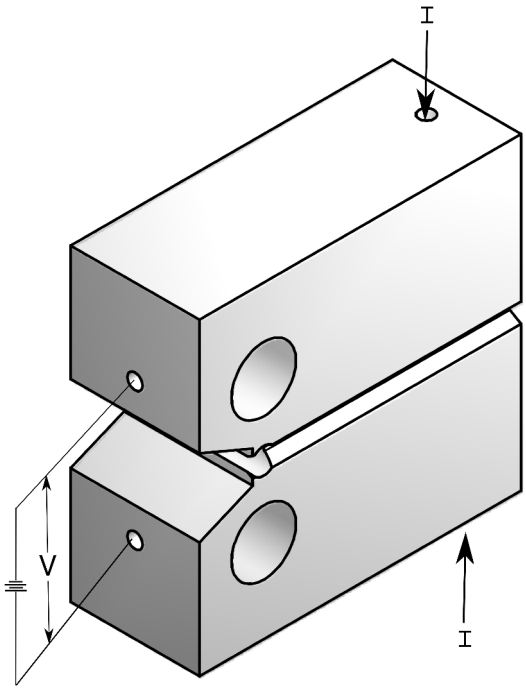

Figure 3.9: CT specimen-point application of current.

By monitoring this potential increase V, and comparing it with a reference potential V_0 measured on the sample unaffected by crack growth at the beginning of the experiments, the crack length a can be determined, with the use of a suitable calibration curves defined as:

$$a = f(V/V_0) \tag{3.11}$$

The use of such nondimensionalized ratio V/V_0 makes the calibration curve independent of material properties, specimen thickness, and magnitude of input current. As a result, only specimen and crack geometry and the locations of current input and potential measurement influence the form of the calibration curve. Calibration curves can be obtained experimentally, analytically or numerically. Ritchie [166] proposed to obtain theoretical calibrations through the use of finite element methods since it provides a rapid and relatively inexpensive means of generating accurate calibrations for any required geometry.

The calibration curve in the present study was calculated using FE code *Zset*. Due to symmetry conditions, only a quarter of the specimen is analyzed. The CT meshed specimen presented in Figure 3.10 was modelled in 3D. Eight-node linear hexahedral elements have been used for the calculation. The mesh near the crack tip was refined to a size of 300 μm. This mesh was generated using the mesh generator ABAQUS. The mesh was imported in $Z-set$ for simulations and then used to solve electrical problem, which consists to find the solution of the following differential equations:

$$\nabla^2 V(x,y,z) = 0 \tag{3.12}$$

$$J = \sigma E = -\sigma \nabla V(x,y,z) \tag{3.13}$$

where J is the vector of current density which is simply the electrical current I per unit area A, σ is the specific material conductivity, E is the vector intensity of the electrical field and

$V(x, y, z)$ is the electrical potential at point (x,y,z). The only material parameter needed in the simulation is the electrical conductivity of Ti $\sigma \approx 1666\ Siemens \cdot mm^{-1}$ for Grade 4.

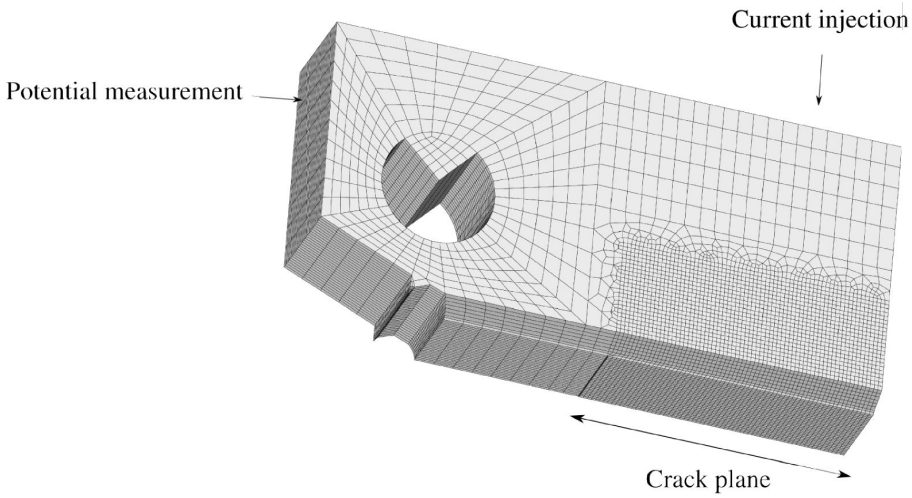

Figure 3.10: 3D CT specimen simulated geometry.

The thermal-electrical analogy was employed in the calculations where electrical current I flowing through an uncracked area can be regarded as the heat flux q. The measured electrical potential difference V is equivalent to the temperature difference T between the two surfaces, and the electrical conductivity σ is analogical to the thermal conductivity k.

$$\vec{q} = -k\nabla T \tag{3.14}$$

The potential was measured for different crack depths, i.e. solving Eq.3.12 for different surface areas, but keeping the current input constant. The calibration curve derived numerically for the CT specimen is shown in Figure 3.11. The PD was expressed then as a function of crack length Δa in the form:

$$\frac{V}{V_0} = \exp(0.07414\Delta a)^{1.00755} \tag{3.15}$$

$$\Delta a = \left(\frac{\log \frac{V}{V_0}}{0.07414}\right)^{1/1.00755} = \left[13.48(\log \frac{V}{V_0})\right]^{0.992} \tag{3.16}$$

As mentioned above, the calibration curve is used for the estimation of the crack propagation Δa during the experiments since optical post-mortem measurements do not allow to distinguish the zone of the crack propagation during the tests from the final unstable fracture. In a very few cases when the zone of the crack propagation Δa during the tests was visible, FE predictions were compared with the experimental results. It was noted that the FE solution lies consistently above the experimentally measured values. Such a discrepancy can arise from the sudden increase of electrical potential signal during the rising load stage illustrated in Figure 3.12. Here the PD signal registered for the specimen loaded up to 15 kN shows a very important rise produced within a short time (5 seconds) followed by the relatively stable increasing signal. This jump is due to the sudden crack mouth opening leading to the rapid change in the PD signal. In turn, the sudden crack opening can be triggered by the crack closure effect after precracking procedure. As a result, the experimental measured ratio of $\frac{V}{V_0}$ gives a bigger value which corresponds to

the longer crack length deduced from the calibration curve. It should be also noted that in the present simulations, the change in electrical resistivity and hence measured potential difference from the crack tip plasticity was not taken into account.

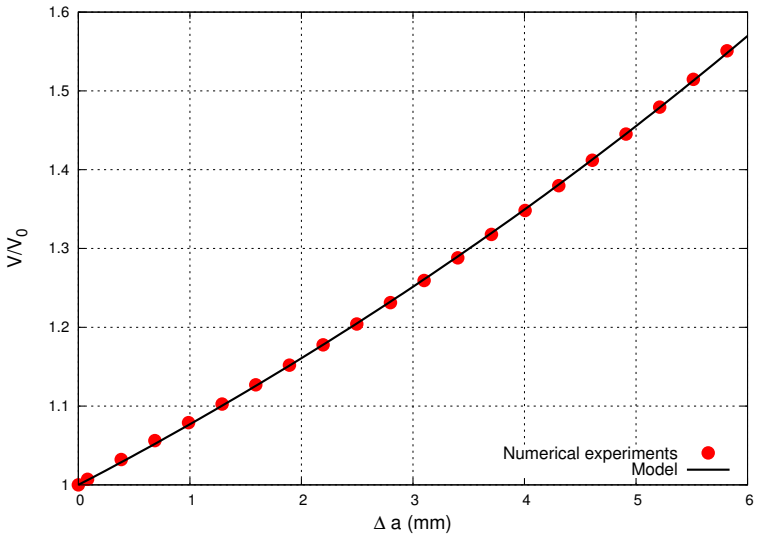

Figure 3.11: Calibration curve of a CT specimen.

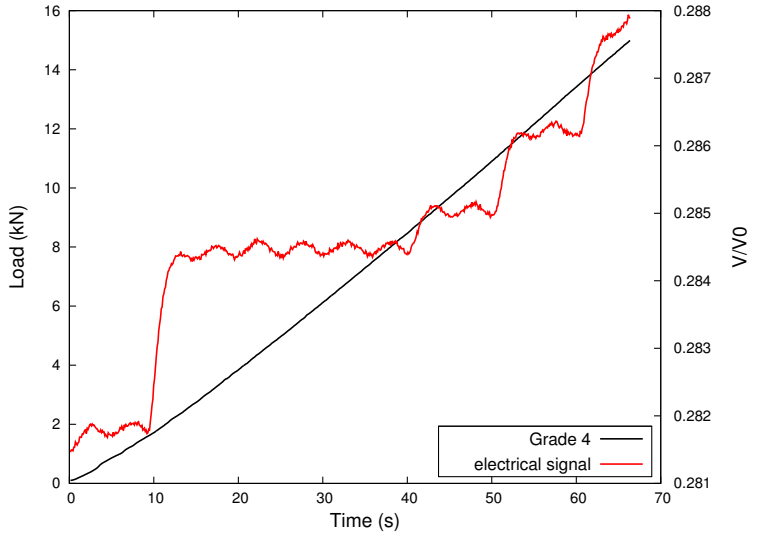

Figure 3.12: Experimental curve for Grade 4 *base* loaded up to 15 kN with the corresponding electrical potential signal.

3.3 Experimental results

3.3.1 Toughness tests

Experimental curves for load as a function of crack opening displacement (COD) for CT specimens machined from the rolled titanium plate in TD of Grade 2 and Grade 4 *base* are presented in Figure 3.13. Specimens of each grade have been loaded with two different displacement rates of 1 mm/min and 0.01 mm/min. The fracture toughness was apparently affected by the loading rate for both Grade 2 and Grade 4 which does not fulfill the requirements of Linear Elastic Fracture Mechanics (LEFM). In the following, the stress intensity referred to as K_{max} will be reported in terms of the maximum load encountered during the fracture test and calculated using the fatigue precrack size. This non-standard stress intensity K_{max} corresponds to the beginning of measurable subcritical crack growth. K_{max} will be used for comparative purpose only, since we will not work with LEFM any futher, as required by the materials behavior. K notion will be considered in this study as a useful quantity that accounts for the load applied to the specimen and to the length of the crack.

The values of K_{Ic} calculated by applying 5% secant criterion and K_{max} are given in Table 3.3. It can be seen that slower strain rate promotes lower K_{max} and K_{Ic} in both Grade 2 and Grade 4 which is consistent with the strain rate jumps experiments presented in Chapter 2. The degree of the deterioration of K_{max} in Grade 2 is more significant with decreasing displacement rate comparing to Grade 4. The measured values of K_{Ic} and K_{max} are significantly lower those reported by Millot [189] (K_{Ic}=111 MPa$\sqrt{m}$ for Grade 2 and K_{Ic}=104 MPa$\sqrt{m}$ for Grade 4). The difference can be conditioned by the chemical composition of the materials and used strain rates in the fracture toughness tests which were not precised in their study.

Material	displacement rate, mm/min	K_{Ic}, MPa$\sqrt{m}$	K_{max}, MPa$\sqrt{m}$
Grade 2 *base*	1	39.7	56.6
Grade 2 *base*	0.01	34.1	51.1
Grade 4 *base*	1	44.9	62.6
Grade 4 *base*	0.01	40.8	58.8

Table 3.3: The comparative results of the fracture toughness tests for Grade 2 *base* and Grade 4 *base* tested at different rate of displacement.

In general, a large difference in the fracture behavior between two grades can be observed. Grade 4 specimen is breaking in a more brutal way comparing to Grade 2, and it shows a higher tensile strength. This observation is consistent with the fact that materials with high tensile strength are usually less ductile. The high strength and eventual quasi-brittle rupture of Grade 4 can be attributed to the higher content of oxygen comparing to Grade 2.

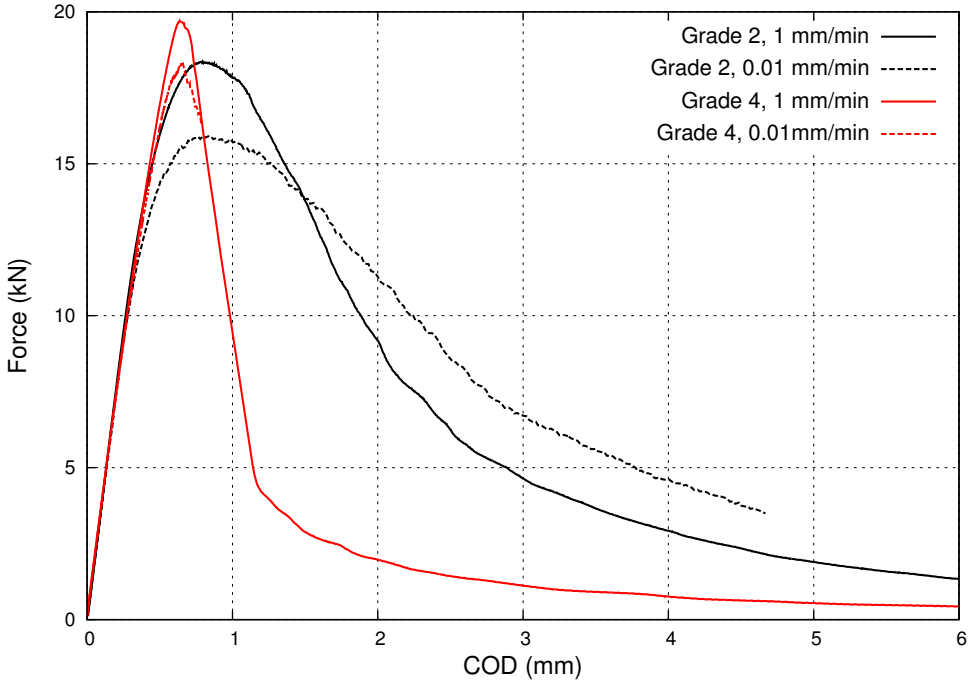

Figure 3.13: Fracture toughness tests on Grade 2 and Grade 4 at displacement rates of 1 mm/min and 0.01 mm/min.

In order to determine the influence of hydrogen, fracture toughness tests were performed on Grade 2 *charged* and Grade 4 *charged* and *degassed* at the strain rate of 1 mm/min. The results are presented in Figures 3.14 and 3.15. As can be seen, the ductility of Grade 2 is increased with the increased hydrogen level from 9 to 34 ppm, but the strength of the material is decreased. Note that the ductility measures the amount of energy required to fracture a material, and it is represented here by the area under the load-displacement curve. Similar effect of hydrogen embrittlement is observed in Grade 4 for *base* and *charged* specimens, however the ductility of Grade 4 did not show strong dependence on hydrogen content. The *degassed* specimen of Grade 4 did not show any significant change in ductility of the material. All three Grade 4 materials are fracturing in a quasi-brittle way. Difference in Young's modulus were found for Grade 2 which could be correlated with the variation in initial crack length of CT speciments and possible problems with the stiffness of the tensile machine.

To a first approximation, the obtained results indicate that hydrogen improves the ductility of the material through increase of plastic strain at the crack tip, but deteriorates the toughness of the material (see Figure 3.16). The softening of the material due to hydrogen can be explained in terms of the hydrogen-enhanced localized plasticity concept [31], which states that the presence of hydrogen in solid solution decreases the barriers to dislocation motion, thereby increasing the amount of deformation at the crack tip. The inceased oxygen content promotes higher K_{max}, however the fracture strain decreases leading to quasi-brittle fracture mode. One of the explanation of the reduced ductility in Grade 4 is oxygen-induced static strain aging, which can promote a solute drag force on dislocations, leading to the limited deformation at the crack

tip [211]. The decreased mobility also results in higher strength, lower ductility and lower toughness. The obtained results are in agreement with the fact that strength and toughness are often mutually exclusive properties in materials.

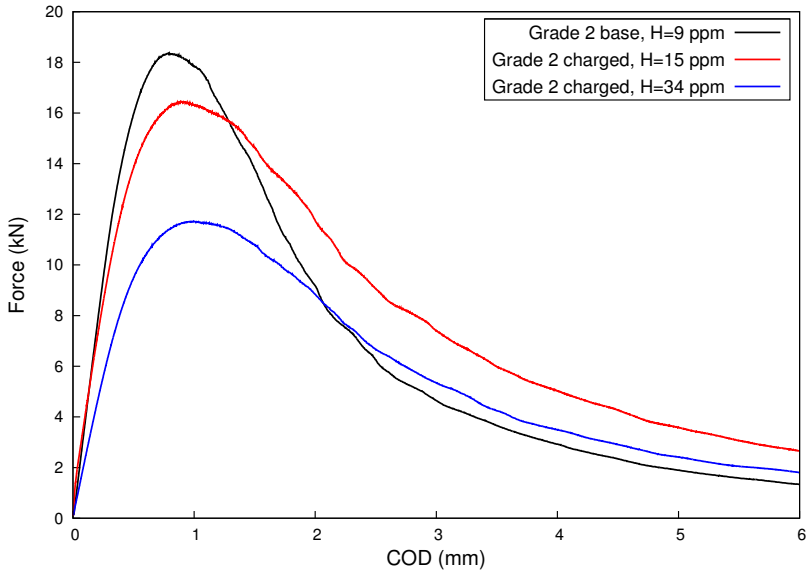

Figure 3.14: Fracture toughness tests on Grade 2 *base* and *charged*.

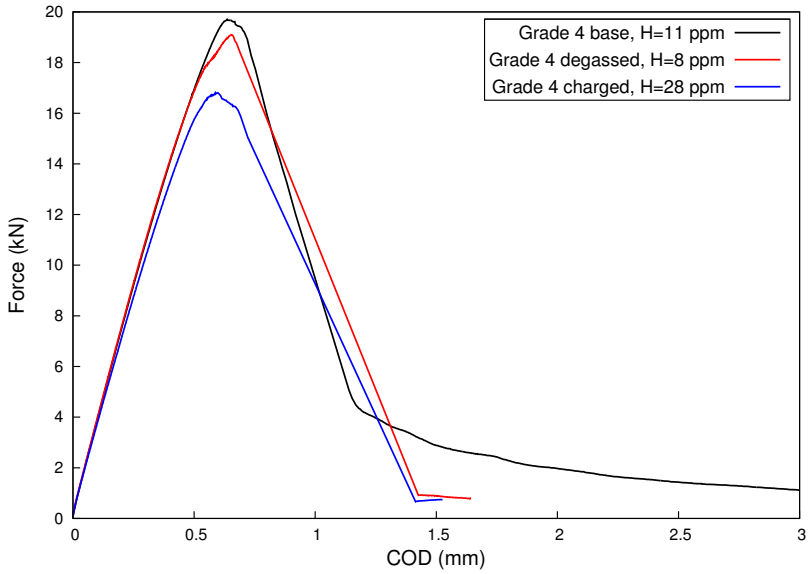

Figure 3.15: Fracture toughness tests on Grade 4 *base*, *degassed* and *charged*.

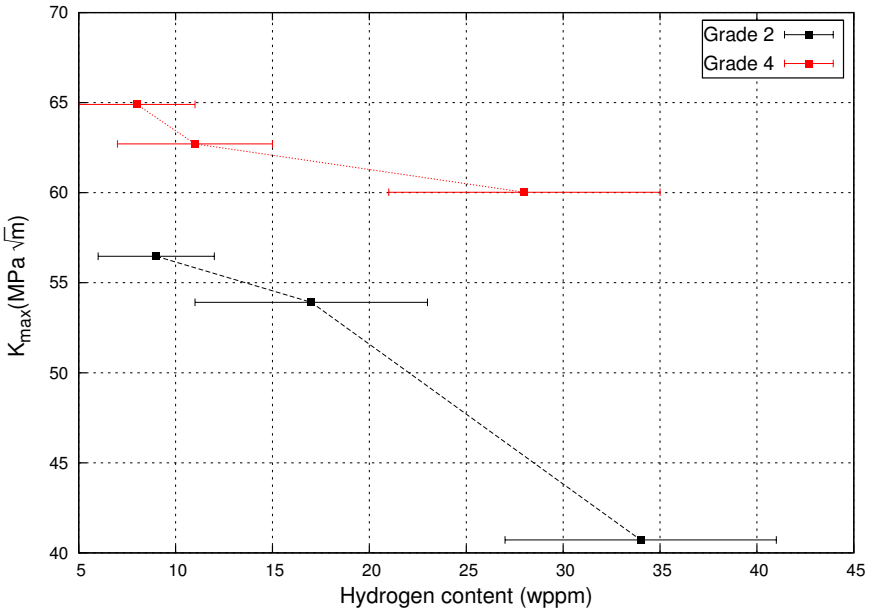

Figure 3.16: Fracture toughness K_{max} given by formula 3.6 for Grade 2 and Grade 4 as a function of hydrogen content.

3.3.2 Sustained load cracking tests

All CT specimens were loaded at a loading rate of 1 mm/min to a given load at room temperature and held under constant load until failure occurred or under constant displacement during a defined period of time. In the SLC tests carried under the constant load the form of the crack opening displacement (COD) vs. time to failure curve illustrated in Figure 3.17 (a) is analogous to that of creep with three distinct stages: (i) Stage I where a certain displacement rate is applied up to the required load; (ii) Stage II corresponding to the crack growth due to SLC; (iii) Stage III or tertiary zone where the material fails due to tearing. Finally, the threshold to SLC K_{th} is calculated from the load at which SLC was not observed within a specified period of time.

The SLC tests under constant displacement are analogous to the relaxation tests. The variation of the load-point force as a function of time to failure is shown in Figure 3.17 (b). The threshold to SLC, K_{th}, was determined by using the experimental value of the load corresponding to a stabilized potential drop signal (which implies the arrest of crack propagation) and the measured fatigue crack depth using the ASTM method for calculation of the stress intensity factor (Eq. 3.6).

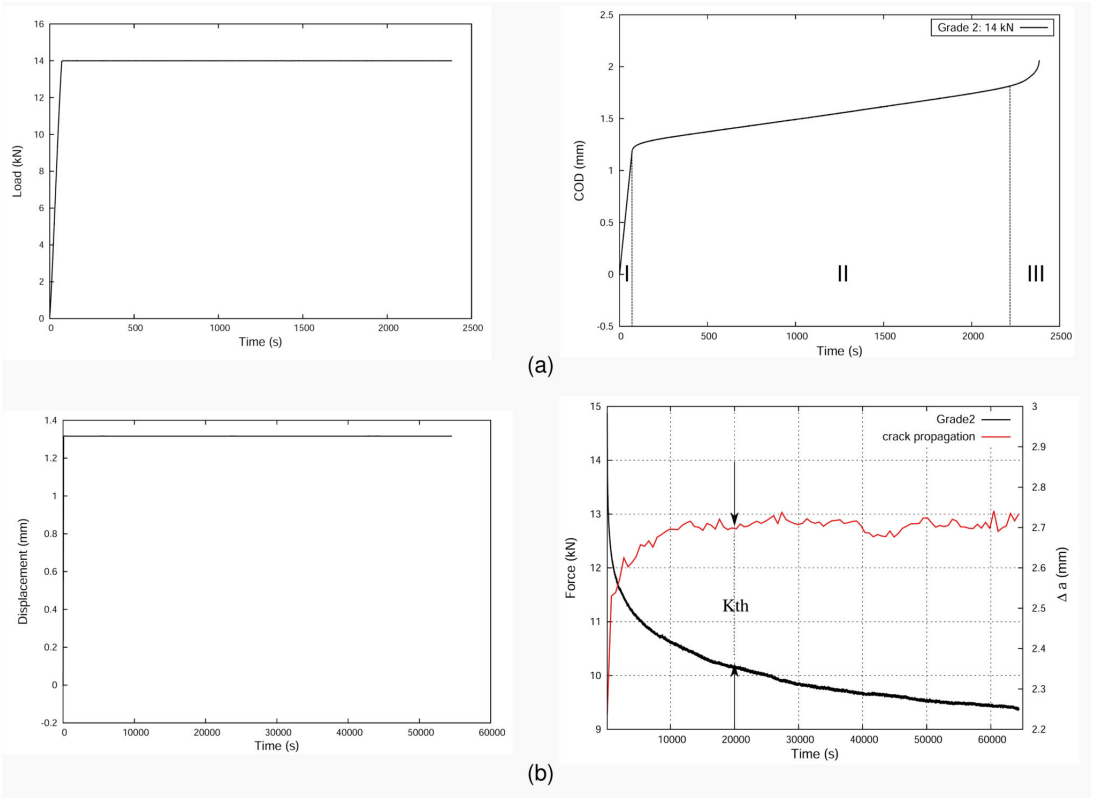

Figure 3.17: Schematic diagram of SLC tests under (a) constant load and (b) constant displacement. Prescribed loading on the left and specimen response on the right.

Figure 3.18 shows the curves of COD vs. time in the logarithmic scale for Grade 2 *base*. For the better presentation in logarithmic scale, the first part of the curve corresponding to Stage I in Figure 3.17(a) is not shown. As can be seen, all specimens exhibited time-dependent sustained load failures and the time to failure is increased with reduction of the applied load. The specimen tested at 11 kN did not break after 11 days. This specimen was later fractured by applying rapidly rising load.

The results of the load evolution with time for the sustained displacement tests for Grade 2 *base* are presented in Figure 3.19. The higher fraction of the flow stress is relaxed in specimen 2 (Test2) which was initially loaded up to 16.6 kN and then kept at constant displacement. The stiffness of the tensile machine can also contribute to the relaxation kinetics.

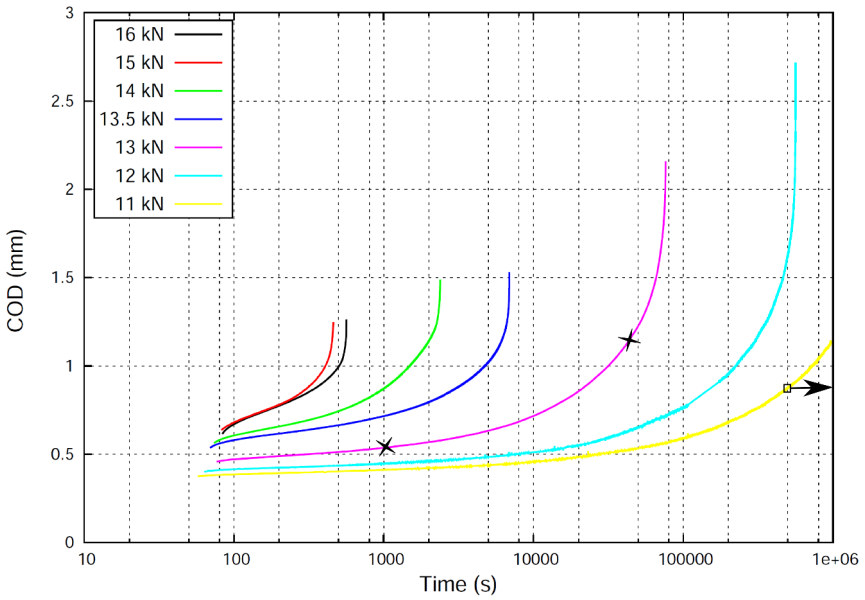

Figure 3.18: Experimental curves of SLC under constant load for Grade 2 *base*. Arrow indicates specimen removed from test before failure.

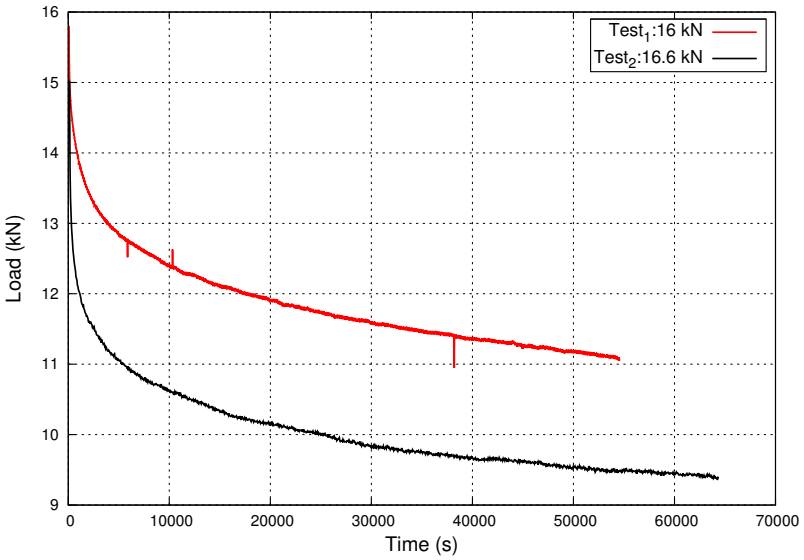

Figure 3.19: Experimental curves of SLC under constant displacement for Grade 2 *base*.

The sustained load curves of Grade 4 *base* CT specimens are shown in Figure 3.20. The results are less consistent compared to Grade 2 *base* which can be possibly attributed to the more brittle fracture mode of Grade 4 as it was noted in the experiments on fast crack propagation. It can be seen that specimens tested at 18 kN (black curve), 17.5 kN (red curve) and 17 kN (blue curve) all start with the same level of COD. The post-mortem crack measurement showed that

both specimens have the same initial crack length. However, the specimen at 17 kN fractures much faster (in 1 min) comparing to the specimen at the higher load of 18 kN (3.5 hours) and 17.5 kN (8 hours). Thus, some additional factors should contribute in the fracture kinetics of this specimen. The specimen at 15 kN did not fracture within 8 days and was broken by applying the rapidly rising load.

The results of the constant displacement test (see Figure 3.21) showed the load relaxation curve at 17 kN (Test1) with a very large load fluctuations. The present test was performed on a different MTS tensile machine with a larger load capacity (250 kN). The obtained results present the best calibration of the load-cell which was possible to obtain on the tensile machine of such capacity.

Figures 3.23 and 3.24 illustrate 'Master' plots for Grade 2 *base* and Grade 4 *base*, respectively, in the coordinates time to failure versus stress intensity factor K. The 'Master' plot for each grade includes all SLC tests under constant load (C1, C2...), constant displacement (R1, R2) and the fracture toughness tests (T1, T2). The corresponding loads applied on the specimens during the tests are given in Tables 3.4 and 3.5. These tables also contain post-mortem measurements of the precrack $a_{precrack}$ which, as can be seen, often exceeds the target length of 2 mm. This variation was conditioned by the difficulty to control the length of the precrack during the precracking procedure. The calculation of a given K is based on the following procedure:

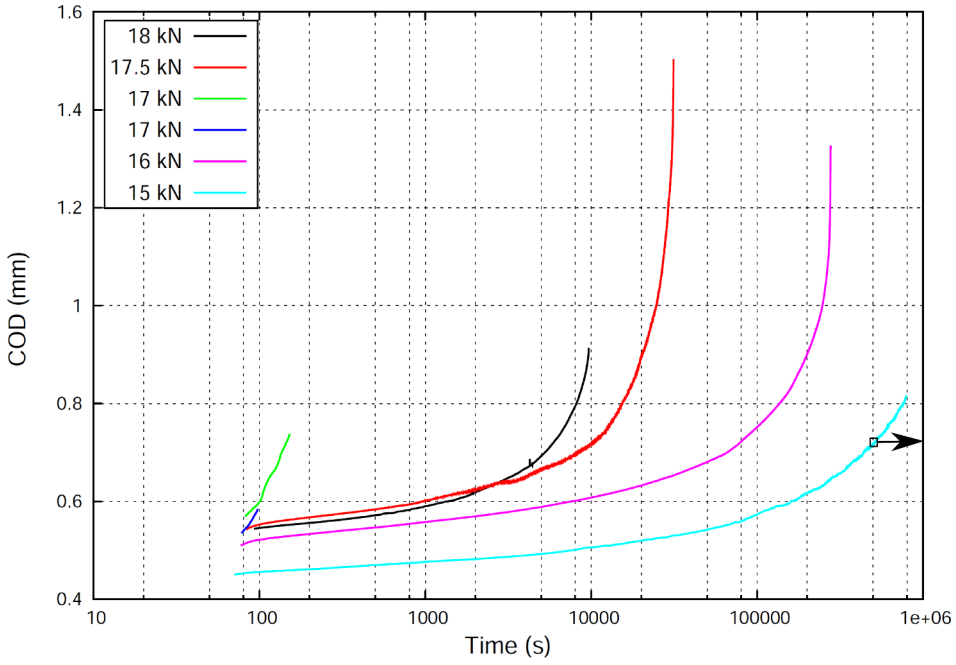

Figure 3.20: Experimental curves of SLC under constant load for Grade 4 *base*. Arrow indicates specimen removed from test before failure.

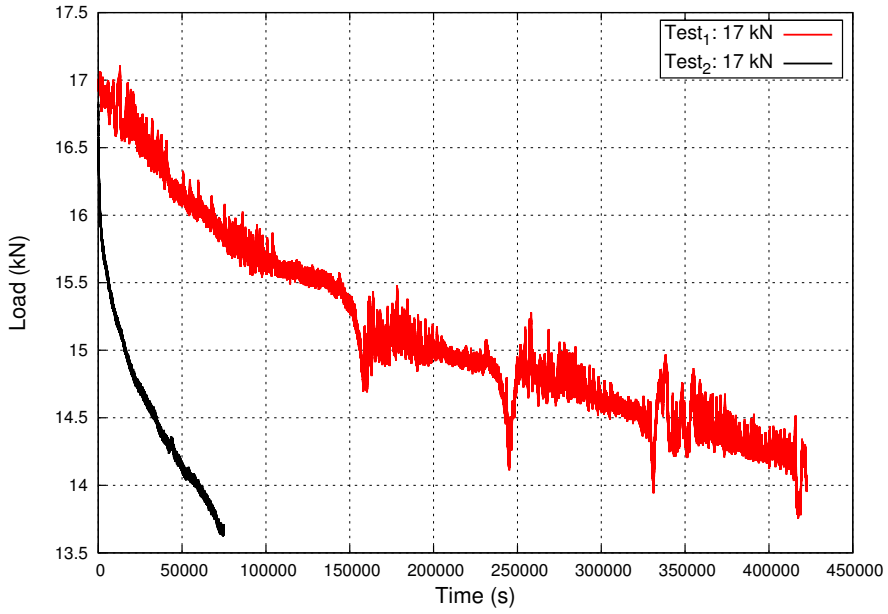

Figure 3.21: Experimental curves of SLC under constant displacement for Grade 4 *base*.

1. First, the precrack $a_{precrack}$ is measured post-mortem. The crack extension Δa produced during the test is hardly distinguishable from the final unstable fracture. That is why this length was estimated based on the experimentally measured value of the potential V/V_0 through the use of the calibration curve and relation:

$$\Delta a = \left(\frac{\log \frac{V}{V_0}}{0.07414} \right)^{1/1.00755} = \left[13.48(\log \frac{V}{V_0}) \right]^{0.992} \tag{3.17}$$

   As a result, the total crack length a (see Figure 3.22) at a given time is equal to:

$$a = a_0 + \Delta a \tag{3.18}$$

   where the initial crack length a_0 is a sum of 14 mm and $a_{precrack}$, i.e.

$$a_0 = a_{precrack} + 14 \tag{3.19}$$

2. Next, the data processing is used to fit the values of a via polynomial function, such that:

$$a_{fit}(t) = a_0 + a_1 t + a_2 t^2 + a_3 t^3 ..., \frac{da_{fit}}{dt} = a_1 + 2a_2 t + ... \tag{3.20}$$

   The chosen polynomial fit simplifies the calculation of the crack growth rate $\frac{da_{fit}}{dt}$.

3. Finally, the K is calculated as:

$$K = \frac{P_i}{(BB_N W)^{1/2}} f\left(\frac{a_{fit}}{W}\right) \tag{3.21}$$

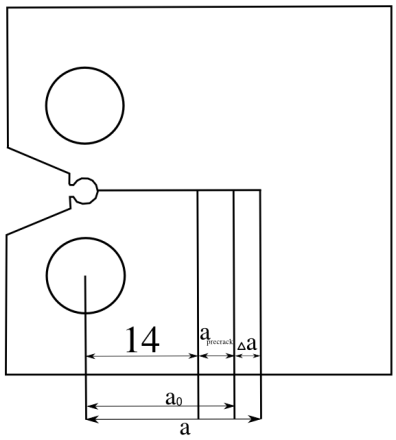

Figure 3.22: Schematic representation of the crack length in a CT specimen.

The examination of the experimental results of the 'Master' curve for Grade 2 *base* shows a trend in the evolution of K_{max}, which can be traced by connecting the points of the 'creep' curves corresponding to the beginning of the unstable crack propagation. The time-dependent cracking behavior can be observed. By taking a closer look at the test C5, three stages of the creep behavior can be distinguished (separated by two stars on the curve): up to 1000 s, the value of K does not change implying the absence of crack propagation. At the same time, the corresponding COD value shown in Figure 3.18 within the same time interval is slightly increasing. This increase can be presumably explained in terms of the crack tip opening displacement (CTOD) which is added in the COD measurement when the important plastic zone at the crack tip of the specimen is developed. The occurrence of the intense plasticity at the crack tip makes the crack behave as if it were longer than its physical size. The development of the important plastic zone can be due to the intense creep at the crack tip. At 1000 s, the slow stable crack propagation starts which is confirmed by the increased value of K in Figure 3.23 and the accelerated growth rate of the COD in Figure 3.18. At 50000 s, a maximum value of toughness K_{max} is achieved and the unstable crack propagation occurs leading to the final failure of the specimen. The above described 3-stage behavior is obtained for almost all creep curves. It is interesting to note that K_{max} can be only partly traced for some curves on Grade 4 *base* (see Figure 3.24) which shows poor reproductibility of the experiments (for example two tests C3 and C4 at 17 kN).

The experimental curves R1 and R2 corresponding to the sustained displacement tests for both grades are separated into two parts: the first part where K decreased due to softening of the material connected with the crack propagation, and the second part in green color where the propagation of the crack is slowed down (the PD signal is stabilized) and further decrease in K occurs due to stress relaxation. The estimated value of K_{th} from the R1 test is about 44 MPa$\sqrt{m}$ and 37.5 MPa$\sqrt{m}$ from the R2 test for Grade 2 *base*. This difference is governed by the hardening induced by the initial load. In the constant load test, the lowest reached value of a threshold approaches to 43 MPa$\sqrt{m}$ (test C7). The greater resistance to SLC is observed for Grade 4 *base*. Both R1 and R2 curves showed K_{th} close to 53-54 MPa$\sqrt{m}$. The lowest attained K_{th} value in the C6 test is 57 MPa$\sqrt{m}$. The summary of the estimated K_{th} values for *base* materials is given in Table 3.6.

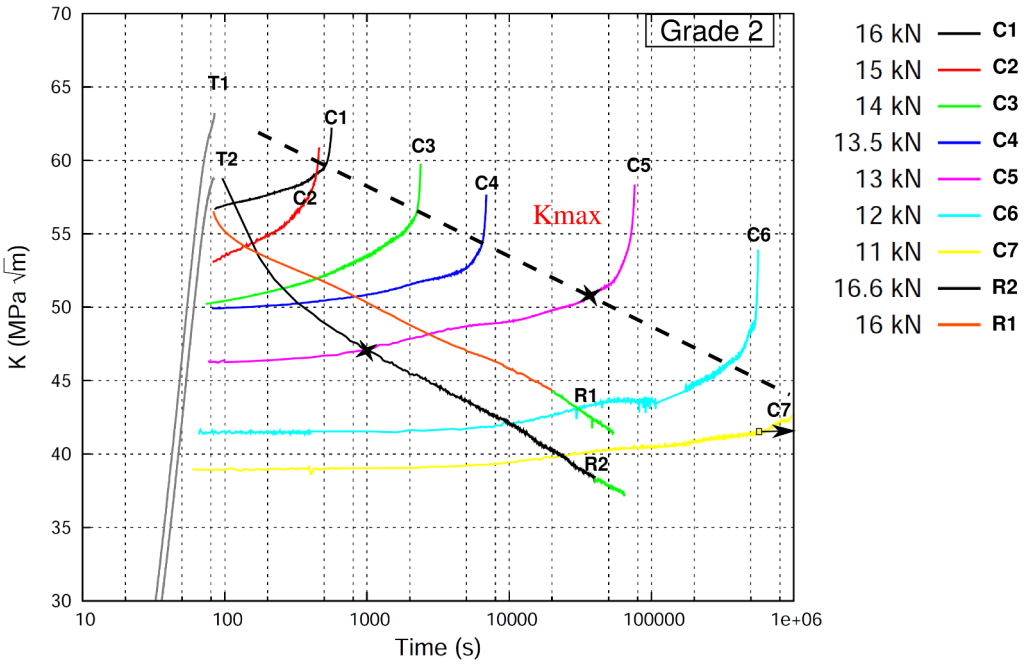

Figure 3.23: Master curve for Grade 2 *base*.

Test No.	Max load, kN	Duration, h	$a_{precrack}$, mm
Toughness test			
T1	18.36		1.74
T2	16.5		2.0
SLC constant load tests			
C1	16	0.15	2.9
C2	15	0.11	3.003
C3	14	0.6	3.075
C4	13.5	2	3.515
C5	13	21	3.00
C6	12	168	2.74
C7	11	264	3.0
SLC constant displacement tests			
R1	16.6	18	2.56
R1	16	15	2.9

Table 3.4: Sustained load cracking and fracture toughness tests using CT specimens for Grade 2 *base*.

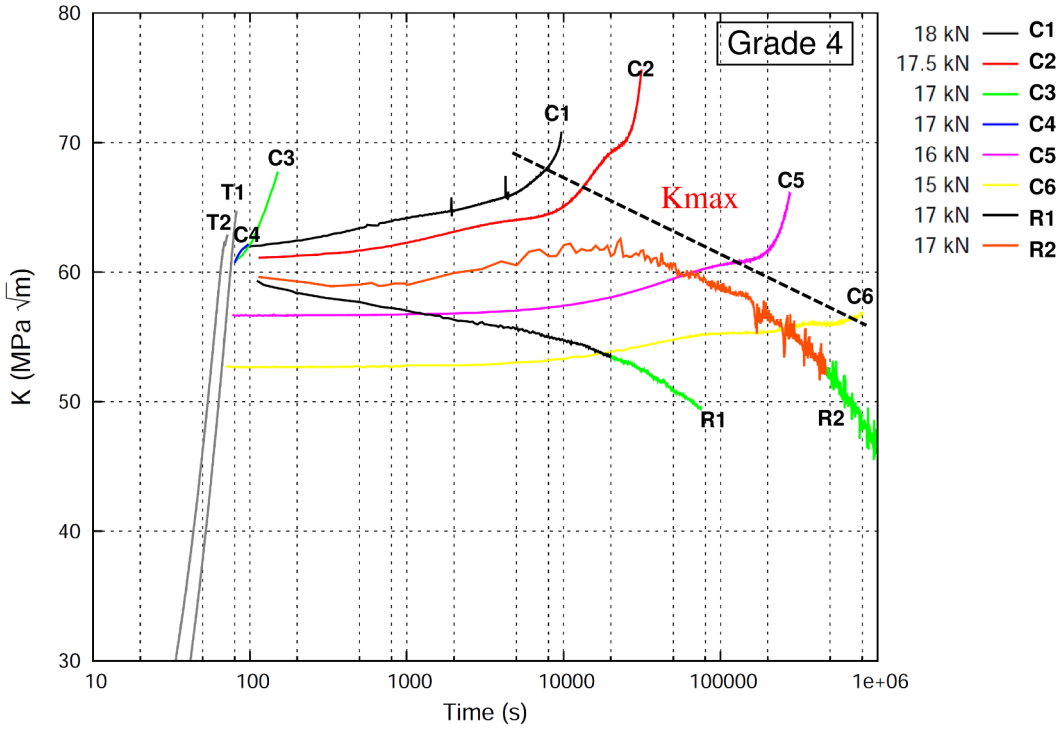

Figure 3.24: Master curve for Grade 4 *base*.

Test No.	Max load, kN	Duration, h	$a_{precrack}$, mm
Toughness test			
T1	19.7		2.10
T2	18.6		2.31
SLC constant load tests			
C1	18	3.5	2.30
C2	17.5	8	2.57
C3	17	0.04	2.72
C4	17	0.03	2.95
C5	16	77	2.73
C6	15	192	2.8
SLC constant displacement tests			
R1	17	21	2.49
R2	17	336	2.21

Table 3.5: Sustained load cracking and fracture toughness tests using CT specimens for Grade 4 *base*.

Test type	K_{th}, MPa$\sqrt{m}$	K_{th}/K_{max}
Grade 2 *base*		
C7	43	0.75
R1	44	0.77
R2	37.5	0.66
Grade 4 *base*		
C7	57	0.91
R1	54	0.86
R2	53	0.84

Table 3.6: Estimated value of the threshold for sustained load cracking K_{th} for Grade 2 *base* and Grade 4 *base*.

It can be seen that in general Grade 4 *base* with higher oxygen and hydrogen level exhibited better sustain load performance comparing to Grade 2 *base*. Grade 2 *based* showed the worst SLC performance with a minimum K_{th} value around 37.5 MPa$\sqrt{m}$ (R1 test), which corresponds to a 34% decrease compared with K_{max}.

The experimental curves of the SLC tests under constant load for Grade 2 *charged* in the coordinates COD vs. time to failure are presented in Figures 3.25. The sustained cracking behavior for Grade 2 *charged* shows a large scatter of time to failure vs. initial loading. So as, for example, the specimen held at 14 kN (red curve) was broken in 1 hour comparing to the one kept at the higher load of 15 kN (black curve) which did not break after 53 hours of test. This specimen was later broken by applying the rapidly rising load. Such a difference in the fracture kinetics can be explained on one hand by the longer length of the initial crack for 14 kN-specimen a_0 (see Table 3.7) which is reflected by the difference in COD level for both curves. On the other hand the amount of hydrogen introduced into material during the charging procedure could also accelerate crack growth in 14 kN-specimen. The chemical analysis showed that 14 kN-specimen contains 33 ppm of hydrogen, while 15 kN-specimen contains 14 ppm. At 33 ppm the solubility limit of hydrogen in Grade 2 is reached and thus the hydrides which make material more brittle could be formed. At the same time, note that the specimen tested at 13 kN (blue curve) failed after 25.8 hours and the specimen tested at 15 kN (black curve), as mentioned above, did not break after 53 hours. Both specimens have the same initial value of COD implying the same initial crack length. However, the post-mortem measurements of the precrack length showed that $a_{precrack}$=3.2 mm for 13 kN and $a_{precrack}$=2.604 mm for 15 kN which would explain the shorter time to failure of 13kN-specimen. The observed discrepancy can be due to the plasticity which takes place at the crack tip leading to the crack tip blunting prior to crack growth initiation. If assuming that hydrogen up to its solubility limit promotes creep at the crack tip in Ti, then the crack tip opening displacement (CTOD) concept should be used by applying the plastic zone correction on COD measurements. In this case the 15 kN-specimen with a shorter initial crack but higher hydrogen content (14 ppm) has the same COD as the 13 kN-specimen with a longer initial crack but lower hydrogen content (10 ppm). For chemical composition see Table 3.7. Note that not all specimens were submitted to chemical composition analysis. Complementary analysis with a scanning electron microscopy (SEM) could be useful to detect if hydrides can be observed at crack tip on all these specimens.

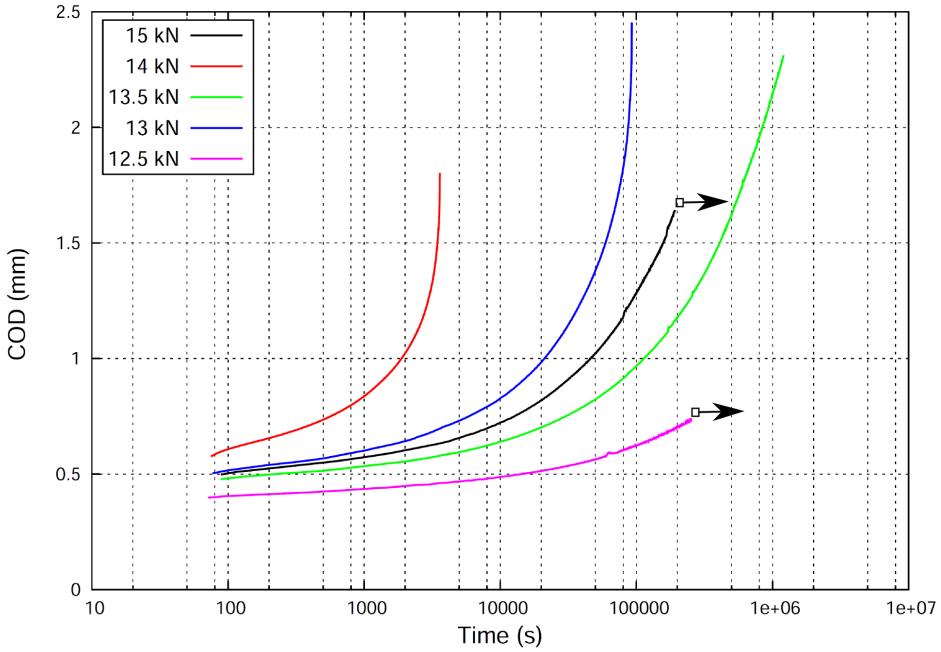

Figure 3.25: Experimental curves of SLC under constant load for Grade 2 *charged*. Arrows indicate specimens removed from test before failure.

The experimental curves of the sustained displacement tests carried out for Grade 2 *charged* are presented in Figure 3.26. Again, very strong load fluctuations can be observed in the Test1 which was tested on a different 250 kN MTS machine.

Analysis of the experimental results of the SLC tests under constant load for Grade 4 *charged* (see Figure 3.27) is limited by the lack of information about the slow cracking kinetics and failure time for two specimens tested at 17 and 15 kN. These both specimens did not break after 2 and 6 days of testing respectively and had to be broken by applying the rapidly rising load due to the lack of time devoted to the experimental studies.

The experimental curves of the sustained displacement tests carried out for Grade 4 *charged* presented in Figure 3.28 show two different kinetics of stress relaxation of the specimen loaded to the same level of load. The faster relaxation kinetics of Test1 can be due to the longer initial crack length.

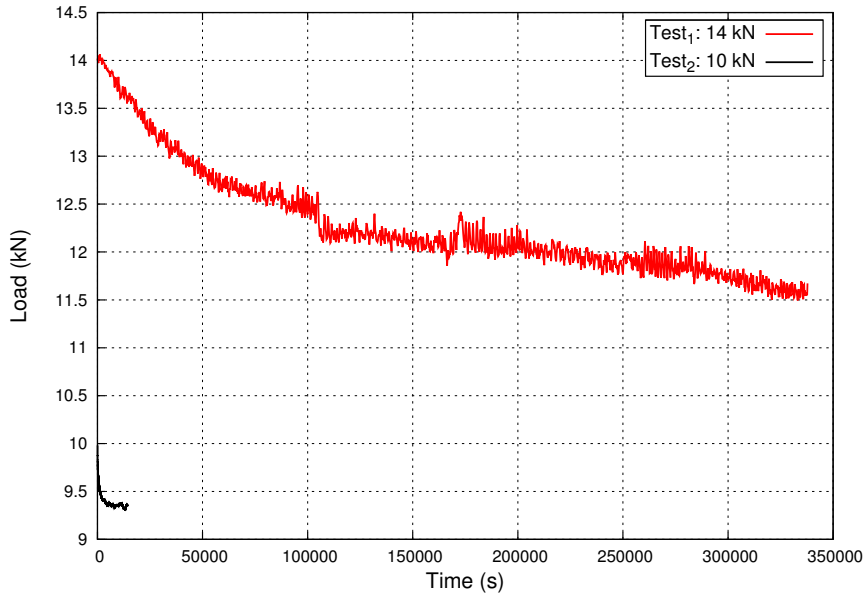

Figure 3.26: Experimental curves of SLC under constant displacement for Grade 2 *charged*.

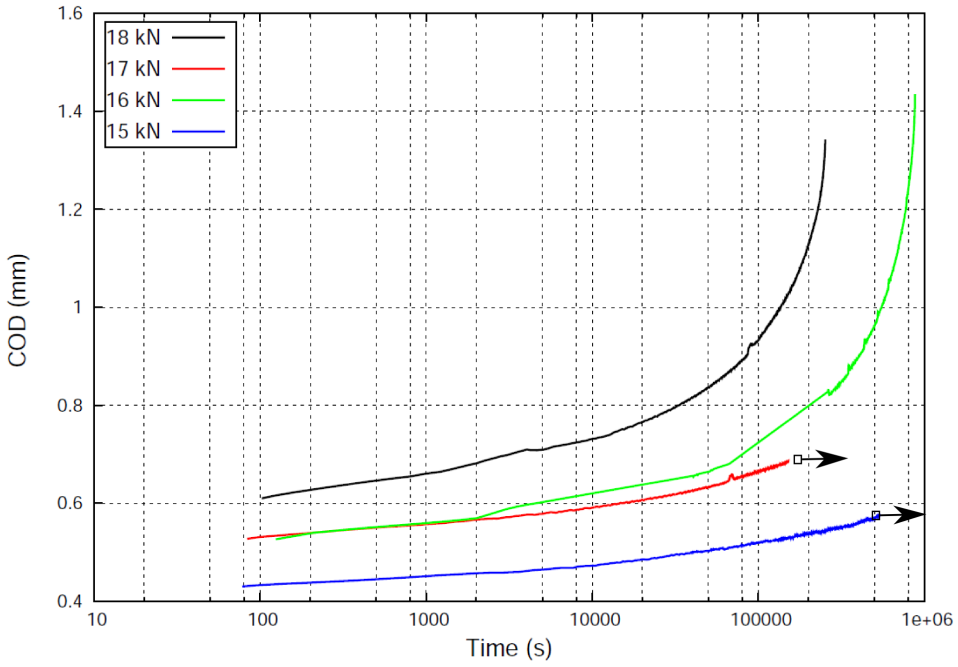

Figure 3.27: Experimental curves of SLC under constant load for Grade 4 *charged*. Arrows indicate specimens removed from test before failure.

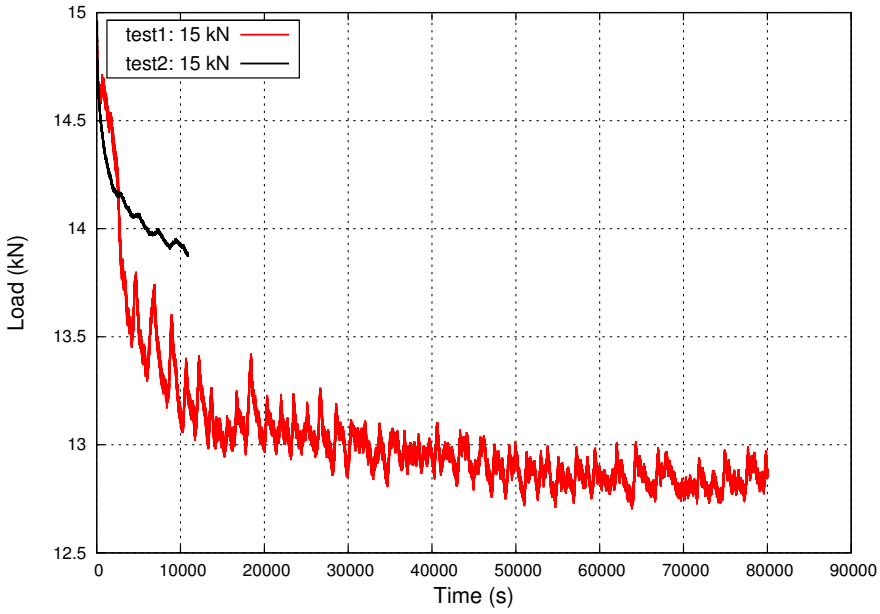

Figure 3.28: Experimental curves of SLC under constant displacement for Grade 4 *charged*.

Based on the presented results, the 'Master' curves were plotted for Grade 2 *charged* and Grade 4 *charged* (Figures 3.29 and 3.30). Compared to Grade 2 *base* 'Master curve', a meaningful analysis of the results of Grade 2 *charged* is more difficult. No clear trend can be drawn about the K_{max} evolution with time. The crack growth in the specimen C2 with the lower initial K is faster than in the C1 specimen showing the higher K level. The same discrepancy is observed for the specimen C3 which did not break after 14 days of sustained load at 13.5 kN and specimen C4 subjected to the lower load of 13 kN and broken after 25.8 hours. It is interesting to note that in the tests under constant load, specimens C1 and C2 were able to reach a higher level of K_{max} compared to the specimen T1 tested in a fast cracking test. Such a discrepancy can be conditioned by the large dispersion in hydrogen content level in the specimens (see Table 3.7) which make it very difficult to compare experiments between them. Hydrogen up to its solubility limit (22-25 ppm for Grade 2 and 29 ppm for Grade 4) can lead to the enhanced creep at the crack tip (hydrogen enhanced localized plasticity mechanisms) while beyond this limit it can participate in the hydrides formation. Both mechanisms have an opposite effect in terms of ductility of the material and thus the obtained results in Figure 3.29 should be carefully analyzed. The large dispersion of the results can be also due to the difference in the initial crack length of the specimens.

The trend of evolution of K_{max} for Grade 4 *charged* is more clear, however an important scatter of a deduced K_{th} value from the R1 and R2 tests can be observed. As in the case of Grade 2 *charged*, C1 and C2 tests showed higher K_{max} compared to the fast cracking test T1.

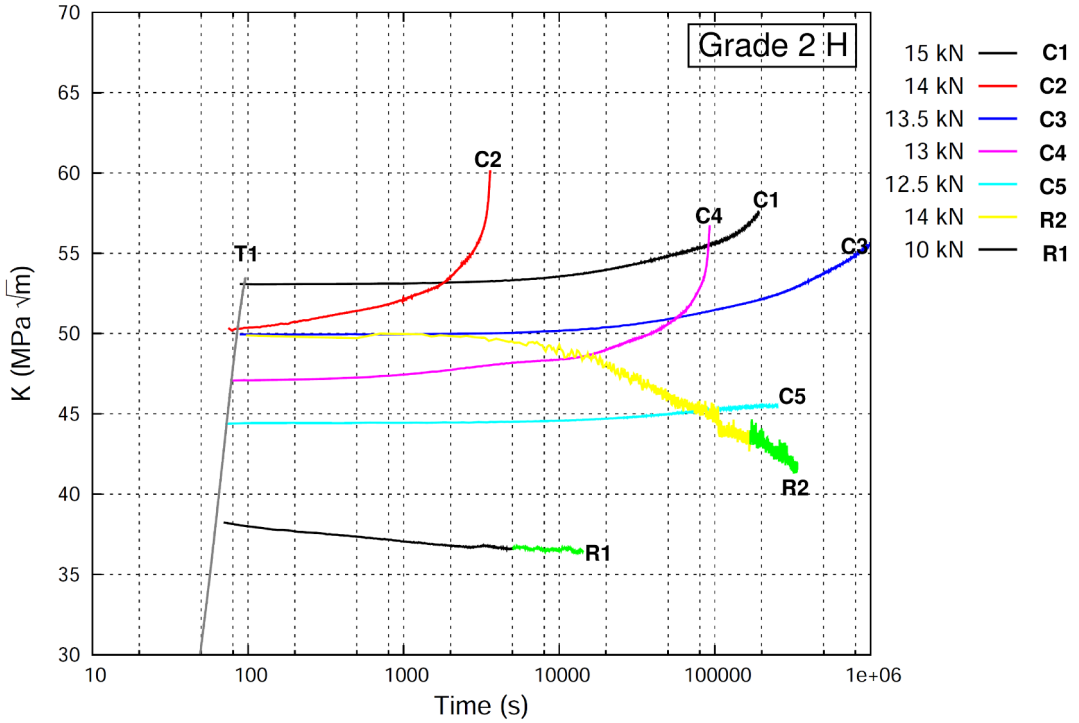

Figure 3.29: Master curve for Grade 2 *charged*

Test No.	Max load, kN	Duration, h	$a_{precrack}$, mm	Hydrogen content, ppm
		Toughness test		
T1	16.72		3.12	17
		SLC constant load tests		
C1	15	53	2.604	14
C2	14	1	3.0	33
C3	13.5	335.5	3.00	33
C4	13	25.8	3.2	10
C5	12.5	70	2.71	
		SLC constant displacement tests		
R1	10	4	3.95	
R2	14	96	3.2	

Table 3.7: Sustained load cracking and fracture toughness tests using CT specimens for Grade 2 *charged*.

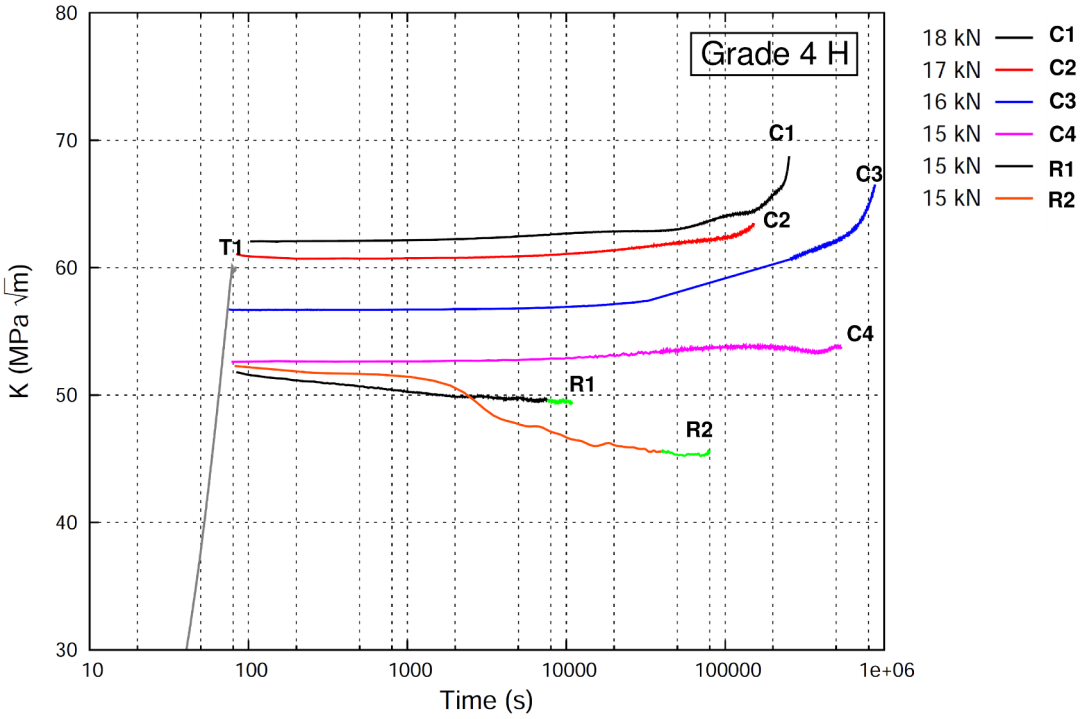

Figure 3.30: Master curve for Grade 4 *charged*

Test No.	Max load, kN	Duration, h	$a_{precrack}$, mm
Toughness test			
T1	16.8		2.7
SLC constant load tests			
C1	18	70	2.64
C2	17	42	2.5
C3	16	243	2.65
C4	15	149	2.6
SLC constant displacement tests			
R1	15	3	2.89
R2	15	22	1.73

Table 3.8: Sustained load cracking and fracture toughness tests using CT specimens for Grade 4 *charged*.

Table 3.9 summarizes the experimentally obtained ratio of K_{th}/K_{max} for materials charged with hydrogen. Grade 2 showed an improvement in resistance to SLC with increased hydrogen content, while the K_{th} of Grade 4 is very scattered and does not allow to draw any direct conclusions.

Test type	K_{th}, MPa$\sqrt{m}$	K_{th}/K_{max}
Grade 2 *charged*		
C5	45.5	0.84
R1	36.5	0.67
R2	44	0.81
Grade 4 *charged*		
C4	54	0.9
R1	50	0.83
R2	45.5	0.75

Table 3.9: Estimated value of the threshold for sustained load cracking K_{th} for Grade 2 *charged* and Grade 4 *charged*.

The comparison of the SLC behavior for *base* and *charged* materials is presented in Figure 3.31- 3.32. As can be seen for both grades, slow crack growth occurred much more rapidly in the *base* material with lower hydrogen content. One possible explanation of the beneficial effect of hydrogen on subcritical crack growth can be connected with the hydrogen-induced softening of the material due to the promotion of creep at the crack tip. In this case, the increased creep strain at the crack tip can decrease the susceptibility to hydrogen embrittlement in the material. The improvement of the resistance to subcritical crack growth in the material with higher quantities of hydrogen was observed by Williams [215] on Ti-6Al-4V. Furthermore, second-stage creep rate was observed to decrease significantly with increasing hydrogen content. Assuming that hydrogen embrittlement requires a finite amount of plastic deformation at the crack tip, it was postulated that the increased creep resistance offsets the increased susceptibility to embrittlement at higher hydrogen contents.

The results of fast cracking tests show a beneficial effect of oxygen and detrimental effect of hydrogen on K_{max}. Both grades of CP α Ti exhibited a very strong strain rate sensitivity (see Figure 3.13). The experiments of sustained cracking test show that materials with high oxygen level (Grade 4 *base* and *charged*) exhibit greater resistance to SLC. Increasing the hydrogen content results in the increase of the resistance to slow cracking.

Throughout the experimental study it was demonstrated that the rate-dependent fracture behavior is extremely sensitive to many factors, including the initial crack length. In order to understand the impact of a hydrogen content modification on the mechanical behavior of a given titanium alloy for a specific load, well controlled experiments with only one parameter changed at a time are necessary. That is why the additional numerical study will be performed in the next chapter in order to investigate the influence of viscoplasticity and hydrogen content on slow and fast cracking behavior at room temperature of CP Ti. The experimental results can be interpreted only by mean of Finite Element (FE) simulation taking into account the viscoplastic behavior of Ti. This is the object of the next Chapter 4.

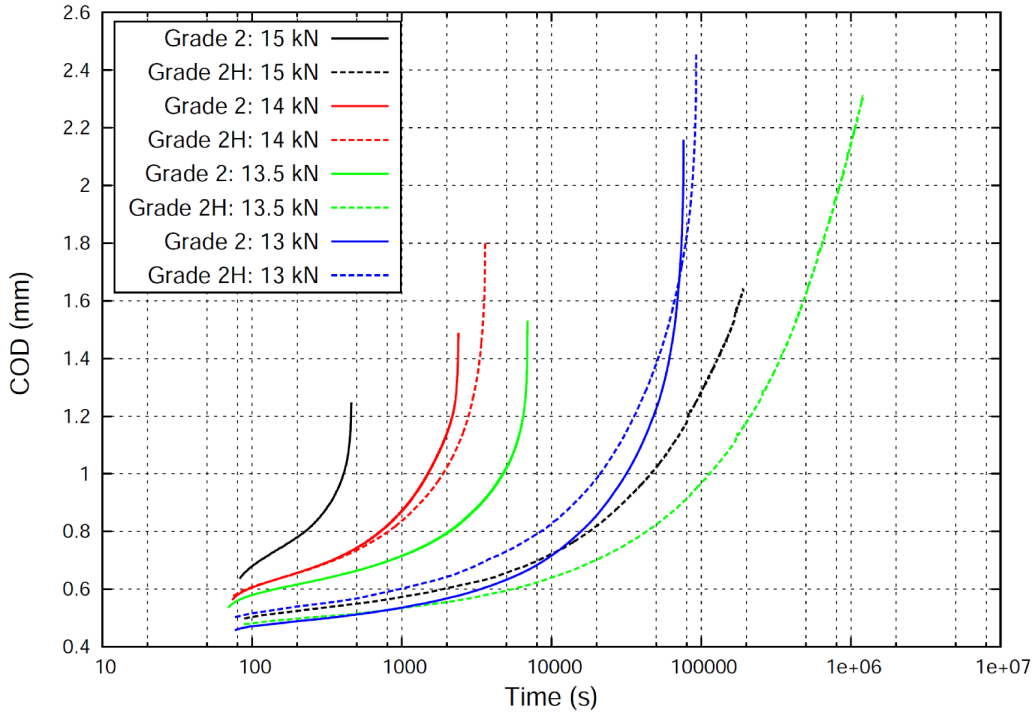

(a)

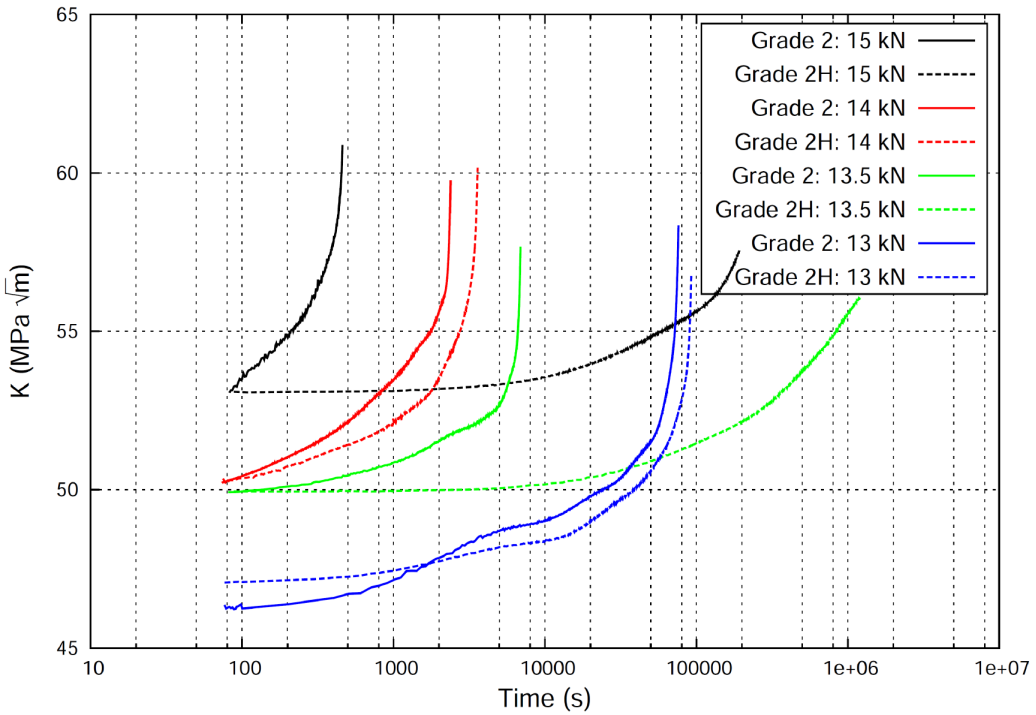

(b)

Figure 3.31: The evolution of: (a) crack opening displacement (COD) vs. time, (b) stress intensity factor vs. time for Grade 2 *base* and Grade 2 *charged*.

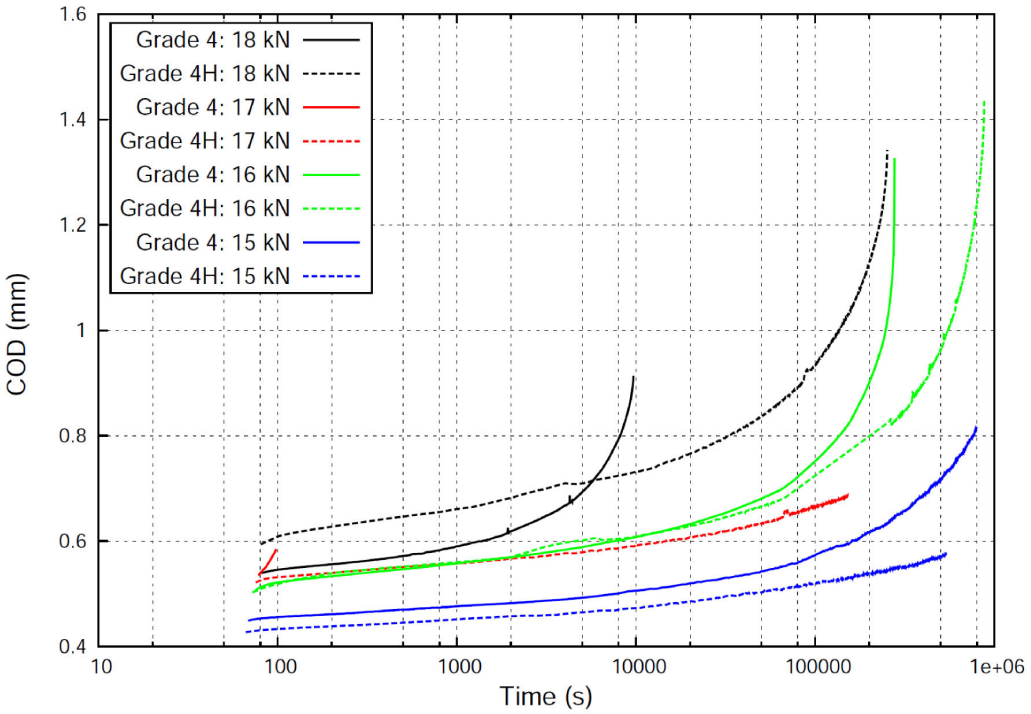

(a)

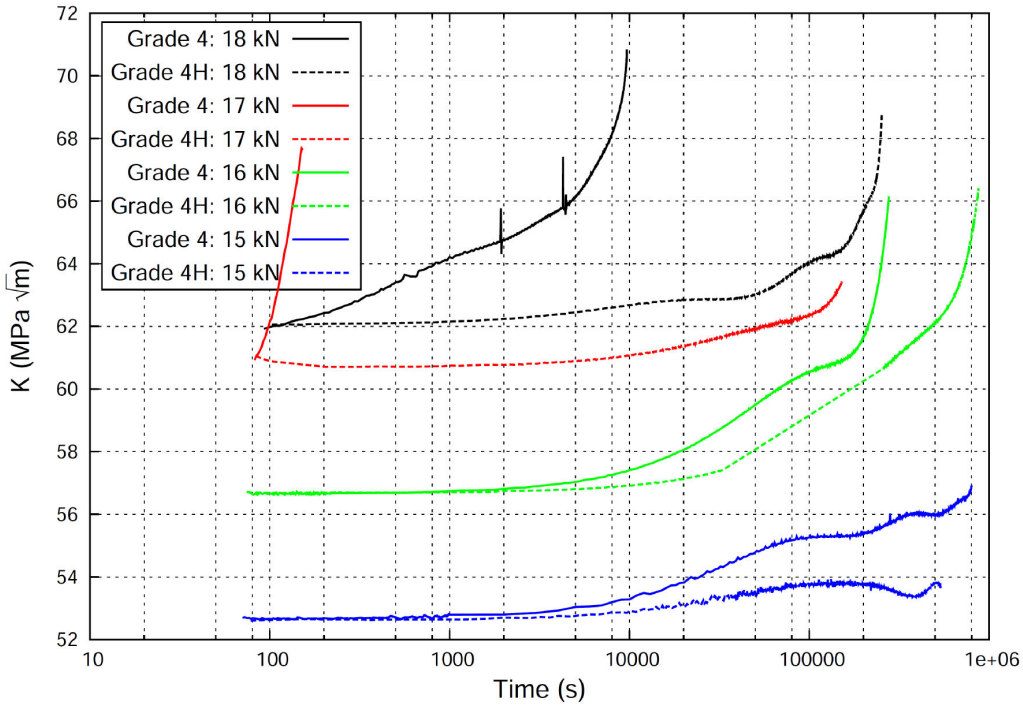

(b)

Figure 3.32: The evolution of: (a) crack opening displacement (COD) vs. time, (b) stress intensity factor vs. time for Grade 4 *base* and Grade 4 *charged*.

3.3.3 Fractography

Optical microscopic observations of the initial microstructures presented in Figure 3.34 shows that Grade 2 *base* (b) consists of equiaxed primary α-grains of a diameter being $\sim$ 40 μm in DL-DT direction. Grade 4 *base* in Figure 3.34 (a) shows equiaxed α+β structure with the primary α grains of $\sim$ 45 μm. The β-phase is mostly situated at the grain boundaries and the triple junctions.

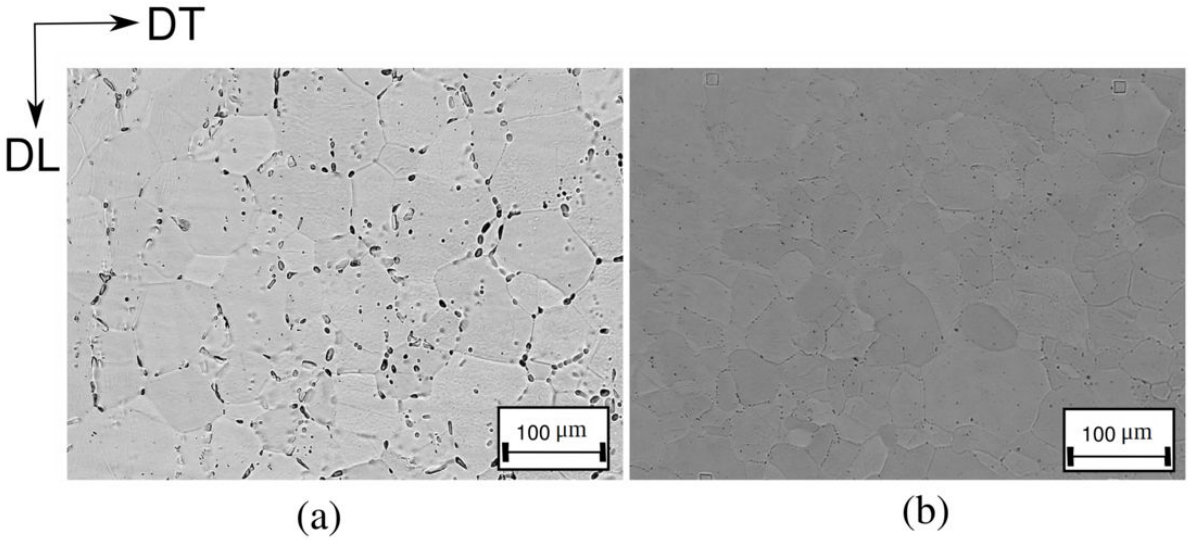

Figure 3.33: Microstructures of a cold-rolled and annealed α Ti of (a) Grade 4 *base* (b) Grade 2 *base* [17].

Generally a straight crack front is maintained during the tests due to the machined side grooves on the CT-specimen. As a result, the crack length was calculated by taking the mean of nine measurements at equidistant points across the thickness of the specimen without any special correction accounted for the crack curvature. Optical microscopic observations showed four distinct fracture zone in the SLC experiments: (1) machined notch; (2) precrack in fatigue; (3) SCL crack growth; (4) Unstable final crack propagation.

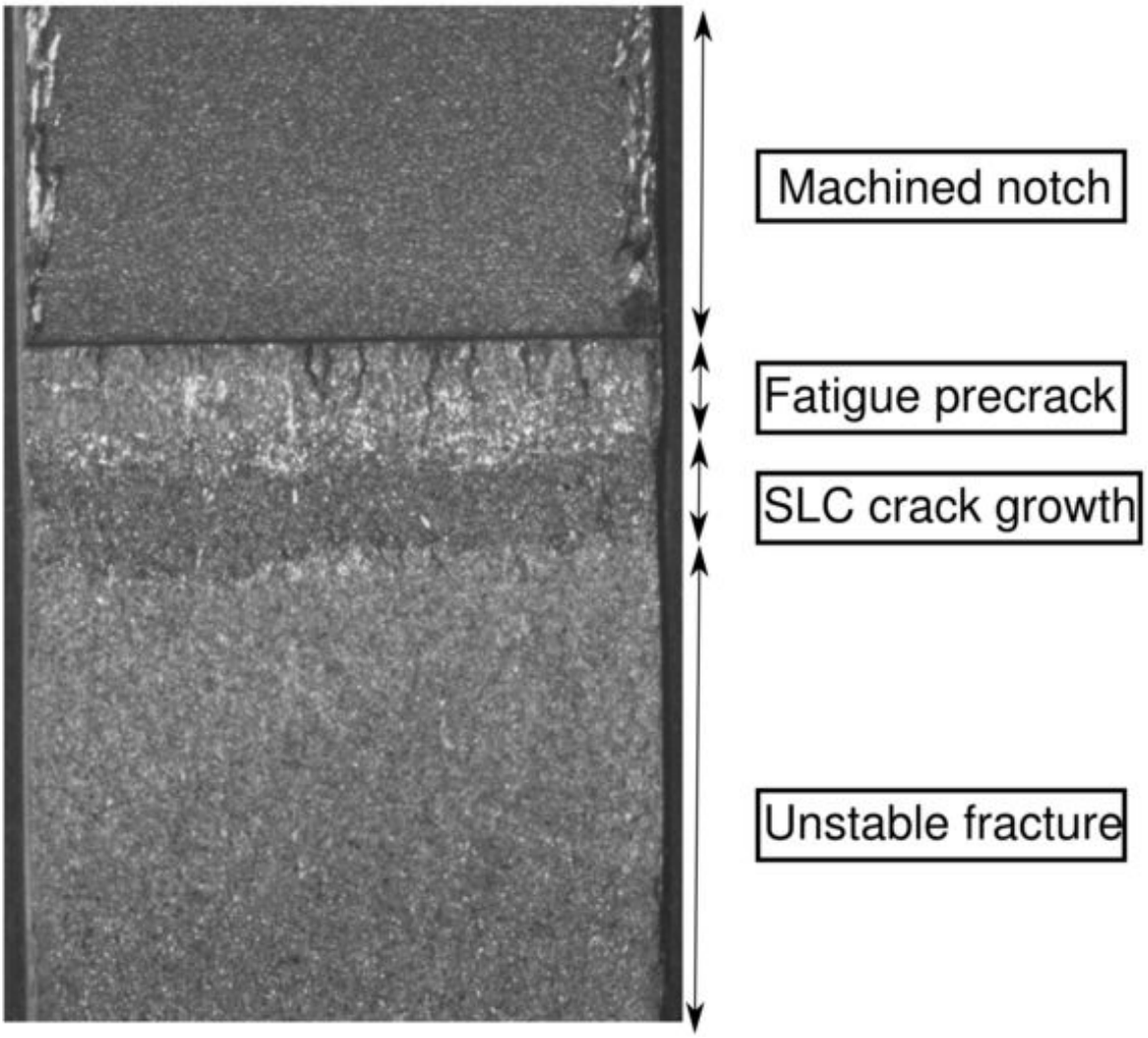

Figure 3.34: Optical microscopic observations of the fracture surface of α Ti of Grade 4 *base* showing four distinc zones.

The fracture surfaces of the fracture toughness specimens were examined in a scanning electron microscope (SEM). It is known from the literature [161, 137], that fracture behavior in HCP metals is significantly dependent on crystallographic orientation, therefore it is important to analyze the activated slip systems during the crack propagation. The schematic illustration of the examined fracture surface in Figure 3.35 shows that the basal (0001) plane is perpendicular to the crack plane, and the c-axis is nearly perpendicular to the loading direction, implying that the grains were oriented for easy prismatic $< a >$ slip.

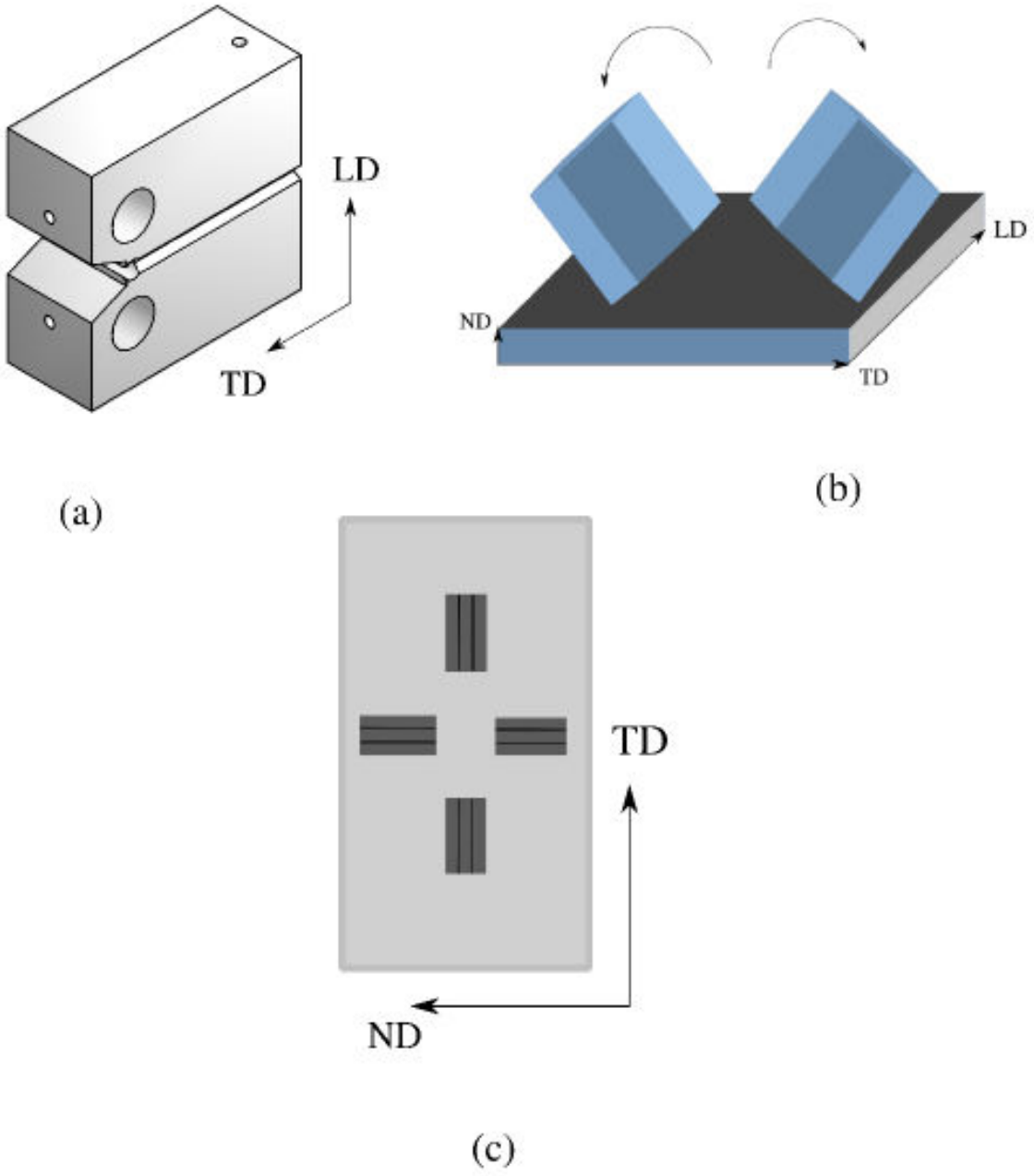

Figure 3.35: Schematic illustration of the examined fracture surface.

Fractography of fracture toughness test specimens revealed readily distinguishable zones of fatigue precracking and final unstable crack propagation. The zone of precrack show smooth flat cleavage facets accompanied by the tear ridges (see Figure 3.36). These ridges represent the boundaries where different planes on the fracture surface have met up. Sometimes secondary cracks are initiated from the ridges sites. The turn-off edges of cleavage plates are relatively angular, which suggests separation by a brittle cracking process [137].

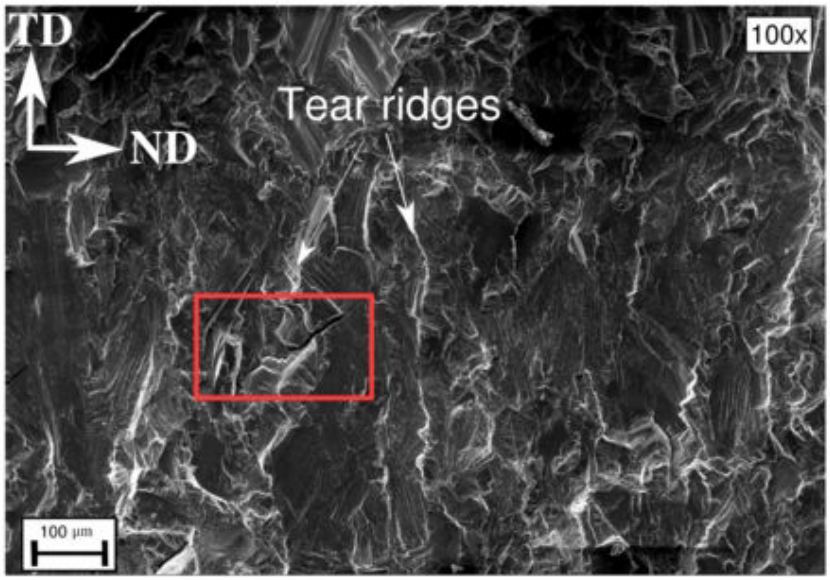

(a)

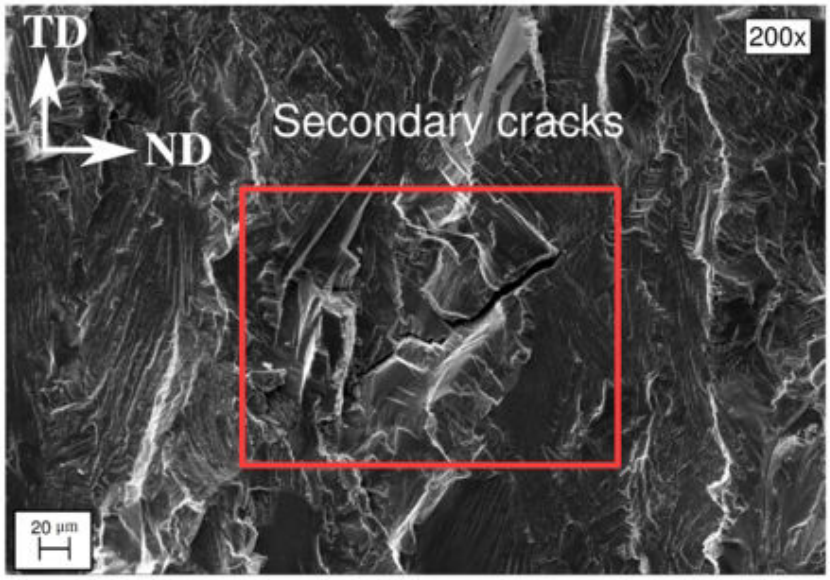

(b)

Figure 3.36: Scanning electron micrographs of fatigue precracking zone in Ti Grade 2.

In the zone of final failure of the specimen, one can observe shallow trough-like grooves called 'fluting', which consists of the ruptured halves of hexagonal shaped voids (Figure 3.37). This is a typical feature of stress-corrosion cracking (SCC) fracture surfaces of α and $\alpha - \beta$ alloys, that was equally observed in the specimens tested under sustained load cracking (SLC) in inert environment and mechanical overload conditions [137]. Flutes are created through the coalescence of elongated tubular cavities (indicated with dashed line in the zone B). The propagation of the crack is due to the coalescence of these tubular cavities. Some groups of flutes are more fine and regular laying parallel to each other (zone A). Small rounded dimples are also detected in the rupture surface (zone C), but they were found to be less numerous than the elongated ones. An unusual hexagonal shape of the cavities is attributed to a lower symmetry of the hexagonal α phase. As a result, fluted fracture can be correlated with the underlying crystallographic orientation of the α phase [161]. In the literature flute formation in α Ti has been associated with a dislocation mechanisms involving extensive planar prismatic $\{10\bar{1}0\}$ $\langle 11\bar{2}0\rangle$ slip [3, 147, 60, 161]. In our case, the texture of the specimen promotes predominant activation of prismatic $< a >$ slip during the fracture process. It confirms a significant role of prismatic $< a >$ slip in the flute formation. Although flutes were observed both with cleavage and with some dimpled areas of fracture (in Grade 2 *base*), they are the manifestation of ductile fracture mode. Since the flute surfaces are $\{10\bar{1}0\}$ planes, then parallel slightly wavy lines frequently observed running lengthwise along the flute surface are mostly slip lines [147].

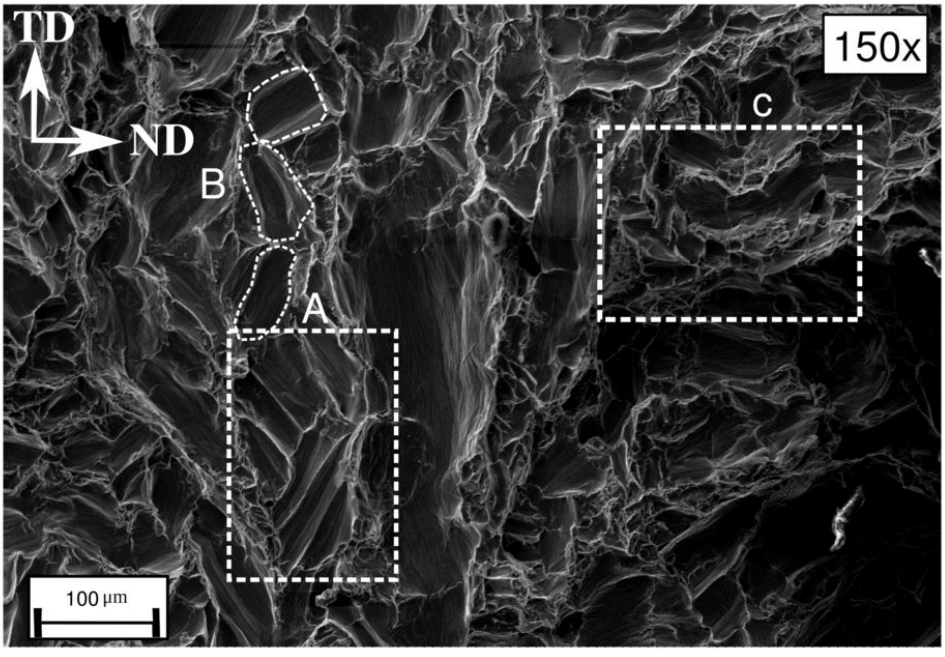

Figure 3.37: Scanning electron micrographs of unstable crack propagation zone in Ti Grade 2.

Fracture surface of Grade 4 presented in Figure 3.38 exhibits more flat brittle interface cracking with cleavage facets in the fatigue precracked zone and many flutes in the zone of overload cracking. The flute peak ridges in Grade 4 are less ragged smoother compared to Grade 2. It might be due to the higher content of oxygen in Grade 4 that is known to increase the difficulty of the occurrence of cross-slip what encourages in turn cleavage, leading to copious flutes formation [137]. The strong anisotropic crystallographic texture of Ti can also favor the formation of flutes if the basal (0001) plane which is the cleavage plane in HCP metals, is perpendicular to the crack plane [210]. It results in a cleaner appearance of the flute ridges of Grade 4.

Fluting, associated with cleavage, has been reported in many studies on titanium and zirconium [210, 3, 130, 60, 100], however in our fractorgaphic observations for both materials (Grade 2 and Grade 4) abundant fluting was detected without cleavage elements in the zone of overload cracking. It might be due to the orientation of the basal (0001) plane which is perpendicular to the crack plane, rendering flutes to be easily seen on the fracture surface of the specimen, while the cleavage facets stay hidden from view.

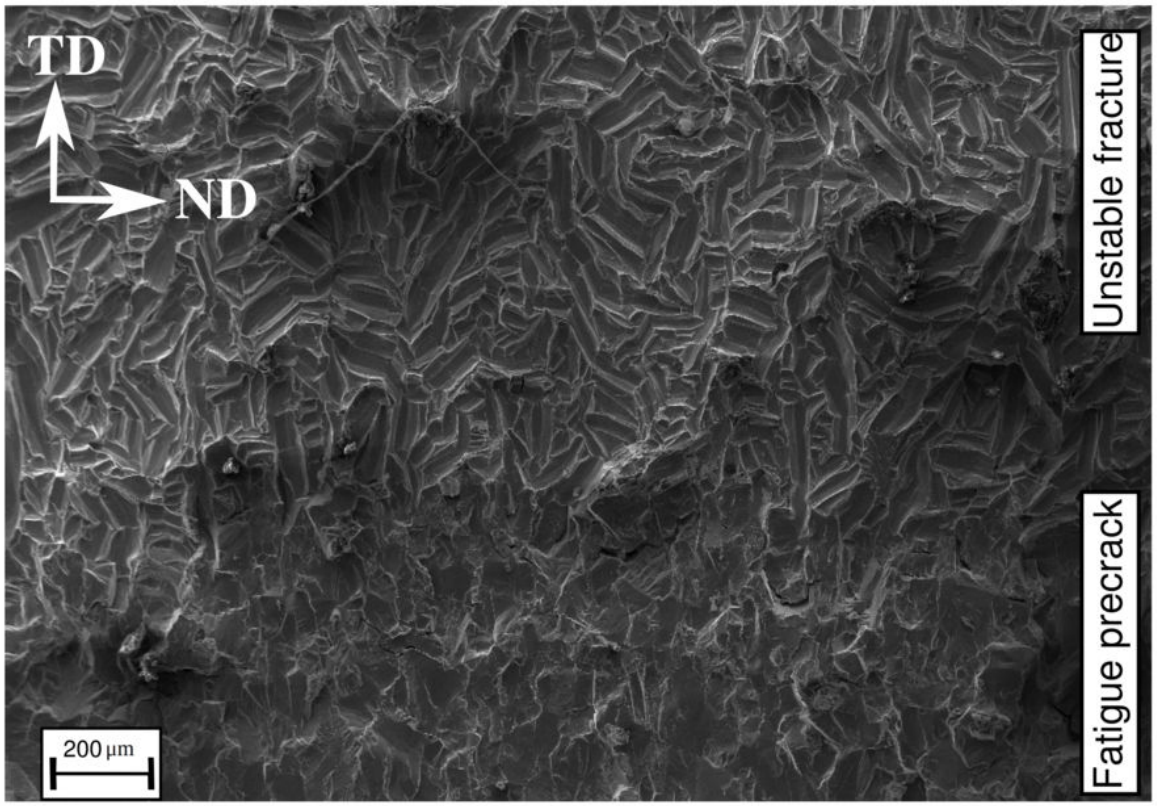

Figure 3.38: Scanning electron micrographs in Ti Grade 4.

The most probable mechanism of flute formation, proposed by Aitchison [3] and Wanhill [210] is schematically illustrated in Figure 3.39. Here two cleavage cracks have overrun each other, and the three-dimensional fracture process cannot be completed by cleavage only (since no orthogonal cleavage plane is available in the HCP α-phase). The flutes act in this case as a link between the different cleavage planes, enabling the fracture to progress through the material.

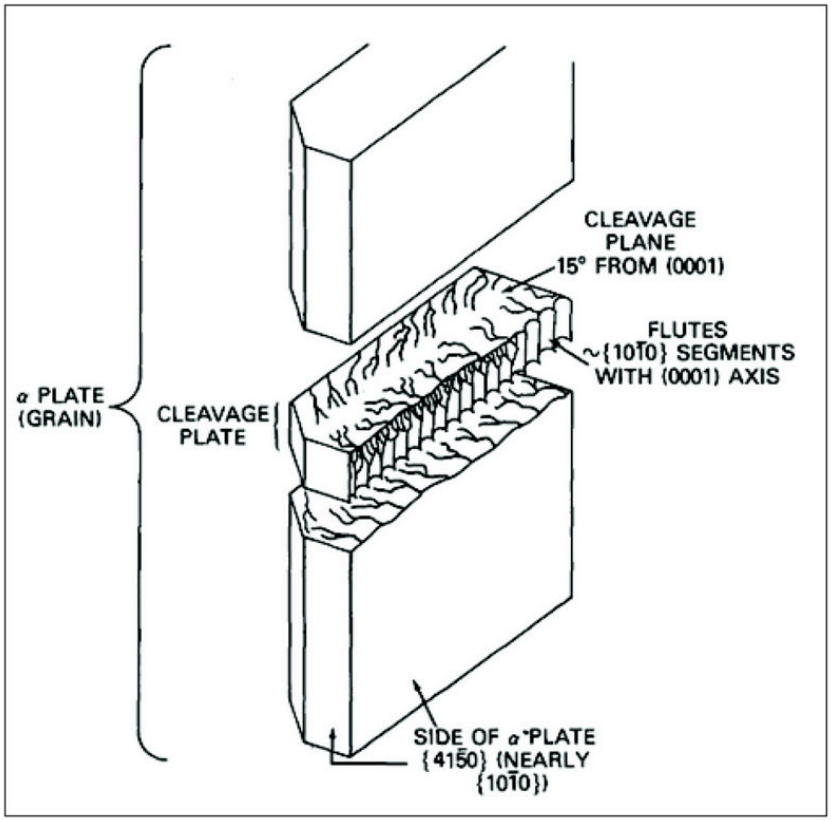

Figure 3.39: Sketch illustrating fluting formation mechanisms by tearing between two overlapping cleavage [137].

Fracture toughness surfaces of Grade 2 *charged* and Grade 4 *charged* were very similar to the observed surfaces of Grade 2 *base* and Grade 4 *base* respectively. Comparison of Figure 3.40 (a) and (b) shows that Grade 4 with a higher level in oxygen produces more regular flutes separated by smooth tear ridges (due to the higher level of oxygen in Grade 4 *charged*) comparing to Grade 2 *charged*. Interstitial hydrogen is known to cause cracking along $\alpha - \beta$ interfaces [93]. As a result, the presence of β phase in Grade 4 promotes secondary cracks in Grade 4 (zones A, B and C in Figure 3.40). In some instances, flutes are found in their cross-sectional view before separation occurred. This shape is hexagonal (zone D in Figure 3.40) which confirms that the walls of the flutes are $\{10\bar{1}0\}$ type planes [147].

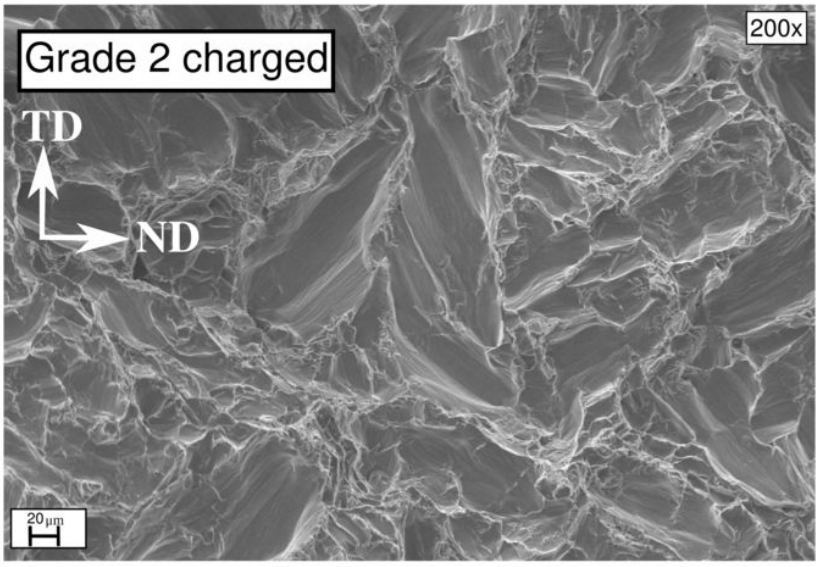

(a)

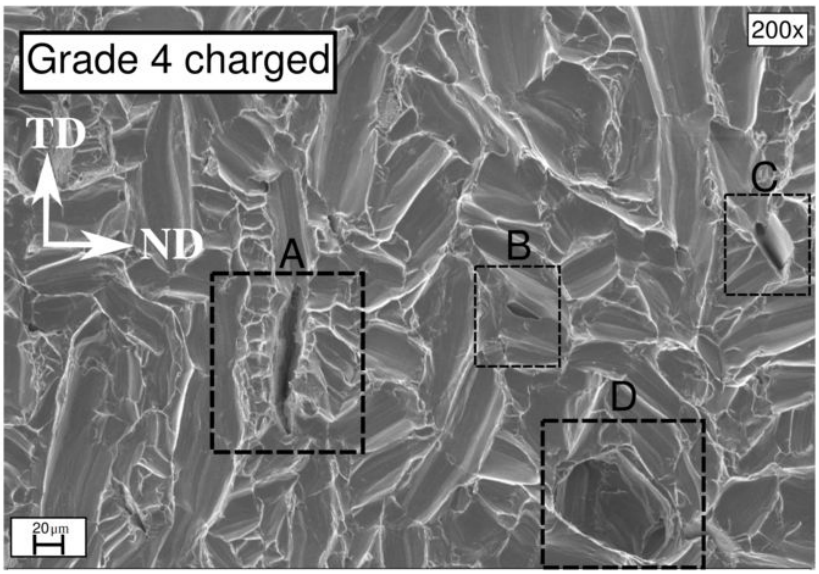

(b)

Figure 3.40: Scanning electron micrographs in Ti Grade 2 *charged* (a) and Grade 4 *charged* (b).

The examined SLC specimens of both Grade 2 and Grade 4 *charged* show three distinguished zones: zone of a precracking in fatigue, zone of slow extension of the crack and the final zone of fast crack propagation (see Figure 3.41). The close-up at all three zones of SLC specimen of Grade 4 *charged* in Figure 3.42(a) shows expected cleavage in the zone of fatigue precracked similar to all previous observations. The zone of slow crack extension due to SLC (Figure 3.42(b)) is characterized by the presence of extensive flutes and some cleavage zones when they are visible (zones A,B,C,D). Unstable crack propagation in Figure 3.42(c) is also showing a widespread fluted fracture, however these flutes are well formed with sharp lines dividing individual flutes from their neighbors compared to the less parallel and more ragged flutes in the SLC zone. Such variation in size and shape can be explained in terms of the kinetics of the cavity growth which is found to be plasticity controlled in HCP metals. During the fast crack propagation, a high global stress promotes nucleation of a large number of cavities in the β-phase regions (in case of Grade 4). These hexagonal cavities do not have enough time to grow, and thus they retain their tubular shape. During the slow crack propagation under sustained load, cavities have enough time to grow and eventually to coalescence, which leads to the evolved shape. Some interesting feature of the surrounded area in Figure 3.42(c) is most likely a β phase which does not cleave, and it constitutes a site for diversion of cracks (Ti Grade 4 consists mainly of α plates with interplate β-phase).

Studies of the fracture surfaces of all specimens show no obvious differences in fracture appearance induced by varying hydrogen content. All specimens showed mixed fracture with β regions fracturing by microvoid coalescence and the α phase fracturing by cleavage [136].

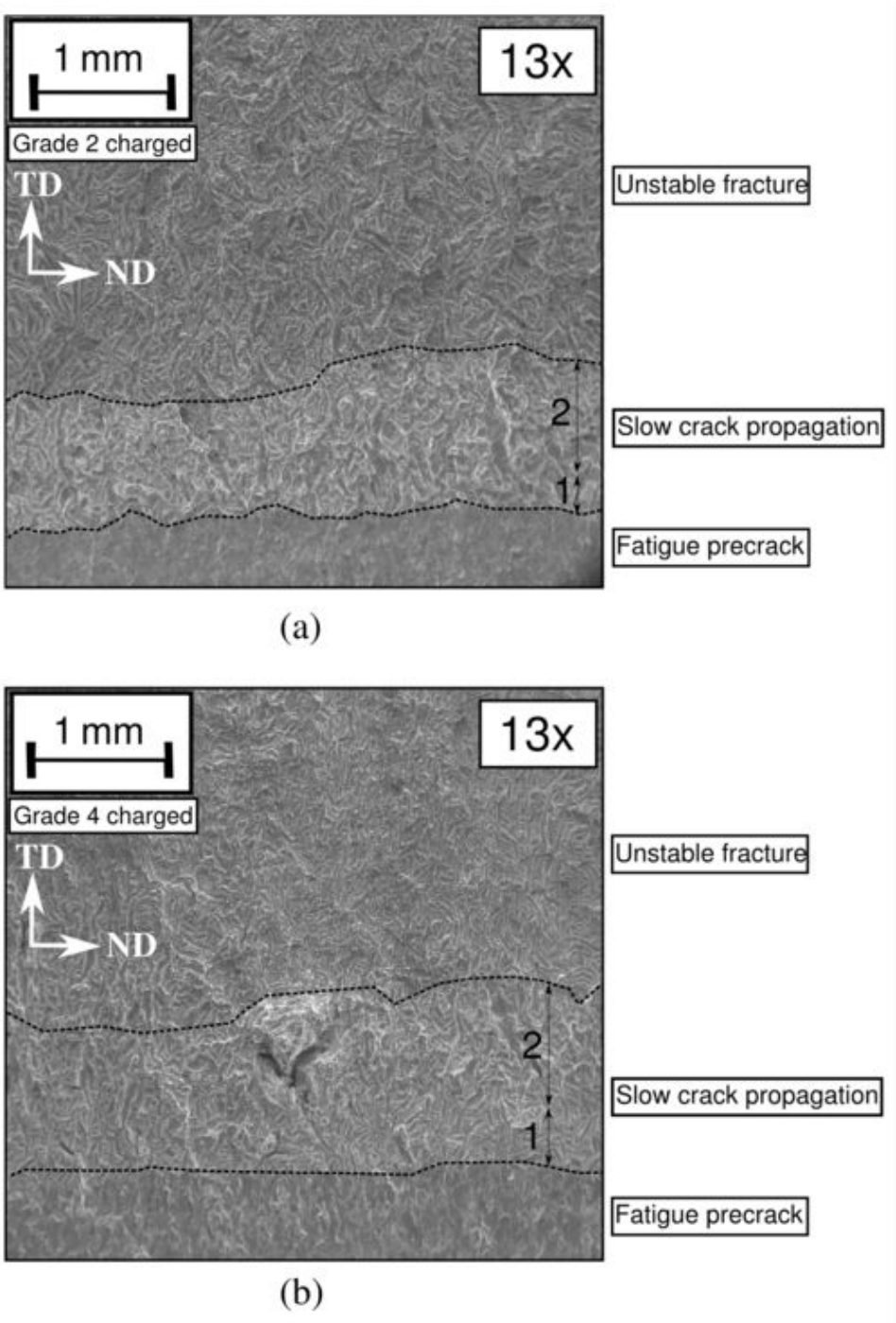

Figure 3.41: Fracture surface of SLC specimens of Ti: (a) Grade 2 *charged* and (b) Grade 4 *charged*.

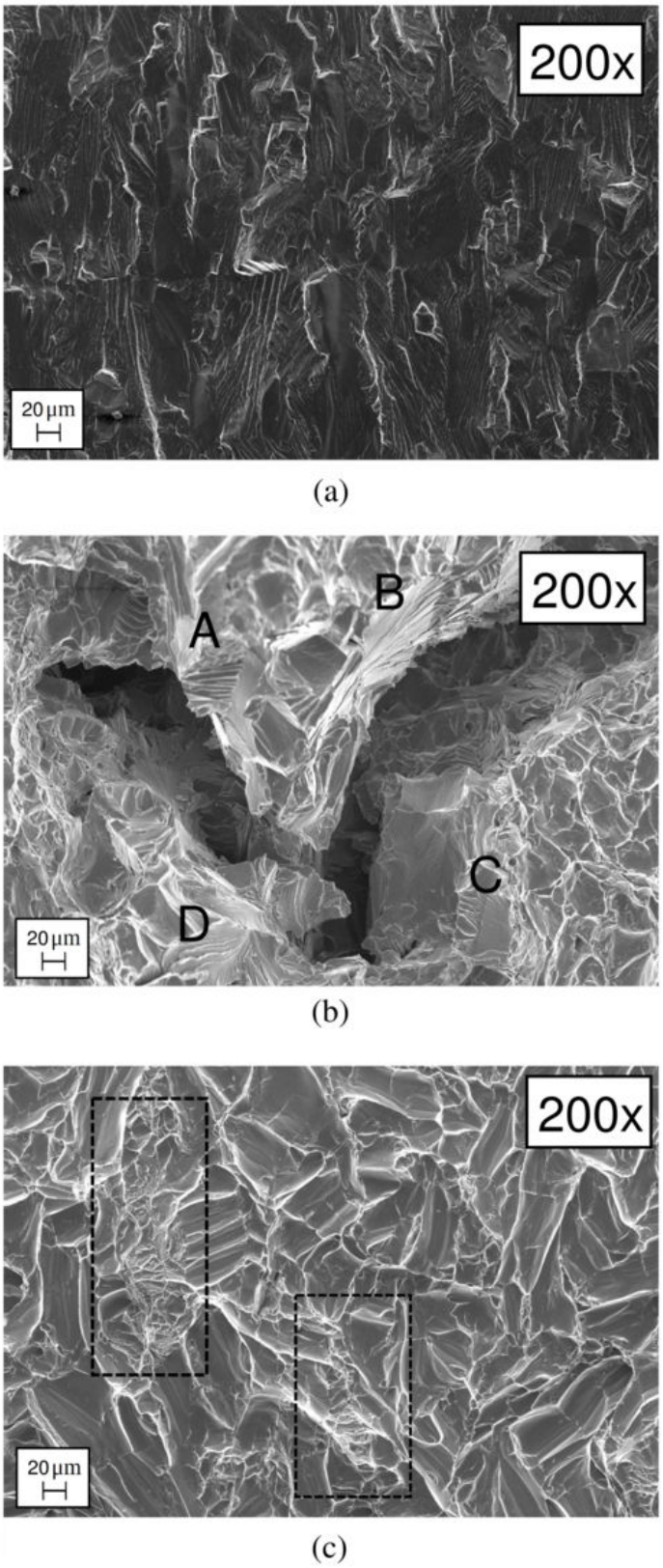

Figure 3.42: All three zones of SLC specimen of Grade 4 *charged*: (a) fatigue-precracked; (b) slow extension under sustained load; (c) rapid unstable cracking.

3.4 Conclusions

In the present chapter the unstable crack growth and the time-dependent failure under static loads in CP α Ti at ambient temperature were studied. Two grades of Ti with different oxygen content (Grade 2 and Grade 4) were submitted to hydrogen charging and degassing in order to obtain two different hydrogen contents for Grade 2 and three different contents for Grade 4. Fracture toughness and sustained load cracking tests followed by fractographic observations were performed on CT specimens, precracked in fatigue. Single-load strategy for SLC testing was employed with a rising and falling K. In a rising K test, CT specimen was held under constant load, and in the falling K test under a fixed displacement. The following conclusions are drawn from this investigation:

- The fast fracture behavior of Ti was slightly modified by the presence of low concentration of hydrogen. The obtained experimental results indicate that increased hydrogen content resulted in a slight decrease in strength and increase in ductility for both Grade 2 and Grade 4. The fracture toughness reported in terms of maximum load encountered during the test, K_{max}, was decreased as hydrogen content was increased for both grades. The comparison of Grade 2 and Grade 4 *base* and *charged*, showed that solute oxygen promotes a high strength in Grade 4 resulting in the higher toughness value.
- Sustained load cracking behavior is subject to modification by low concentrations of hydrogen: increasing the hydrogen content results in a greater resistance to slow cracking. Possible explanation of such beneficial effect of hydrogen is the hydrogen-enhanced localized plasticity at the crack tip which prevents the attainment of the high localized stresses necessary for fracture. It was also observed that materials with high oxygen level (Grade 4 *base* and *charged*) exhibit greater resistance to SLC.
- Fractographic examinations showed that both the SLC and fast fracture surfaces of all alloys contained examples of both cleavage and microductile fracture represented by fluting. Flute formation in α Ti is associated with a dislocation mechanisms involving extensive planar prismatic $\{10\bar{1}0\}$ $\langle 11\bar{2}0\rangle$ slip. Comparing to Grade 2 *base* and *charged*, the fracture surface of Grade 4 *base* and *charged* exhibits more flat brittle interface cracking with cleavage facets in the fatigue precracked zone and many regular flutes in the zone of overload cracking. It might be due to the higher content of oxygen in Grade 4 that is known to increase the difficulty of the occurrence of cross-slip what encourages in turn cleavage, leading to copious flutes formation. Studies of the fracture surfaces of all specimens showed no obvious differences in fracture appearance induced by varying hydrogen content in Grade 2 and Grade 4.
- Given the complexity associated with time-dependent fracture behavior of CP α Ti, viscoplasticity based FE simulation approach is needed to analyze the deformation and damage mechanisms and to model hydrogen-induced subcritical crack growth.

Chapter 4

Simulation of viscoplastic deformation and cracking in Ti

Résumé

Dans le but de comprendre les phénomènes observés lors de la campagne expérimentale et de prévoir le comportement du matériau dans les essais de ténacité et de la rupture différée, il est nécessaire de proposer un modèle du comportement du matériau étudié. Ce modèle de comportement s'articule autour de deux parties couplées tenant compte de différents phénomènes: le comportement viscoplastique du matériau et le comportement du modèle vis-a-vis de l'endommagement. Un modèle macroscopique élasto-viscoplastique anisotrope à écrouissage mixte a été adopté pour simuler la déformation des éprouvettes de type CT lors des essais de ténacité et de la rupture différée par éléments finis. La modélisation d'une ouverture monotone de la fissure sans prise en compte de la propagation de la fissure montre une large zone de déformation plastique en pointe de fissure. En supposant que l'hydogène est en équilibre avec la contrainte hydrostatique, on observe un pic de concentration d'hydrogène en pointe de fissure.
Un modèle cohésif de type Crisfield a été employé pour représenter la fissuration. Les résultats des simulations montrent que la fissuration intervient de manière trop précoce sans développement suffisant de la plasticité. Une approche alternative qui permet un couplage plus fort entre viscoplasticité et rupture est proposée.

Contents

4.1 Introduction

4.1.1 Local approach to fracture

The experimental results presented in the previous chapter clearly showed that the fracture resistance of CP α-Ti cannot be interpreted in terms of a single parameter, such as K_{Ic} used in Linear Elastic Fracture Mechanics (LEFM) where the variation of the stiffness of the material is assumed to be caused by crack extension only. Non Linear Fracture Mechanics (NLFM) with J_{Ic} or crack tip opening displacement (CTOD) cannot be used neither for the analysis of the fracture behavior of CP α Ti since this approach does only hold for time-independent processes. HRR field (Hutchinson-Rice-Rosengren) where a fracture criterion of J_c was proposed to play a role of K_{Ic} in NLFM is neither adopted for viscous materials. Fracture mechanics of creeping solids is using C^* as the equivalent of the J-integral is applied to metals at high temperatures and/or loaded at high strain rate which is not the case in the present study. The fracture crack growth in the present study was seen to be strongly affected by many factors such as loading rates, material microstructure, chemical composition, loading history and etc. All these factors cannot be interpreted in terms of global approach to fracture. As a result, an alternative local approach to fracture (LAF) is proposed to study the crack propagation resulting from the elastic-viscoplastic material behavior and local damage near the tip of the crack. This approach allows to take into account the micromechanisms of failure such as stress and strain distribution at a crack tip. The identification and determination of the micromechanical parameters is possible through the hybrid methodology of combined testing and numerical solution [25, 74].

To perform a LAF numerically, different phenomenological constitutive models have been developed in the last 30 years for brittle, ductile and creep fracture. The constitutive model must satisfy two conditions: it should be micromechanically based and it should provide reliable description of the crack tip stress-strain field. Analysis of a ductile rupture requires fully coupled damage models that can properly capture the increase and subsequent decrease of the load carrying capacity of the material taking place in the region in front of the crack tip due to the combined process of material hardening and material softening by the nucleation, growth and coalescence of voids. The most well-known micromechanical model of the microvoid nucleation and growth was derived by Gurson [87], and later modified by Gurson-Tvergaard-Needleman (GTN model) to capture void coalescence [200, 203, 204]. Gurson model introduces a strong coupling between deformation and damage. A new internal variable representing the volumetric fraction of voids or porosity, f, is introduced. The evolution of the porosity is a function of stress and strain, and its gradual increase leads to a loss of material stiffness, until final fracture occurs. Gurson model was futher improved [195, 194] and extended [151, 220, 65, 28].

Alternative local approach to fracture known as cohesive zone modeling (CZM) was originally proposed by Dugdale [64] and Barenblatt [16]. Nowadays, the CZM is employed for a wide variety of problems and materials. The underlying idea is to combine an energetic criterion at a microscale with a stress criterion [25]. The crack propagation is described through the separation of the two crack surfaces in the process zone by a continuous traction-separation law. Various CZMs with different shapes of the traction-displacement response and the parameters used to describe that shape were later proposed by different authors [92, 169, 201]. Needleman [143] investigated void nucleation by interface debonding of inclusions in plastically deforming solids. An exponential type of fraction-separation law to simulate the particle debonding the metal matrices was suggested in his study [143]. Tvergaard and Hutchinson [203] applied a trapezoidal shape of the traction-separation law to study the ductile fracture in an Al alloy by using the experimental resistance curves for simulating crack extension. Subsequently, Lin [122] and co-workers extended this approach to model the crack growth resistance in homogeneous

as well as heterogeneous materials under small scale yielding and large scale yielding. The prevailing part of cohesive crack tip research and application is related to FE implementations and corresponding cohesive elements. The CZM elements are usually placed at the interface (see Figure 4.1) and describe the interface traction as a function of the opening displacement with the help of traction-separation laws (TSL). Energy is dissipated when these elements are opened until complete loss of traction occurs. The process or cohesive zone is the zone wherein energy is dissipated [91].

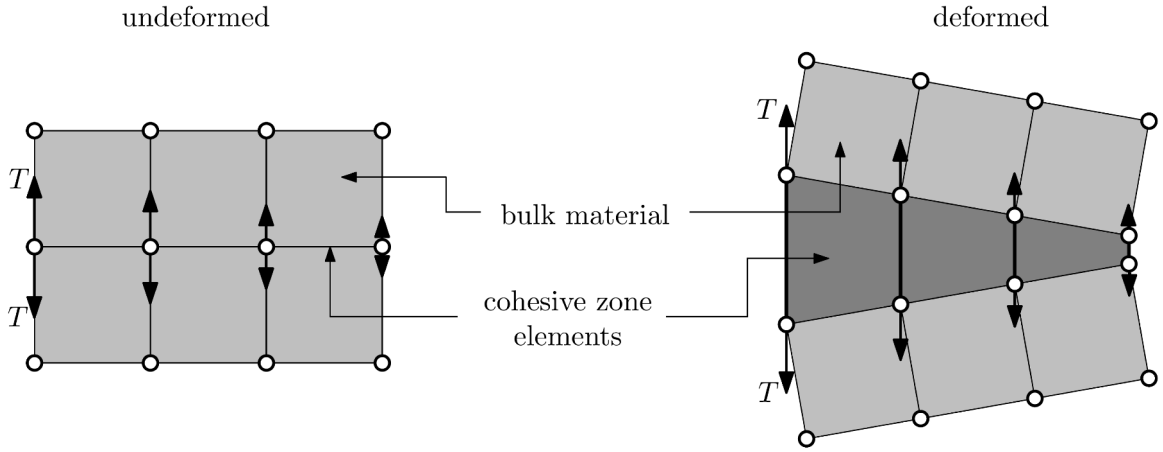

Figure 4.1: Schematic representation of mode I opening of cohesive zone elements [91].

One of the advantages of using cohesive elements in modeling fracture is to split the total dissipated energy into the energy dissipated by plastic deformation and the energy of separation. In this way, it is possible to evaluate the damage and deformation processes separately, but coupled. Besides, as long as cohesive elements adequately resolve the fracture process zone of the material, no mesh dependency is expected in using CZMs [9]. CZM is particularly attractive for practical application since it requires only two parameters, which can be determined in experiments. In a CZM the crack can propagate along any path where the CZ elements are placed. The CZM can model both brittle and ductile interfaces, and it is easy to implement in the mesh. Therefore, CZM was chosen to model the crack growth for CP α Ti of Grade 2 and Grade 4.

4.1.2 Modeling of hydrogen-induced crack propagation

Numerous models exist that describe material degradation and its effect on structural integrity caused by hydrogen embrittlement. The proposed mechanisms on which these models are based include stress induced hydride formation and cleavage (or delayed hydride cracking DHC), hydrogen enhanced localized plasticity (HELP) and hydrogen enhanced decohesion (HEDE). According to the of HELP mechanism, the presence of hydrogen in solid solution reduces elastic energies of interaction between moving dislocations and a variety of obstacles. Since the interaction energy is reduced, the stress required for dislocation motion is decreased and thereby plasticity is enhanced. As a result, the amount of deformation that occurs in a localized region adjacent to the fracture surface is increased [191]. This phenomenon is supported

by the experimental observations in FCC [168], BCC [190], and HCP [182] metals.

The hydrogen effect ahead of a crack tip on the local behavior and macroscopic fracture processes can be studied through the numerical modeling in the absence or in the presence of hydrogen content. In the absence of hydrogen, modeling of ductile crack propagation was performed by monitoring damage evolution in the material ahead of a crack tip through the Gurson-Tvergaard flow potential for porous plastic solids [87, 202] or by using cohesive zone approach [16, 64]. In the presence of hydrogen concentration, the idea of hydrogen-induced subcritical crack growth modeling is based on the assumption that diffusible hydrogen is in equilibrium with the hydrostatic stress and that hydrogen trapped by dislocations is a function of the strain field [118, 119, 1, 186, 61, 174, 191, 179].

Ahn [1] studied hydrogen-induced material softening which promotes crack propagation through hydrogen-assisted void growth and coalescence. Crack propagation was modeled by CZ elements whose traction-separation law was determined through void cell calculations that address the hydrogen effect on void growth and coalescence. The hydrogen enhanced localized plasticity was described by using the local flow stress which represents a decreasing function of the hydrogen concentration in equilibrium with local hydrostatic stress and plastic strain. It was concluded that hydrogen accelerates void growth and coalescence and promotes crack propagation by linking simultaneously a finite number of voids with the crack tip.

In the recent study of Dadfarnia [61] it was noted that cohesive element method may not preserve the fidelity of the fields close to the crack tip since the stress and hydrogen fields are coupled. Alternative nodal release approach in the neighborhood of a crack tip was proposed to understand the interaction among stress, strain, and transient hydrogen accumulation from external gas. A model for hydrogen-induced stress-controlled crack propagation under sustained load was proposed. The model is based on two assumptions: (i) local material fracture strength is a decreasing function of local hydrogen concentration and (ii) crack propagation takes place when the opening stress ahead of a crack tip exceeds the local fracture strength over a characteristic distance. It was demonstrated numerically that diffusion-controlled crack propagation can explain the existence of both stages in the velocity versus stress intensity factor curve (V-K).

In spite of the large number of studies of HELP phenomenon, most of the existing models incorporate elastic-plastic behavior of the material exhibiting rate independence. One of the critical question remaining unanswered is how hydrogen affects the time-dependent nature of plasticity. The objective of the present chapter is to model the mechanical behavior of Ti with an elastic-viscoplastic constitutive law which accounts for material anisotropy of mechanical properties and time-dependent behavior. The phenomenological constitutive formulation of the viscoplastic behavior of CP α Ti of Grade 2 and Grade 4 is based on the experimental database provided by LMS Ecole Polytechnique [17]. Next, using a local approach to fracture, a cohesive zone model is proposed in order to predict the crack growth for rapidly rising and sustained loading conditions and to investigate the phenomenon of hydrogen embrittlement-assisted crack growth. Using the elastic-viscoplastic behavior for continuum elements, the solution is computed with the FE model. The results of the numerical simulations are presented. The discussion of some alternative relevant approaches to SLC simulations follows in the last part of this chapter.

4.2 Viscoplastic anisotropic model for α Ti

4.2.1 Experimental results

An anisotropic macroscopic elastic-viscoplastic model for CP α Ti of Grade 2 and 4 is proposed in this section. The identification of the model is based on the experimental data provided by *Laboratoire de Mécanique des Solides* of Ecole Polytéchnique [17] composed of the tests performed at room temperature on both TD and LD cylindrical samples of Grade 2 and Grade 4. Tensile tests were performed at a fixed strain rate of $2 \times 10^{-4} s^{-1}$ and with tenfold upward and downward strain-rate jumps ranging from 2×10^{-6} to $2 \times 10^{-2} s^{-1}$. True stress-strain curves presented in Figure 4.2 (a) show a higher yield stress when specimens are tested along the TD than along the LD for both materials. The tests with strain-rate jumps (Figure 4.2 (b)) show the macroscopic apparent positive strain rate sensitivity. These tests allow to identify the viscoplastic parameters.

Creep tests were carried out at room-temperature at different loads with an imposed strain rate of $2 \times 10^{-4} s^{-1}$ during the loading stage. Most tests were interrupted after 200 h, unless fracture occurred before [18]. The resulted creep curves for Grade 2 and Grade 4 are plotted on Figure 4.3. Depending on the nominal stress, creep saturation or secondary and tertiary creep leading to fracture were observed. In most cases, a 200 hours test was sufficient to reach a steady-state or minimum creep rate, ranging from 2×10^{-5} to 2×10^{-8} s^{-1}. The early stage of creep in Grade 4 showed unusual incubation period for nominal load of 376 MPa along LD and 425 MPa along TD followed by the spontaneous increase in the creep rate. Normal transient creep was observed for Grade 2.

Repeated relaxation tests presented in Figure 4.4(a) were composed of loading to a certain level of strain, followed by the interruption for a relaxation period of 20 hours (material is submitted to constant displacement), and subsequent unloading and reloading to a higher strain level. After each unloading down to 20 MPa, the specimen of Grade 2 was aged for 4 hours at constant displacement and then reloaded. In total, 5 relaxation cycles were performed. For Grade 4, the unloading between two relaxation cycles was extended until compression without any following aging time. Slightly opened hysteresis loops evidenced the significance of the kinematic hardening components X_i. Figure 4.4(b) shows the relaxation kinetics during the repeated relaxation tests on performed on Grade 2 and Grade 4 along TD and LD.

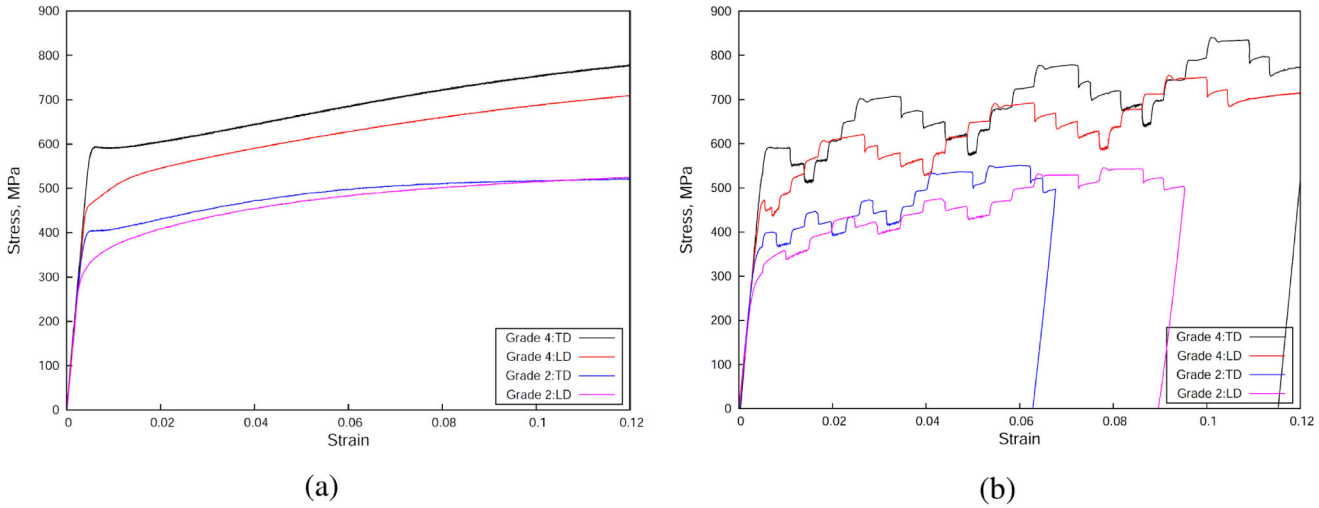

Figure 4.2: Tensile tests on Grade 2 and Grade 4 on the cylindrical specimens in TD and LD: (a) at $\dot{\varepsilon} = 2 \times 10^{-4}$ s^{-1} and (b) with strain-rate jumps at $\dot{\varepsilon} = 2 \times 10^{-2} - 2 \times 10^{-6}$ s^{-1}.

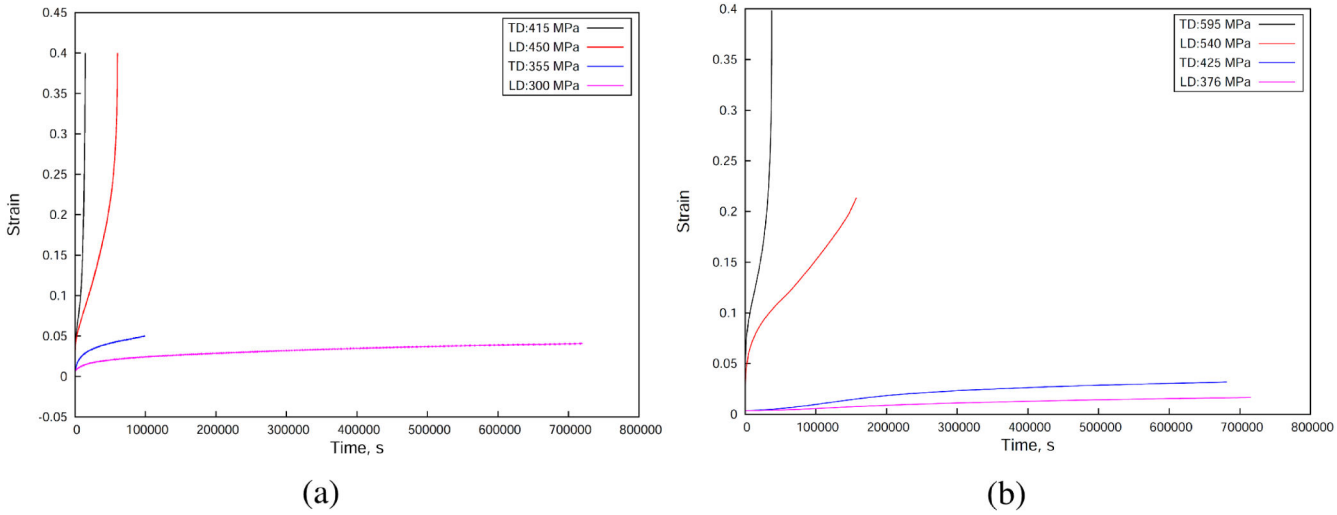

Figure 4.3: Creep tests in TD and LD on (a) Grade 2 (b) Grade 4.

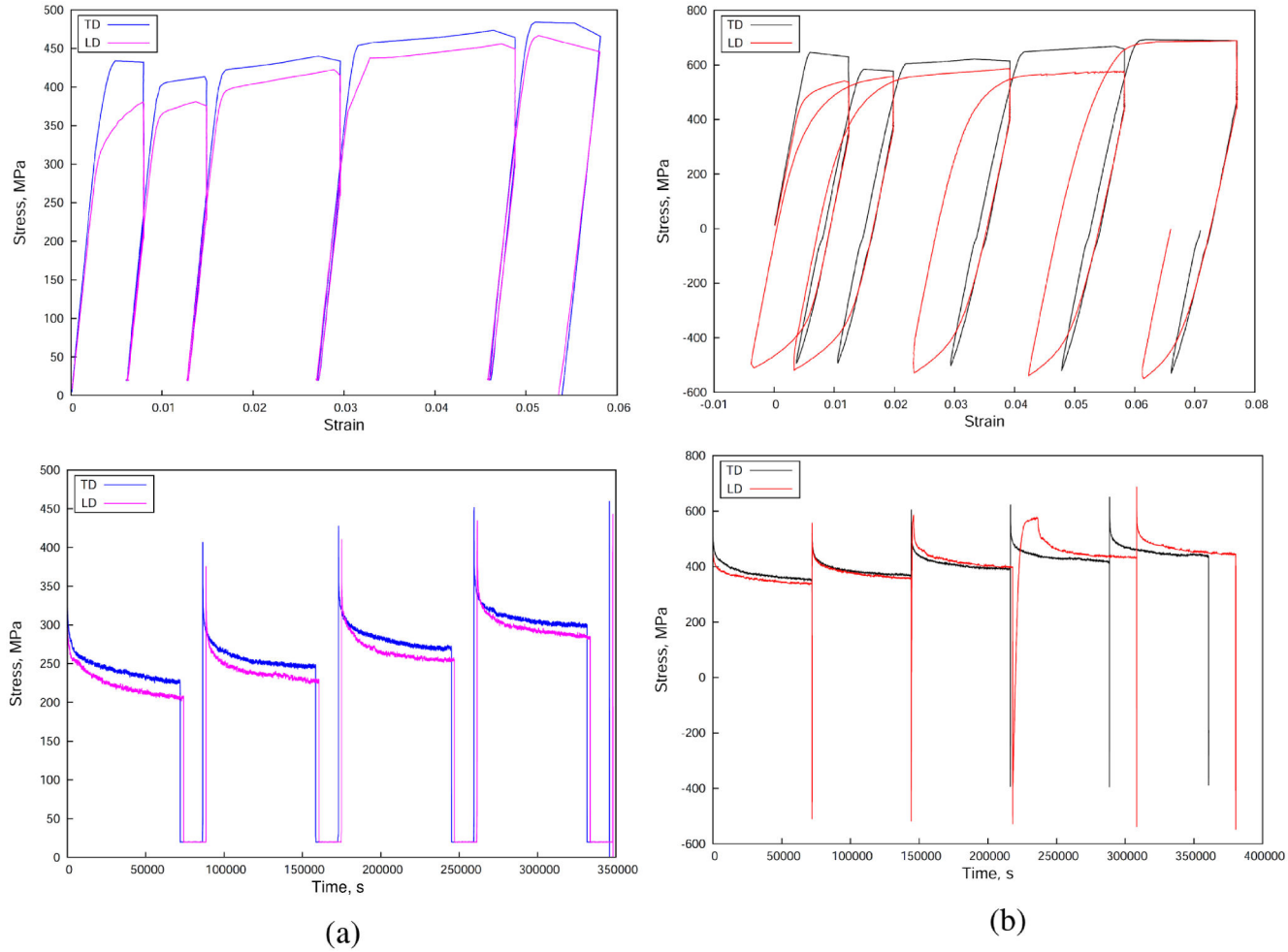

Figure 4.4: Relaxation tests on the cylindrical specimens in TD and LD on (a) Grade 2 (b) Grade 4.

4.2.2 Constitutive equations

The constitutive equations were formulated in the small strain framework for the parameters identification. Note that in the later FE simulations on CT specimens these equations will be used in a large deformation framework. The total deformation $\underset{\sim}{\varepsilon}$ is the sum of elastic and plastic strains:

$$\underset{\sim}{\varepsilon} = \underset{\sim}{\varepsilon}^e + \underset{\sim}{\varepsilon}^p \tag{4.1}$$

The yield criterion is

$$f(\underset{\sim}{\boldsymbol{\sigma}}; p; \underset{\sim}{\boldsymbol{X}}_i) = \sigma_{eq}\left(\underset{\sim}{\boldsymbol{\sigma}} - \sum_i \underset{\sim}{\boldsymbol{X}}_i\right) - R(p) \tag{4.2}$$

where $R(p)$ is an isotropic strain hardening which includes the initial yield stress R_0, and which depends on the accumulated plastic strain p. Q is the saturated value of hardening and b is the rate at which the saturation is reached. H is the slope of a linear strain hardening term. It is defined as:

$$R(p) = R_0 + Hp + Q\left(1 - e^{-bp}\right) \tag{4.3}$$

The nonlinear kinematic hardening variable $\underset{\sim}{\boldsymbol{X}}_i$ was introduced into the model to improve the description of relaxation tests with unloading.

$$\underset{\sim}{\boldsymbol{X}}_i = \frac{2}{3} C_i \underset{\sim}{\boldsymbol{\alpha}}_i, \qquad i = [1,2,3], \qquad \dot{\underset{\sim}{\boldsymbol{\alpha}}}_i = \left(\underset{\sim}{\boldsymbol{n}} - D_i \underset{\sim}{\boldsymbol{\alpha}}_i\right) \dot{p} \tag{4.4}$$

The viscoplastic flow rule is a hyperbolic sine of the yield criterion:

$$\dot{p} = \dot{p}_0 \sinh \left\langle \frac{f}{\sigma_0} \right\rangle \tag{4.5}$$

The anisotropy of plastic deformation is presented with the help of the yield criterion of a Hill type which depends only on the deviatoric stresses:

$$\sigma_{eq}(\underset{\sim}{\boldsymbol{\sigma}} - \sum_i \underset{\sim}{\boldsymbol{X}}_i) = \sqrt{\frac{3}{2} \left(\underset{\sim}{\boldsymbol{\sigma}}^{dev} - \sum_i \underset{\sim}{\boldsymbol{X}}_i\right) : \underset{\approx}{\boldsymbol{H}} : \left(\underset{\sim}{\boldsymbol{\sigma}}^{dev} - \sum_i \underset{\sim}{\boldsymbol{X}}_i\right)} \tag{4.6}$$

The Hill matrix $\underset{\approx}{\boldsymbol{H}}$ is defined as a 4th rank tensor:

$$\underset{\approx}{\boldsymbol{H}} = \begin{pmatrix} hill_a & 0 & 0 & 0 & 0 & 0 \\ 0 & hill_b & 0 & 0 & 0 & 0 \\ 0 & 0 & hill_c & 0 & 0 & 0 \\ 0 & 0 & 0 & hill_d & 0 & 0 \\ 0 & 0 & 0 & 0 & hill_e & 0 \\ 0 & 0 & 0 & 0 & 0 & hill_f \end{pmatrix} =$$

$$= \begin{pmatrix} 2F - G + 2H & 0 & 0 & 0 & 0 & 0 \\ 0 & 2F + 2G - H & 0 & 0 & 0 & 0 \\ 0 & 0 & -F + 2G + 2H & 0 & 0 & 0 \\ 0 & 0 & 0 & 2L & 0 & 0 \\ 0 & 0 & 0 & 0 & 2M & 0 \\ 0 & 0 & 0 & 0 & 0 & 2N \end{pmatrix} \tag{4.7}$$

The material parameters to be identified are:
- Isotropic elasticity: E and ν
- Classical isotropic strain hardening: R_0, Q, b, H
- Nonlinear kinematic hardening: C_i, D_i
- Viscous part: $\dot{p_0}$, σ_0
- The components of the Hill criterion: $hill_a$, $hill_b$, $hill_c$, $hill_d$, $hill_e$, $hill_f$

Thus, the identification of 18 parameters is needed for the modeling of the mechanical behavior of the material.

4.2.3 Identification of the model parameters

The material parameters introduced by the above described model were identified by comparing the experiments with simulations performed with the help of the identification package of

Zset software on a volume element. The system of differential equations defined in the previous section was numerically solved in the Zset solver with a 4th order Runge-Kutta method with automatic time stepping. Numerical optimization method is the Levenberg-Marquardt algorithm which is used to solve non-linear least squares problems. The parameters identification involves the minimization of the sum of the squares of the errors between experimental and simulated stress values at all recorded prescribed strain values for each experimental curve. Different weighting factors were attributed to the tests depending on the 'importance' in the function evolution. The results for Grade 4 are presented in Table 4.1.

Parameters	Unit	Value
E	MPa	106674
ν	-	0.3
$hill_a$	-	0.22
$hill_b$	-	0.375
$hill_c$	-	1.75
$hill_d, hill_e, hill_f$	-	1.6
$\dot{p_0}$	s^{-1}	1.52e-8
σ_0	MPa	16
R_0	MPa	200
H	MPa	7.4
Q	MPa	47
b	-	9.6
C_{1i}	MPa	58367
D_{1i}	-	1086
C_{2i}	MPa	2313
D_{2i}	-	221
C_{3i}	MPa	1397
D_{3i}	-	7.5

Table 4.1: Identified material parameters for Ti Grade 4

The numerical predictions of tensile, creep and relaxation tests obtained with the set of identified model parameters are presented in Figures 4.5 - 4.8. In general, the anisotropy and viscoplastic behavior of the material are correctly taken into account with the set of identified parameters, even though some detailed features remain imperfectly described. The yield peak in tensile TD test (Figure 4.5(b)) cannot be correctly predicted since no aging variables were integrated into the model. For tensile test performed in LD direction (Figure 4.5(a)), an overestimation of the magnitude of hardening rate is observed. The same problem is detected for the tests with strain rate jumps especially at higher strain rates (see Figure 4.6 (a,b)). The

hysteresis loops in relaxation tests are well described (see Figure 4.7), however the model underestimates the amount of stress relaxation. Finally, the predicted response of the creep test does not reproduce well the incubation period observed for Grade 4 TD at 376 MPa along LD and at 425 MPa along TD (Figure 4.8 (b)) which was attributed to the oxygen-induced dynamic strain aging [18]. At the same time, the model predicts well the primary, secondary and even tertiary creep strain presented in Figure 4.8 (a). The prediction of the tertiary creep is possible due to the application of the true stress as an input of the simulation. Note that a variation between experiments and simulations in some tests is due to the inability of the used viscoplastic flow rule to account for the wide range of the experimental conditions such as, for example, strain-rates, varying from $\dot{\varepsilon} = 10^{-2}$ s^{-1} in the strain-rate jump tests to $\dot{\varepsilon} = 10^{-8}$ s^{-1} in the creep tests. The choice was done to get a better description for low strain rates.

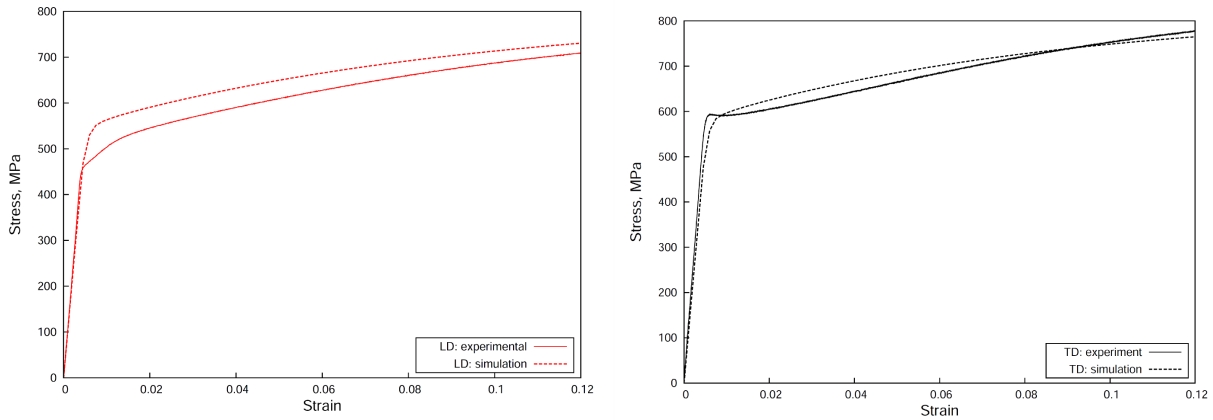

Figure 4.5: True stress-strain curves for simulated tensile test for Grade 4: (a) LD (b) TD.

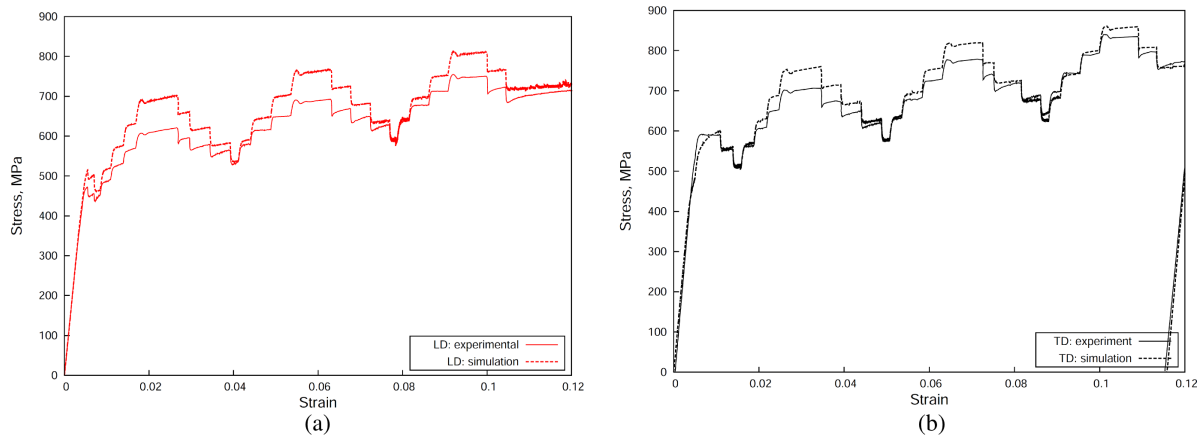

Figure 4.6: True stress-strain curves for simulated jump test for Grade 4: (a) LD (b) TD.

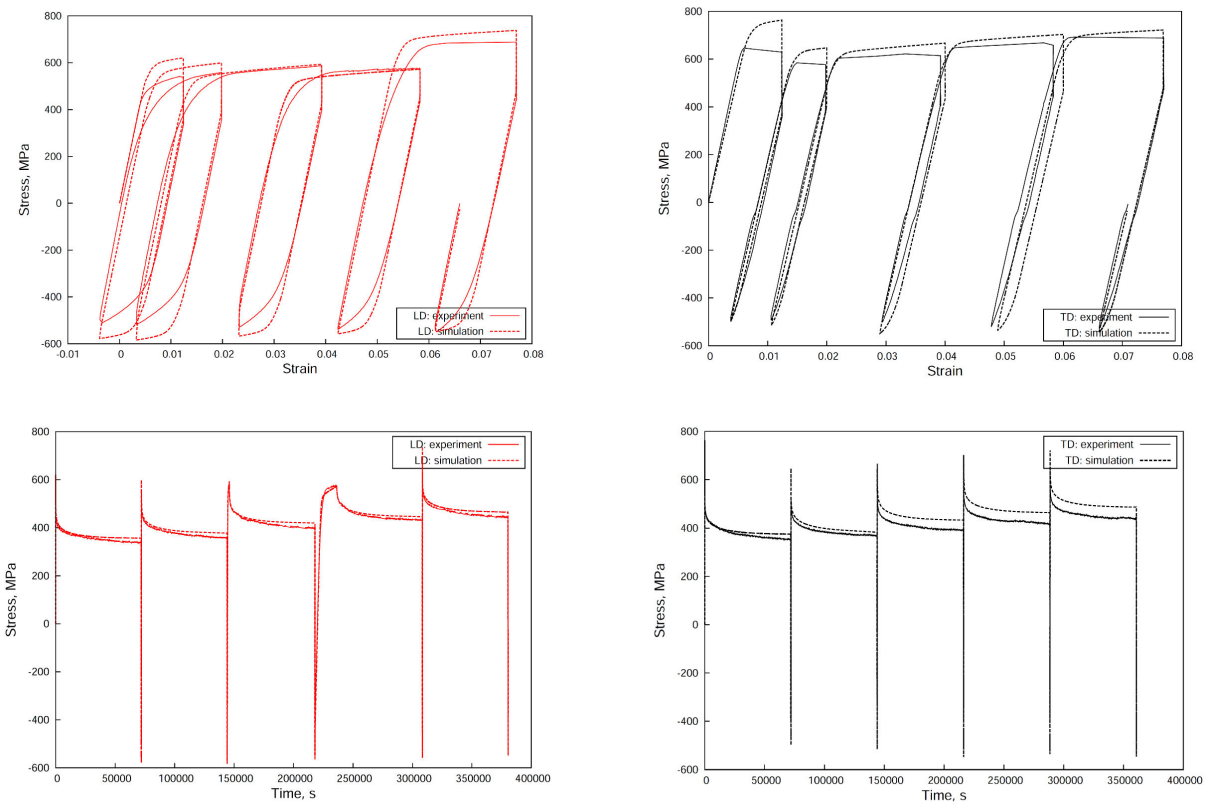

Figure 4.7: True stress-strain curves for simulated relaxation test for Grade 4: (a) LD (b) TD.

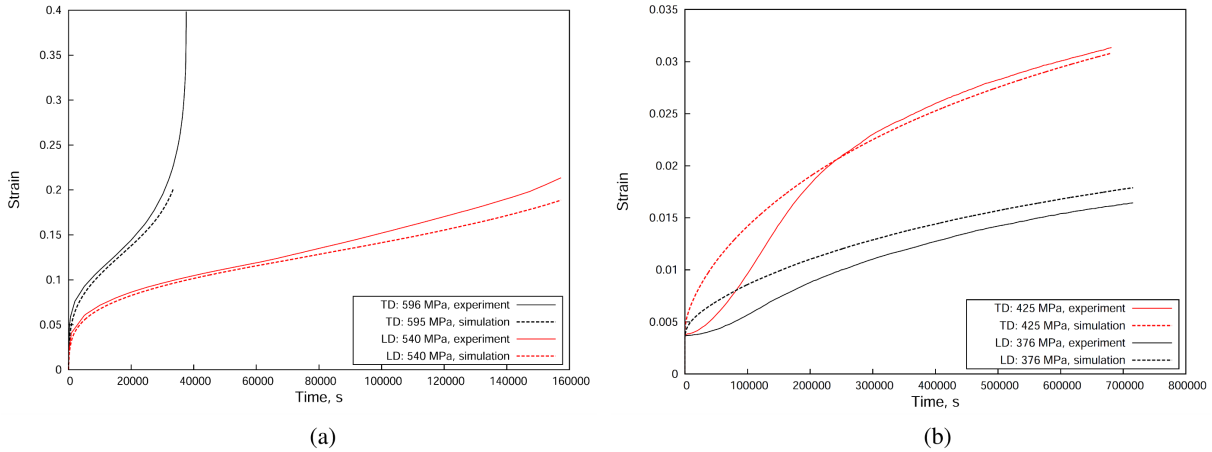

Figure 4.8: True stress-strain curves for simulated creep test for Grade 4: (a) in TD at 595 MPa and in LD at 540 MPa (b) in TD at 425 MPa and in LD at 376 MPa.

The identified materials parameters for Grade 2 are given in Table 4.2.

Parameters	Unit	Value
E	MPa	106742
ν	-	0.3
$hill_a$	-	0.53
$hill_b$	-	0.44
$hill_c$	-	2.7
$hill_d, hill_e, hill_f$	-	1.6
$\dot{p_0}$	s^{-1}	1.52e-8
σ_0	MPa	16
R_0	MPa	170
H	MPa	7.5
Q	MPa	48.4
b	-	12.44
C_{1i}	MPa	43316
D_{1i}	-	1485
C_{2i}	MPa	2329
D_{2i}	-	164
C_{3i}	MPa	877
D_{3i}	-	13

Table 4.2: Identified material parameters for Ti Grade 2.

The numerical predictions of tensile, creep and relaxation tests obtained with the set of identified model parameters are presented in Figures 4.9 - 4.12. In general, simulations of the monotonic tensile test and jump test in the TD are in better agreement with the experimental results comparing to the LD. The hysteresis loops in relaxation tests are well described (see Figure 4.11), however the model underestimates the amount of stress relaxation for both TD and LD tests. One of the possible way to improve the description would be to introduce a static recovery term which was not done in the present model for the sake of simplicity. Finally, the predicted response of the creep test reproduces well the experiments performed at elevated stresses with the primary, secondary and tertiary creep strains, however does not capture the response of the test at 300 MPa in LD. The incubation period observed for the creep of Grade 4 in Figure 4.8 (b) and which can be attributed to the effect of strain aging, was not captured in the simulation since the present model does not include parameters describing strain aging effects.

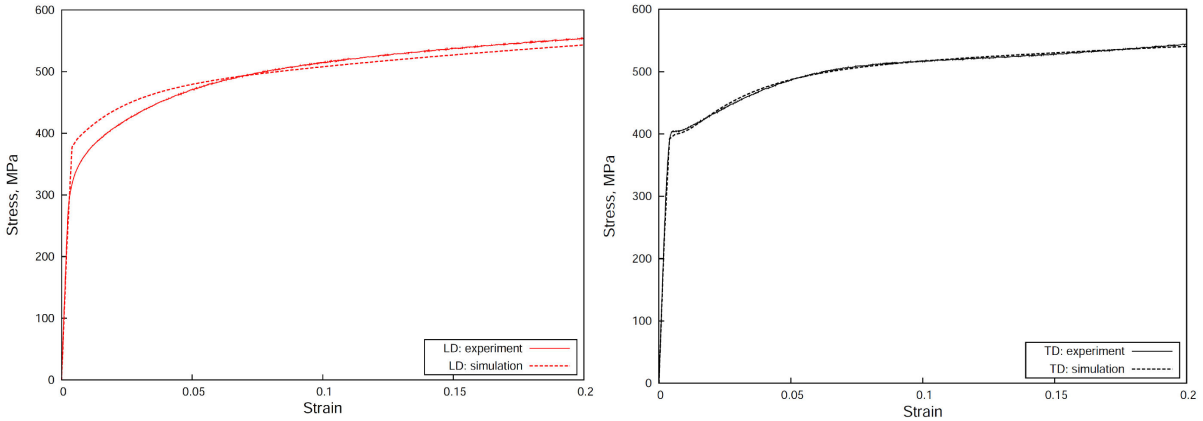

Figure 4.9: True stress-strain curves for simulated tensile test for Grade 2: (a) LD (b) TD.

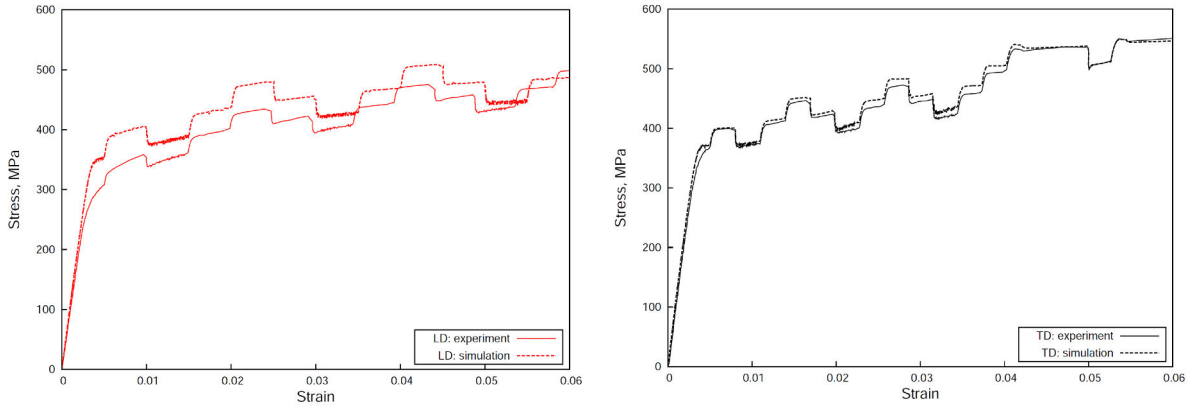

Figure 4.10: True stress-strain curves for simulated jump test for Grade 2: (a) LD (b) TD.

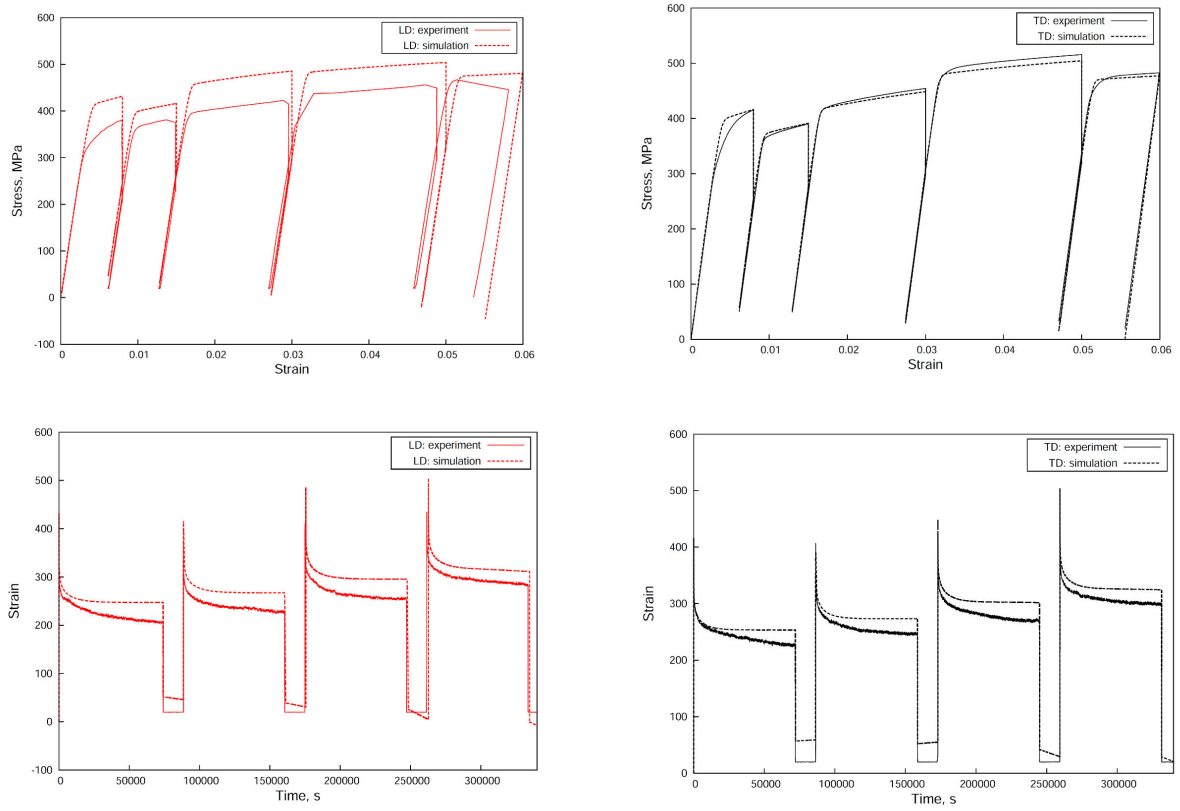

(a) (b)

Figure 4.11: True stress-strain curves for simulated relaxation test for Grade 2: (a) LD (b) TD.

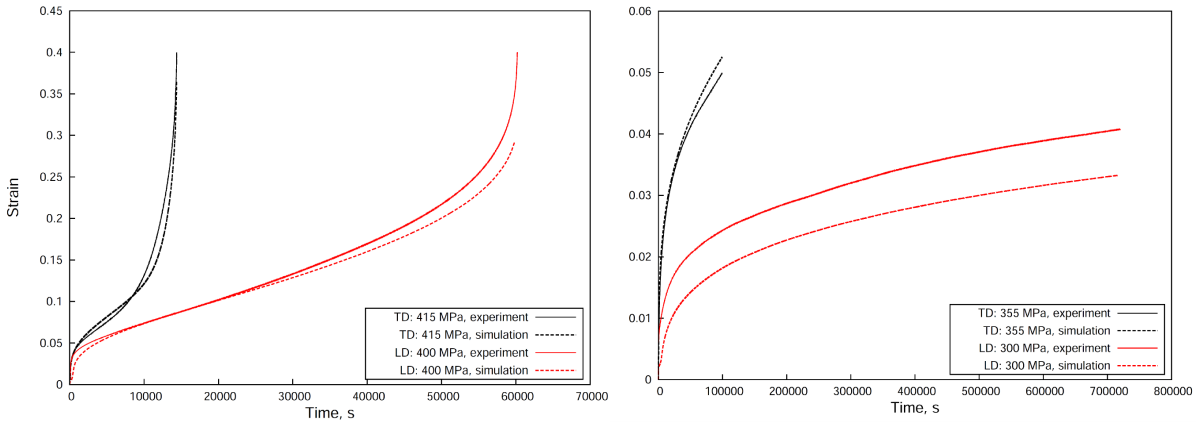

(a) (b)

Figure 4.12: True stress-strain curves for simulated creep test for Grade 2: (a) in TD at 415 MPa and in LD at 400 MPa (b) in TD at 355 MPa and in LD at 300 MPa.

Figure 4.13 shows the predicted evolutions of the Lankford coefficient calculated as:

$$L_{LD} = \frac{\varepsilon_{p22}}{\varepsilon_{p33}} \qquad L_{TD} = \frac{\varepsilon_{p11}}{\varepsilon_{p33}} \tag{4.8}$$

where ε_p is the viscoplastic strain along a given direction. The plastic strain though-the-thickness ε_{p33} is negative, however in-plane plastic strain (ε_{p22} for LD and ε_{p11} for TD) is positive. As a result, Lankford coefficient shows a negative value which is in contrast to the experimentally measured value of Lankford coefficients [17]. This illustrates the inability of Hill criterion to fully account for anisotropic behavior in the simulations since only two out of six constants can be determined from tests. However by using in simulations the Lankford coefficients that were experimentally identified from strain field measurements [17], the response of the CT specimen did not show any important modifications. Thus, all the following tests were simulated with a set of the identified parameters.

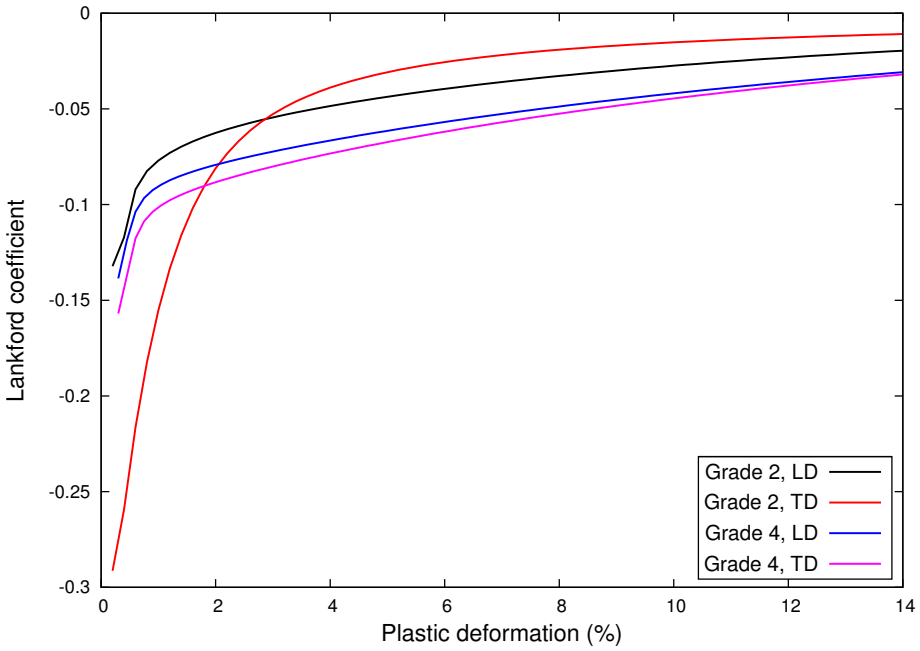

Figure 4.13: Lankford coefficient evolution based on the identified model parameters for Grade 2 (TD and LD) and Grade 4 (TD and LD).

4.2.4 Simulation results

In the previous section constitutive equations describing viscoplastic behavior of the material taking anisotropy into account were formulated and the model parameters were identified. A further step consists in employing this model to examine stress and strain state at the crack tip. For this, simulations of Mode I loadings on CT specimen were performed in large strain formalism. Due to the symmetry conditions only a quarter of the CT specimen was used in simulations. The same mesh of 17 mm thick sample as for the electrical calculation in Chapter3 is used with c3d8 elements (with 8-node linear hexahedral elements) for the elements of the

specimen. The mesh is composed of 88218 nodes and 82040 elements, with a mesh refinement in the region around the crack tip leading to a local mesh size of 300 μm. The loading pins (red on Figure 4.14) were modeled by element sets in the shape of a wedge with purely elastic rigid properties. The contact between the loading pin and the specimen is not accounted for. The sample is loaded by applying a vertical displacement in y direction of 1 mm/min on the center of a wedge which is located at the center of the hole machined in the CT-specimen [25]. The simulations are carried out in 3D. The load-line-displacement is obtained at the blue point N_1 and load-line-crack opening displacement (COD) at the blue point N_2.

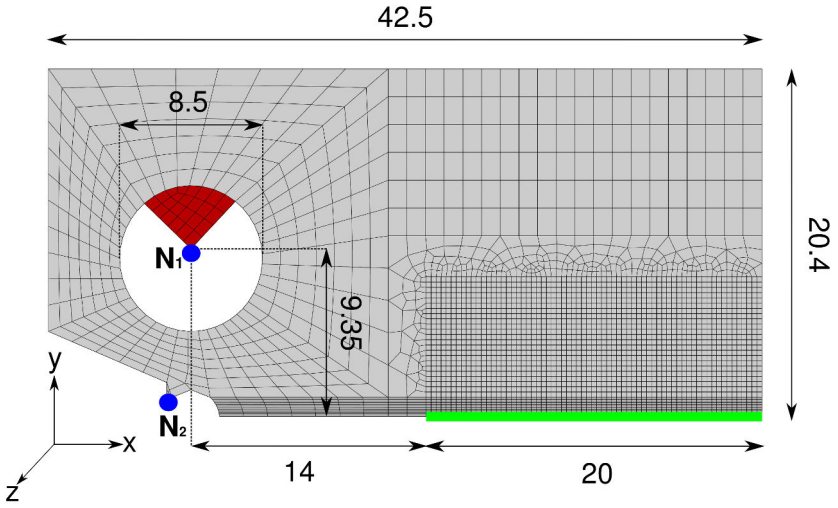

Figure 4.14: Dimensions of the simulated CT-specimen (mm). The green line represents uncracked ligament. The pin load is in red. The blue point N_1 and N_2 are for load-line displacement and load-line COD measurements.

Figure 4.15 shows the load vs. COD experimental curve with measured initial crack size of 15.74 mm and two simulation curves with the initial crack size of 15.89 and 18 mm for Grade 2. All tests were simulated under a constant displacement rate of 1 mm/min without crack propagation. Obviously, the solution cannot account for the decrease in force when critical COD is attained. Therefore, the simulated curves deviate from the experimental curve at 0.5 mm COD because of the onset of ductile crack tearing. It must be pointed out that the simulation curve obtained with the initial crack length of 15.89 mm does not allow the correct prediction of the elastic behavior of material. Only when increasing the initial crack length up to 18 mm, the model yields the correct elastic slope. The reason why the model produces a stiffer solution was not detected yet. For the comparative purpose it was decided to perform all the following simulations on the CT specimen with the initial crack length of 18 mm.

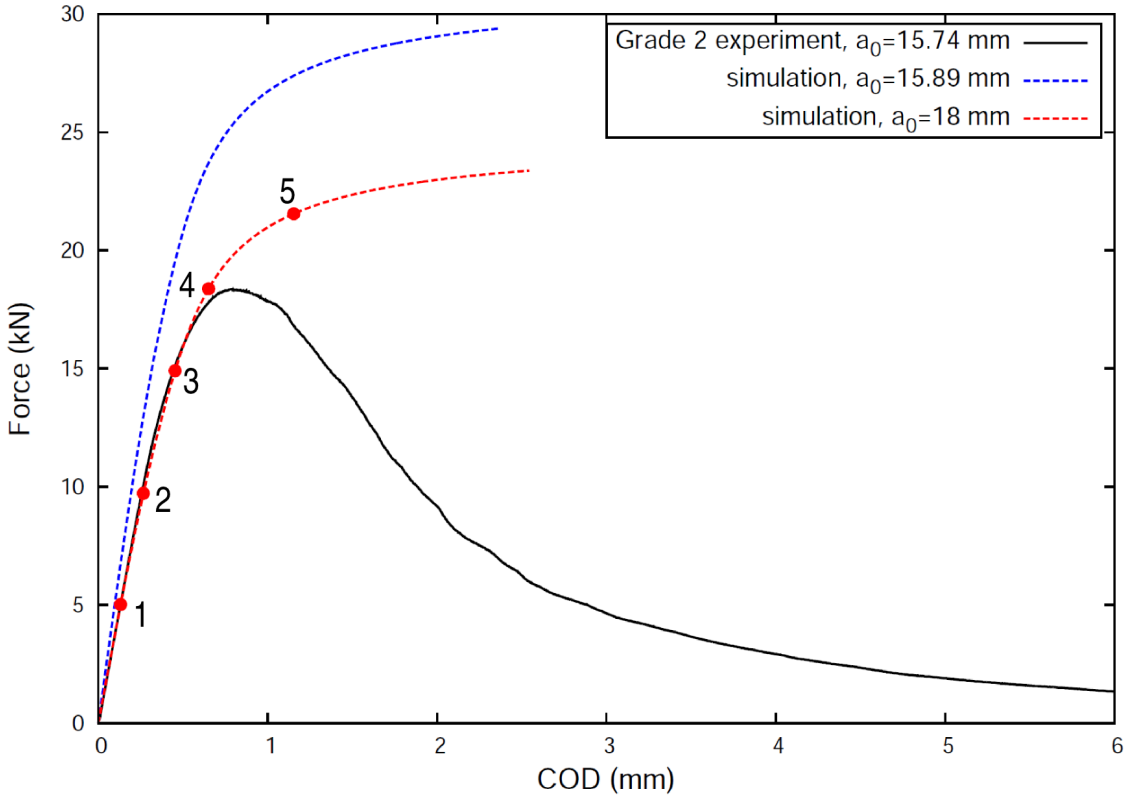

Figure 4.15: Simulation of CT specimen for Grade 2 with viscoplastic model with different initial crack size.

Experimental and simulated load vs. COD curves for Grade 4 are shown in Figure 4.16. As in the case of Grade 2, the correct model prediction is obtained only when the initial crack length reaches 18 mm. The simulated curve deviates from the experimental at COD=0.6 mm because of the onset of crack propagation.

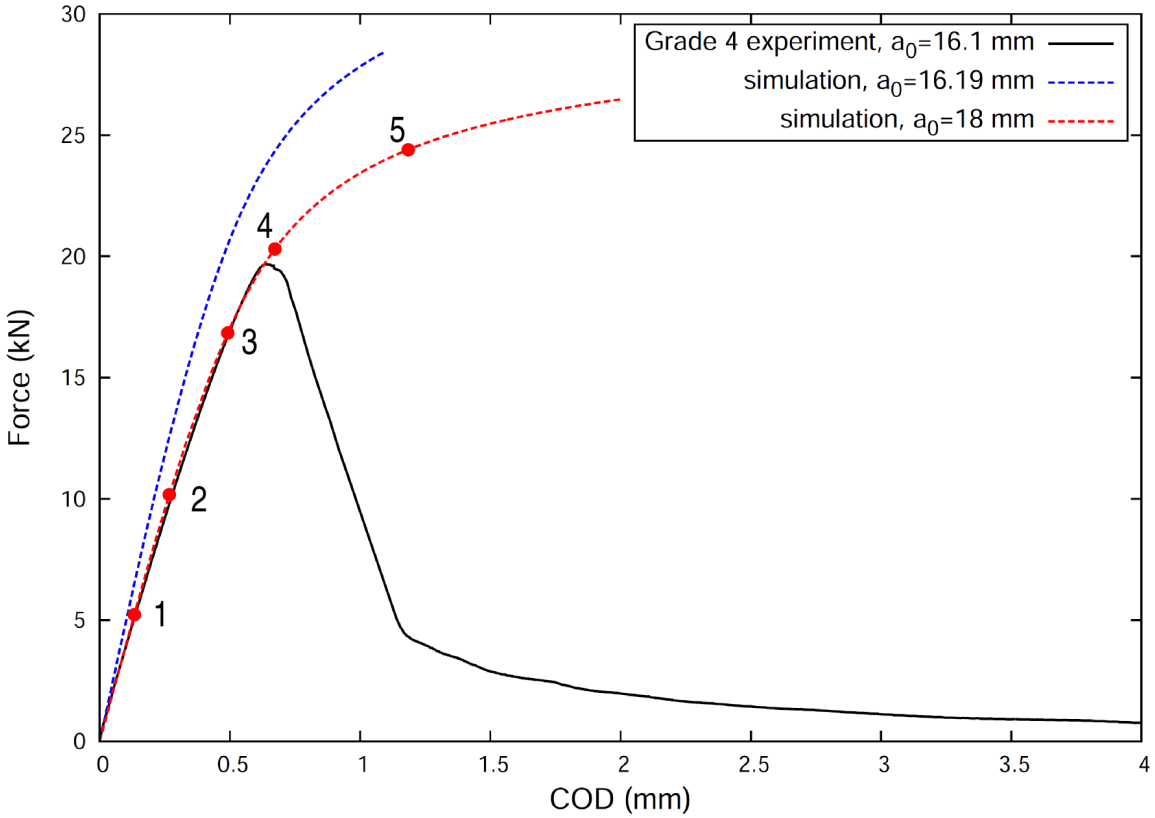

Figure 4.16: Simulation of CT specimen for Grade 4 with viscoplastic model with different initial crack size.

Series of maps of accumulated plastic strain at the crack tip of the CT specimen for Grade 2 and Grade 4 are shown in Figure 4.17 for 5 macroscopic COD levels defined in Figures 4.15 and 4.16 with points on load-COD curves. The strong plasticity at the crack tip is evidenced for both Grade 2 and Grade 4 before the onset of crack tearing. Similar size and similar elliptical shape of the plastic zone on the plane side without side groove is observed for both Grade 2 and Grade 4. A large plastic zone formed ahead of the crack tip before fracture confirms the ductile fracture behavior of Ti. Due to the similarity in plastic zone for both Grade 2 and Grade 4, further analysis of the crack tip stress-strain field will be given only for Grade 2.

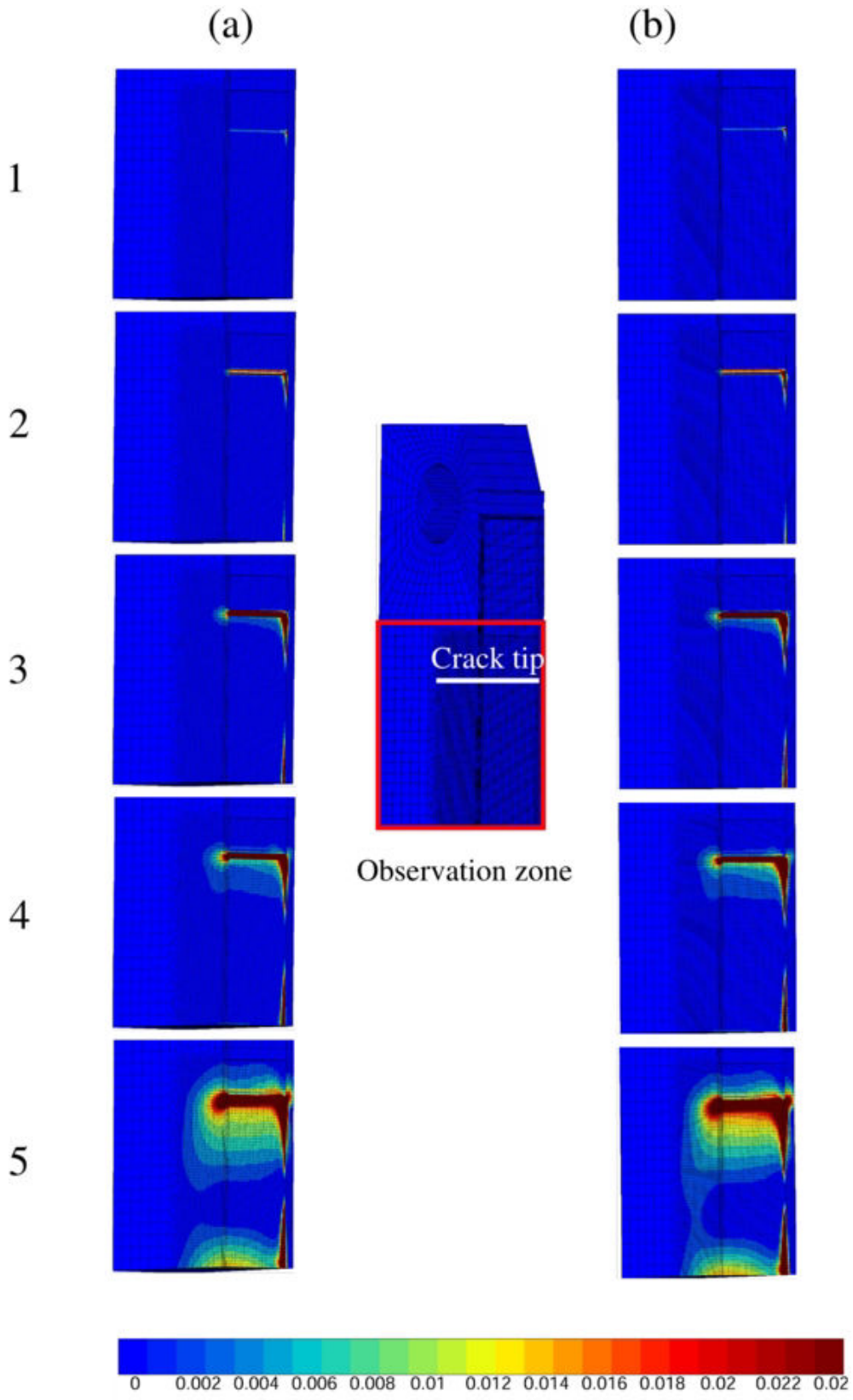

Figure 4.17: Maps of simulated accumulated plastic strain at the crack tip for (a) Grade 2 and (b) Grade 4. The left numbers refer to the points on the Force-COD curves of Figure 4.15 and 4.16.

Present viscoplastic model was used to simulate the material deformation behavior under constant load and constant displacement. The variation of COD with time under constant load of 13 kN for Grade 2 is shown in Figure 4.18. The difference in the level of COD between simulated and experimental curves is conditioned by the initial crack length. Note that this example will be used in the next section 4.2.5 in the discussion on the effect of hydrogen on the cracking behavior. Figure 4.19 shows the equivalent plastic strain at four different COD corresponding to the points on the simulated curve. The obtained results indicate the strain increase with time, which confirms the occurrence of the time-dependent deformation at the crack tip.

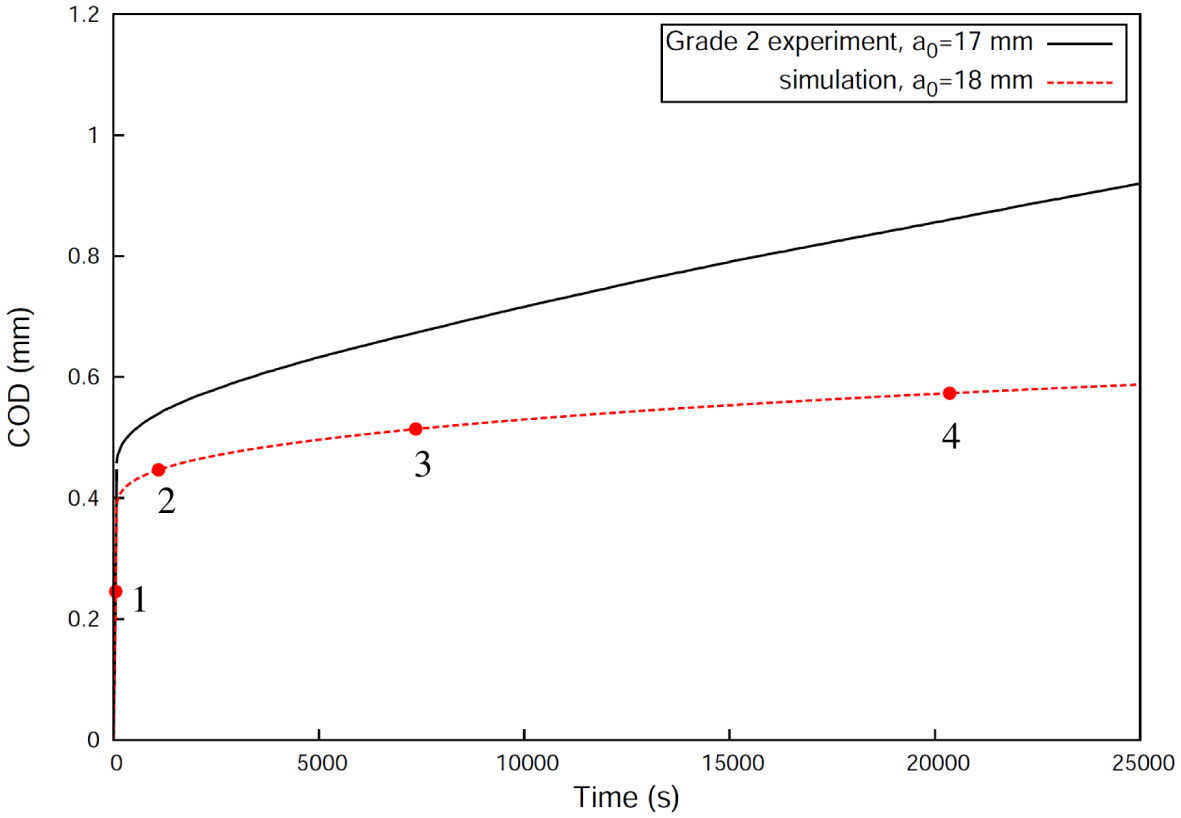

Figure 4.18: The creep deformation behavior of the CT specimen for Grade 2 at constant load of 13 kN.

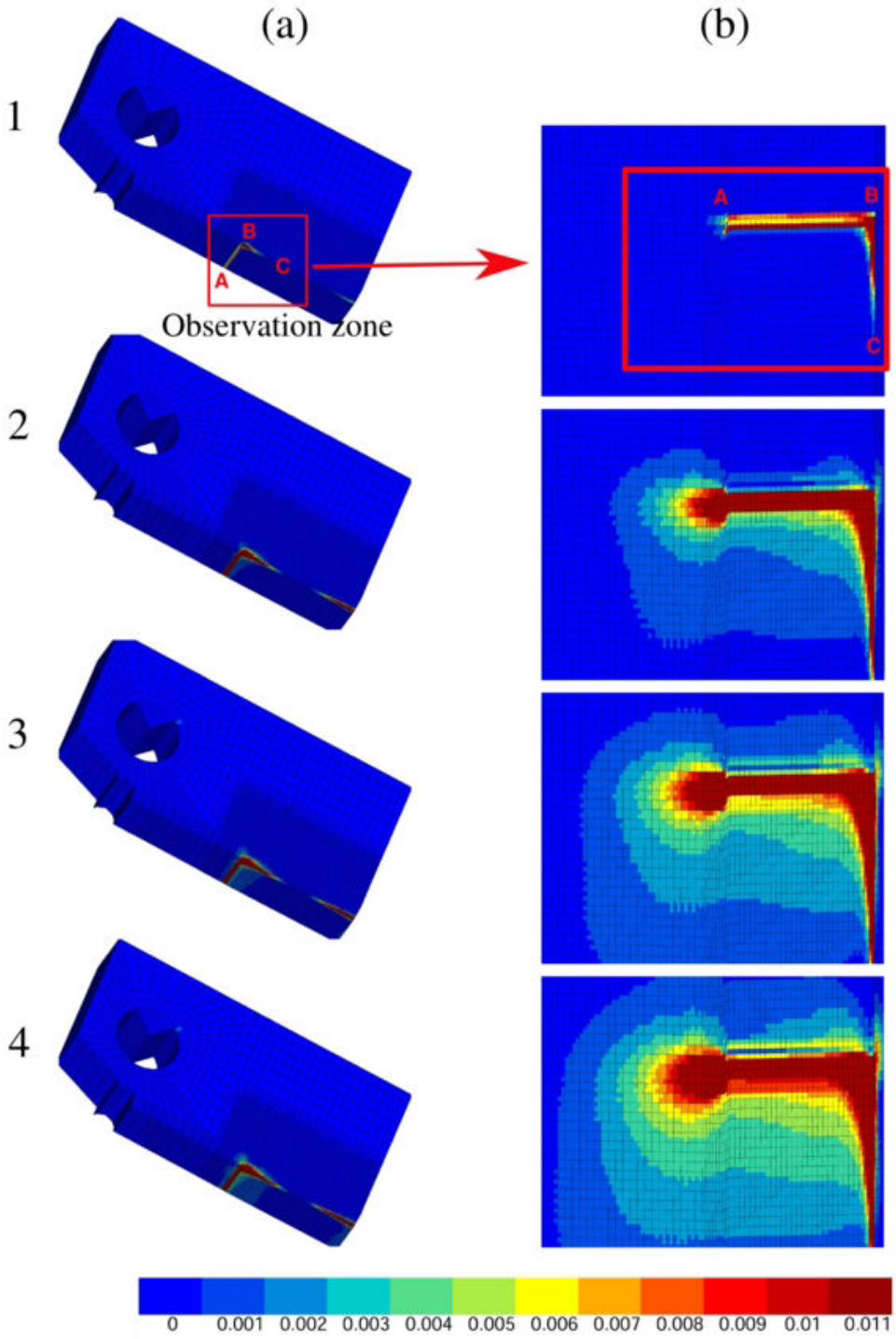

Figure 4.19: Maps of accumulated plastic strain at the crack tip for Grade 2 simulated at constant load of 13 kN: (a) grooved side and (b) zoom at the observation zone.

The simulated and experimental COD vs. time curves for Grade 4 in the constant load test at 18 kN are presented in Figure 4.20. The simulated curve is situated slightly above the experimental one, which is governed by the length of the initial crack used in the simulation.

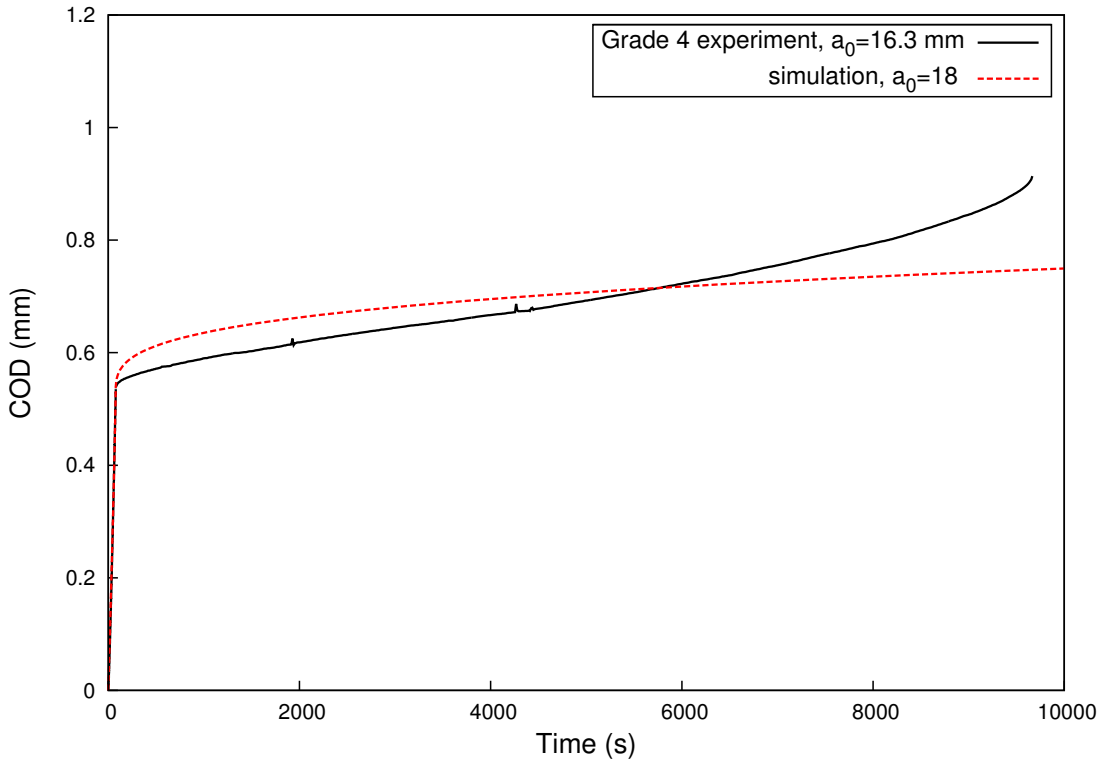

Figure 4.20: The creep deformation behavior of the CT specimen for Grade 4 at constant load of 18 kN.

The presented viscoplastic model was used to simulate tests at constant displacement for Grade 2 and Grade 4. Figures 4.21 and 4.22 compare the experimental curve in continuous line with the computational curve in dot line for Grade 2 and Grade 4, respectively. Grade 2 which in the experiment relaxes the load from 16.6 kN down to 10.5 kN in the first 10000 s, in the simulation is able to relax only down to 12.5 kN. Larger amount of the relaxation in the experiments is due to the slow crack propagation which decreases the load-carrying capacity of the material. In the simulation the crack growth is not taken into account and therefore the load relaxation is only governed by the material viscoplasticity. Moreover, the model does not account for the stiffness of the tensile machine which can also play a role in the relaxation kinetics. Figure 4.22 shows load relaxation from 17 kN for Grade 4 during the 10000 s period down to 15.75 kN in the experiment and down to 15.4 kN in the simulation. In this case the model overestimated the amount of the relaxed load.

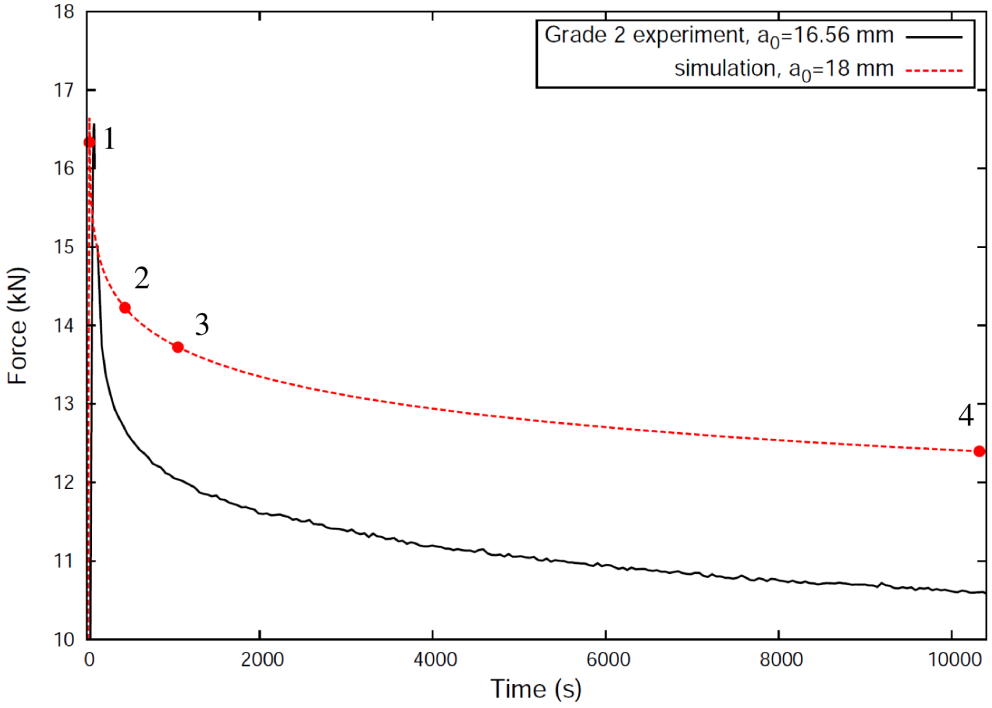

Figure 4.21: The load relaxation behavior of the CT specimen for Grade 2.

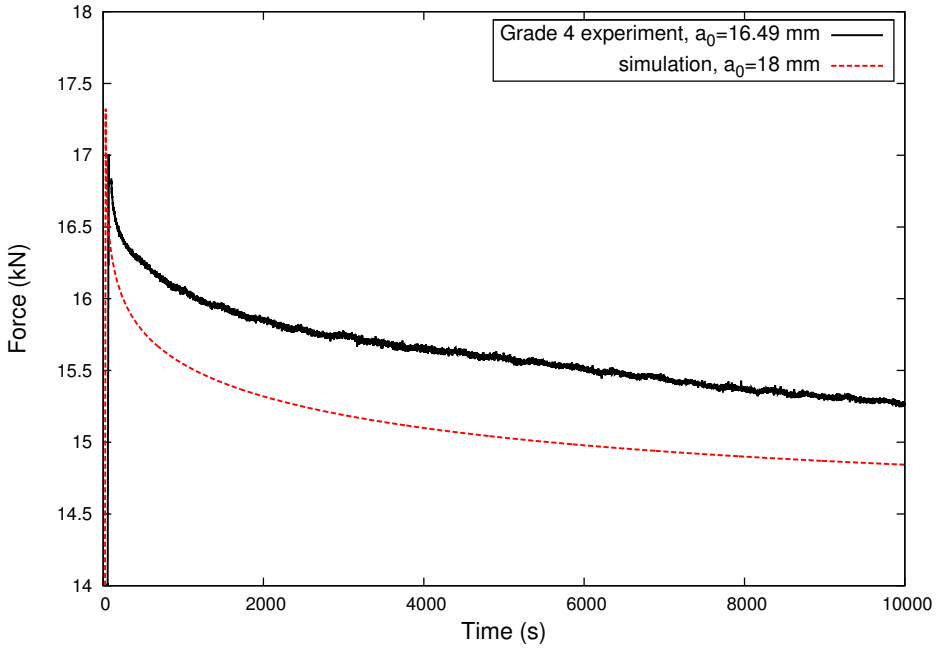

Figure 4.22: The load relaxation behavior of CT specimen for Grade 4.

Figure 4.23 illustrates the distribution of the plastic strain at the crack tip for Grade 2 at constant displacement test at different times corresponding to the points on the simulated curve in Figure 4.21. It can be seen that the deformation tends to saturate with time.

The presented simulations on CT specimen evidence the occurrence of time-dependent deformation at crack tip under various testing conditions which can be attributed to a room-temperature creep and relaxation.

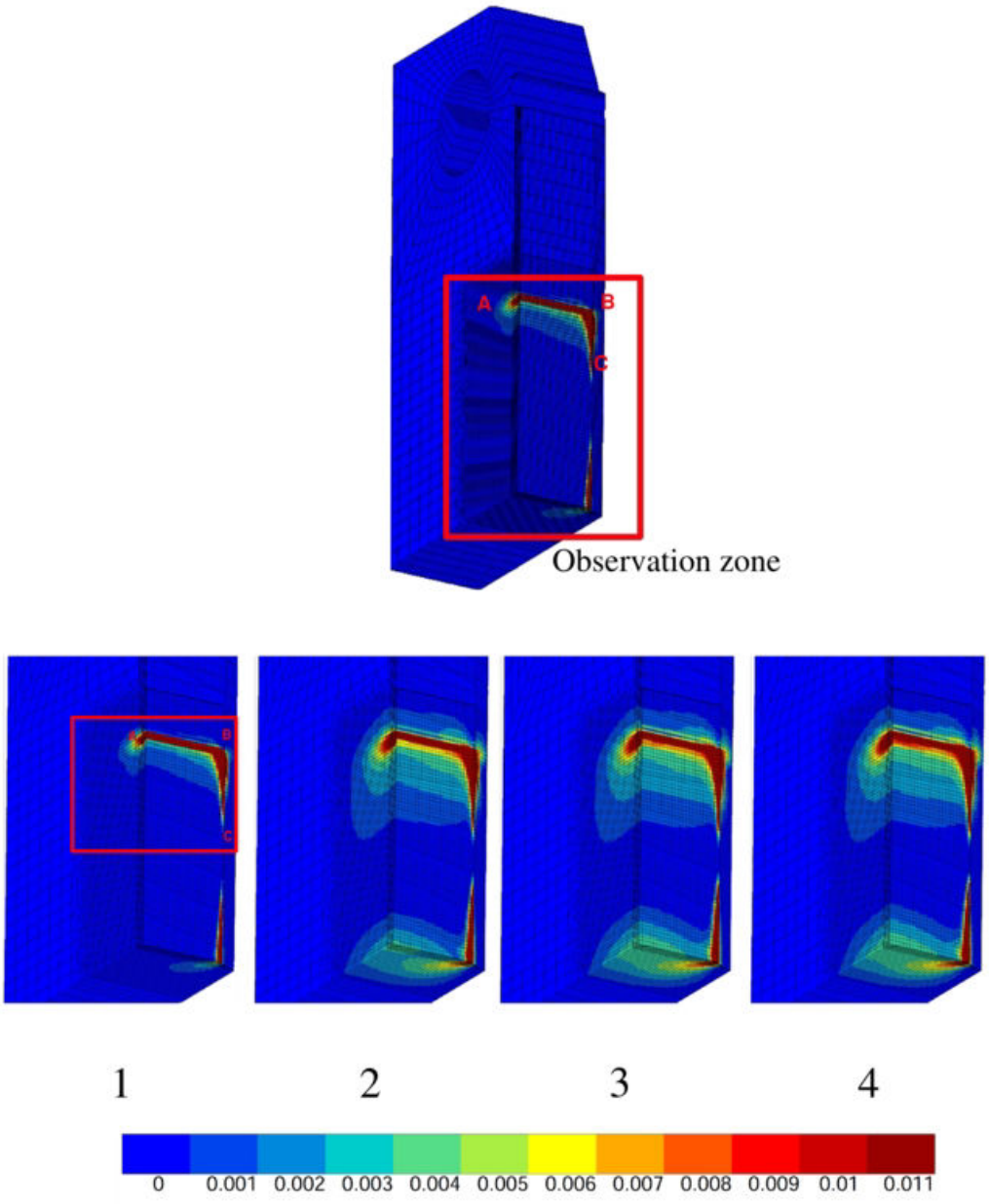

Figure 4.23: Maps of accumulated plastic strain at the crack tip for Grade 2 simulated at constant displacement.

As a next step, the viscoplastic model was used to evaluate the hydrogen distribution at the crack tip. For this, it is assumed that hydrogen concentration in normal interstitial sites is in equilibrium with hydrostatic stress [149] which dictates the amount of hydrogen accumulation in the stressed lattice relatively to the stress-free lattice [118]. Total hydrogen concentration at a point is determined based on the hydrostatic stress through [186]:

$$c(t) = c_0 \exp\left(\frac{\sigma_{kk} \upsilon_H}{3RT}\right) \tag{4.9}$$

where c_0 is the hydrogen concentration of the stress-free crack face in equilibrium with the hydrogen gas, $\sigma_{kk}/3$ is the local hydrostatic stress, υ_H is the partial molar volume of hydrogen ($2{\cdot}10^{-6}\,\frac{m^3}{mol}$), R is the gas constant ($8.314\,\frac{J}{Kmol}$), T=293 K.

The presented simulations do not consider hydrogen transport (trapping effect by dislocations), but assumes instantaneous hydrogen diffusion in the normal interstitial lattice sites (NILS) (diffusion coefficient of hydrogen in α Ti $D \approx 9.5{\times}10^{-9}$ m^2/s at room temperature). The aim of the analysis is to study the distribution of hydrostatic stress (and thus hydrogen distribution) in the vicinity of a blunting hydrogen-induced crack tip in elastic-viscoplastic material for different types of loading.

Figure 4.24 shows the calculated profile of the hydrogen concentration along the ligament of a CT specimen for Grade 2 in the tests with monotonic rising load. Each curve represents the evolution of hydrogen concentration at a given time along the ligament. Hydrogen content achieves the highest value of 12 ppm at a distance of 0.66 mm ahead of the crack tip. At the crack tip, hydrogen concentration is equal to the initial value of 9 ppm due to the used constant lattice hydrogen concentration boundary condition [105]. Maximum hydrogen concentration of 15 ppm is localized ahead of the crack tip for Grade 4 and it recovers to its normal value of 11 ppm at a distance of 10 mm. The evolution of hydrogen concentration confirms that the investigated systems do not form hydrides (the solubility limit of H in Grade 2 and Grade 4 is $\approx$ 25-30 ppm). The presented curves show that hydrogen tends to get concentrated ahead of the crack tip and its content increases during the monotonic rising load test. It is also confirmed by the series of maps of hydrogen distribution in the CT specimen presented in Figure 4.26.

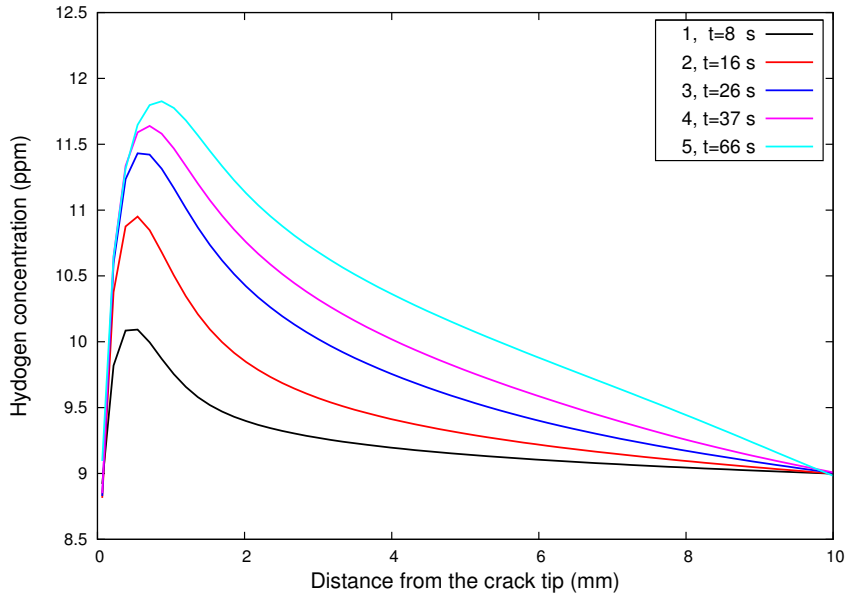

Figure 4.24: Evolution of hydrogen concentration ahead a crack tip during monotonic rising load test for Grade 2. The units of the scale are ppm.

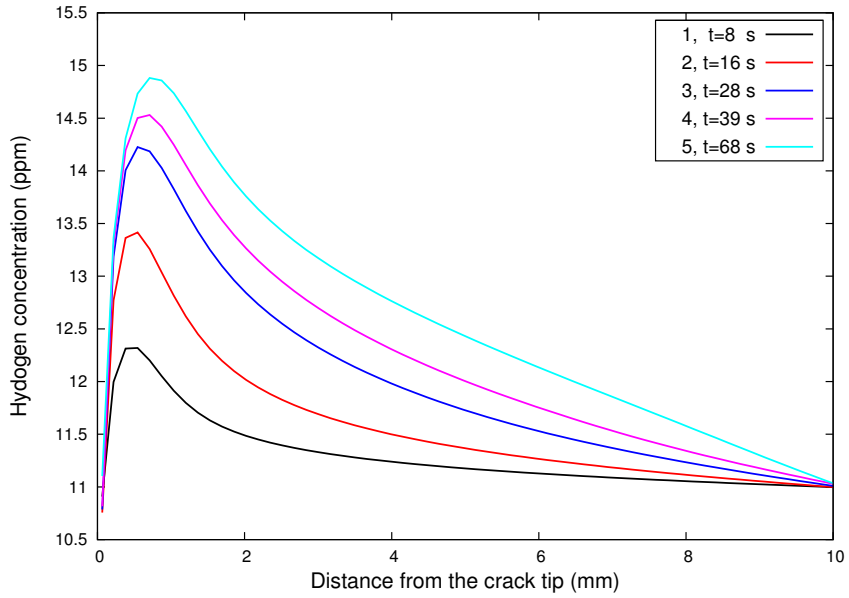

Figure 4.25: Evolution of hydrogen concentration ahead a crack tip during monotonic rising load test for Grade 4. The units of the scale are ppm.

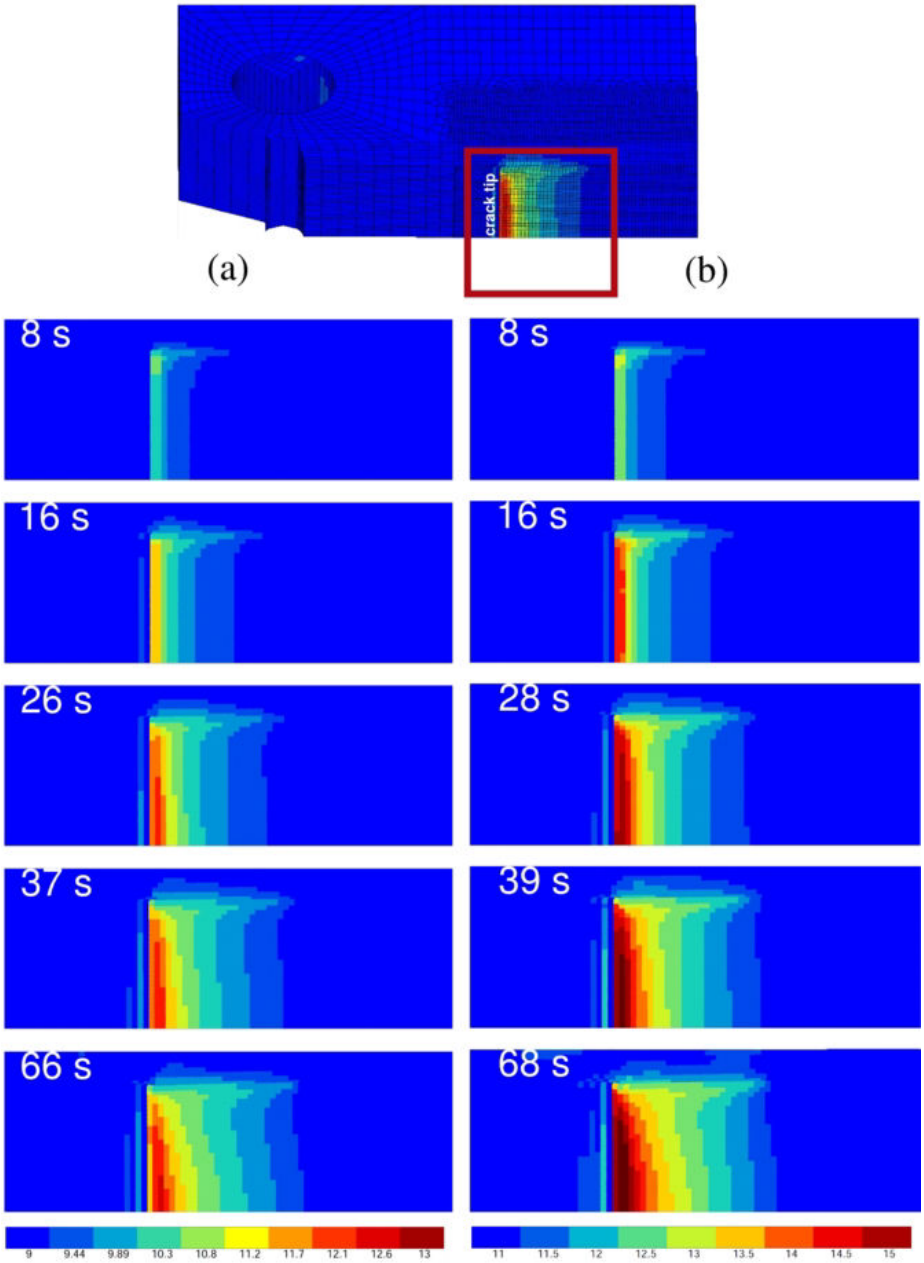

Figure 4.26: Distribution of hydrogen concentration ahead a crack tip during monotonic rising load test for (a) Grade 2 and (b) Grade 4. The units of the scale are ppm.

Figures 4.27 and 4.28 illustrate the distribution of hydrogen concentration in the test under static applied load of 13 kN for Grade 2 and 18 kN for Grade 4. The corresponding maps of hydrogen distribution are given in Figure 4.29. It can be seen that hydrogen concentration ahead of the crack tip decreases a bit with time. This drop is a consequence of the decrease of hydrostatic stresses that cannot be maintained on the blunted crack tip due to the increased plastic strain at the crack tip (see Figure 4.19). Since in the present model the effect of the kinetics of hydrogen transport to the sites where degradation occurs is not taken into account, then the resultant hydrogen concentration decreases with time.

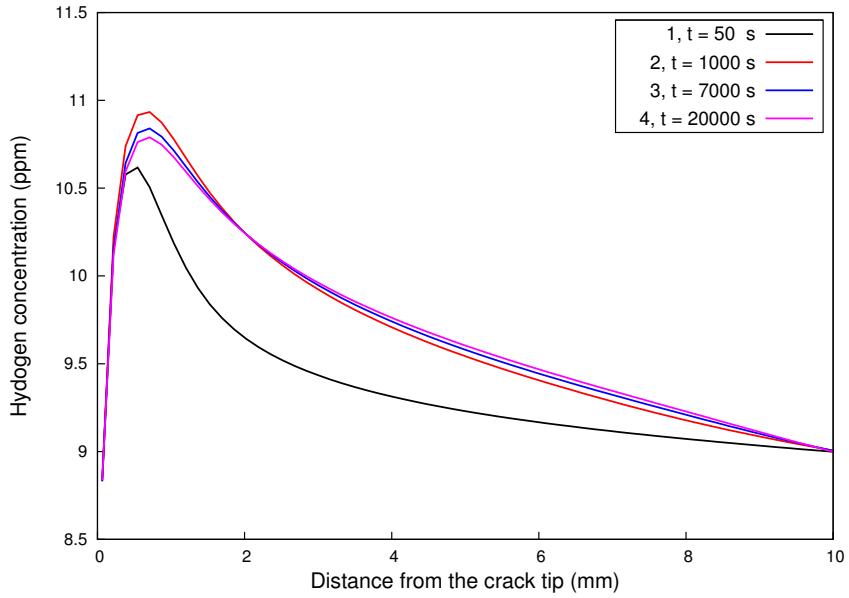

Figure 4.27: Evolution of hydrogen concentration ahead a crack tip for Grade 2 in creep test at 13 kN. Scale units are ppm.

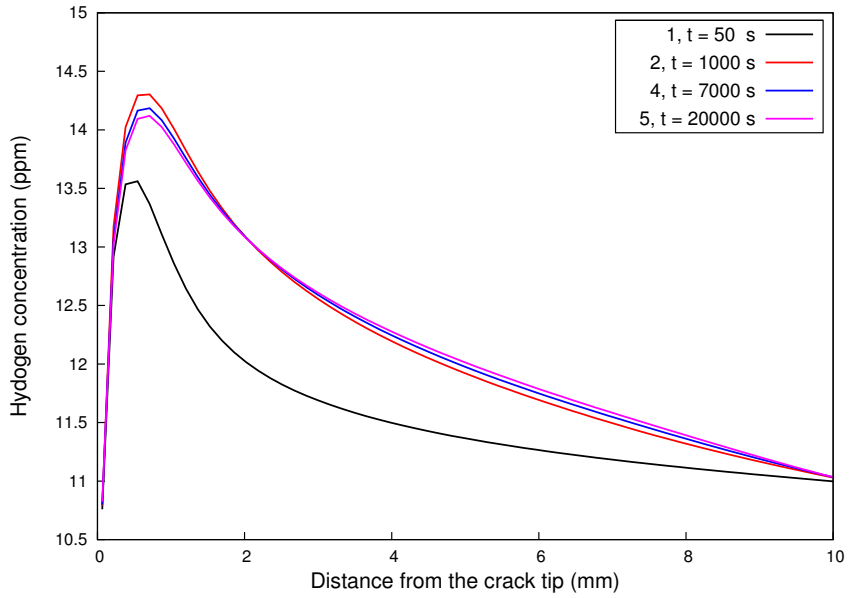

Figure 4.28: Evolution of hydrogen concentration ahead a crack tip for Grade 4 in creep test at 18 kN. Scale units are ppm.

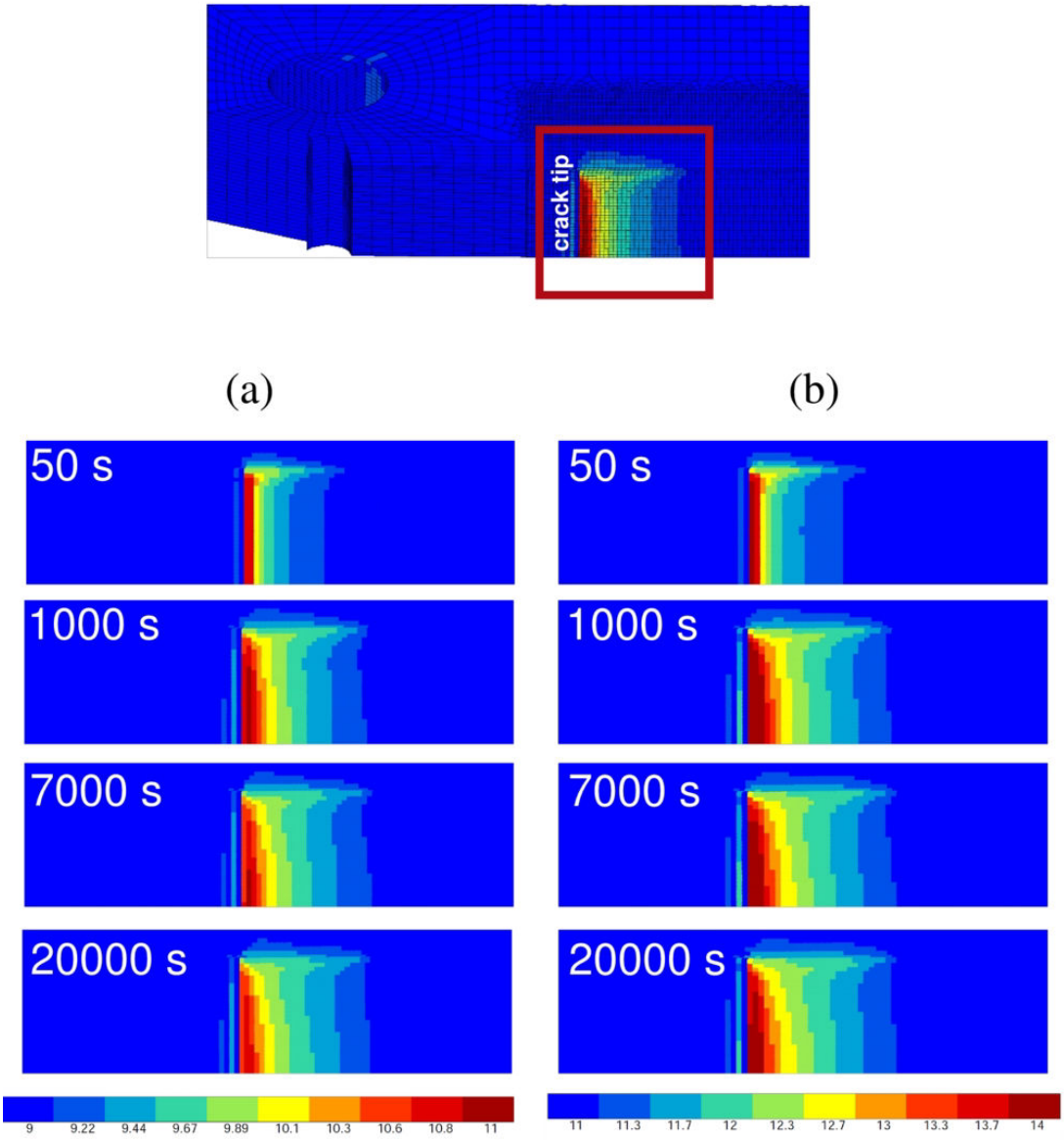

Figure 4.29: Distribution of hydrogen concentration ahead a crack tip during creep test for (a) Grade 2 at 13 kN and (b) Grade 4 at 18 kN. Scale units are ppm.

In the existing studies on hydrogen embrittlement where non-linear diffusion of hydrogen was coupled with elastic-plastic deformation, the effect of loading time on hydrogen diffusion near the blunting crack tip was investigated [96]. The loading time was found to be an important factor in monotonic loading. With increasing loading time, the time for hydrogen diffusion increases leading to the additional supply of hydrogen into trap sites. Note that traps are associated with structural materials defects such as dislocations or dislocation debris. Increasing hydrogen concentration enhances the dislocation mobility and therefore increases the amount of plastic strain. On the other hand, the increased plastic strain leads to the decrease of hydrostatic stress, and thus to the decrease in maximum value of hydrogen lattice concentration. As a result, the crack growth must slow down which was experimentally observed in Chapter 3.

Figure 4.30 and 4.31 shows the evolution of the hydrogen concentration in the tests where macroscopic displacement remains constant. In this type of test as the stress intensity factors

drops, there is a concomitant decrease in hydrostatic stress and thus in hydrogen concentration field (see Figure4.32).

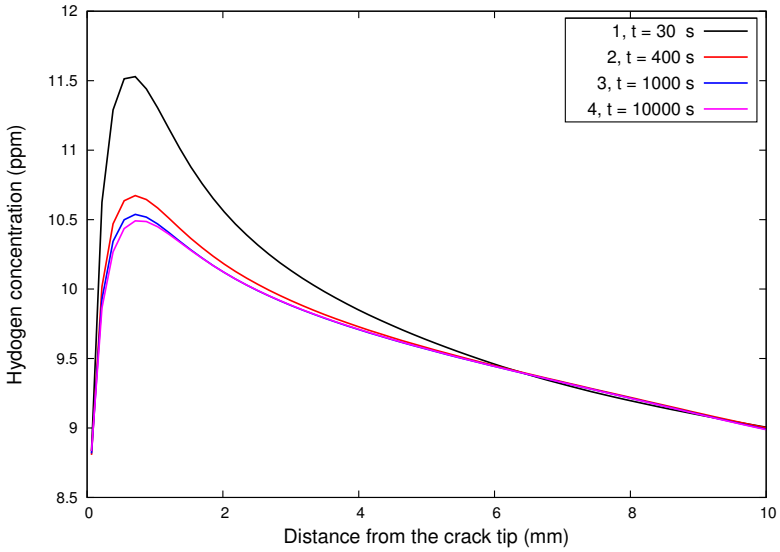

Figure 4.30: Evolution of hydrogen concentration ahead a crack tip for Grade 2 in relaxation test. Scale units are ppm.

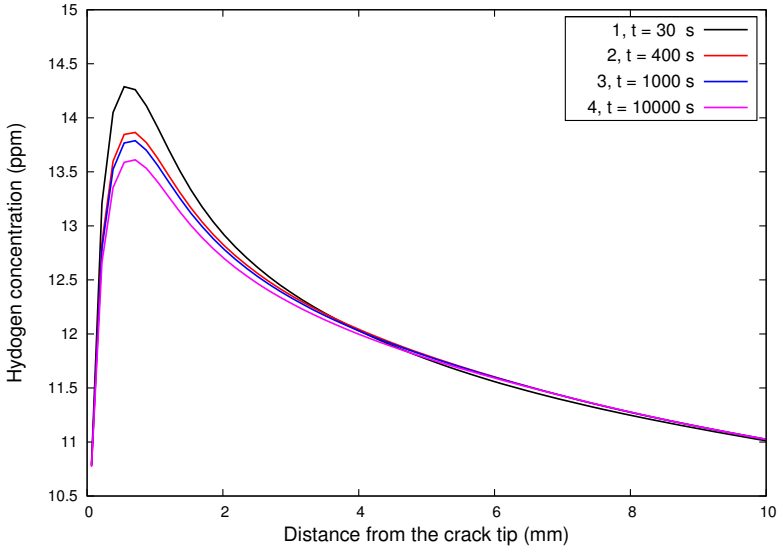

Figure 4.31: Evolution of hydrogen concentration ahead a crack tip for Grade 4 in relaxation test. Scale units are ppm.

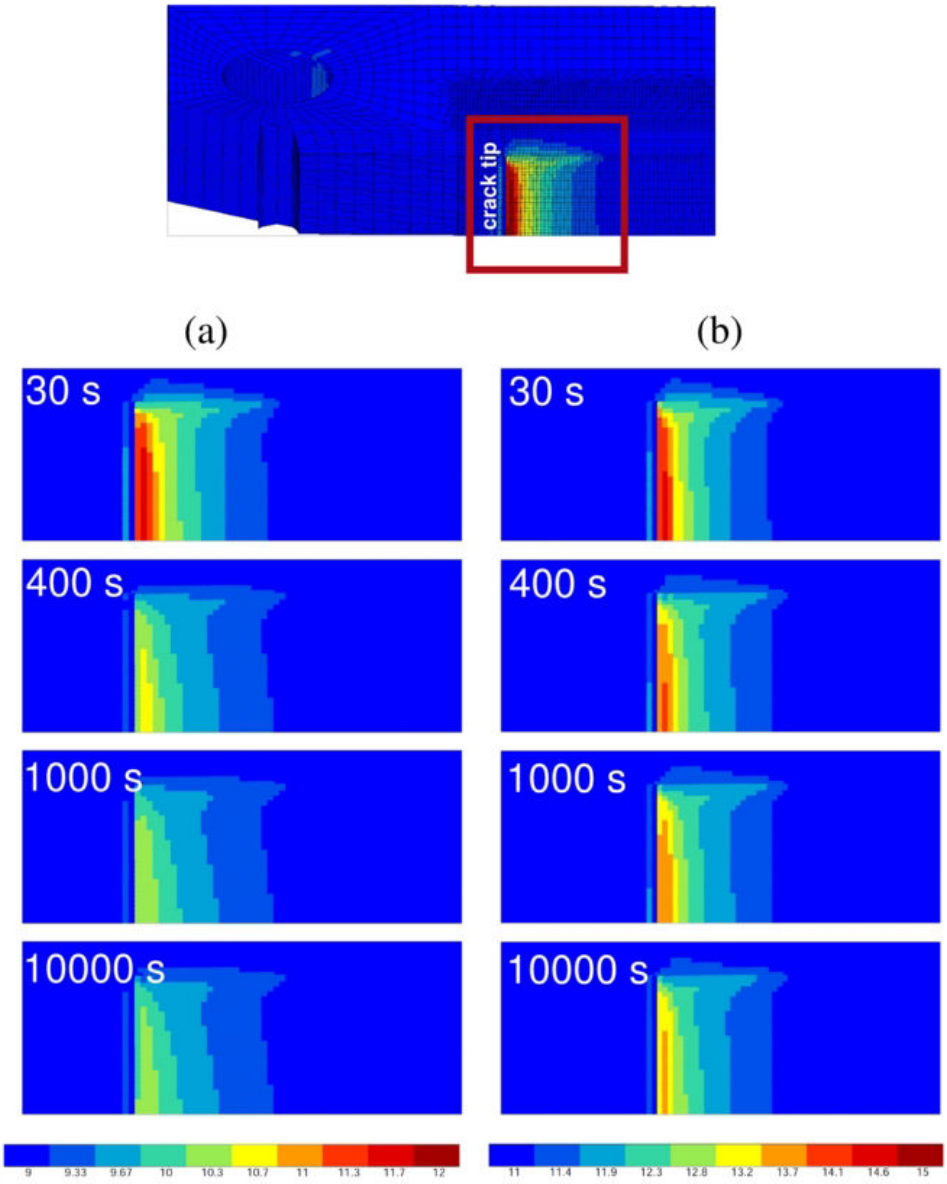

Figure 4.32: Distribution of hydrogen concentration ahead a crack tip during relaxation test for (a) Grade 2 and (b) Grade 4. Scale units are ppm.

The proposed elastic-viscoplastic constitutive model was used to analyze time dependence that was observed under deformation and creep behavior in CP α Ti. The simulations were verified by experimental results. The calculated strain fields under different loading conditions confirm the significance of creep at crack tip, which increases with time and load. The distribution of hydrogen concentration based on the values of hydrostatic stress in the vicinity of a blunting crack tip was analyzed. The numerical results indicate that hydrogen tends to get concentrated ahead of the crack tip where its concentration reaches 12 ppm for Grade 2 and 15 ppm for Grade 4.

4.2.5 Discussion on the hydrogen effect on the plastic behavior

The further discussion on the hydrogen effect on fast and slow crack propagation in α Ti will be based on the experimental curves obtained for Grade 2 *base* and Grade 2 *charged* in the fracture toughness test presented in Figure 4.33 and in the SLC test under constant load of 13 kN presented in Figure 4.34. Note that the results of constant load test are presented in the coordinates $\triangle$ COD vs. time where $\triangle$ COD = COD-COD_0. According to Birnbaum and Sofronis [31], hydrogen induces material softening at the microscale by enhancing the dislocation mobility by reducing the strength of barriers to dislocation motion. In a continuum mechanics formalism, softening can be described through a decrease in a local flow σ_Y stress with increasing hydrogen content such that [190]:

$$\sigma_Y = \sigma_0^H \left(1 + \frac{\varepsilon^p}{\varepsilon_0}\right)^{1/n} \tag{4.10}$$

where σ_0^H is the initial yield stress in the presence of hydrogen that decreases with increasing hydrogen concentration, ε_0 is the initial yield strain in the absence of hydrogen, ε^p is the logarithmic strain in uniaxial tension, and n is the hardening exponent that is assumed to remain unaffected by hydrogen [118]. The hydrogen effect on the local continuum flow can be modeled through the initial yield stress σ_0^H as:

$$\sigma_0^H = \phi(c)\sigma_0 \tag{4.11}$$

where $\phi(c)$ is a monotonically decreasing function of the local hydrogen concentration measured in atoms per solvent lattice atom, and σ_0 is the initial yield stress in the absence of hydrogen [186]. All authors who used this approach had precised that Eq. 4.10 and 4.11 should be viewed as an attempt to quantify to a first approximation the experimental understanding of the hydrogen effect on dislocation mobility in the continuum formalism [186, 1, 118].

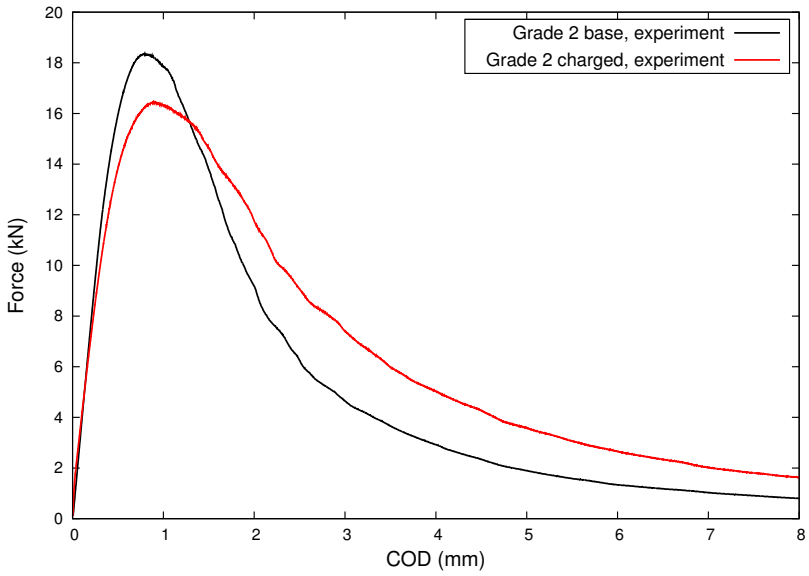

Figure 4.33: Experimental fracture toughness curves for Grade 2 *base* (9 ppm H) and *charged* (15 ppm H).

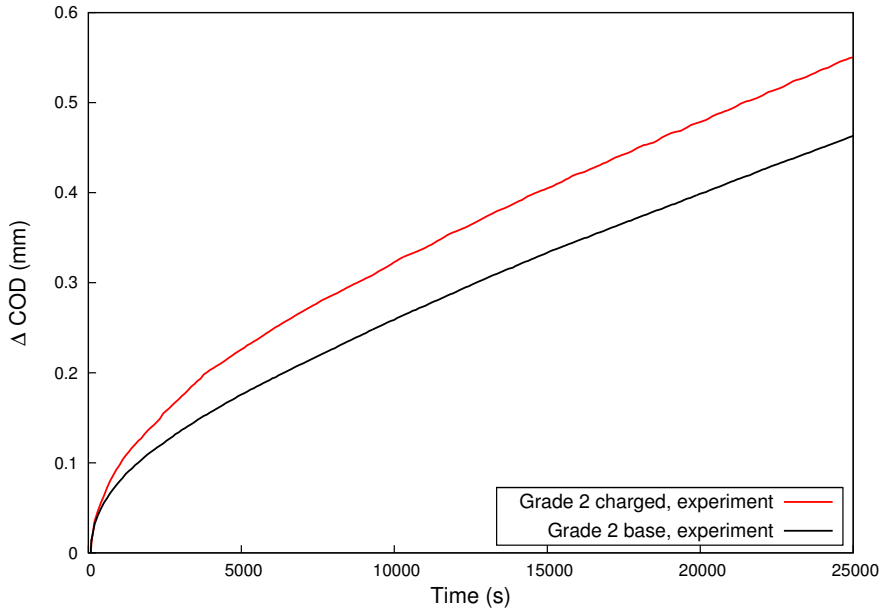

Figure 4.34: Experimental curves of SLC under constant load of 13 kN for Grade 2 *base* and *charged*.

In the present study the softening effect of hydrogen was evidenced in the fracture toughness tests (see Figure 4.33). The decreased yield stress was also observed in the tensile tests with strain rate jumps carried out on forged billet of Ti0 (see Figure 4.35) with different levels of hydrogen that can be found in thesis work of Barkia [17]. It is important to note that, the experimental results of strain rate jump tests carried out on Grade 2 and Grade 4 failed to reveal any consistent effect of hydrogen content [17].

If assuming that the increased hydrogen concentration C_H results in a decreasing yield stress σ_0^H of the material due to the enhanced dislocation mobility at the crack tip (hydrogen enhanced localized plasticity mechanism), as schematically presented in Figure 4.36, then the intense creep can take place at the crack tip. The resultant measured crack opening displacement (COD) which includes the contribution from the crack propagation and CTOD (crack tip opening displacement) will be larger for the material with higher hydrogen concentration. This is actually the case in the SLC test under constant load of 13 kN presented in Figure 4.34 for Grade 2 *base* and *charged*.

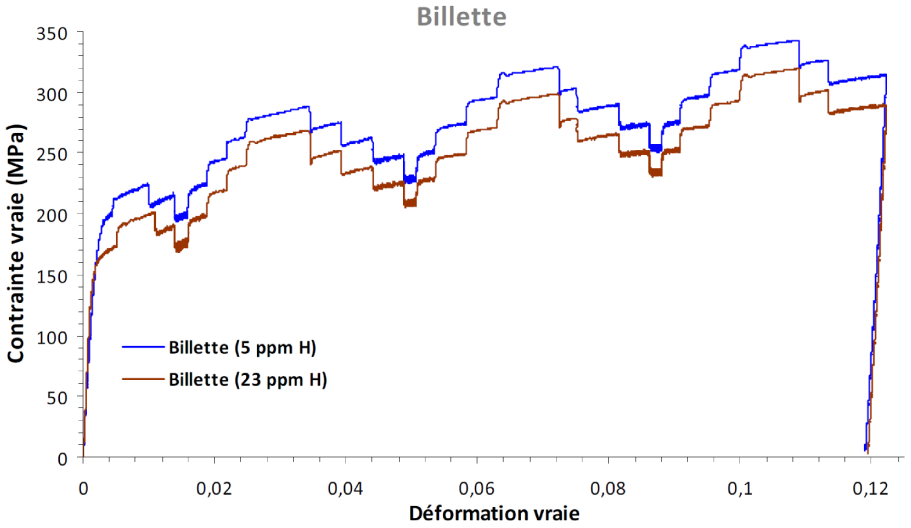

Figure 4.35: Comparison of experimental stress-strain curve of Ti0 with different level of hydrogen [17].

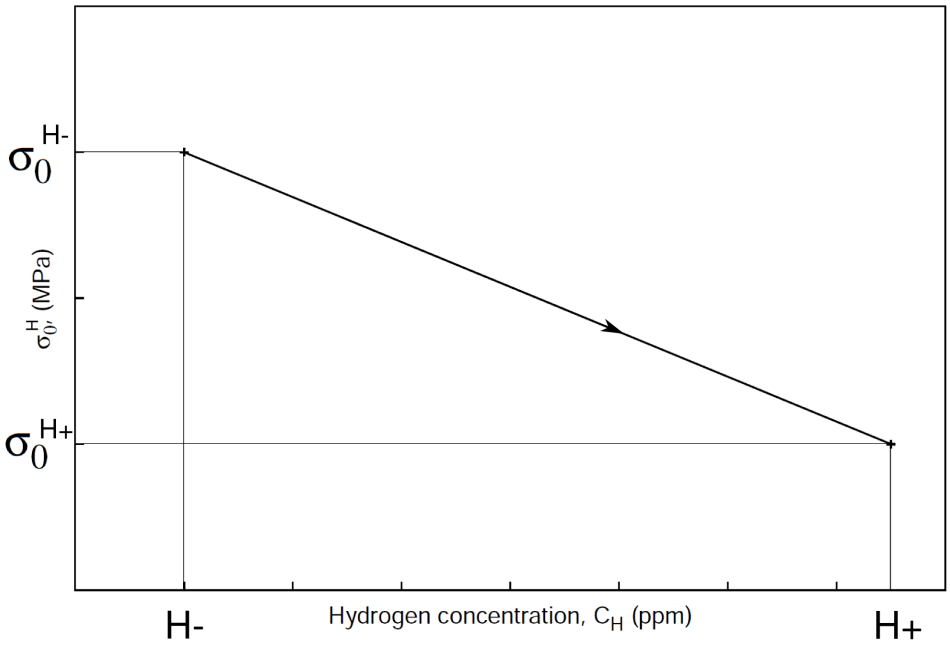

Figure 4.36: Schematic illustration of yield stress as a function of hydrogen concentration.

In order to validate the proposed interpretation of the fracture behavior in Ti Grade 2 in the presence of hydrogen, numerical simulations were carried out on CT specimen with a lower value of yield stress (decreased at 10% from 170 MPa down to 153 MPa). The value of 10 % was choosen based on the experimental results of strain rate jump tests obtained for Ti0 (see Figure 4.35) with different levels of hydrogen. The comparison of the experimental and simulation results of fast cracking for Grade 2 *base* and *charged* is presented in Figure 4.37. The correct prediction of the fast cracking behavior for *charged* material is obtained. The decreased strength of the material with hydrogen (due to the lower yield stress) resulted in the degradation of the fracture toughness. Figure 4.38 shows the FE simulations and experiments of SLC tests under constant load of 13 kN for Grade 2 *base* and *charged* in the coordinates COD vs. time. The obtained results show a good reproduction of the tendency of COD to increase in the material with lower yield stress.

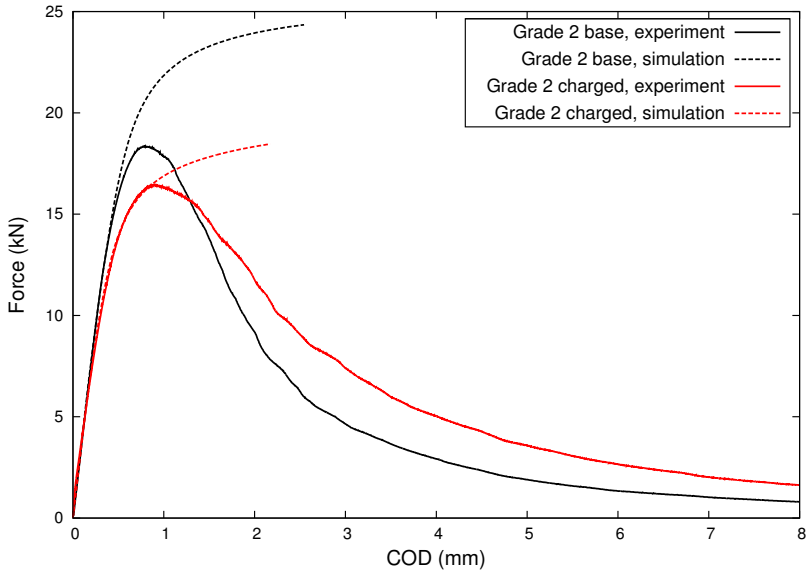

Figure 4.37: Comparison of experimental and simulation fracture toughness behavior of the CT specimen of Grade 2 *base* and *charged*.

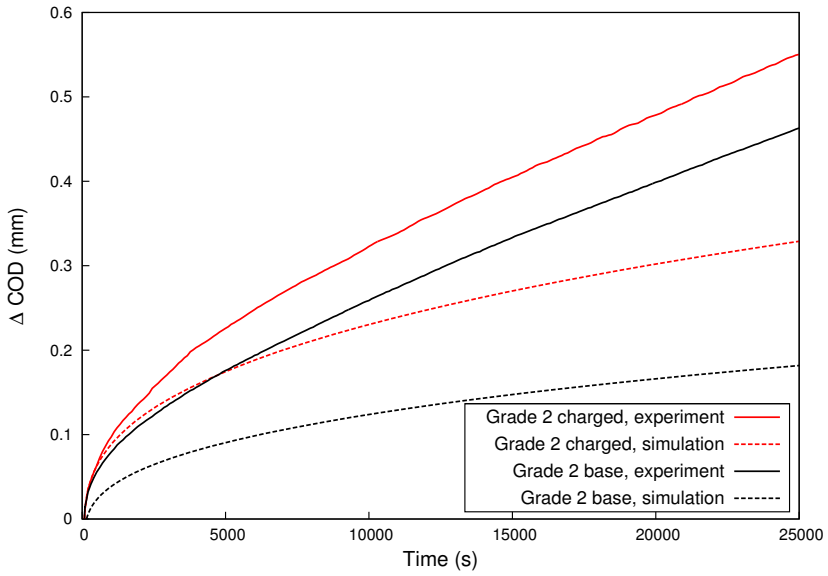

Figure 4.38: Comparison of experimental and simulation creep deformation behavior of the CT specimen of Grade 2 *base* and *charged* at constant load of 13 kN.

An attempt was made to identify the criterion of crack propagation in the SLC tests. At first the RKR (Ritchie-Knott-Rice) criterion for stress-controlled crack extension was used, which stays that fracture occurs when the local opening stress ahead of a crack tip exceeds the critical local fracture strength of the material over a characteristic distance related to the material microstructure [167]. Figure 4.39 shows normalized opening stress σ_{22}/σ_0 ahead of the crack tip at t=10000 s for *base* and *charged* material. *Charged* material shows lower opening stress compared to the *base* material. The maximal σ_{22} vs. time is traced in Figure 4.40 for both materials. It can be seen that the critical value of the opening stress is attained for both materials during the ramp up period, which means that the crack starts propagating within the first 100 s. However, as it was shown in Figure 3.31 (b), the stress intensity factor for both Grade 2 *base* and Grade 2 *charged* starts increasing (implying crack propagation) only after 1000 s. It is clear from this figure that the RKR criterion cannot explain the experimentally observed delay in crack occurrence in the *charged* material.

In contrast, if now assuming that the crack propagation needs the attainment of critical value of the local strain $\varepsilon_{critical}$ at crack tip, then the delayed fracture in the *charged* material can be explained as follows: hydrogen increases the plasticity at the crack tip (HELP mechanisms) and at the same time it can increase the capacity of the material to overcome plastic deformation before fracture, thus increasing the value of the critical strain $\varepsilon_{critical}$. Schematically it can be represented in Figure 4.41, where the enhanced creep strain at the crack tip in the presence of hydrogen (denoted as $H+$) increases the capacity of the material to deform before the beginning of crack extension. As a result, the time to failure in slow cracking is increased for the material with higher hydrogen content as it is shown in Figure 4.42.

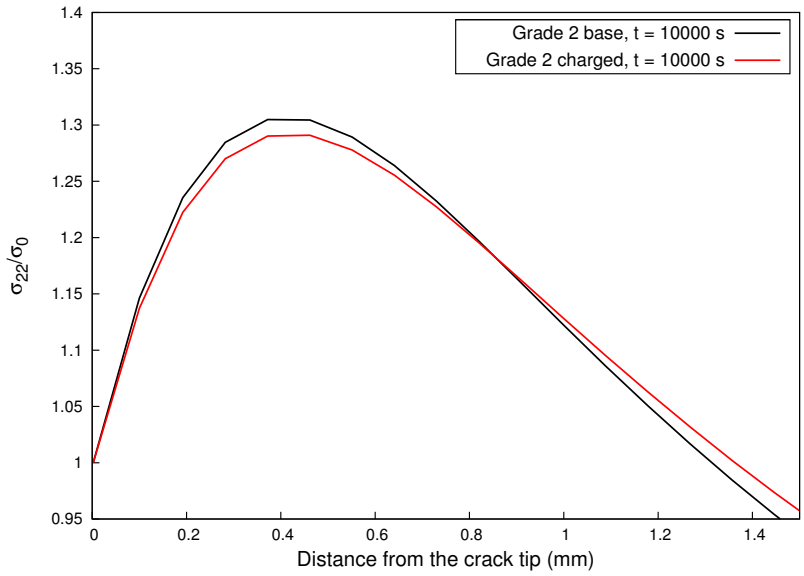

Figure 4.39: Simulated normalized opening stress σ_{22}/σ_0 near the crack tip at t=10000 s for Grade 2 *base* and *charged*.

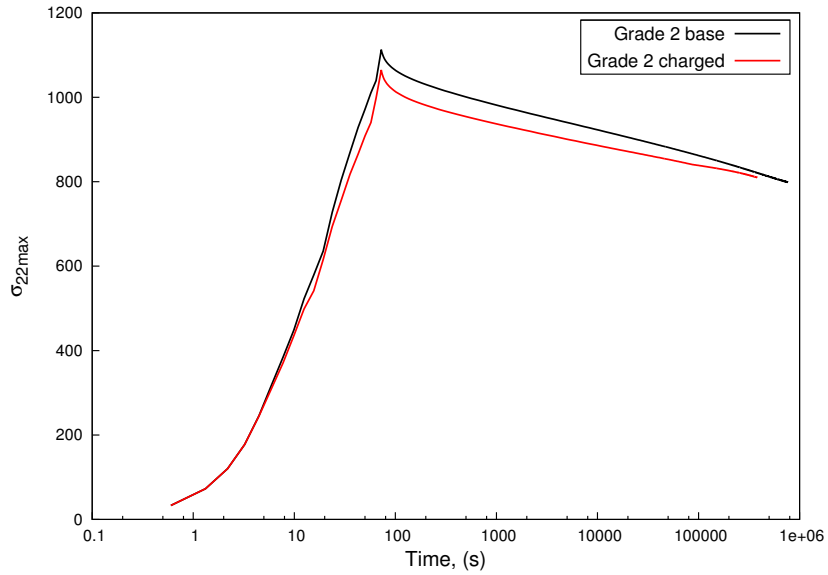

Figure 4.40: The evolution of the simulated maximal opening stress σ_{22} for Grade 2 *base* and *charged*.

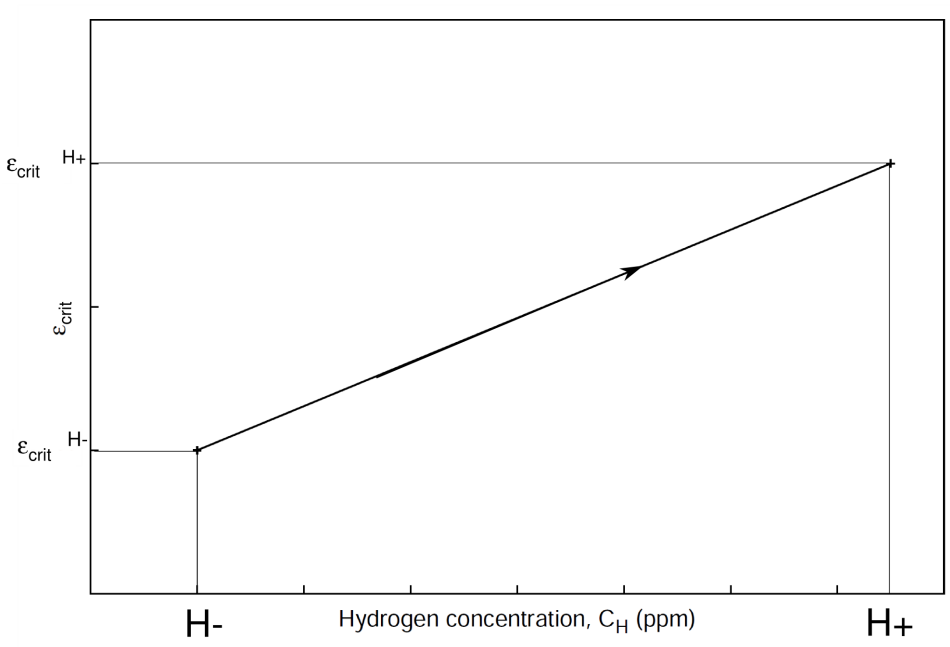

Figure 4.41: Schematic illustration of plastic strain due to creep as a function of hydrogen concentration.

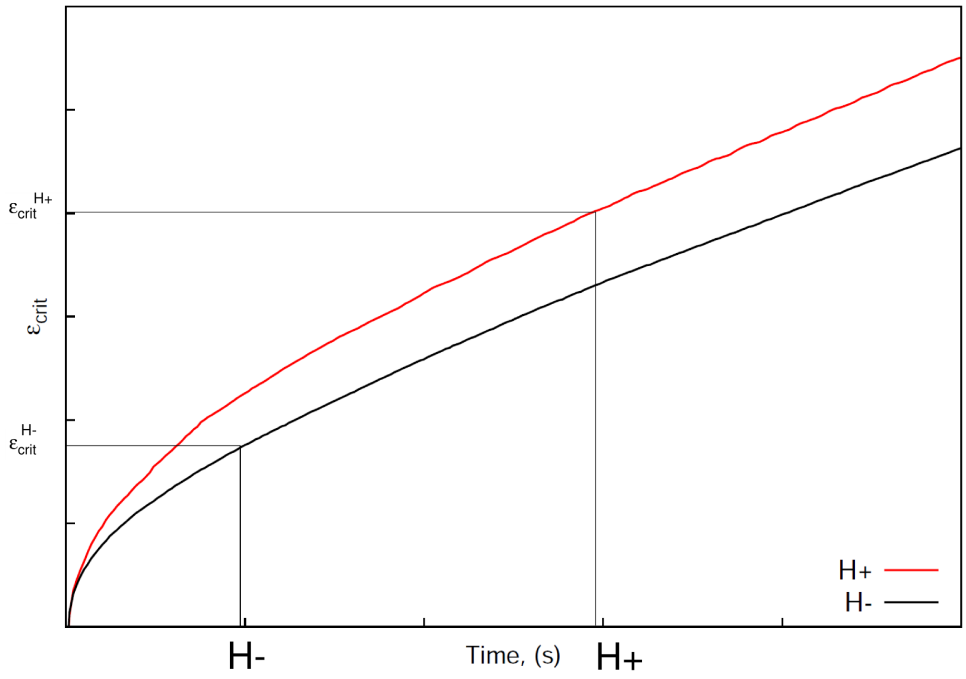

Figure 4.42: Schematic illustration of plastic strain due to creep as a function of time for different hydrogen concentration.

These results taken together suggest that hydrogen softens material at the crack tip leading to the fracture toughness decrease as (K_{fast}) and improvement in the resistance to SLC (K_{slow}) as presented in Figure 4.43. It should be noted that such interpretation of the beneficial effect of hydrogen enhanced localized plasticity on the fracture behavior of Ti alloys differs from the usual 'classical' interpretation of fracture under HELP mechanism. According to this 'classical' interpretation, HELP leads to the constrained plasticity, and localized plastic fracture process. As a result, a localized deformation zone which develops ahead of the crack makes material response more brittle.

The proposed interpretation of the beneficial effect of hydrogen on SLC behavior and detrimental effect on fracture toughness is only a try to explain in a simple way the anomalous behavior observed in Ti in the presence of hydrogen. The present analysis does not address the connection between hydrogen and classical ductile rupture mechanisms such as void nucleation, growth and coalescence. Further studies with more sophisticated extended model which can account for the main ductile rupture modes in the viscoplastic material is needed to elucidate the understanding of fracture in the presence of hydrogen.

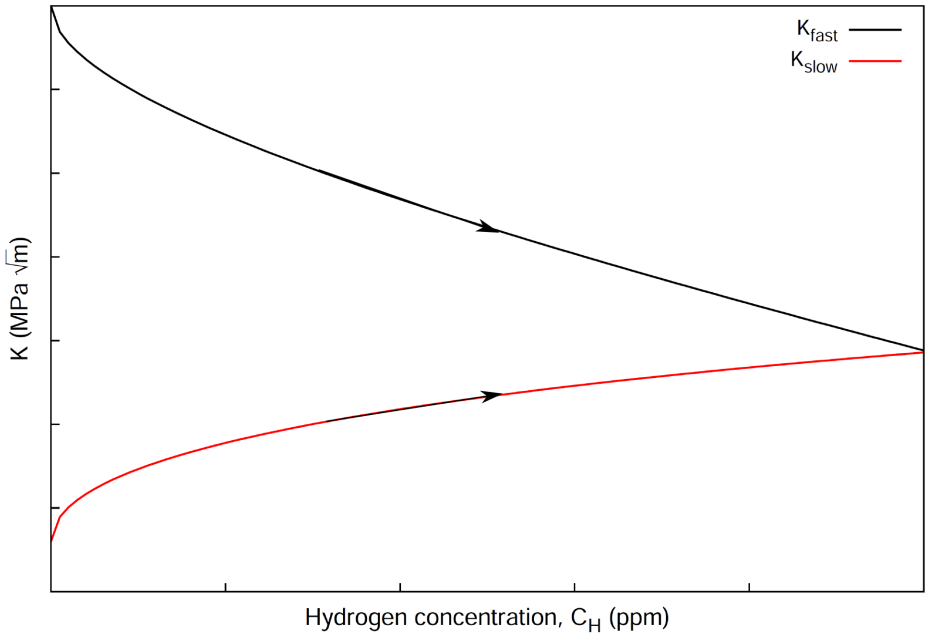

Figure 4.43: Schematic illustration of variation of fracture toughness (K_{fast}) and threshold stress intensity (K_{slow}) with hydrogen concentration.

4.3 Simulation of crack growth

4.3.1 Cohesive zone model approach

Identification of CZM parameters

In the previous section constitutive equations describing viscoplastic behavior of the material and taking anisotropy into account were formulated and the model parameters were identified. A further step consists in applying this model to study the crack propagation in the conditions when sustained load cracking phenomenon was experimentally observed. Note that hydrogen effects on the fracture behavior is not taken into account at this step. The cohesive zone approach was chosen for modeling crack propagation. At first, simulations of fracture toughness tests on 3D CT specimen were performed in order to identify the parameters of the cohesive zone elements. The cohesive law is generally described by two parameters: the normal cohesive traction T, and the separation distance normal to the crack plane, δ. As the first approximation, a Crisfield-debonding model which is described through the evolution of a scalar variable λ representing the damage was used [5]. This damage variable λ ranges from 0 for the interface in perfect cohesion to 1 for the completely debonded state. This decohesion parameter λ is defined as:

$$\lambda = \frac{1}{\eta}\frac{\langle\kappa\rangle}{1+\langle\kappa\rangle}$$

where

$$\begin{cases} \langle\kappa\rangle = \sqrt{\left(\frac{\langle u_N\rangle}{\delta_{0N}}\right)^2 + \left(\frac{u_T}{\delta_{0T}}\right)^2} - 1 \\ \eta = 1 - \frac{\delta_{0N}}{\delta_N} = 1 - \frac{\delta_{0T}}{\delta_T} \end{cases} \tag{4.12}$$

The normal and shear opening displacements are denoted u_N and u_T, respectively, and the values δ_N and δ_T correspond to the normal and shear displacements at complete separation for pure normal and pure shear modes respectively. The parameters δ_{0N} and δ_{0T} represent the opening displacements corresponding to the maximum cohesive traction of the normal and shear components. The brackets $\langle\ \rangle$ indicate that a negative normal displacement plays no role in the decohesion. The normal and shear components of the cohesive traction T, i.e. T_N and T_T are defined as:

$$\begin{cases} T_N = T_{max}(1-\lambda)\frac{u_N}{\delta_{0N}} \\ T_T = \alpha T_{max}(1-\lambda)\frac{u_T}{\delta_{0T}} \end{cases} \tag{4.13}$$

where α is a constant representing the relative magnitude of $\|T_T\|$ with respect to T_N, and T_{max} is the maximum allowable stress. As a result, Crisfiel cohesive zone model is fully described by three parameters: the maximum stress T_{max}, the separation δ_N and the characteristic separation δ_{0N} at which the maximum traction is experienced. The ratio of δ_{0N}/δ_N and δ_{0T}/δ_T have to be equal in order to avoid the restrictions of the evolution equations for the damage parameters [5].

We consider only fracture in Mode I, leading to $u_T = 0$. As a result, the relation between traction-separation can be presented as in the Figure 4.44 which depicts the characteristic separation δ_{0N} at which the maximum traction, T_{max}, is experienced. Energy dissipated during crack propagation is defined as the area under the traction-separation curve.

$$G_c = \frac{1}{2}T_{max}\delta_N = \frac{K_{Ic}^2}{E}(1-\nu^2) \tag{4.14}$$

where G_c is the critical energy release rate, K_{Ic} is the fracture toughness of the material, E is the Young's modulus.

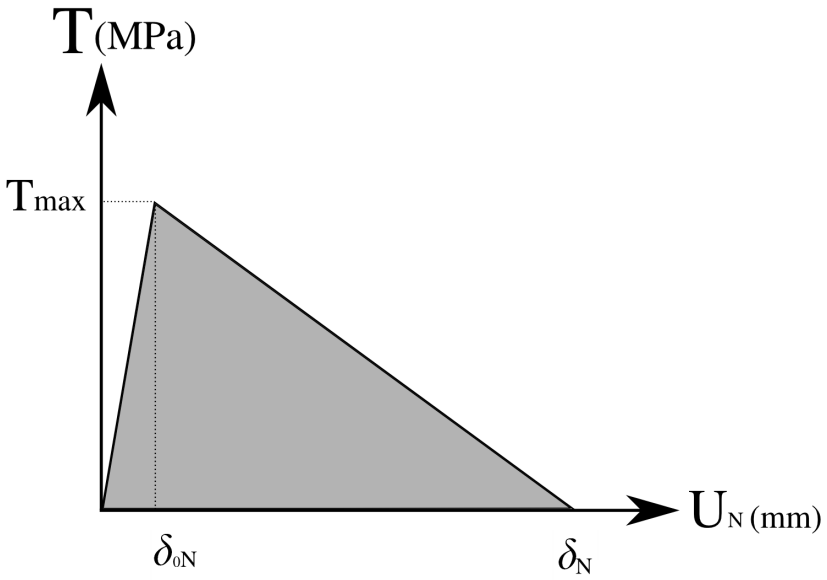

Figure 4.44: Relation traction-displacement on the cohesive zone.

Simulations of Mode I loadings on CT specimen with cohesive zone approach were performed. Figure 4.45 shows the load-line vs. COD measured from FEM simulations with the initial crack size of 16.19 mm. T_{max} and the ratio of δ_{0N}/δ_N were calibrated on the experimental test data for Grade 4. The simulations with CZM gives a reasonable approximation to the experimental load-COD curve. It is important to note that the introduction of the CZM allows to 'correct' the elastic slope of the model by choosing an appropriate parameters of the CZ.

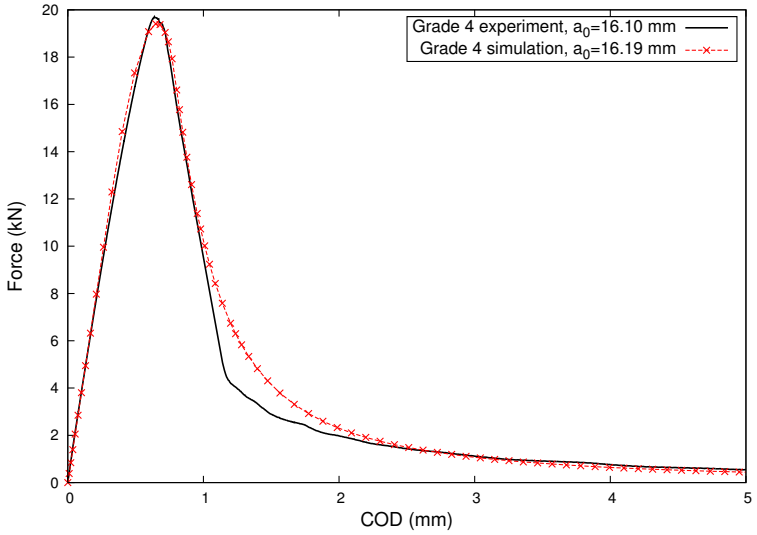

Figure 4.45: Simulation of CT specimen for Grade 4 with cohesive zone model.

Several computations were run for several model parameters sets to calibrate the cohesive

zone model with the experimental data. As expected, T_{max} and δ_{0N} have a strong influence on the fracture behavior. An increase of the cohesive strength T_{max} makes the load higher (Figure 4.46), while the increase of the ratio δ_{0N}/δ_N allows to change the slope of the curve corresponding to the material stiffness (Figure 4.47). The values of the sets of cohesive zone parameters which provides the best fit to the experimental curves of Grade 4 CT specimens are given in Table 4.3.

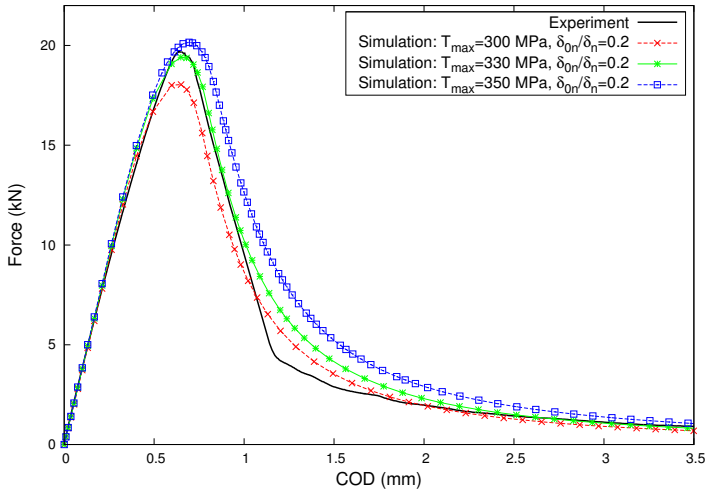

Figure 4.46: Simulation of CT specimen for Grade 4 using different T_{max}.

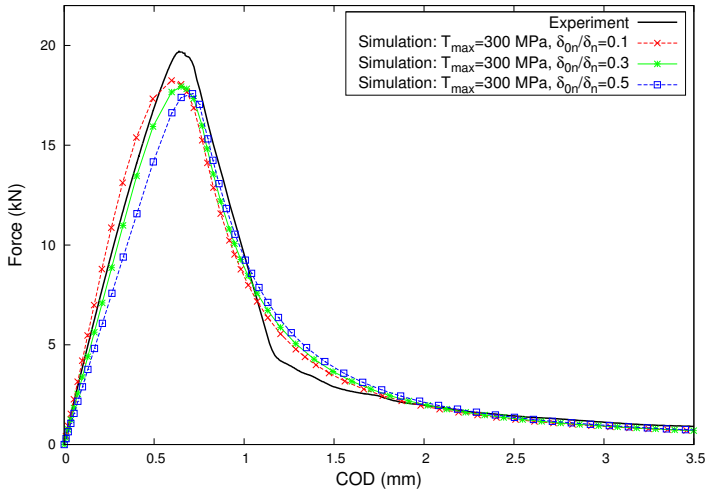

Figure 4.47: Simulation of CT specimen for Grade 4 using different ratio of δ_{0N}/δ_N.

T_{max}, MPa	δ_{0N}, mm	δ_N, mm	δ_{0N}/δ_N
Grade 4			
330	0.048	0.24	0.2

Table 4.3: Identified cohesive zone model parameters for Ti Grade 2 and Grade 4.

Figure 4.48 shows the cohesive zone elements corresponding to the predicted crack extension along the crack plane for several loading stages. The crack front is straight as it was observed in the experiments. Limitations of the present CZM that will be discussed furher did not allow to get any appropriate set of the CZ parameters for Grade 2 which shows more ductile rupture behavior.

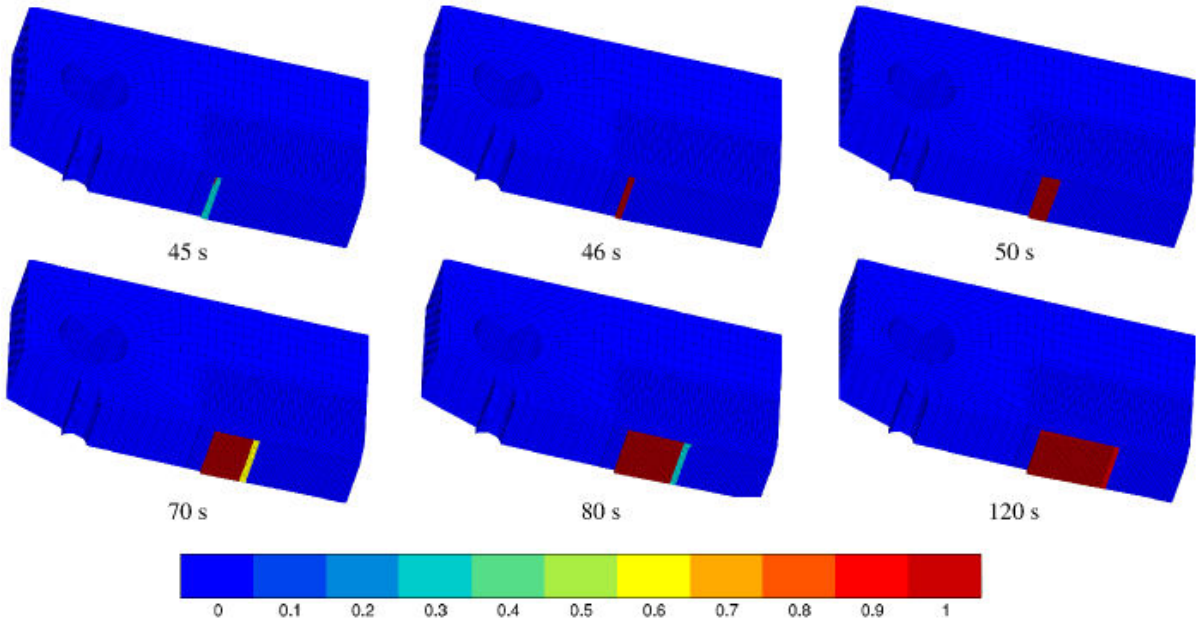

Figure 4.48: The damage variable λ which represents broken CZM elements at the crack.

Limitations of the presented CZM approach

Figure 4.49 shows a comparison of experimental and simulated crack extension. It can be observed that the simulated crack starts growing earlier (at 45 s) than the experimental measurements (at 90 s). The load as a function of crack extension $\triangle\ a$ is plotted in Figure 4.50. It is seen again that the maximum force is reached at a smaller simulated crack length compared to the experimental results. All plots imply that the calculated crack velocity is much larger than the experimental value.

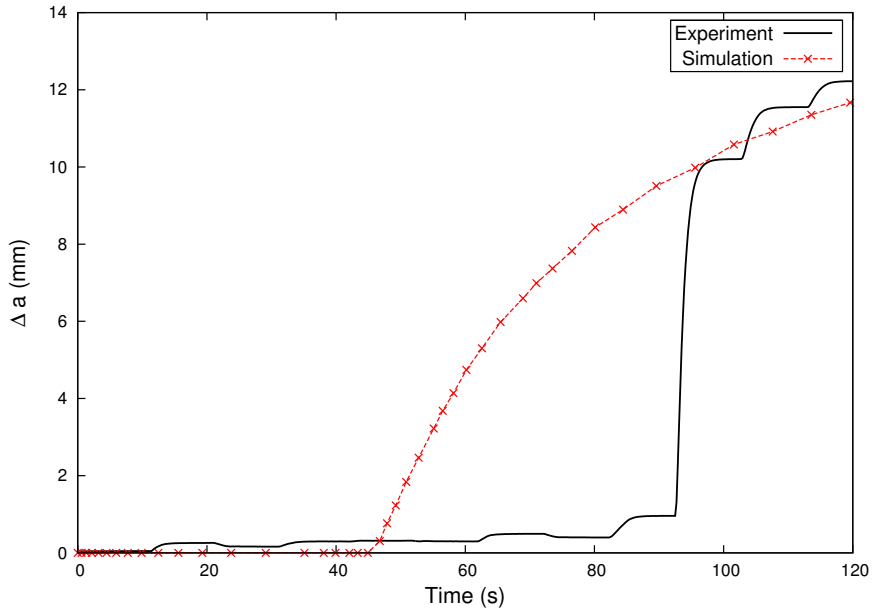

Figure 4.49: Comparison of experimental and simulated crack growth curves.

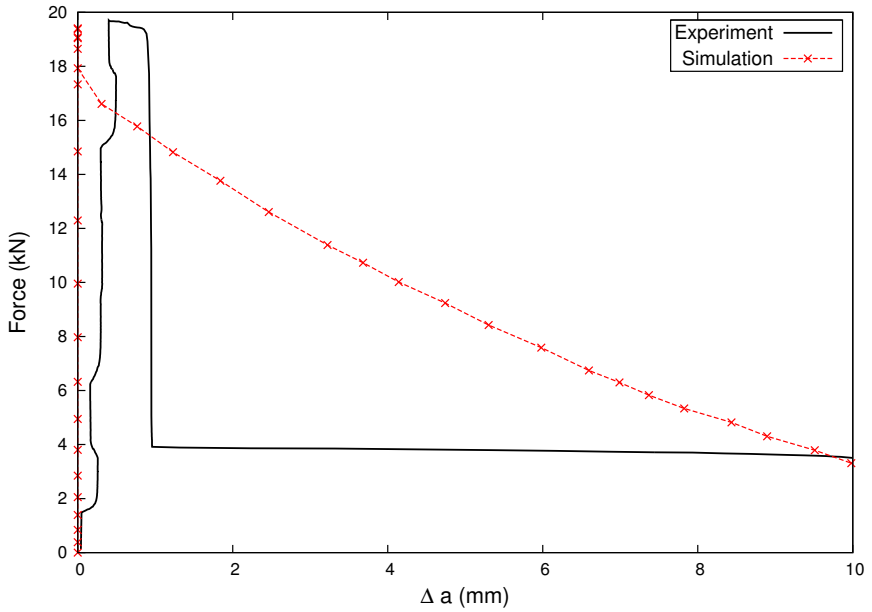

Figure 4.50: Comparison of experimental and simulated load-crack growth curves.

Figure 4.51 illustrates the numerical load-time curve for Grade 4 tested at 1 mm/min with four points marked with the letters a, b, c and d to identify the main parts of the debonding process: (a) elastic loading, (b) onset of fracture, (c) crack propagation and (d) almost complete crack propagation. The corresponding accumulated plastic strain at the interface is presented in Figure 4.52. It can be noted that the plastic zone does not appear around the crack tip during the elastic loading (at point a) contrary to what is expected. Instead, the plastic zone is confined to a very small volume at the edge of a crack plane. The plastic deformation which is normally preceding the crack initiation is almost absent in the present simulations. As a result, the specimen does not experience any plasticity and it breaks much earlier than it was experimentally observed in almost brittle way. Presumably, the discrepancy in the crack growth speed can be attributed to the inability of the present CZ model to account for the rate dependence of the energy dissipated during crack propagation. Although the bulk material's behavior is time-dependent due to the viscoplastic formulation, the CZ law used in the present model is rate-independent, namely, the tractions within the cohesive zone depend only on the surface opening displacements, independently on how fast the material separate. The model does not account for the rate dependence of the interface response and it appears to lose the effectiveness for the simulation of the present time-dependent fracture process. Therefore an alternative approach is needed in order to be able to simulate the phenomenon of SLC in CP α Ti.

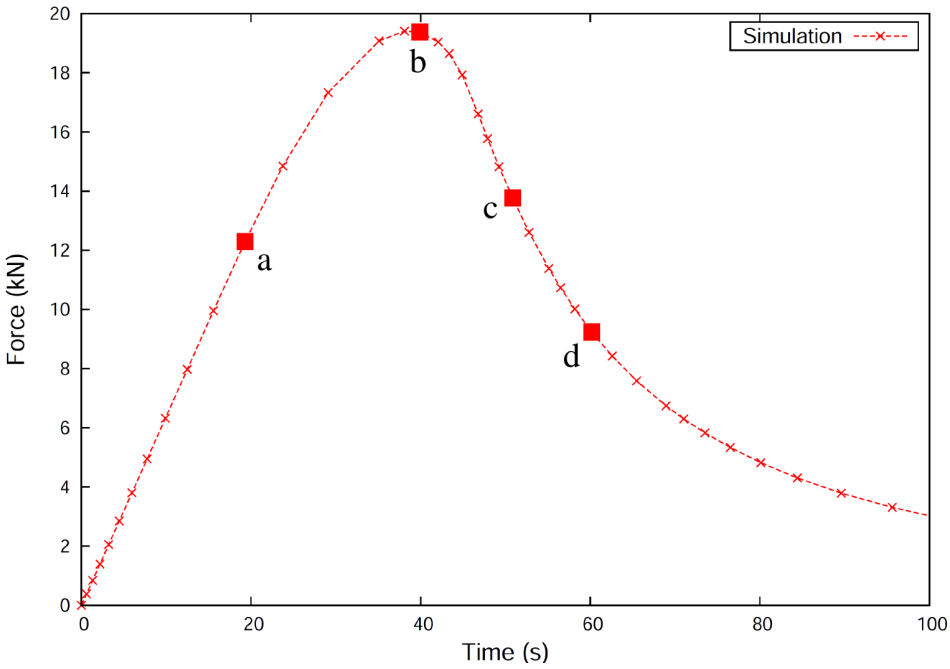

Figure 4.51: Numerically obtained load-time curve for Grade 4 for displacement rate of 1 mm/min showing the points of the debonding process referred to in Figure 4.52.

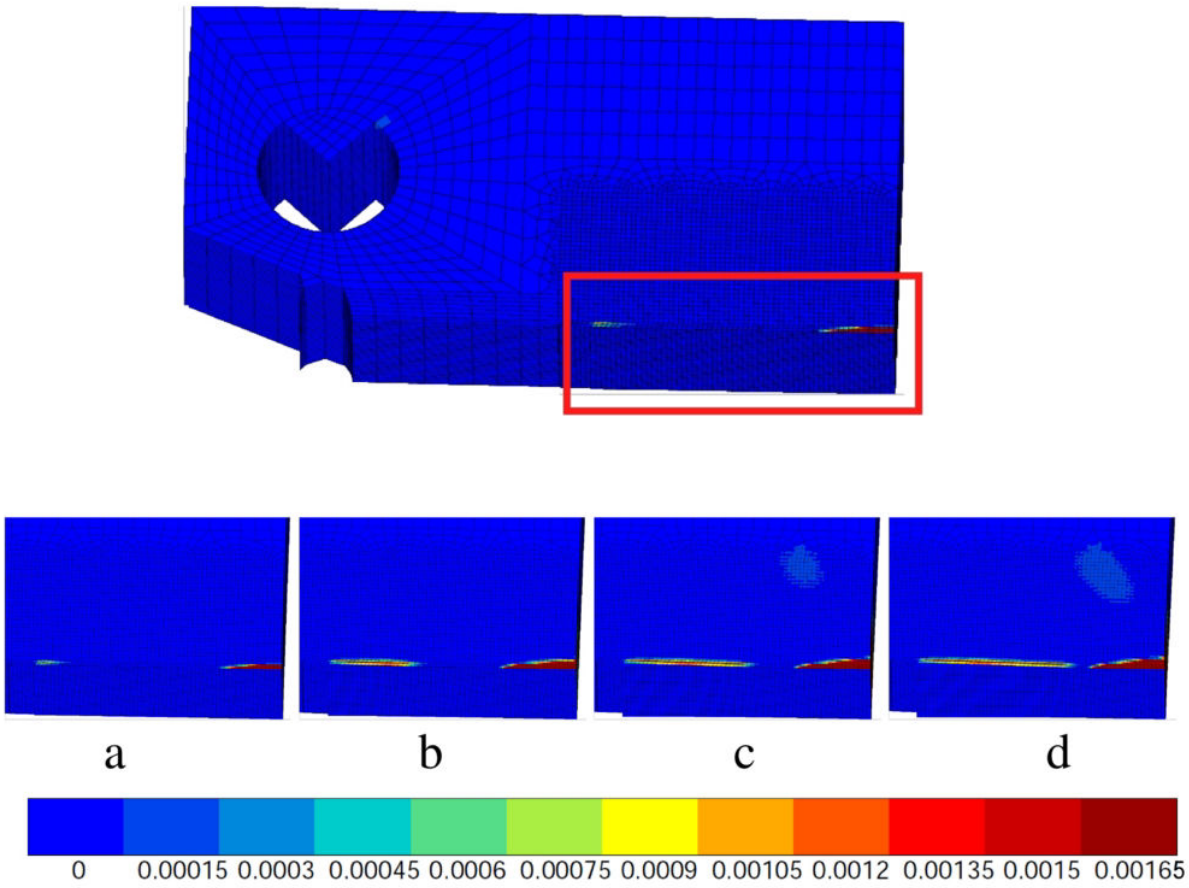

Figure 4.52: Plastic accumulated strain p at the interface.

4.4 Conclusions

The aim of the present chapter was to formulate a constitutive model which incorporates rate dependence of the material into cracking behavior of CP α Ti of Grade 2 and Grade 4. The phenomenological elastic-viscoplastic model was used to analyze the stress and strain fields at the crack tip of CT specimens before and during crack propagation. The main results of the modeling are the following:

- The calculated strain fields under different loading conditions confirm the significance of creep at crack tip, which increases with time and load.
- By assuming that hydrogen concentration in normal interstitial sites is in equilibrium with hydrostatic stress the distribution of hydrogen concentration in the vicinity of a blunting crack tip was analyzed. The numerical results indicate that hydrogen tends to get concentrated ahead of the crack tip where its concentration reaches 12 ppm for Grade 2 and 15 ppm for Grade 4.
- Based on the experimental results described in Chapter 3 and the performed elastic-viscoplastic simulations, an attempt was made to interpret the observed behavior in terms of hydrogen localized plasticity mechanism (HELP). The critical plastic strain at the crack tip was proposed as a criterion of crack propagation in the sustained load cracking tests. According to this interpretation hydrogen increases the plasticity at the crack tip and at the same time it can increase the capacity of the material to overcome plastic deformation before failure, thus increasing the value of the critical strain. As a result, the time to failure in slow cracking is increased for the material with higher hydrogen content.

Next, cohesive zone model of Crisfield was proposed to predict the crack growth for rapidly rising and sustained loading conditions. The results of the numerical simulations showed that the plastic zone was confined to a very small volume at the edge of a crack plane. The plastic deformation which is normally preceding the crack initiation was almost absent in the present simulations. As a result, the specimen did not experience any plasticity and it breaks much earlier than it was experimentally observed in almost brittle way. Presumably, the discrepancy in the crack growth speed can be attributed to the inability of the present CZ model to account for the rate dependence of the energy dissipated during crack propagation.

One way to account for the viscoplasticity in the model of crack propagation under sustained load is to introduce a phenomenological rate-dependent cohesive law. A number of CZM and modelling strategies have been presented covering this approach [222, 223, 57, 6, 120, 113]. The Gurson model [87] is another possibility to model ductile rupture. This model introduces a strong coupling between deformation and damage. The Gurson model was extended for viscoplastic materials [28] assuming that the flow stress σ_f, depends on both the plastic strain p and the plastic strain rate $\dot{p}$.

General conclusions and prospects

In the present study the role of oxygen and hydrogen in the viscoplastic behavior of commercially pure α Ti of Grade 2 and Grade 4 was investigated. The phenomena of static and dynamic strain aging (SSA and DSA) were explored and the physically based scenario of anomalous behavior was suggested. A new phenomenological elastic-viscoplastic aging model coupled with crystal plasticity was proposed to simulate the SSA and DSA effects. Finite element simulations were performed on the polycrystalline aggregates for different number of grains taking into consideration the effect of anisotropy of Ti. A novelty of the simulation approach consisted in the spatio-temporal decoupling of plastic events within the structure at the appropriate scale due to the appropriate crystalline description of the mechanical structure. An additional advantage of the present model which recognizes the crystalline nature of the mechanical structure and thus accounts for the lower symmetry of the HCP crystals was to provide a clear interpretation of the lack of mobility of the SSA and DSA strain localization bands in contrast with their counterparts, usually observed in Fe or Al based alloys, which appear highly mobile and able to cross easily all grain boundaries.

Next, the influence of hydrogen and oxygen on fast and slow cracking behavior in Ti was experimentally studied. The rate-dependent fracture behavior of Ti which is extremely sensitive to many factors such as initial crack length, hydrogen content or imposed strain rate did not allow to draw clear trends from the experimental results. That is why a constitutive viscoplastic model which accounts for material anisotropy of mechanical properties and time-dependent behavior was formulated which permitted to analyze the stress and strain fields at the crack tip in the presence of hydrogen.

An attempt was made to interpret the observed behavior in terms of hydrogen localized plasticity mechanism (HELP). The critical plastic strain at the crack tip was proposed as a criterion of crack propagation in the sustained load cracking tests. According to this interpretation hydrogen increases the plasticity at the crack tip and at the same time it can increase the capacity of the material to overcome plastic deformation before fracture, thus increasing the value of the critical strain. As a result, the time to failure in slow cracking is increased for the material with higher hydrogen content.

Main results

The role of crystallography

The crystallography of hexagonal close-packed α Ti was found to play an important role in the phenomena of static and dynamic strain aging. The experimental studies on commercially pure α Ti of Grade 2 and Grade 4 revealed a yield stress anomaly corresponding to static strain aging peak when the material is loaded in transverse direction. The presence of the stress peak was attributed to the pinning of the activated pyramidal $\langle c+a \rangle$ edge dislocations by the solute atoms of oxygen. At the lower strain rates small serrations on the stress-stain curves typical for the Portevin-Le Chatelier (PLC) effect have been observed in the presence of macroscopic positive strain rate sensitivity (SRS). These serrations were ascribed to the non-planar core of long and rectilinear $< a >$ screw-type dislocations the mobility of which governs the room-temperature deformation of α Ti. The sessile core structure of immobile screw dislocations can recombine into planar, glissile and metastable configurations in one of the three possible glide planes. Thus pinned by their core structure, screw dislocations in this waiting position can be mobilized by the arrival of individual or even more efficiently groups of dislocations that will form dislocation avalanches and generate localized strain bursts. These localized strain bursts imply that locally (on the level of a grain) the value of strain exceeds the macroscopic strain experimentally imposed to the material. Such self-organized critical dynamic events (SOCD) represent the serrations on the stress-strain curve testifying of the negative sign of the local SRS.

The above described mechanisms of SSA and DSA were implemented in the formulation of a mesocopic viscoplastic model coupled with crystal plasticity which enabled to establish the link between the microstructure and the observed mechanical properties. The Finite Element simulations were carried out for flat extruded polycrystalline specimens and on full 3D periodic aggregates. The simulations of SSA gave a good description of the stress-strain curves with a correct prediction of the material anisotropy. The strain field observations revealed complex strain localization phenomena taking place within some grains, that did not lead to the formation and propagation of macroscopic shear bands across the entire specimen. Instead, strain heterogeneities create patterns that are inclined approximately 45° to the LD forming so-called meso-Lüders bands.

Slight serrations corresponding to DSA on both TD and LD specimens were numerically obtained. The numerical model predicts initiation and propagation of macroscopic PLC bands in the expected strain rate domain. Those macroscopic bands are formed due to the cooperative behavior of the grains, where the strain is localized. The PLC effect was obtained even in the presence of positive macroscopic SRS.

The crystallography also defines a significant plastic anisotropic behavior observed in both Grade 2 and Grade 4. Both materials show a higher yield stress when specimens are tested along the TD than along the LD. Such anisotropic mechanical response of the material in LD and TD directions is mainly due to the pronounced texture, which is a consequence of rolling processing. The higher flow stress for the material loaded along TD compared to LD was suggested to be due to the lower amount of favorably oriented grains with the activated $< a >$-type slip which normally governs the plastic deformation of α Ti. In that orientation the accommodation of plastic deformation is occurring due to the activation of $< c+a >$ pyramidal slip, with the highest CRSS which contributes to the higher flow stress recorded in the TD. The simulations results confirmed the role of $< c+a >$ and $< a >$ glide in the observed anisotropic behavior.

The role of viscoplasticity

Viscosity plays a crucial role in the deformation behavior of Ti alloys. Significant viscoplastic behavior was observed in the creep tests on both Ti Grade 2 and Grade 4. The high strain-rate sensitivity (SRS) was confirmed in the tensile tests with tenfold upward/downward strain-rate jumps performed on TD and LD specimens. The identification of the viscoplastic material parameters was complicated since the used viscoplastic flow rule had to account for the wide range of strain-rates, varying from $\varepsilon = 10^{-2}$ s^{-1} in the strain-rate jump tests to $\dot{\varepsilon} = 10^{-8}$ s^{-1} in the creep tests. The low strain rates were favored during the optimization procedure resulting in a better description of the creep tests.

The viscoplasticity of Ti alloys affects the fast and slow fracture behavior. Fracture toughness experiments performed on both grades revealed the dependence of the material response on the loading rates. The viscoplastic behavior was also evidenced in the experiments of sustained load cracking when material was submitted to constant load or constant displacement. The local approach to fracture was used in order to study the viscoplasticity and the crack tip and crack propagation resulting from local damage near the crack tip. The phenomenological constitutive elastic-viscoplastic model was used to assess stress-strain fields at the crack tip of compact tension (CT) specimens before and during the crack propagation. The calculated strain fields under different loading conditions confirmed the significance of creep at the crack tip, which increases with time and load.

An importance of viscoplasticity in the fracture behavior in Ti was confirmed in the simulations of the crack growth with a cohesive zone model (CZM) approach. The results of the numerical simulations showed inability of the present CZM to account for the rate dependence of the energy dissipated during crack propagation and thus emphasized the necessity to introduce rate dependency in a strategy of crack growth modeling.

The role of oxygen

In the present study it was suggested that interstitial atoms of oxygen by interacting with $\langle c + a \rangle$ dislocations can be responsible for the occurrence of the anomalous yield point phenomenon in the samples strained along TD.

Interstitial solute atoms of oxygen were found to significantly alter mechanical behavior of CP α Ti. Interstitially dissolved oxygen strengthens Ti, however detriments materials ductility. An increase in the oxygen content from 1600 ppm in Grade 2 up to 3200 ppm in Grade 4 leads to higher strength. The changes in mechanical properties can be attributed to the interaction between interstitial oxygen atoms and mobile $< c + a >$ dislocations resulting in SSA.

Experimental studies on fast and slow fracture behavior in Ti of Grade 2 and Grade 4 showed that solute oxygen promotes a high strength in Grade 4 resulting in the higher maximum stress intensity factor (designated K_{max}) and better resistance to sustained load cracking (SLC). At the same time, Grade 4 specimens broke in a more brutal way comparing to Grade 2, which confirmed the fact that materials with high tensile strength are usually less ductile. The high strength and eventual quasi-brittle rupture of Grade 4 was attributed to the higher content of oxygen comparing to Grade 2.

The role of hydrogen

The experimental studies on fast and slow crack growth performed on specimens with various hydrogen content clearly showed that increased hydrogen content results in a slight decrease in strength (softening effect) and increase in ductility for both Grade 2 and Grade 4. The frac-

ture toughness decreased with increased hydrogen content whereas the sustained load cracking resistance was increased. Such beneficial effect of hydrogen on SLC behavior was explained in terms of the hydrogen enhanced localized plasticity mechanism which suggests that hydrogen can accelerate the creep at the crack tip which prevents the attainment of the high localized stresses necessary for fracture.

In a continuum mechanics formalism, it was proposed to describe hydrogen softening through a decrease in the initial yield stress dependent on hydrogen concentration. The crack propagation criterion based on the RKR-type micromechanical model which says that fracture occurs when the local opening stress ahead of a crack tip exceeds the critical local fracture strength of the material over a characteristic distance failed to explain of the occurrence of crack delay in the presence of hydrogen in the slow cracking tests. Instead, the assumption of critical deformation was used which suggests that the enhanced creep at the crack tip in the presence of hydrogen can increase the critical plastic strain needed for crack propagation, thus delaying the fracture. The proposed scenario was simulated with elastic-viscoplastic model without crack propagation. The simulation results correctly reproduced the trends observed in the experiments on the material with increased hydrogen content.

Prospects

Short-term perspectives

The present work leads to the following short-term prospects:

- One of the further step of strain aging modeling with the introduced crystal plasticity is to hold actual 3D multiscale crystal plasticity computations based on real grain shapes, orientations and actual neighborhood of grains of real samples in order to accurately determine the local mechanical field in polycrystalline materials as well as stress-strain heterogeneities developed in grains during deformation.
- The identification of the interaction matrix which would enable the correct prediction of the self and latent hardening of different slip systems is highly adviced. Additionally it is important to study the viscosities of different slip systems which variation can be used to improve the understanding of the observed anisotropy and strain rate dependence of the strain rates sensitivity as it was done in the work of Roth [171].
- The identified strain aging model can be used for the simulation of the creep behavior in order to establish the link between the combined influence of residual atoms of oxygen and hydrogen and the viscoplastic behavior of Ti.
- From the experimental point, it would be interesting to conduct the experiments at low strain rates in order to validate numerically predicted PLC bands.
- To continue the numerical investigation of the phenomenon of sustained load cracking in the presence of hydrogen, a formulation of the physically based model which would link the microstructural material response such as void nucleation, growth and coalescence in the presence of hydrogen with the macroscopic continuum deformation model of a cracked geometry is required. The notion of the hydrogen transport and hydrogen diffusion should be introduced into the model. The crack propagation needs to be modeled with an approach which introduces a strong coupling between deformation and damage such as the Gurson model extended for viscoplastic material or CZM approach with an adopted for viscoplastic material traction-separation law.

Long-term perspectives

The following long-term perspectives can be suggested:

- The perspectives of the proposed strain aging model are rather extensive. It can be used to predict the risk of creep-induced failure of engine disks made of Ti and thus improve the safety of the aircraft transport.
- The proposed macroscopic viscoplastic model facilitates the study of the sustained-load cracking phenomenon observed in the parts made of Ti for submarine applications.
- The progress in the understanding of the viscoplatic behavior of Ti can clarify the behavior of zirconium and zinc since these two metals share many characteristics.
- The proposed multiscale approach of hydrogen-related fracture problems could be applied to other metals exposed to a hydrogen environment in various industrial domains.
- Experimental and numerical studies on Ti at high and low temperatures could help to get a better understanding of the physical mechanisms which control the viscoplastic behavior of titanium an Ti alloys.

Appendix A

Crystal lattice notation for HCP materials

A.1 Hexagonal notation

1. Possible notations

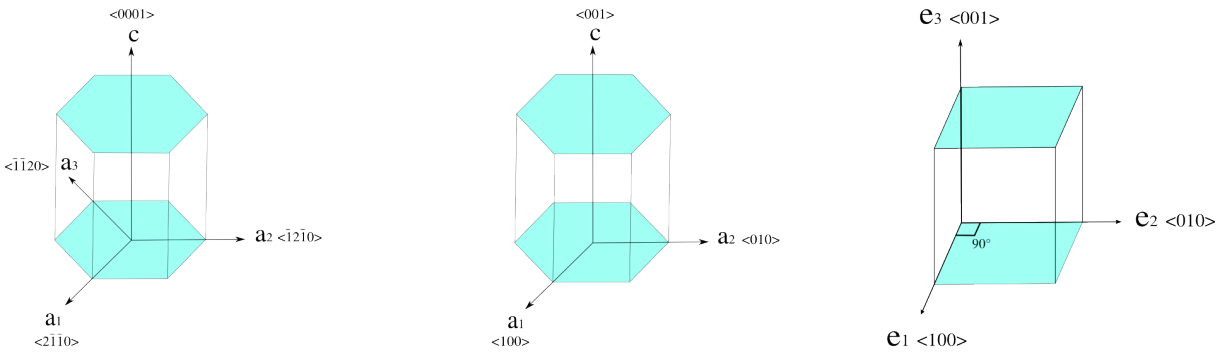

(a) (b) (c)

Figure A.1: (a) hexagonal (4 index) Miller-Bravais notation for unil cell non-orthonormal, (b) primitive hexagonal unit cell (3 index) non-orthonormal and (c) ortonormal hexagonal (3 index).

2. Planes and directions in 3 index Miller notation

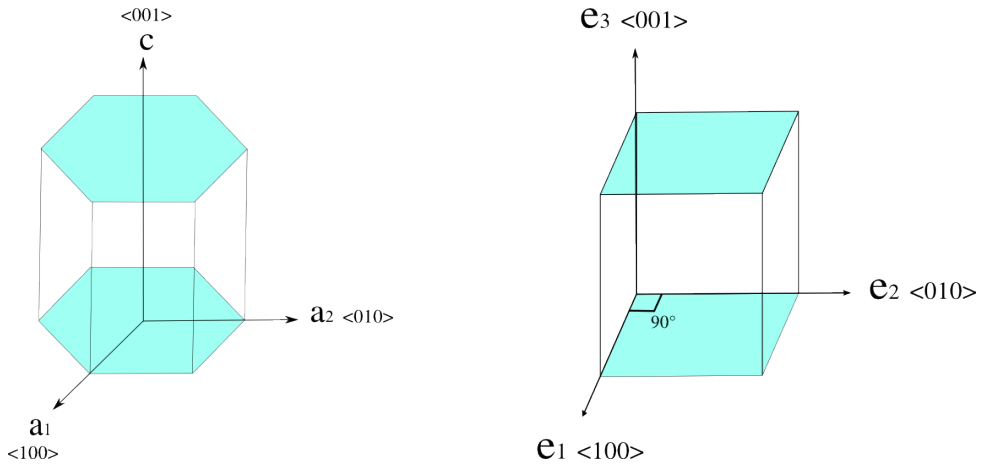

Direction notation:$< uvw >$
Plane notation:$\{hkl\}$
Weiss Zone Law: $hu + kv + lw = 0$
In the hexagonal system with 3 index Miller notation the direction $< uvw >$ is NOT perpendicular to $\{uvw\}$ plane (as in cubic system)

3. Planes and directions in 4 index Miller-Bravais notation

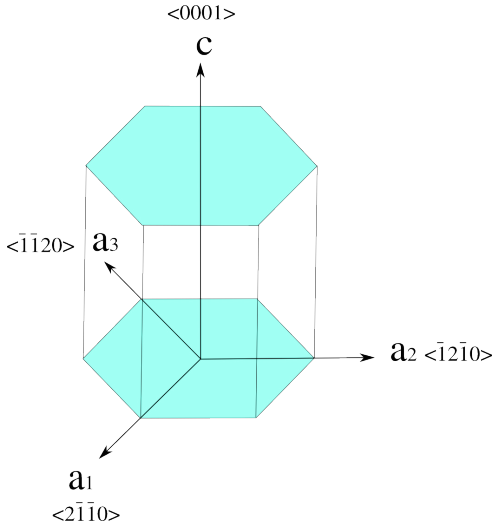

Direction notation:$< UVTW >$
Plane notation:$\{HKIL\}$, $I = -(H + K)$

4. Relation between hexagonal notations
   - From 4 index to 3 index

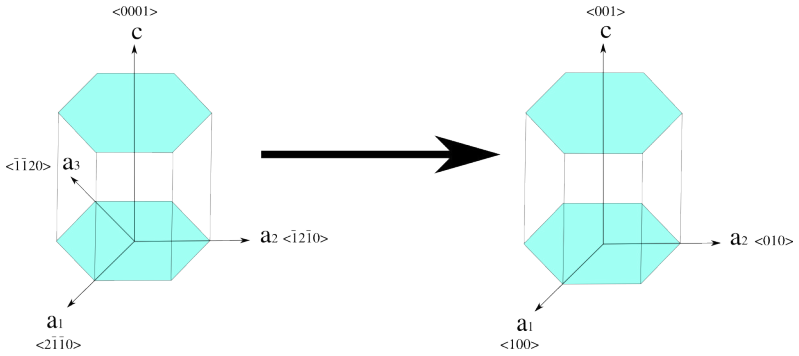

Direction: from $< UVTW >$ to $< uvw >$
$u = U - T$
$v = V - T$
$w = W$
Plane: from $\{HKIL\}$ to $\{hkl\}$
$h = H$
$k = K$
$l = L$

   - From 3 index to 4 index

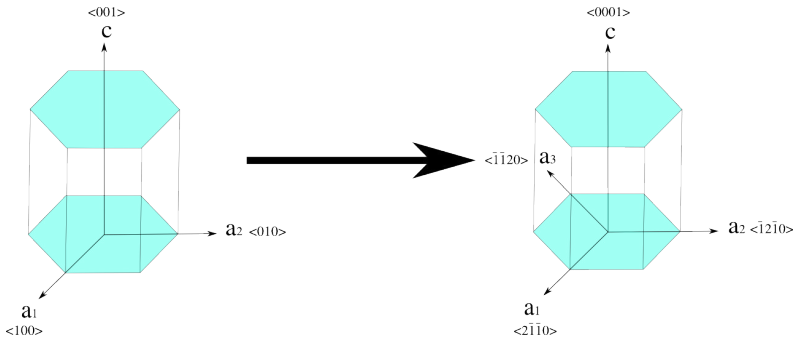

Directions and planes: from $< uvw >$ to $< UVTW >$
$U = 2u - v$
$V = 2v - u$
$T = -(u + v)$
$W = 3w$
Plane: from $\{hkl\}$ to $\{HKIL\}$
$H = h$
$K = k$
$I = -(h + k)$
$L = l$

– From 3 index to 3 index ortohexagonal

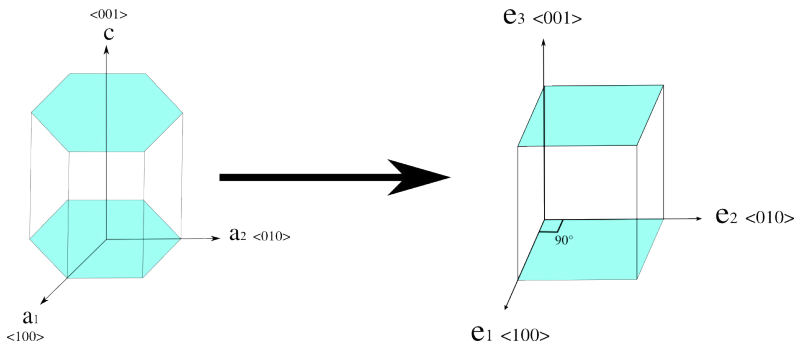

Direction: from $< uvw >$ to $< xyz >$

$$\begin{pmatrix} 1 & -1/2 & 0 \\ 0 & \sqrt{3}/2 & 0 \\ 0 & 0 & c/a \end{pmatrix} \cdot \begin{pmatrix} u \\ v \\ w \end{pmatrix} = \begin{pmatrix} x \\ y \\ z \end{pmatrix}$$

Plane:from $\{hkl\}$ to $\{abc\}$

$$\begin{pmatrix} 1 & 0 & 0 \\ 1/\sqrt{3} & 2/\sqrt{3} & 0 \\ 0 & 0 & a/c \end{pmatrix} \cdot \begin{pmatrix} h \\ k \\ l \end{pmatrix} = \begin{pmatrix} a \\ b \\ c \end{pmatrix}$$

A.2 Schmid factor law

Schmid Law: $|\tau^s| = |\underset{\sim}{\sigma} : \underset{\sim}{m}^s| = \tau_c$

$\underset{\sim}{m}^s = \frac{1}{2}(\underline{l}^s \otimes \underline{n}^s + \underline{n}^s \otimes \underline{l}^s)$

$\underline{n}^s$: normal to the slip plane
$\underline{l}^s$: slip direction

A.3 Examples of analytical calculation of Schmid factor

grain orientation (0. 0. 0.)

load direction [100], c/a=1.587

1. pyramidal slip system $\pi_1 < a > (10\bar{1}1)[1\bar{2}10]$

First method

– Write down the normal to the plane $(10\bar{1}1)$ in the vector form (assuming that the normal to a plane $\{hkil\}$ is $[hki\frac{3}{2}\left(\frac{a}{c}\right)^2 l]$) [1]Partridge

$$\vec{n} = \vec{a}_1 - \vec{a}_3 + \frac{3}{2}\left(\frac{a}{c}\right)^2\left(\frac{c}{a}\right)\vec{c} = \begin{pmatrix} 1 \\ 0 \\ 0 \end{pmatrix} - \begin{pmatrix} -\frac{1}{2} \\ -\frac{\sqrt{3}}{2} \\ 0 \end{pmatrix} + \frac{3}{2}\frac{a}{c}\begin{pmatrix} 0 \\ 0 \\ 1 \end{pmatrix} = \frac{3}{2}\begin{pmatrix} 1 \\ \frac{1}{\sqrt{3}} \\ \frac{a}{c} \end{pmatrix}$$

– The norm of the vector $\vec{n}$
$\|\vec{n}\| = \frac{3}{2}\sqrt{1 + \frac{1}{3} + \left(\frac{a}{c}\right)^2}$
– Write down the direction of slip $[1\bar{2}10]$ in the vector form

$$\vec{d} = \vec{a}_1 - 2\vec{a}_2 + \vec{a}_3 = -3\vec{a}_2 = -3\begin{pmatrix} -\frac{1}{2} \\ \frac{\sqrt{3}}{2} \\ 0 \end{pmatrix} = 3\begin{pmatrix} \frac{1}{2} \\ -\frac{\sqrt{3}}{2} \\ 0 \end{pmatrix}$$

– The norm of the vector $\vec{d}$
$\|\vec{d}\| = 3\sqrt{\frac{1}{4} + \frac{3}{4}} = 3$
– Calculation of Schmid factor
$\frac{3/2 \cdot 3/2}{3/2\sqrt{\frac{4}{3} + \left(\frac{a}{c}\right)^2} \cdot 3} = 0.38$

Second method

– Transformation from 4 index to 3 index notation

$(10\bar{1}1) \rightarrow (101)$

$[1\bar{2}10] \rightarrow [0\bar{1}0]$

– Transformation from 3 index to orthohexagonal (Cartesian coordinates)

$$\begin{pmatrix} 1 & 0 & 0 \\ 1/\sqrt{3} & 2/\sqrt{3} & 0 \\ 0 & 0 & a/c \end{pmatrix} \cdot \begin{pmatrix} 1 \\ 0 \\ 1 \end{pmatrix} = \begin{pmatrix} 1 \\ 1/\sqrt{3} \\ a/c \end{pmatrix}$$

$$\begin{pmatrix} 1 & -1/2 & 0 \\ 0 & \sqrt{3}/2 & 0 \\ 0 & 0 & c/a \end{pmatrix} \cdot \begin{pmatrix} 0 \\ -1 \\ 0 \end{pmatrix} = \begin{pmatrix} 1/2 \\ -\sqrt{3}/2 \\ 0 \end{pmatrix}$$

– Calculation of scalar product

$$cos\alpha = \begin{pmatrix} 1 \\ 1/\sqrt{3} \\ a/c \end{pmatrix} \cdot \begin{pmatrix} 1 \\ 0 \\ 0 \end{pmatrix} = \frac{1}{\sqrt{\frac{4}{3} + (\frac{a}{c})^2}} = 0.76$$

$$cos\gamma = \begin{pmatrix} 1/2 \\ -\sqrt{3}/2 \\ 0 \end{pmatrix} \cdot \begin{pmatrix} 1 \\ 0 \\ 0 \end{pmatrix} = \frac{1}{2}$$

– Calculation of Schmid factor

$$m = cos\alpha \cdot cos\gamma = -\frac{1}{2\sqrt{\frac{4}{3} + (\frac{a}{c})^2}} = 0.38$$

2. pyramidal slip system $\pi_1 < a + c > (10\bar{1}1)[11\bar{2}\bar{3}]$

– Transformation from 4 index to 3 index notation

$(10\bar{1}1) \rightarrow (101)$

$[11\bar{2}\bar{3}] \rightarrow [11\bar{1}]$

– Transformation from 3 index to orthohexagonal (Cartesian coordinates)

$$\begin{pmatrix} 1 & 0 & 0 \\ 1/\sqrt{3} & 2/\sqrt{3} & 0 \\ 0 & 0 & a/c \end{pmatrix} \cdot \begin{pmatrix} 1 \\ 0 \\ 1 \end{pmatrix} = \begin{pmatrix} 1 \\ 1/\sqrt{3} \\ a/c \end{pmatrix}$$

$$\begin{pmatrix} 1 & -1/2 & 0 \\ 0 & \sqrt{3}/2 & 0 \\ 0 & 0 & c/a \end{pmatrix} \cdot \begin{pmatrix} 1 \\ 1 \\ -1 \end{pmatrix} = \begin{pmatrix} 1/2 \\ \sqrt{3}/2 \\ -c/a \end{pmatrix}$$

– Calculation of scalar product

$$cos\alpha = \begin{pmatrix} 1 \\ 1/\sqrt{3} \\ a/c \end{pmatrix} \cdot \begin{pmatrix} 1 \\ 0 \\ 0 \end{pmatrix} = \frac{1}{\sqrt{\frac{4}{3} + (\frac{a}{c})^2}} = 0.76$$

$$cos\gamma = \begin{pmatrix} 1/2 \\ \sqrt{3}/2 \\ -c/a \end{pmatrix} \cdot \begin{pmatrix} 1 \\ 0 \\ 0 \end{pmatrix} = \frac{1}{2\sqrt{1 + (\frac{c}{a})^2}} = 0.2665$$

– Calculation of Schmid factor

$$m = cos\alpha \cdot cos\gamma = 0.2025$$

3. pyramidal slip system $\pi_1 < a + c > (\bar{1}101)[\bar{2}11\bar{3}]$

– Transformation from 4 index to 3 index notation

$(\bar{1}101) \rightarrow (\bar{1}11)$

$[\bar{2}11\bar{3}] \rightarrow [\bar{1}0\bar{1}]$

– Transformation from 3 index notation into orthohexagonal (Cartesian Coordinates)

$$\begin{pmatrix} 1 & 0 & 0 \\ 1/\sqrt{3} & 2/\sqrt{3} & 0 \\ 0 & 0 & a/c \end{pmatrix} \cdot \begin{pmatrix} -1 \\ 1 \\ 1 \end{pmatrix} = \begin{pmatrix} -1 \\ 1/\sqrt{3} \\ a/c \end{pmatrix}$$

$$\begin{pmatrix} 1 & -1/2 & 0 \\ 0 & \sqrt{3}/2 & 0 \\ 0 & 0 & c/a \end{pmatrix} \cdot \begin{pmatrix} -1 \\ 0 \\ -1 \end{pmatrix} = \begin{pmatrix} -1 \\ 0 \\ -c/a \end{pmatrix}$$

– Calculation of scalar product

$$cos\alpha = \begin{pmatrix} -1 \\ 1/\sqrt{3} \\ a/c \end{pmatrix} \cdot \begin{pmatrix} 1 \\ 0 \\ 0 \end{pmatrix} = -\frac{1}{\sqrt{\frac{4}{3} + (\frac{a}{c})^2}} = -0.76$$

$$cos\gamma = \begin{pmatrix} -1 \\ 0 \\ -c/a \end{pmatrix} \cdot \begin{pmatrix} 1 \\ 0 \\ 0 \end{pmatrix} = -\frac{1}{\sqrt{1 + (\frac{c}{a})^2}} = -0.5331$$

– Calculation of Schmid factor

$$m = cos\alpha \cdot cos\gamma = 0.4051$$

A.4 Numerical calculation of Schmid factor via Zebulon

Basal slip $(0001)< 1\bar{2}10 >$		
Plane	Direction	Schmid factor
(0002)	$[1\bar{2}10]$	0
(0002)	$[2\bar{1}\bar{1}0]$	0
(0002)	$[11\bar{2}0]$	0
Prismatic slip $\{10\bar{1}0\} < 1\bar{2}10 >$		
$(10\bar{1}0)$	$[1\bar{2}10]$	-0.433
$(01\bar{1}0)$	$[2\bar{1}\bar{1}0]$	0
$(\bar{1}100)$	$[11\bar{2}0]$	0.433
Pyramidal slip $\pi_1 < a >\{10\bar{1}1\} < 11\bar{2}0 >$		
$(10\bar{1}1)$	$[1\bar{2}10]$	-0.38
$(01\bar{1}1)$	$[2\bar{1}\bar{1}0]$	0
$(\bar{1}101)$	$[11\bar{2}0]$	0.38
$(\bar{1}011)$	$[1\bar{2}10]$	0.38
$(0\bar{1}11)$	$[2\bar{1}\bar{1}0]$	0
$(1\bar{1}01)$	$[11\bar{2}0]$	-0.38
Pyramidal slip $\pi_1 < a + c > \{10\bar{1}1\} < 11\bar{2}3 >$		
$(10\bar{1}1)$	$[2\bar{1}\bar{1}3]$	0
$(10\bar{1}1)$	$[11\bar{2}3]$	0.2026
$(01\bar{1}1)$	$[11\bar{2}3]$	0.4052
$(01\bar{1}1)$	$[\bar{1}2\bar{1}3]$	0.4052
$(\bar{1}101)$	$[\bar{1}2\bar{1}3]$	0.2026
$(\bar{1}101)$	$[\bar{2}113]$	0
$(\bar{1}011)$	$[\bar{2}113]$	0
$(\bar{1}011)$	$[\bar{1}\bar{1}23]$	0.2026
$(0\bar{1}11)$	$[\bar{1}\bar{1}23]$	0.4052
$(0\bar{1}11)$	$[1\bar{2}13]$	0.4052
$(1\bar{1}01)$	$[1\bar{2}13]$	0.2026
$(1\bar{1}01)$	$[2\bar{1}\bar{1}3]$	0

A.5 Comparison of results

pyramidal slip system $\pi_1 < a >$	pyramidal slip system $\pi_1 < a + c >$
Analytical calculation	
0.38	0.4051
Zebulon calculation	
0.38	0.4052
EBSD	
0.32	0.46

Bibliography

[1] D. Ahn, P. Sofronis, and R. Dodds. Modeling of hydrogen-assisted ductile crack propagation in metals and alloys. *International Journal of Fracture*, 145(2):135–157, 2007.

[2] H. Ait-Amokhtar and C. Fressengeas. Crossover from continuous to discontinuous propagation in the Portevin-Le Chatelier effect. *Acta Materiala*, 58(4):1342–1349, 2010.

[3] I. Aitchison and B. Cox. Technical note interpretation of fractographs of scc in hexagonal metals. *Corrosion*, 28(3):83–87, 1972.

[4] A. Alankar, P. Eisenlohr, and D. Raabe. Dislocation density-based crystal plasticity constitutive model for prismatic slip in α-titanium. *Acta Materiala*, 59(18):7003–7009, 2011.

[5] G. Alfano and M. A. Crisfield. Finite element interface models for the delamination analysis of laminated composites: mechanical and computational issues. *International Journal for Numerical Methods in Engineering*, 50(7):1701–1736, 2001.

[6] D. Allen and C. Searcy. A micromechanical model for a viscoelastic cohesive zone. *International Journal of Fracture*, 107(2):159–176, 2001.

[7] M. Amateau, H. Burrier, and L. Ebert. Brittle fracture in alpha-titanium. *Transactions of the ASM*, 59:920–929, 1966.

[8] J. Anderson. *Fracture mechanics: fundamentals and applications.* 3rd ed. Taylor and Francis, 2005.

[9] M. Anvari. *Simulation of dynamic fracture in aluminum structures.* PhD thesis, Norwegian University of Science and Technology, 2008.

[10] ASTM. Standart test method for measurement of fracture toughness. (E1820-11), 2013.

[11] A. Ayman, S. Salem, R. Kalidindi, and R. Doherty. Strain hardening of titanium: role of deformation twinning. *Acta Materialia*, 51(14):4225–4237, 2003.

[12] D. Banerjee and J. Williams. Perspectives on titanium science and technology. *Acta Materiala*, 61(3):844–879, 2013.

[13] S. Banerjee and P. Mukhopadhyay. *Phase Transformations. Examples from Titaniuma dn Zirconium Alloys.* Elsevier, 2007.

[14] F. Barbe, L. Decker, D. Jeulin, and G. Cailletaud. Intergranular and intragranular behavior of polycrystalline aggregates. part 1 : F.e. model. *International Journal of Plasticity*, 17:513–536, 2001.

[15] F. Barbe, S. Forest, and G. Cailletaud. Intergranular and intragranular behavior of polycrystalline aggregates. part 2 : Results. *International Journal of Plasticity*, 17:537–563, 2001.

[16] G. Barenblatt. The mathematical theory of equilibrium cracks in brittle fracture. *Advances in Applied Mechanics*, 7:55–129, 1962.

[17] B. Barkia. *Viscoplasticité á l'ambiante du titane en relation avec ses teneurs en oxygène et hydrogène*. PhD thesis, Ecole Polytechnique, 2014.

[18] B. Barkia, V. Doquet, J. Couzinié, and I. Guillot. Room-temperature creep and stress relaxation in commercial purity titanium-influence of the oxygen and hydrogen contents on incubation phenomena and aging-induced rejuvenation of the creep potential. *Materials Science and Engineering A*, 624:79–89, 2015.

[19] B. Barkia, V. Doquet, J. Couzinié, I. Guillot, and E. Héripré. In situ monitoring of the deformation mechanisms in titanium with different oxygen contents. *Materials Science and Engineering A*, 636:91–102, 2015.

[20] A. Barnoush. *Hydrogen embrittlement*. PhD thesis, Norwegian University of Science and Technology, 2011.

[21] M. Battaini. *Deformation behavior and twinning mechanisms of commercially pure titanium alloys*. PhD thesis, Monash Universtity, 2008.

[22] C. Beachem. A new model for hydrogen-assisted cracking (hydrogen embrittlement). *Metallurgical Transactions*, 3(2):437–455, 1972.

[23] J. Belotteau, C. Berdin, S. Forest, A. Parrot, and C. Prioul. Mechanical behavior modeling in the presence of strain aging. *Fracture of Nano and Engineering Materials and Structures*, 8:827–828, 2006.

[24] A. Benallal, T. Berstad, T. Borvik, A. Clausen, and O. Hopperstad. Dynamic strain aging and related instabilities : experimental, theoretical and numerical aspects. *Eur.J.Mech.*, 25:397–424, 2006.

[25] C. Berdin, J. Besson, S. Bugat, and R. Desmorat. *Local approach to fracture*. Les Presses de l'Ecole des Mines, 2004.

[26] M. Berveiller and A. Zaoui. An extension of the self-consistent scheme to plastically-flowing polycrystals. *Journal of the Mechanics and Physics of Solids*, 26(5-6):325–344, 1978.

[27] J. Besson, G. Cailletaud, J.-L. Chaboche, and S. Forest. *Non-Linear Mechanics of Materials*, volume 167 of *Solid mechanics and its applications*. Springer, 2010.

[28] J. Besson, D. Steglich, and W. Brocks. Modeling of cracks growth in round bars and plane strain specimens. *International Journal of Solids and Structures*, 38:8259–8284, 2001.

[29] M. Bharathi, M. Lebyodkin, G. Ananthakrishna, C. Fressengeas, and L. Kubin. The hidden order behind jerky flow. *Acta Materialia*, 50(11):2813–2824, 2002.

[30] M. P. Biget and G. Saada. Low-temperature plasticity of high-purity α-titanium single crystals. *Philosophical Magazine A*, 59(4):747–757, 1989.

[31] H. Birnbaum and P. Sofronis. Hydrogen-enhanced localized plasticity-a mechanism for hydrogen-related fracture. *Materials Science and Engineering A*, 176(1-2):191–202, 1994.

[32] R. Boyer and W. Spurr. Characteristics of sustained load cracking and hydrogen effects in ti-6al-4v. *Metallurgical Transactions A*, 9A:23–29, 1978.

[33] M. Brandes, M. Baughman, M. Mills, and J. Williams. The effect of oxygen and stress state on the yield behavior of commercially pure titanium. *Materials Science and Engineering A*, 551:13–18, 2012.

[34] M. Brandes and M. Mills. Static recovery in titanium alloys at lower temperatures. *Materials Science and Engineering A*, 387-389:570–575, 2004.

[35] F. Bridier, P. Villechaise, and J. Mendez. Analysis of the different slip systems activated by tension in a $\alpha - \beta$ titanium alloy in relation with local crystallographic orientation. *Acta Materiala*, 53(3):555–567, 2005.

[36] T. Britton, F. Dunne, and A. Wilkinson. On the mechanistic basis of deformation at the microscale in hexagonal close-packed metals. *Proceedings of the Royal Society of London A*, 471:20140881, 2015.

[37] S. Bross, P. Hähner, and E. Steck. Mesoscopic simulations of dislocation motion in dynamic strain ageing alloys. *Computational Materials Science*, 26:46–55, 2003.

[38] B. Brown and C. Beachem. A study of the stress factor in corrosion cracking by use of the pre-cracked cantilever beam specimen. *Corrosion Science*, 5(11):745–750, 1965.

[39] H. Burte, E. Erbin, G. Hahn, and R. Kotfila. Hydrogen embrittlement of titanium alloys. *Metal Progress*, 67:115–120, 1955.

[40] J. Butler. Lüders front propagation in low carbon steels. *Journal of the Mechanics and Physics of Solids*, 10(4):313–318, 1962.

[41] D. Caillard and A. Couret. Dislocation movements controlled by friction forces and local pinning in metals and alloys. *Materials Science and Engineering A*, 322(1-2):108–117, 2002.

[42] D. Caillard and J. Martin. *Thermally Activated Mechanisms in Crystal Plasticity*, volume 8 of *Pergamon Materials Series*. Pergamon, 2003.

[43] G. Cailletaud. A micromechanical approach to inelastic behaviour of metals. *International Journal of Plasticity*, 8(1):55–73, 1992.

[44] G. Cailletaud, O. Diard, F. Feyel, and S. Forest. Computational crystal plastiticy : from single crystal to homogenized polycrystals. *Technische Mechanik*, 23:130–145, 2003.

[45] L. Casarotto, R. Tutsch, R. Ritter, H. Dierke, F. Klose, and H. Neuhauser. Investigation of plc bands with optical techniques. *Computational Materials Science*, 32:316–322, 2005.

[46] T. Cass. *Slip modes and dislocation substructures in titanium and titanium-aluminium single crystals*. The Science, Technology and Application of Titanium. Pergamon Press, 2007.

[47] J. Cheng and S. Nemat-Nasser. A model for experimentally-observed high-strain-rate dynamic strain agin in titanium. *Acta Materialia*, 48(12):3131–3144, 2000.

[48] D. R. Chichili, K. T. Ramesh, and K. J. Hemker. The high-strain-rate reponse of alpha-titanium: experiments, deformation mechanisms and modeling. *Acta Mater.*, 46:1025–1043, 1998.

[49] K. Chihab, Y. Estrin, L. Kubin, and J. Vergnol. The kinetics of the portevin-le chatelier bands in an al-5atalloy. *Scripta Metallurgica*, 21(2):203–208, 1987.

[50] S. Cho and I. Chasiotis. Elastic properties and representative volume element of polycrystalline silicon for mems. *Experimental Mechanics*, 47:37–49, 2007.

[51] Y. Chun, S. Yu, S. Semiatin, and S. Hwang. Effect of deformation twinning on microstructure and texture evolution during cold rolling of cp-titanium. *Materials Science and Engineering: A*, 398:209–219, 2005.

[52] A. Churchman. The yield phenomena, kink bands and geometric softening in titanium crystals. *Acta Metallurgica*, 3:22–29, 1955.

[53] C. Clarke, D. Hardie, and B. Ikeda. Hydrogen-induced cracking of commercial purity titanium. *Corrosion Science*, 39(9):1545–1559, 1997.

[54] E. Clouet. Screw dislocation in zirconium: Ab-initio study. *Physical review B*, 86:144104, 2012.

[55] D. Colas, E. Finot, S. Flouriot, S. Forest, M. Mazière, and T. Paris. Investigation and modeling of the anomalous yield point phenomenon in pure tantalum. *Materials Science and Engineering A*, 615:283–295, 2014.

[56] H. Conrad. Effect of interstitial solutes on the strength and ductility of titanium. *Progress in Materials Science*, 26(2-4):123–403, 1981.

[57] A. Corigliano and M. Ricci. Rate-dependent interface models : formulation and numerical applications. *International Journal of Solids and Structures*, 38(4):547–576, 2001.

[58] A. Cottrell. A note on the portevin-le chatelier effect. *Phil. Mag*, 44:829–832, 1953.

[59] A. Couret and D. Caillard. Dissociations and friction forces in metals and alloys. *Journal de Physique III*, 1(6):885–907, 1991.

[60] J. Crepin, T. Bretheau, and D. Caldemaison. Cavity growth and rupture of β treated zirconium: a crystallographic model. *Acta Materiala*, 44(12):4927–4935, 1996.

[61] M. Dadfarnia, B. Somerday, P. Schembri, P. Sofronis, and J. Foulk. On modeling hydrogen-induced crack propagation under sustained load. *JOM*, 66(8):1390–1398, 2014.

[62] M. Doner and H. Conrad. Deformation mechanisms in commercial Ti-50A (0.5 at.pct O_{eq}) at intermediate and high temperatures (0.3 - 0.6 Tm). *Metallurgical Transactions*, 4(12):2809–2817, 1973.

[63] J. Donoso and R. Reed-Hill. Static strain-aging in commercial purity α titanium. *Metallurgical Transactions A*, 8(6):945–948, 1977.

[64] D. Dugdale. Yielding of steel sheets containing slits. *Journal of the Mechanics and Physics of Solids*, 8:100–104, 1960.

[65] A. Eberle, D. Klingbeil, and J. Schicker. The calculation of dynamic jr-curves from the finite element analysis of a charpy test using a rate-dependent damage model. *Nuclear Engineering and Design*, 198(1-2):75–87, 2000.

[66] C. Efstathiou, H. Sehitoglu, and J. Lambros. Multiscale strain measurements of plastically deforming polycrystalline titanium: Role of deformation heterogeneities. *International Journal of Plasticity*, 26:93–106, 2010.

[67] D. Eliezer, E. Tal-Gutelmacher, and T. Boellinghaus. Hydrogen embrittlement in hydride and non hydride-forming systems-microstructural/phase changes and cracking mechanisms. *International conference on fracture 11*, Turin, 2005.

[68] B. Escaig. L'activation thermique des déviations sous faibles contraintes dans les structures h.c. et c.c. *Physica Status Solidi b*, 28(2):463–474, 1968.

[69] J. Evans and R. Douthwaite. Snoek ordering and rapid strain ageing in iron-nitrogen alloys. *Acta Metallurgica*, 21:49–54, 1973.

[70] S. Farenc, D. Caillard, and A. Couret. An in situ study of prismatic glide in α-titanium at low temperatures. *Acta Metallurgica et Materialia*, 41(9):2701–2709, 1993.

[71] S. Farenc, D. Caillard, and A. Couret. A new model for the peak of activation area of α-titanium. *Acta Metallurgica et Materialia*, 43(10):3669–3678, 1995.

[72] E. Fisher and D. Renken. Single-Crystal Elastic Moduli and the HCP-BCC Transformations in Ti,Zr,and Hf. *Physical Review*, 135(2A):482–494, 1964.

[73] J. W. Flowers, K. O'Brien, Jr., and P. McEleney. Elastic Constants of Alpha Titanium Single Crystals of 25° C. *Journal of the Less-Common Metals*, pages 393–395, 1964.

[74] D. Francois, A. Pineau, and A. Zaoui. *Mechanical Behaviour of Materials. Volume II: Viscoplasticity, Damage, Fracture and Contact Mechanics*. Springer, 2013.

[75] C. Fressengeas, A. Beaudoin, M. Lebyodkin, L. Kubin, and Y. Estrin. Dynamic strain aging: a coupled dislocation-solute dynamic model. *Materials Science and Engineering A*, 400-401:226–230, 2005.

[76] J. Friedel. *Dislocations*. Addison-Wesley, 1964.

[77] R. Gangloff. *Hydrogen Assisted Cracking of High Strength Alloys*, volume 6 of *Comprehensive Structural Integrity*. Elsevier, 2003.

[78] G. Gao and S. Dexter. Effect of hydrogen on creep behavior of ti-6al-4v alloy at room temperature. *Metallurgical Transactions A*, 18A:1125–1130, 1987.

[79] A. Garde, A. Santhanam, and R. Reed-Hill. The significance of dynamic strain aging in titanium. *Acta Metallurgica*, 20(2):215–220, 1972.

[80] M. Ghazisaeidi and D. Trinkle. Core structure of a screw dislocation in ti from density functional theory and classical potentials. *Acta Materiala*, 60(3):1287–1292, 2012.

[81] M. Glavicic, A. Salem, and S. Semiatin. X-ray line-broadening analysis of deformation mechanisms during rolling of commercial-purity titanium. *Acta Mater*, 52:647–655, 2004.

[82] J. Gong and A. Wilkinson. Anisotropy in the plastic flow properties of single-crystal α titanium determined from micro-cantilever beams. *Acta Materiala*, 57:5693–5705, 2009.

[83] S. Graff. *Viscoplastic behavior of zirconium alloys in the temperatures range 20 °C-400 °C: characterization and modeling of strain ageing phenomena*. PhD thesis, Ecole des Mines de Paris, 2006.

[84] S. Graff, S. Forest, J. Strudel, C. Prioul, P. Pilvin, and J.-L. Béchade. Finite element simulations of dynamic strain ageing effects at v-notches and crack tips. *Scripta Materialia*, 52(11):1181–1186, 2005.

[85] S. Graff, S. Forest, J.-L. Strudel, C. Prioul, P. Pilvin, and J.-L. Béchade. Strain localization phenomena associated with static and dynamic strain ageing in notched specimens: experiments and finite element simulations. *Materials Science and Engineering A*, 387-389:181–185, 2004.

[86] J. Gu and D. Hardie. Effect of hydrogen on the tensile ductility of ti-6al-4v. *Journal of Materials Science*, 32:609–617, 1997.

[87] A. Gurson. Continuum theory of ductile rupture by void nucleation and growth: Part i-yield criteria and flow rules for porous ductile media. *Journal of Engineering Materials and Technology*, 99:2–15, 1977.

[88] D. Hardie and S. Ouyang. Effect of hydrogen and strain rate upon the ductility of mii-annealed ti-6al-14v. *Corrosion science*, 41:155–177, 1999.

[89] V. Hasija, S. Ghosh, J. Michael, and S. Joseph. Deformation and creep modeling in polycrystalline ti6al alloys. *Acta Materialia*, 51:4533–4549, 2003.

[90] E. Héripré, M. Dexet, J. Crépin, and L. Gélébart. Coupling between experimental measurements and polycrystal finite element calculations for micromechanical study of metallic materials. *International Journal of Plasticity*, 23:1512–1539, 2007.

[91] F. Hermes. Process zone and cohesive element size in numerical simulations of delamination in bi-layers. Master's thesis, Eindhoven University of Technology, 2014.

[92] A. Hillerborg, M. Modeer, and P. Petersson. Analysis of crack formation and crack growth in concrete by means of fracture mechanics and finite elements. *Cement and Concrete Research*, 6(6):773–782, 1976.

[93] H. Hoeg, B. Hollund, and I. Hall. Effect of hydrogen on the fracture properties and microstructure of ti-6al-4v. *Metal Science*, 14:50–56, 1980.

[94] D. Hull and D. J. Bacon. *Introduction to dislocations*. Pergamon, 1984.

[95] H. Jousset. *Viscoplasticité et microstructures d'un alliage de titane: effets de la temperature et de la vitesse de sollicitation*. PhD thesis, Ecole des Mines de Paris, 2008.

[96] H. Kanayama, M. Ogino, and R. Miresmaeili. Hydrogen transport in a coupled elastoplastic-diffusion anaysis near a blunting crack tip. *Journal of Computational Science and Technology*, 2(4):499–510, 2008.

[97] J. Keeler and A. Geisler. Preferred orientations in rolled and annealed titanium. *Journal of Metals*, 206:80–90, 1957.

[98] P. Kelly and P. Smith. Strain-ageing in Zirconium-oxygen alloys. *J. Nucl. Mat.*, 46:23–34, 1973.

[99] W. Kiessel and M. Sinnot. Creep properties of commercially pure titanium. *Transactions AIME*, 197:331–338, 1953.

[100] D. Knorr and R. Pelloux. Effects of texture and microstructure on the propagation of iodine stress corrosion cracks in zircaloy. *MetTransA*, 13A(1):73–83, 1982.

[101] S. Kok, M. Bharathi, A. Beaudoin, C. Fressengeas, G. Ananthakrishna, L. Kubin, and M. Lebyodkin. Spatial coupling in jerky flow using polycrystal plasticity. *Acta Materiala*, 51(13):3651–3662, 2003.

[102] T. Kostrivas, L. Smith, and M. Gittos. Sustained load cracking in titanium alloys. pages 1–10. Proceedings of OMAE, 2003.

[103] T. Kostrivas, L. Smith, and M. Gittos. Sustained load cracking of titanium alloy weldments. pages 1–10. Proceedings of OMAE, 2005.

[104] J. Krafft. An interpretation of the yoder-griffis-crooker observations of sustained-load cracking in ti-6ai-4v. *Journal of Engineering Materials and Technology*, 96:275–282, 1974.

[105] A. Krom, R. Koers, and A. Bakker. Hydrogen transport near a blunting crack tip. *Journal of the Mechanics and Physics of Solids*, 47:971–992, 1999.

[106] L. Kubin and Y. Estrin. The Portevin-Le Chatelier effect in deformation with constant stress rate. *Acta Metallurgica*, 33(3):397–407, 1985.

[107] L. Kubin and Y. Estrin. Collective dislocation behaviour in dilute alloys and the Portevin-Le Chatelier effect. *Journal of the Mechanical Behavior of Materials*, 2:255–292, 1989.

[108] L. Kubin and Y. Estrin. Evolution of dislocation densities and the critical conditions for the Portevin-le Chatelier effect. *Acta Metallurgica et Materialia*, 38(5):697–708, 1990.

[109] L. Kubin and Y. Estrin. Dynamic strain ageing and the mechanical response of alloys. *Journal de Physique III*, 1(6):929–943, 1991.

[110] L. Kubin, Y. Estrin, and C. Perrier. On static strain ageing. *Acta Metallurgica et Materialia*, 40(5):1037–1044, 1992.

[111] P. Lacombe. Influence of impurities on the mechanical properties of titanium and titanium alloys. volume 4, pages 2705 – 2721. Titanium'84: science and technology, in: 5th Proceedings of the World Conference on Titanium, 1985.

[112] P. Lacombe. L'effet Portevin-Le Chatelier, ses caractéristiques et ses conséquences sur les hétérogénéités de déformation plastique. *Matériaux et Techniques*, 73:5–15, 1985.

[113] C. Landis, T. Pardoen, and J. Hutchinson. Crack velocity dependent toughness in rate dependent materials. *Mechanics of Materials*, 32(11):663–678, 2000.

[114] T. Lebedkina and M. Lebyodkin. Effect of deformation geometry on the intermittent plastic flow associated with the portevin-le chatelier effect. *Acta Materiala*, 56(19):5567–5574, 2008.

[115] B. Legrand. *Influence de la structure électronique sur la facilité relative des glissements dans les métaux de structure hexagonale compacte.* PhD thesis, Université Pierre et Marie Curie., 1984.

[116] H. Li, C. Boehlert, T. Bieler, and M. Crimp. Analysis of slip activity and heterogeneous deformation in tension and tension-creep of Ti-5Al-2.5Sn (wt %) using in-situ SEM experiments. *Philosophical Magazine*, 92(23):2923–2946, 2012.

[117] H. Li, D. Mason, T. Bieler, C. Boehlert, and M. Crimp. Methodology for estimating the critical resolved shear stress ratios of α-phase Ti using EBSD-based trace analysis. *Acta Materiala*, 61:7555–7567, 2013.

[118] Y. Liang, D. Ahn, P. Sofronis, R. Dodds, and D. Bammann. Effect of hydrogen trapping on void growth and coalescence in metals and alloys. *Mechanics of Materials*, 40(3):115–132, 2008.

[119] Y. Liang, P. Sofronis, and R. Dodds. Interaction of hydrogen with crack-tip plasticity: effects of constraint on void growth. *Materials Science and Engineering: A*, 366(2):397–411, 2004.

[120] K. Liechti and J. Wu. Mixed-mode, time-dependent rubber/metal debonding. *Journal of the Mechanics and Physics of Solids*, 49(5):1039–1072, 2001.

[121] Y. Lii, V. Ramachandran, and R. Reed-Hill. Some aspects of the variation of the strain anisotropy in titanium. *Metallurgical Transactions*, 1:447–453, 1970.

[122] G. Lin, A. Cornec, and K. Schwalbe. Three-dimensional finite element simulation of crack extension in aluminum alloy 2024fc. *Fatigue and Fracture of Engineering Materials and Structures*, 21(10):1159–1173, 1998.

[123] W. Lomer. The yield phenomenon in polycrystalline mild steel. *Journal of the Mechanics and Physics of Solids*, 1(1):64–73, 1952.

[124] G. Lütjering and J. Williams. *Titanium*. Springer, 2007.

[125] A. Marais, M. Mazière, S. Forest, A. Parrot, and P. Le Delliou. Identification of a strain-aging model accounting for lüders behavior in a c-mn steel. *Philosophical Magazine*, 92(28-30):3589–3617, 2012.

[126] H. Margolin. Stress, hydrogen segregation, and fracture in a-b titanium alloys. *Metallurgical Transactions A*, 7A:1233–1235, 1976.

[127] G. Martin, L. Nazé, and G. Cailletaud. Numerical multi-scale simulations of the mechanical behavior of β-metastable titanium alloys Ti5553 and Ti17. *Procedia Engineering*, 10:1803–1808, 2011.

[128] M. Mazière, J. Besson, S. Forest, B. Tanguy, H. Chalons, and F. Vogel. Numerical aspects in the finite element simulation of the Portevin-Le Chatelier effect. *Computer Methods in Applied Mechanics and Engineering*, 199:734–754, 2010.

[129] P. McCormick. Theory of flow localization due to dynamic strain ageing. *Acta Metallurgica*, 36:3061–3067, 1988.

[130] C. McMahon and D. Truax. Mechanisms of stress-corrosion cracking of titanium-aluminum alloys in methanol-hcl solutions. *Corrosion*, 29(2):47–55, 1973.

[131] L. Méric, P. Poubanne, and G. Cailletaud. Single crystal modeling for structural calculations. part 1: Model presentation. *Journal of Engineering Materials and Technology*, 113:162–170, 1991.

[132] S. Mesarovic. Dynamic strain aging and plastic instabilities. *Journal of the Mechanics and Physics of Solids*, 43(5):671–700, 1995.

[133] D. Meyn. Cleavage in ti-8al-1mo-1v caused by hydrogen gas. *Metallurgical Transactions*, 3(8):2302–2305, 1972.

[134] D. Meyn. A procedure for investigating the effect of hydrogen content on toughness and sustained lead cracking resistance of titanium alloys, with some results for ti-6ai-4v. pages 1–16. Naval Research Laboratory, 1972.

[135] D. Meyn. Effect of hydrogen on fracture and inert-environment sustained load cracking resistance of α-β titanium alloys. *Metallurgical Transactions*, 5:2405–2414, 1973.

[136] D. Meyn. Effect of hydrogen content on inert environment sustained load crack propagation mechanisms of Ti-6Al-4V. pages 383–392. Environmental degradation of engineering materials in hydrogen, 1981.

[137] D. Meyn and E. Brooks. Microstructural origin of flutes and their use in distinguishing striationless fatigue cleavage from stress-corrosion cracking in titanium alloys. *Fractography and Materials Science ASTM STP 733*, pages 5–31, 1981.

[138] N. Moody and W. Gerberich. Hydrogen-induced slow crack growth in ti-6al-6v-2sn. *Metallurgical Transactions A*, 11(6):973–981, 1980.

[139] N. Moody and W. Gerberich. The effect of stress state on internal hydrogen-induced crack growth in ti-6ai-6v-2sn. *Metallurgical Transactions A*, 13(6):1055–1061, 1982.

[140] S. Naka. *Etude des mecanismes de déformation plastique a basse temperature de monocristaux de titane* α. PhD thesis, Université d'Orsay, 1983.

[141] S. Naka, L. P. Kubin, and C. Perrier. The plasticity of titanium at low and medium temperatures. *Philosophical Magazine A*, 63(5):1035–1043, 1991.

[142] S. Naka, A. Lasalmonie, P. Costa, and L. P. Kubin. The low-temperature plastic deformation of α-titanium and the core structure of a-type screw dislocations. *Philosophical Magazine A*, 57(5):717–740, 1988.

[143] A. Needleman. A continuum model for void nucleation by inclusion debonding. *Journal of Applied Mechanics*, 54(3):525–531, 1987.

[144] D. Nelson, H.G. Williams and J. Stein. Environmental hydrogen embrittlement of an α-β titanium alloy: Effect of microstructure. *Metallurgical Transactions*, 3(1):469–475, 1972.

[145] H. Nelson. Environmental hydrogen embrittlement of an α-β titanium alloy: Effect of hydrogen pressure. *Metallurgical Transactions*, 4(1):364–367, 1973.

[146] S. Nemat-Nasser, W. Guo, and J. Cheng. Mechanical properties and deformation mechanisms of a commercially pure titanium. *Acta Materiala*, 47(13):3705–3720, 1999.

[147] R. Nixon and D. Hawkins. Nature of fluted fracture observed in welds in titanium plate. *Materials Science and Technology*, 5(3):288–292, 1989.

[148] H. Numakura and M. Koiwa. Hydride precipitation in titanium. *Acta Metallurgica*, 32(10):1799–1807, 1984.

[149] R. Oriani. The diffusion and trapping of hydrogen in steel. *Acta Metallurgica*, 18:147–157, 1970.

[150] N. Osipov, A.-F. Gourgues-Lorenzon, B. Marini, V. Mounoury, F. Nguyen, and G. Cailletaud. Fe modelling of bainitic steels using crystal plasticity. *Philosophical Magazine*, 88(30-32):3757–3777, 2008.

[151] J. Pan, M. Saje, and A. Needleman. Localization of deformation in rate sensitive porous plastic solids. *International Journal of Fracture*, 21(4):261–278, 1983.

[152] D. Pao, P.S. Meyn, R. Bayles, F. C.R., and G. Yoder. Effect of ripple loads on sustained-load cracking in titanium alloys. *Scripta Metallurgica*, 33(3):497–501, 1995.

[153] W. Pardee and N. Paton. Model of sustained load cracking by hydride growth in titanium alloys. *Metallurgical Transactions A*, 11A:1391–1400, 1980.

[154] R. Parisot, S. Forest, A.-F. Gourgues, A. Pineau, and D. Mareuse. Modeling the mechanical behavior of a multicrystalline zinc coating on a hot-dip galvanized steel sheet. *Computational Materials Science*, 19(1-4):189–204, 2000.

[155] P. Partridge. The crystallography and deformation modes of hexagonal close-packed metals. *Metallurgical Reviews*, 12:169–194, 1967.

[156] N. Paton and W. Backofen. Plastic deformation of titanium at elevated temperatures. *Metallurgical Transactions*, 1:2839–2847, 1970.

[157] E. Paula, E. Silva, J. Com-Nougue, G. Beranger, and P. Lacombe. Relation entre la cinetique de vieillissement apres deformation du zirconium-α et la diffusion anisotrope de l'oxygene à courte distance. *Scripta Metallurgica*, 5:795–800, 1971.

[158] P. Penning. Mathematics of the Portevin-Le Chatelier effect. *Acta Metallurgica*, 20(10):1169–1175, 1972.

[159] M. Philippe, E. Bouzy, and J. Fundenberger. Textures and anisotropy of titanium alloys. *Materials Science Forum*, 273-275:511–522, 1998.

[160] M. J. Philippe, M. Serghat, P. Van Houtte, and C. Esling. Modelling of texture evolution for materials of hexagonal symmetry - ii. application to zirconium and titanium α or near α alloys. *Acta Metall Mater*, 43:16191630, 1995.

[161] A. Pilchak and J. Williams. Crystallography of fluted fracture in near α titanium alloys. *Metallurgical and Materials Transactions A*, 41:22–25, 2010.

[162] A. A. Pochettino, N. Gannio, C. Vial Edwards, and R. Penelle. Texture and pyramidal slip in ti, zr and their alloys. *Scripta Metallurgica and Materiala*, 27:1859–1863, 1992.

[163] C. Pujol, L. Levy, and L. Allais. Fluage α-zr à 200 °c: comportement macroscopique et approche micro-structurale. pages 13–23, Saclay, 1995. INSTN, Journée d'Etudes sur le Zirconium.

[164] R. Quey, P. Dawson, and F. Barbe. Large-scale 3D random polycrystals for the finite element method: Generation, meshing and remeshing. *Computer Methods in Applied Mechanics and Engineering*, 200:1729–1745, 2011.

[165] D. Raabe, M. Sachtleber, Z. Zhao, F. Roters, and S. Zaefferer. Micromechanical and macromechanical effects in grain scale polycrystal plasticity experimentation and simulation. *Acta Materiala*, 49:3433–3441, 2001.

[166] R. Ritchie and K. Bathe. On the calibration of the electrical potential technique for monitoring crack growth using finite element methods. *International Journal of Fracture*, 15(1):47–55, 1979.

[167] R. Ritchie, J. Knott, and J. Rice. On the relationship between critical tensile stress and fracture toughness in mild steel. *Journal of the Mechanics and Physics of Solids*, 21(6):395 – 410, 1973.

[168] I. Robertson and H. Birnbaum. An hvem study of hydrogen effects on the deformation and fracture of nickel. *Acta Metallurgica*, 34:353–366, 1986.

[169] J. Rose, J. Smith, and J. Ferrante. Universal features of bonding in metals. *Phys. Rev. B*, 28:1835–1845, 1983.

[170] F. Rosi and F. Perkins. Mechanical properties and strain aging effects in titanium. *Transactions American Society Metals*, 45:972–992, 1953.

[171] A. Roth, M. Lebyodkin, T. Lebedkina, J.-S. Lecomte, T. Richeton, and K. Amouzou. Mechanisms of anisotropy of mechanical properties of α-titanium in tension conditions. *Materials Science and Engineering A*, 596:236–243, 2014.

[172] G. Sandoz. Subcritical crack propagation in Ti-8Al-1Mo-1V alloys in organic environments, salt water and inert environments. volume 67, pages 684–690, Houston, Texas, 1969. Proceedings of conference on fundamental aspects of stress corrosion cracking.

[173] D. Sastry and K. Vasu. Dislocation dynamics in α titanium. *Acta Metallurgica*, 20(3):399–405, 1972.

[174] I. Scheider, M. Pfuff, and W. Dietzel. Simulation of hydrogen assisted stress corrosion cracking using the cohesive model. *Engineering Fracture Mechanics*, 75:4283–4291, 2008.

[175] G. Schoeck. Moving dislocations and solute atoms. *Physical Review*, 102:1458–1459, 1956.

[176] G. Schoeck and A. Seeger. The flow stress of iron and its dependence on impurities. *Acta Metallurgica*, 7:469–477, 1959.

[177] A. Seeger. On the theory of the low-temperature internal friction peak observed in metals. *Philosophical Magazine*, 1(7):651–662, 1956.

[178] O. Senkov and J. Jonas. Dynamic strain aging and hydrogen-induced softening in α titanium. *Metallurgical Transactions A*, 27(7):1877–1887, 1996.

[179] S. Serebrinsky, E. Carter, and M. Ortiz. A quantum-mechanically informed continuum model of hydrogen embrittlement. *Journal of the Mechanics and Physics of Solids*, 52(10):2403–2430, 2004.

[180] D. Shechtman and D. G. Brandon. Orientation dependent slip in polycrystalline titanium. *Journal of Materials Science*, 8:1233–1237, 1973.

[181] D. Shih and H. Birnbaum. Evidence of {FCC} titanium hydride formation in β titanium alloy: An x-ray diffraction study. *Scripta Metallurgica*, 20(9):1261–1264, 1986.

[182] D. Shih, I. Robertson, and H. Birnbaum. Hydrogen embrittlement of titanium: In situ tem studies. *Acta Metallurgica*, 36(1):111–124, 1988.

[183] R. Singh and R. Kishore. Hydrogen charging, hydrogen content analysis and metallographic examination in Zr alloys. *BARC report*, pages 1–50, 2003.

[184] F. Siska, S. Forest, G. P., and D. Weygand. Finite element simulations of the cyclic elastoplastic behaviour of copper thin films. *Modelling and Simulation in Materials Science and Engineering*, 15(1):S217–S238, 2007.

[185] J. Snoek. Effect of small quantities of carbon and nitrogen on the elastic and plastic properties of iron. *Physica*, 8(7):711–733, 1941.

[186] P. Sofronis, Y. Liang, and N. Aravas. Hydrogen induced shear localization of the plastic flow in metals and alloys. *European Journal of Mechanics - A/Solids*, 20(6):857–872, 2001.

[187] G. Sposito. *Advances in potential drop techniques for non-destructive testing*. PhD thesis, Imperial College London, 2009.

[188] J. Strudel. Interactions between dislocations and impurities. pages 169–180. Japan-France seminar on fundamental aspects of mechanical properties and microstructure evolution of stainless steels at high temperature, 1984.

[189] M. T. Creep and creep cracking of a heat exchanger component of submarine made of ASTM pure titanium grade 4 and grade 2. volume 5, pages 51–55, London 9-10 Oct., 2003. Royal Institution of Naval Architects, Int. Conf. Advandced Marine Materials, Technologies and Applications.

[190] T. Tabata and H. Birnbaum. Direct observations of hydrogen enhanced crack propagation in iron. *Scripta Metallurgica*, 18:231–236, 1984.

[191] A. Taha and P. Sofronis. A micromechanics approach to the study of hydrogen transport and embrittlement. *Engineering Fracture Mechanics*, 68(6):803–837, 2001.

[192] E. Tal-Gutelmacher and D. Eliezer. Hydrogen-assisted degradation of titanium based alloys. *Materials Transactions*, 45(5):1594–1600, 2004.

[193] C. Teodosiu. *Large plastic deformation of crystalline aggregates.* CISM Courses and Lectures No. 376. Springer Verlag, 1997.

[194] P. Thomason. A three-dimensional model for ductile fracture by the growth and coalescence of microvoids. *Acta Metallurgica*, 33(6):1087–1095, 1985.

[195] P. Thomason. A view on ductile-fracture modelling. *Fatigue and Fracture of Engineering Materials and Structures*, 21(9):1105–1122, 1998.

[196] A. Troiano. The role of hydrogen and other intersititals in the mechanical behavior of metals. *ASM Transactions Quarterly*, 52(1):54–80, 1960.

[197] M. Tsai and J. Howe. Lengthening kinetics of (0110)y-tih precipitates in alpha-ti in the temperature range of 25c to 80c. *Metallurgical Transactions*, 26:2219–2226, 1995.

[198] H. Tsukahara and T. Iung. Finite element simulation of the Piobert-Lüders behavior in an uniaxial tensile test. *Materials Science and Engineering A*, 248:304–308, 1998.

[199] H. Tsukahara and T. Iung. Piobert-Lüders and Portevin-Le Chatelier instabilities. Finite element modelling with ABAQUS. *Journal de Physique IV*, 9:157–164, 1999.

[200] V. Tvergaard. On localization in ductile materials containing spherical voids. *International Journal of Fracture*, 18(4):237–252, 1982.

[201] V. Tvergaard. Effect of fibre debonding in a whisker-reinforced metal. *Materials Science and Engineering*, 125:203–213, 1990.

[202] V. Tvergaard. Material failure by void growth and coalescence. *Advances in applied mechanics*, 27:83–151, 1990.

[203] V. Tvergaard and J. Hutchinson. The relation between crack growth resistance and fracture process parameters in elastic-plastic solids. *Journal of the Mechanics and Physics of Solids*, 40:1377–1397, 1992.

[204] V. Tvergaard and A. Needleman. Analysis of the cup-cone fracture in a round tensile bar. *Acta Metallurgica*, 32(1):157–169, 1984.

[205] A. Vassel. Etude du phenomene de rupture differee dans l'air de l'alliage ta6v. *Journal of the Less-Common Metals*, 69:293–299, 1980.

[206] K. Veevers and W. Rotsey. Effect of irradiation of strain ageing in annealed Zircaloy-2. *J. Nucl. Mat.*, 27:108–111, 1968.

[207] K. Veevers and K. Snowden. Strain ageing of quenched Zircaloy-2. *J. Nucl. Mat.*, 47:311–316, 1973.

[208] H. Wang, C. Berdin, M. Mazière, S. Forest, C. Prioul, A. Parrot, and P. Le-Delliou. Experimental and numerical study of dynamic strain ageing and its relation to ductile fracture of a c-mn steel. *Materials Science and Engineering: A*, 547:19–31, 2012.

[209] R. Wanhill. A consideration of cleavage in alpha titanium. *Acta Metallurgica*, 21(9):1253–1258, 1973.

[210] R. Wanhill. Fractographic interpretation of subcritical cracking in a high-strength titanium-alloy (imi 550). *Corrosion*, 29(11):435–441, 1973.

[211] R. Warda, V. Fidelris, and E. Teghtsoonian. Dynamic strain aging during creep of α zr. *Metallurgical Transactions*, 4:1201–1206, 1973.

[212] M. Wasz, F. Brotzen, R. McLellan, and A. Griffin. Effect of oxygen and hydrogen on mechanical properties of commercial purity titanium. *International Materials Review*, 41(1):1–15, 1996.

[213] J. Weiss, T. Richeton, F. Louchet, and M. Lebyodkin. Evidence for universal intermittent crystal plasticity from acoustic emission and high resolution extensometry. *Physical review B*, 76(22):224110, 2007.

[214] D. Williams. Subcritical crack growth under sustained load. *Metallurgical Transactions*, 5:2351–2358, 1974.

[215] D. Williams. Effects of hydrogen in titanium alloys on subcritical crack growth under sustained load. *Materials Science and Engineering*, 24:53–63, 1976.

[216] J. Williams. Effect of specimen thickness on subcritical crack growth unser sustained load. *Materials Science and Engineering*, 18:149–155, 1975.

[217] J. Williams and M. Blackburn. The identification of a non-basal slip vector in titanium and titanium-aluminium alloys. *Physica Status Solidi b*, 25:K1–K3, 1968.

[218] J. Williams, A. Sommer, and P. Tung. The influence of oxygen concentration on the internal stress and dislocation arrangements in α titanium. *Metallurgical Transactions*, 3(11):2979–2984, 1972.

[219] D. Wilson and B. Russell. Stress induced ordering and strain-ageing in low carbon steels. *Acta Metallurgica*, 7:628–631, 1959.

[220] M. Worswick, Z. Chen, A. Pilkey, D. Lloyd, and S. Court. Damage characterization and damage percolation modelling in aluminum alloy sheet. *Acta Materiala*, 49(14):2791–2803, 2001.

[221] T. Xiaoli, G. Haicheng, Z. Shufen, and C. Laird. Loading mode dependence of deformation microstructure in a high-purity titanium single crystal oriented for difficult glide. *Materials Science and Engineering A*, 189:77–84, 1994.

[222] C. Xu, T. Siegmund, and K. Ramani. Rate-dependent crack growth in adhesives: I. modeling approach. *International Journal of Adhesion and Adhesives*, 23(1):9–13, 2003.

[223] C. Xu, T. Siegmund, and K. Ramani. Rate-dependent crack growth in adhesives ii. experiments and analysis. *International Journal of Adhesion and Adhesives*, 23(1):15–22, 2003.

[224] M. Yeh and J. Huang. Internal hydrogen-induced subcritical crack growth in ti-6al-4v. *Scripta Materialia*, 36(12):1415–1421, 1997.

[225] M. Yeh and J. Huang. Hydrogen-induced subcritical crack growth in ti-6ai-4v alloy. *Materials Science and Engineering A*, A242(1-2):96–107, 1998.

[226] A. Yilmaz. The portevin-le chatelier effect: a review of experimental findings. *Science and Technolology of Advanced Materials*, 12:063001, 16 p., 2011.

[227] G. Yoder, C. Griffis, and T. Crooker. The cracking of ti-6al-4v alloys under sustained load in ambient air. *Journal of Enginering Materials and Technology*, 96(4):268–274, 1974.

[228] M. Yoo, S. Agnew, J. Morris, and K. Ho. Non-basal slip systems in HCP metals and alloys: source mechanisms. *Materials Science and Engineering A*, 319-321:87–92, 2001.

[229] Q. Yu, L. Qi, and T. Tsuru. Origin of dramatic oxygen solute strengthening effect in titanium. *Science*, 347(6222):635–639, 2015.

[230] S. Zaefferer. A study of active deformation systems in titanium alloys: dependence on alloy composition and correlation with deformation texture. *Materials Science and Engineering A*, 344:20–30, 2003.

[231] S. Zhang, P. McCormick, and Y. Estrin. The morphology of Portevin-Le Chatelier bands: finite element simulation for Al-Mg-Si. *Acta Materiala*, 49(6):1087–1094, 2001.

[232] Zset Software. *http://www.zset-software.com*, 1996.

Analyse multi-échelles de la viscoplasticité à froid et de la rupture différée du titane en relation avec ses teneurs en hydrogène et oxygène

Résumé: Le titane et ses alliages qui sont largement répandus dans l'industrie aéronautique, sont concernés par le fluage à température ambiante ce qui conduit à une réduction de la résistance et provoque le phénomène de rupture différée. Une partie des études montrent que ce comportement viscoplastique inhabituel à température ambiante est lié aux phénomènes d'interactions entre les dislocations et les atomes interstitiels comme l'hydrogène et l'oxygène, aussi appelés vieillissement statique et dynamique. Le but de cette étude à la fois expérimentale et numérique multi-échelles est de mieux comprendre les effets souvent antagonistes et en partie couplés de l'oxygène et de l'hydrogène en solution sur le comportement viscoplastique du titane non-allié de phase alpha.
Dans un premier volet, un scenario du vieillissement statique et dynamique dans le titane non-allié de phase alpha est proposé. La présence du pic de traction est attribuée à la ségrégation des atomes interstitiels d'oxygène sur les dislocations coin de vecteur de Burgers $< c + a >$. Dans le cas du vieillissement dynamique les instabilités observées, typiquent de l'effet Portevin-Le Chatelier, sont associées à l'étalement du cœur non planaire des dislocations vis de vecteur de Burgers $< a >$. Une loi de comportement prenant en compte les effets liés aux interactions entre dislocations et atomes en solution a été développée. Le modèle de Kubin-Estrin-McCormick qui permet de prendre en compte l'effet du vieillissement a été étendu au cas de la plasticité cristalline. Les simulations par éléments finis ont été réalisées sur des agrégats polycristallins avec différents nombres de grains.
Ensuite, les essais de fissuration (ténacité et rupture différée) ont été réalisés sur les matériaux bruts, et chargés en hydrogène. Enfin, des simulations numériques de la rupture de ces éprouvettes ont été réalisées pour toutes les conditions expérimentales testées en utilisant le modèle de comportement mécanique macroscopique identifié. Un modèle de zone cohésive a été développé pour la simulation de la propagation des fissures.
Mots clés: titane, ténacité, rupture différée, influence de l'hydrogène et de l'oxygène, vieillissement dynamique et statique, propagation de fissure

Multiscale investigation of room-temperature viscoplasticity and sustained load cracking of Titanium. Influence of hydrogen and oxygen content

Abstract: Widely used for aircraft or rocket engine manufacturing titanium and its alloys are prone to the room-temperature creep that leads to the phenomenon of sustained load subcritical crack growth. One of the major cause of such unusual viscoplastic behavior of titanium is the phenomena of static and dynamic strain aging which represents an interaction between dislocations and interstitial atoms of oxygen and hydrogen. The aim of the present experimental and numerical multiscale study is to investigate the influence of the interstitial hydrogen and oxygen on the viscoplastic behavior and the resistance to sustained load cracking in commercially pure titanium of phase alpha.
In a first step, a scenario of static and dynamic strain aging was proposed. The presence of the stress peak was attributed to the segregation of interstitial atoms of oxygen on the edge $< c + a >$ dislocations. In case of dynamic strain aging, the observed instabilities, typical for the Portevin-Le Chatelier effect, were associated with the non-planar core of screw $< a >$-type dislocations. The crystal plasticity was introduced into the phenomenological model in order to capture the strain aging phenomena and the anisotropy of the mechanical properties. The modeling approach for strain aging suggested by Kubin-Estrin-McCormick is based on the internal variable called the aging time which corresponds to the waiting time of a dislocation in a pinned state. Finite element simulations were then performed on the polycrystalline aggregates for different number of grains.
At the next step, fracture toughness and sustained load cracking tests were performed on the material with different level of hydrogen. Finally, numerical simulations of toughness and sustained load cracking tests using the identified viscoplastic model were carried out for all experimental conditions. A cohesive zone model was then introduced ahead of the crack tip to simulate crack propagation.
Keywords: titanium, toughness, sustained load cracking, hydrogen and oxygen influence, dynamic and static strain aging, numerical crack propagation

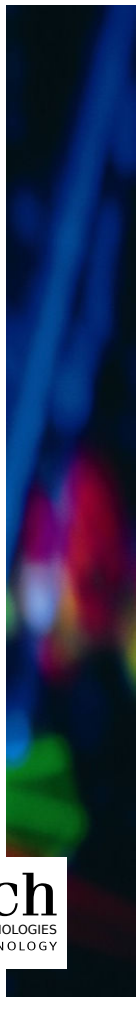

MINES ParisTech

ParisTech
INSTITUT DES SCIENCES ET TECHNOLOGIES
PARIS INSTITUTE OF TECHNOLOGY